

Shape programmable multi-stable polymer actuators

Présentée le 9 mars 2021

Faculté des sciences et techniques de l'ingénieur
Laboratoire des Microsystèmes Souples
Programme doctoral en microsystèmes et microélectronique

pour l'obtention du grade de Docteur ès Sciences

par

Bekir AKSOY

Acceptée sur proposition du jury

Prof. M. Gijs, président du jury
Prof. H. Shea, directeur de thèse
Prof. C. Majidi, rapporteur
Prof. S. Seelecke, rapporteur
Prof. D. Floreano, rapporteur

As you start to walk on the way, the way appears.

– Rumi

Acknowledgements

I am deeply grateful to Prof. Herbert Shea for giving me the opportunity to join his research group and for this continued support, valuable guidance throughout my doctoral study. I deeply appreciate your generosity of the time we spent on our long discussions, critiques, and ideas that has made my research experience productive and fulfilling.

I would like to express my deepest appreciation to Prof. Carmel Majidi, Prof. Stefan Seelecke, and Prof. Dario Floreano, who graciously accepted to review this thesis, and to Prof. Martin Gijs for being the jury president.

On behalf of everyone working on our microfluidic project, I would like to thank Robert Jan Boom, Bas-Jan Hoogenberg, Marko Blom from Micronit Microtechnologies (the Netherlands) for their collaboration and their work on the fabrication of the chip. I would like to give special thanks to Nadine Besse who help me to transfer the approach she developed for the haptics to our microfluidics study. Thank you for the the insights and recommendations. I would also like to thank Olexandr Gudozhnik for his help on the experimental setup.

The support and collaboration of the LMTS members have always been invaluable to me. I would like to thank Mathias Imboden, Alexandre Poulin, Ulas Adiyani, Juan Zarate, Samuel Rosset, Christine de Saint-Aubin, Samuel Schlatter, Xiaobin Ji, Francesca Sorba, Alexis Marette, Rubaiyet Haque, Danick Briand, Vito Cacucciolo, Jean-Baptiste Chossat, Krishna Manaswi Digumarti, Yufei Hao, Robert Marius Hennig, Ronan Julien Hinchet, Jaemin Kim, Djen Timo Kühnel, Marine Le Quang, Brince Paul Kunnel, Michael James Henry Smith, Fabio Beco Albuquerque, James Alec Pierce Bourely, Silvia Demuru, Nicolas Francis Fumeaux, Min Gao, Giulio Grasso, Alessio Mancinelli, Morgan Monroe, Sylvain Thomas Schaller, Ryan van Dommelen, Valentin Py for their support and helpful suggestions, and for the great working environment. A special thank to Myriam Poliero for her very kind help and Edouard Leroy for his help with the experimental setup.

I am grateful to my family and my friend for their unconditional support and encouragement, and Selen for always being there for me.

Neuchâtel, March 2, 2021

B. A.

Abstract

Recent advances in soft actuators have enabled systems that are safer to interact with, better at handling fragile objects, and able to produce complex shapes with fewer components. However, being inherently soft differs these actuators from their rigid counterparts and requires the development of particular approaches to achieve complex and advanced functionalities. This thesis contributes to the soft actuator field through their integration with shape memory polymers (SMPs) to add attributes such as reconfiguration, latchability, and load-bearing. In this study, SMPs are combined with 1) pneumatic, 2) dielectric elastomer, and 3) electromagnetic soft actuators.

I developed a matrix of densely-packed individually addressable latchable microfluidic valves driven with a single pneumatic source combined with SMPs and stretchable heaters. Microfluidic platforms with 4×4 and 4×2 valve matrices in a $15\text{mm} \times 15\text{mm}$ area are demonstrated. The valves are individually addressable and latchable allow extended cycles (> 3000) and long-term latching ($> 15h$). This method enables to increase the number of actuators independently of the pressure controller. It is an effective technique to address the large array of pneumatic actuators and is a promising approach to develop microfluidic large-scale integration systems.

I created reconfigurable and multi-stable soft surfaces by integrating dielectric elastomer actuators (DEAs) with SMP fibers and an array of stretchable heaters. Multiple distinct configurations are dynamically programmed by spatially tuning the rigidity of SMP fibers, locally reducing their stiffness by two orders of magnitude by Joule heating. In this system, the orientation and the location of the soft and hard regions define the deformed shapes when the DEA is actuated. Multimorphing ability is demonstrated by gripping objects with different shapes. Cooling down the SMP fibers locks these shapes into place and allows keeping the device in the actuated state at zero power. I developed an analytical model combining beam theory and shape memory effect to determine the design parameters for large deformations ($> 300^\circ$ tip deflection angle) and high blocking forces ($> 27\text{mN}$).

Finally, I developed shape programmable electromagnetic soft beams with multiple degrees of freedom by embedding liquid metal coils in silicone structure with SMP hinges. Each hinge is individually addressable by Joule heating and can twist or bend depending on the direction of the magnetic field. All types of deformations can be locked by cooling down the SMP layers. When cold, the beam has a robust mechanical structure and allows high blocking forces. Complex shape profiles are achieved through hierarchical deform-and-latch operations, a

Abstract

useful feature for applications that require sophisticated transformations.

Keywords: Reconfigurable active surfaces, latchable soft actuators, dielectric elastomer actuators, electromagnetic soft actuators

Contents

Acknowledgements	i
Abstract	iii
List of Figures	ix
List of Tables	xiii
1 Introduction	1
1.1 Background and motivation	1
1.2 Research objectives	4
1.3 Thesis outline and contributions	6
2 Fundamentals of soft actuators	9
2.1 Summary	9
2.2 Overview of soft actuators	9
2.3 Pneumatic soft actuators (PSA)	13
2.3.1 Working mechanism	13
2.3.2 Fabrication	13
2.3.3 Applications	14
2.3.4 Discussion	15
2.4 Dielectric elastomer actuators (DEAs)	15
2.4.1 Working mechanism	15
2.4.2 Fabrication	16
2.4.3 Applications	16
2.4.4 Discussion	18
2.5 Electromagnetic soft actuators (EMSAs)	18
2.5.1 Working mechanism	18
2.5.2 Fabrication	18
2.5.3 Applications	19
2.5.4 Discussion	20
2.6 Shape memory polymers (SMPs)	20
2.6.1 Working mechanism	20
2.6.2 Applications	21

2.6.3	Discussion	23
2.7	Comparison of soft actuators	23
2.8	Combining soft actuators with shape memory polymers	26
2.8.1	Size scaling of shape memory soft actuators	28
3	Individually addressable and latchable arrays of SMP valves	31
3.1	Summary	31
3.2	Introduction to microfluidic large scale integration (mLSI)	32
3.3	Working principle of SMP valves	33
3.4	Design and modeling of valve array	34
3.4.1	Valve design	34
3.4.2	Operating cycles of normally-open valves	34
3.4.3	Heater design	36
3.4.4	Thermo-mechanical characterization of valves diaphragm	37
3.4.5	Optimization of SMP thickness	38
3.5	Diaphragm fabrication and device assembly	39
3.6	Experimental setup for testing SMP valves	40
3.7	Performance of SMP valves under cyclic and latching operations	40
3.8	Electromechanical degradation of the valve diaphragm	42
3.9	Demonstration of SMP valves as reagent mixer and peristaltic pump	44
3.10	Conclusion	46
4	Development and modeling of reconfigurable and latchable DEAs	49
4.1	Summary	49
4.2	Introduction to shape morphing in DEAs	50
4.3	Main challenges of combining DEAs with thermo-responsive SMPs	53
4.3.1	The effect of temperature on DEA actuation	53
4.3.2	Stiffening effect of the electrodes on the actuation strain	54
4.3.3	Asymmetrical deformation due to fiber stiffening	55
4.3.4	Effect of dielectric prestretch on voltage-stretch behaviour	57
4.3.5	The effect of local temperature change on prestretched DEAs	58
4.3.6	Stress-Strain-Temperature behavior of SMP and non-SMP materials	59
4.4	Reconfigurable and latchable planar DEAs	60
4.4.1	Working principle of planar DEAs	60
4.4.2	Dynamic mechanical analysis of carbon-loaded SMP fibers	63
4.4.3	Finite element model for thermal optimization	63
4.4.4	Analytical model of prestretched planar DEAs for high actuation and locked strains	64
4.4.5	Device fabrication and experimental procedure	70
4.4.6	Experimental results of in-plane deformations and latching	71
4.5	Reconfigurable and latchable shape-morphing DEAs	74
4.5.1	Design concept and working mechanism	74
4.5.2	Design optimization for large deformation and high holding force	76

4.5.3	Device fabrication	80
4.5.4	Multiple latched shapes in a single device	81
4.5.5	Mirror shapes with antagonistic DEAs	83
4.5.6	Model validation using the tip deflection angle and blocking force	85
4.5.7	Using the model to improve the actuation and latching performances . .	87
4.6	Conclusion	89
5	Latchable soft electromagnetic actuators with multi-degree of freedom	91
5.1	Introduction to soft electromagnetic actuators (SEMAs)	92
5.2	Working mechanism of the latchable multi-DoF SEMAs	93
5.3	Thermal limitation of LMC current on SMP material	96
5.3.1	Temperature effect of the LMC current on the choice of SMP material . .	96
5.3.2	The selection of the SMP material	97
5.4	The joints design and SMP thickness optimization	101
5.4.1	Design of the joints and their torsional and bending stiffness	101
5.4.2	Optimization of the SMP thickness for large actuation and latched deformations	103
5.4.3	Heater design	110
5.5	Device fabrication and experimental setup	113
5.5.1	Device fabrication	113
5.5.2	Magnetic field measurement of the plate magnet	114
5.5.3	Experimental setup for actuation and latching tests	115
5.5.4	Experimental procedure to deform and latch operations	116
5.6	Experimental results and discussion	116
5.6.1	Twist-and-latch experiments	116
5.6.2	Bend-and-latch experiments	121
5.7	Picking up objects by sequential deform and latch operations	125
5.8	Experimental validation of the model	126
5.9	Stiffness measurement of the joints	126
5.10	Conclusion and Outlook	128
6	Conclusion and Outlook	133
6.1	Conclusion	133
6.1.1	SMP based latchble microfluidic valve arrays	133
6.1.2	Reprogramming the shape of the dielectric elastomer sheets	133
6.2	Latchable multi-degree of freedom electromagnetic actuator	134
6.3	Outlook	134
6.3.1	Stretchable electromagnetic pump	134
6.3.2	SMP for tunable boundary conditions	135
A	Thermo-mechanical analysis of SMP and SMP+SEBS+CB/PDMS	139
B	Latching planar DEAs at different time scales	141

Contents

C DMA of the membranes of the reconfigurable DEAs	143
D Modeling the actuation and latching of SMP integrated DEAs	145
Bibliography	151
Nomenclature	163
List of Publications	165
Curriculum Vitae	167

List of Figures

1.1	Soft wearable actuators and gentle grippers	2
1.2	Soft actuators with improved shape functionalities	3
2.1	Classification of soft actuators	10
2.2	Pneumatic actuation based soft grippers and haptic gloves	14
2.3	Dielectric elastomer devices	17
2.4	Magnetically responsive soft actuators	19
2.5	Working principle of thermo-responsive SMPs	21
2.6	Shape memory polymer devices	22
2.7	Performance comparison of soft actuators	25
2.8	SMP integrated soft actuators	26
3.1	Microfluidic platform with 4x4 latching SMP valves and the reagent mixer with 4X2 SMP valves.	32
3.2	Working principle of SMP valves.	33
3.3	Normally-open and normally-closed valve designs	35
3.4	Schematics of the valving cycle.	35
3.5	Design of stretchable CB/PDMS heaters	36
3.6	Dynamic mechanical analysis of the SMP.	37
3.7	Thickness optimization of the SMP layer.	38
3.8	Fabrication process flow of SMP valves.	39
3.9	Experimental setup for SMP valves.	40
3.10	The performance of SMP valves under extended cyclic and long-term latching operations.	41
3.11	Electromechanical characterization of the valve diaphragm.	43
3.12	Demonstration of SMP valves as a reagent mixer.	44
3.13	Demonstration of SMP valve array as a peristaltic pump.	45
3.14	Computed pneumatic pressure required to close a valve.	48
4.1	Dynamically reconfigurable and latchable DEAs	50
4.2	Shape programming in DEAs using passive layer and stiff fibers	51
4.3	Shape programming and shape latching in DEAs using variable stiffness SMP fibers	52
4.4	The effects of ambient temperature on the actuation strain.	54

List of Figures

4.5	The effects of the electrode stiffening on the actuation strain.	55
4.6	The effect of fiber stiffening on the actuation strain.	56
4.7	The states of prestretched DEAs	57
4.8	The effects of prestretch and local heating on the actuation strain	58
4.9	Stress-strain-temperature behaviors of materials	61
4.10	The image and exploded view of the reconfigurable and latchable planar DEA .	62
4.11	Working principle of reconfigurable planar DEAs	62
4.12	Young's moduli of SMP and CB-SMP as functions of temperature	63
4.13	Finite element model for thermal optimization	65
4.14	Optimization of fiber cross-section and prestretch	66
4.15	Assembled planar DEA and experimental procedure	70
4.16	Sequentially actuating and latching a DEA in two in-plane directions.	72
4.17	Results cross design	73
4.18	Working principle of multistable reconfigurable dielectric elastomer sheets. . .	75
4.19	Modeling multistable dielectric elastomer sheets for large actuation and latched deformations	76
4.20	Angle of tip deflection at the actuated and latched states	77
4.21	Bending stiffness of curved dielectric elastomer sheets at latched state	79
4.22	Photographs of a device latched at six different configurations.	81
4.23	Deforming and latching a DEA around its vertical and diagonal axes	82
4.24	Pick-and-place objects with different shapes.	83
4.25	Reconfigurable antagonistic DEA	84
4.26	Experimental validation of the modeling using the tip deflection angle and blocking force	86
4.27	The effect of the layers order on the actuation, latching, and load-bearing ability of the devices	88
5.1	Transforming an electromagnetic soft beam into complex shapes by twisting and bending	92
5.2	Working mechanism and device layers of multi-DoF soft electromagnetic beams	95
5.3	Temperature effect of the LMC current on the choice of SMP material.	97
5.4	Young's moduli of low T_g and high T_g SMP materials as functions of temperature	98
5.5	Temperature of the joints and the electromagnetic force as functions of LMC current	99
5.6	Design of joints and their bending and torsional stiffness as functions of temper- ature	102
5.7	Calculation of electromagnetic torque on twisted segments	104
5.8	Optimization of SMP thickness for large torsional deformation in actuation and latched states	105
5.9	Calculation of electromagnetic force for bent segments	107
5.10	Optimizing SMP thickness for large bending deformation at actuation and latched states	109

5.11	Temperature difference between the SMP layers in different heater designs . . .	111
5.12	Measured temperature difference between the SMP layers in one-heater design	112
5.13	The fabrication flow process of the soft electromagnetic devices	113
5.14	Magnetic field measurement of a permanent magnet	114
5.15	Experimental setup used for actuation and latching experiments	115
5.16	Experimental procedure of deform-and-latch cycle	117
5.17	Twist-and-latch experiments at different LMC currents	118
5.18	Joints temperature during the actuation and shape fixation steps.	119
5.19	Sequentially twisting and latching of three joints	120
5.20	Bend-and-latch experiments	122
5.21	Sequential bending and latching of the joints	123
5.22	Complex shape achieved by twisting and bending	124
5.23	Picking up objects by deforming and latching through different joints	125
5.24	Experimental validation of the model	127
5.25	Stiffness measurement of the joints at room temperature	129
6.1	Stretchable electromagnetic pump	135
6.2	Reconfigurable buckled actuators using SMP and liquid-metal	136
A.1	Young's moduli of SMP and SMP+SEBS+CB/PDMS vs. temperature	139
B.1	Strain evolution in a latched DEA at different time scales	142
C.1	Thermo-mechanical characterization of the membranes of the reconfigurable DEAs	144
D.1	Stress-strain-temperature diagram of thermo-responsive SMPs and of the materials without shape memory effect	146

List of Tables

2.1	Critical factors determining the choice of soft actuation mechanism	23
2.2	Performance comparison of soft actuators.	30
4.1	Stretch values and cross-sectional areas of the membranes at different states. .	67
4.2	Material parameters used in the analytical model for tip deflection angle	78
4.3	The dimensions and the Young's moduli of the materials used in the analytical model for the calculation of the bending stiffness	79
4.4	The dimensions of the final geometry	80
5.1	Materials parameters used in FEM for thermal analysis	100
5.2	Parameters used in electromagnetic force calculation	100
5.3	Materials parameters used in the FEM simulation for thermal analysis	110

1 Introduction

1.1 Background and motivation

Polymer based actuators have enabled soft machines that are better at handling very fragile objects, safer to interface the machines with living organisms, and able to perform complex tasks with fewer components. Their soft nature allows compliant wearable technologies which are nearly imperceptible to human senses as shown in Figure 1.1a. [1] The manipulation of delicate and fragile objects becomes more convenient with the low contact pressure between the polymer actuator and the object, ensuring the minimal harm to manipulated object, e.g. Figure 1.1b shows a gentle and secure grasping of a jellyfish using a pneumatic soft actuator. [2]

The soft machines achieve a rich variety of functionality through simple shape changes unlike their rigid counterparts which function through the rotation or translation of joints and gears. The combination of complex 3D shapes and surface-related functionalities has a wide range of applications in biotechnology, actuators/sensors, and engineering of complex metamaterials. [3] Dynamic control of the shape can bring multifunctionality to devices and therefore is of the utmost importance. [4] Developing approaches to produce well-described shape morphings can broaden their mechanical functionalities and advance their abilities.

Two examples are selected to demonstrate the improvement of shape functionalities by the fiber stiffening and by electroadhesion. The actuators with patterned fibers are shown to evolve into unique shapes upon electrical actuation, enabling flexible designs of gripping actuators for soft robotics (see Figure 1.2a). [5] By morphing the soft actuator into desired shapes enables to hold various objects which are challenging to grasp with only one shape transformation. Figure 1.2b shows the improved shear holding force with the fringing electric field of the patterned electrodes in a dielectric elastomer actuator. [6] These fringe fields create electroadhesion forces on the object surface in contact, generating substantial holding forces in the gripper. This way the low force limitation in soft structures is greatly improved for lifting load while the clamping pressure is kept low, proving to be a promising candidate for manipulating delicate objects.

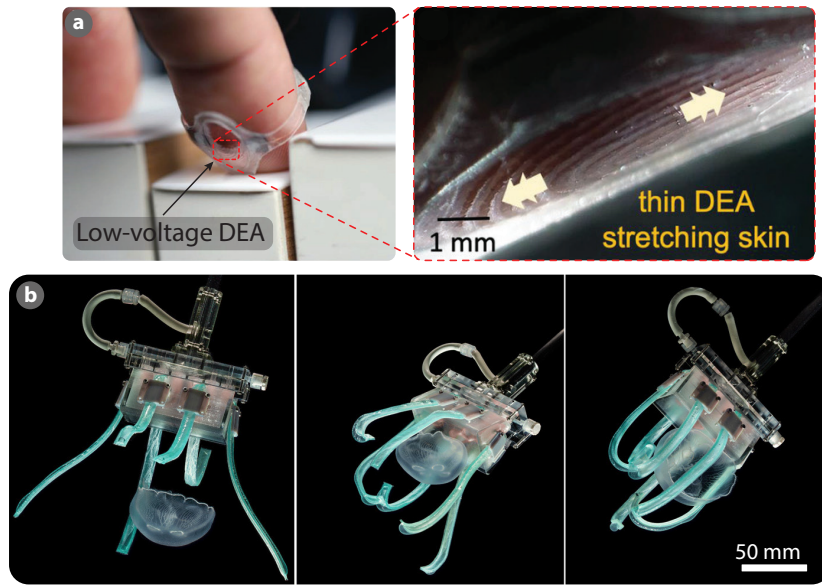


Figure 1.1: Soft actuators are safer to interact with and more gentle to manipulate delicate organisms. a) Playing the piano while wearing a dielectric elastomer based haptic actuator that stretches the fingertip ridges when actuated. [1] b) A pneumatic based soft gripper carefully grasping and releasing a jellyfish. [2]

Performing complex function with the compliant soft actuators requires high efficiency, strength-to-weight ratio, work capacity, and shape programmability. Like an artificial muscle, soft actuators with these properties would substantially advance technologies for potential applications in aerospace, robotics, medical devices, energy harvesting devices, and wearables. [7] Research in soft robotics and wearable technologies has led to increasing demand for shape-changing materials. [8] An advanced material system that combines most of these functionalities outperforms the traditional ones. Developing a material systems to achieve reconfiguration, latchability, and load-bearing is utmost crucial and yet challenging. Because being inherently soft differs these actuators from their rigid counterparts and requires development of particular approaches to achieve complex and advanced functionalities.

Although polymer based actuators allows highly compliant devices for various applications ranging from soft robotics to microfluidics, they are limited to low the number of transducers, are weak at withstanding the external loads, and lack the latching ability. For example, the soft devices based on pneumatic or dielectric elastomer actuation generally have a single actuator or a few coupled actuators driven by the same control signal. [9] Soft pneumatic actuators have bulky components for controlling the pressure. Dielectric elastomer actuators, as another example, require driving voltage in the kV range, limiting the possible applications mostly due to the cost and large size of the control electronics. [10] Increasing the number of these soft actuators and individually controlling them is therefore a challenging task.

The soft nature of the polymer actuators enables compliance systems suitable for haptics and

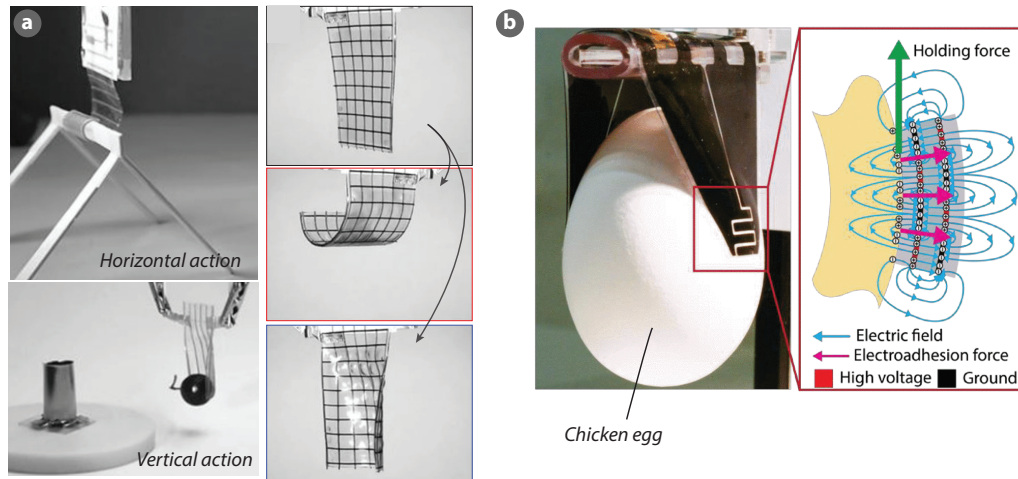


Figure 1.2: Soft actuators with improved shape functionalities. a) The elastomer actuators bend to conform to the shape of both a grape and a wood-beam structure. A dielectric elastomer sheet with two stiff fibers sets and two actuators bend with a vertical curvature when the side with horizontally aligned fiber is actuated and bends with a horizontal curvature when the side with vertically aligned fiber is actuated. [5] b) The fringing electric fields is optimized to generate electroadhesion forces on the object surface in contact, which are used to generate substantial holding forces in the gripper. [6]

soft robotics. They can achieve very large deformations with small forces. However, this makes these soft devices very weak against the external loads. Controlling their stiffness, e.g. very soft during the actuation and very stiff once the actuation is achieved, would overcome the load-bearing issue and would open the doors for more applications. Developing compliant, robust as well as load-bearing soft actuators is utmost crucial and yet difficult to achieve. Another drawback of the soft actuators is that they return to their initial (undeformed) positions once the stimulation (power) is removed. To keep them in their actuated states for the long period of the time requires a continuous power. This can trigger some failure mechanisms such as delamination between the layers under a continuous pneumatic pressure or electrical breakdown of dielectric elastomer actuators under high DC electric field.

Shape memory polymers offers appealing features to overcome these drawbacks of the soft actuators and to develop the ideal reconfigurable actuator arrays that can instantly change both their shapes and their mechanical properties. They have tunable stiffness with various stimuli, can be programmed in different formations, and allow high holding forces. While SMPs have been used for reversible shape changes in medical implants and haptic taxels, they have not been implemented for reconfigurable complex and multiple distinct shapes control. This thesis combines thermo-responsive shape memory polymers with soft actuators to develop hybrid devices that 1) can be instantly reconfigured for any complex shape transformation, 2) can fix their deformation for any given configuration without a continuous power, and 3) can withstand high external loads while maintaining its programmed shape.

The hybrid approach that I have developed throughout the my doctoral study allows both the reconfiguration and shape memory abilities and can be adapted for various soft actuation

mechanisms. This can lead to novel perspectives in the emerging fields of the soft robotics and haptics. The weakness of soft actuators against the external forces, for example, can be overcome with these variable stiffness actuators. The multi-degrees of freedom soft electromagnetic beams that we developed can hold objects (252 g) that are 126 times heavier than the actuator weight (2 g). Since these hybrid devices can be operated in their soft deformable states and can be locked in their rigid load-bearing states they can take advantages of both soft and rigid actuators. This will bridge the gap between the conventional and soft robotics, offering the advantages of both fields.

The reconfiguration ability of these hybrid actuators is an appealing method for transforming two-dimensional (2-D) structure into 3-D shapes and contours, which can be used to create physically 3-D visual displays for human-computer interaction. [11] Combining shape-changing interfaces with controllable surface stiffness would augment our interaction with digital information (more interactive platforms) and would create novel interaction paradigms in this field. This way we can not only feel the surface of the virtual object but also their surface rigidity and textures. Reconfiguration of topologies can do more than just change the shape profile; it can also transport objects on its surface. [12] This may be accomplished, for instance, by creating wavelike profiles that cause the object to roll or slide in the desired direction, which can easily be achieved using the method we have developed.

1.2 Research objectives

The main objective of this thesis is to advance the mechanical functionalities of the soft actuators by combining them with the shape memory polymers. Two main focused areas of the improvement are the shape reconfiguration (reprogrammable shapes), the shape fixation, and the blocking force. The reconfiguration enables us to transform the polymer actuators into desired shapes with more conformal wrapping of object with multi-degrees of freedom. The shape fixation allows us to latch the actuators in any given deformed state with high blocking force. The latching also helps us to keep the device in the actuated state for long periods of time which can prevent the actuator failures due to long-term DC actuations.

This thesis specifically focuses on the integration of thermo-responsive shape memory polymers with the pneumatic, the electric elastomer, and electromagnetic soft actuators. In all integrations, the actuators become more robust that can withstand high external loads and they can be reprogrammed to achieve multiple stable shapes. Each integration also brings unique advantages, e.g. the number of pneumatic actuators can be significantly increased independent of pneumatic source which greatly reduced the size of the setup.

The advantages of combining SMP with soft actuators are listed as:

- **Increased load-bearing ability:** Shape memory polymers can be very soft at above their glass transition temperature and very rigid at room temperature. When their deformation is fixed by the SMP layers at low temperatures, they mechanically improve

the robustness of the actuators, becoming less sensitive to environmental variation and also can withstand high external forces.

- **Zero-power actuated states:** The shape fixation ability of the SMPs can allow us to mechanically latch the device in the actuated position. This way we confine the energy consumption into the actuation step only and can remove the power source when the actuation is achieved. This enables more energy efficient systems where long-term actuation is needed, e.g. this eliminates the need of applying continuous power to hold a position.
- **Arraying / scalability:** Sometimes its difficult to array soft actuators as their stimuli source or control unit does not allow an easy scaling. Pneumatic soft actuators, for instance, require pumps and pressure regulating units which are generally bulky. If we want to make a set of pneumatics actuators, then we need a separate pump and regulator to individually control each actuator in the array, which is usually impractical. Integrating SMP with an array of soft actuators enables us to use different addressing systems for selective actuation, e.g. electrical addressing instead of pneumatic addressing.
- **Reconfigurability / tunable boundary conditions:** When a SMP is integrated with a soft actuator, the overall rigidity of this integration is generally determined by the stiffness of SMP. As the Young's modulus of the SMPs can be tuned using a stimuli, we can easily change the mechanical stiffness of the integration. We can use SMPs as structural materials for soft actuators and by adjusting their properties we can modify their of the boundaries, e.g. SMP can be used as a frame for prestretched DEAs.

The integration of stimuli responsive SMPs with the soft actuators, on the other hand, introduces some challenges to be addressed:

- **Integrated stimuli source:** Every SMP requires a stimulus source for its actuation. When it is combined with a soft actuator, the stimulus source needs to be integrated to the system and also needs to be synchronized with the other components. Therefore, the requirements should be analysed in detail and the SMP type needs to be chosen carefully.
- **Fabrication complexity:** Combining SMPs with soft actuators usually requires a fabrication recipe of multilayered structures, i.e. layers for dielectric elastomer + SMP layer + layer for soft heaters (for thermo-responsive SMPs). Depending on the fabrication method, there are several challenges in multilayer fabrication, e.g. de-lamination between the layers, surface properties between the adjacent layers, solvent suitability of different layers, curing conditions.
- **Stiffening effect of SMPs:** The soft actuators usually generate limited forces. Attaching a SMP layer to these actuators induces a stiffening effect on the device performance, reducing the achievable deformation. The stiffening effect due to any additional layer, therefore, should be taken into account. Since SMPs are usually stiffer than the materials used for soft actuators, a through-out analysis and calculation is required to minimize the performance loss.

- **Increasing time response:** This is a crucial aspect when combining SMPs with fast soft actuators, i.e. SMP + DEAs. SMP integration increases the time response of these systems. How fast we can actuate them is now limited by the time constant of the SMP. To make these devices fast enough, we need to design an efficient method to apply stimuli.

1.3 Thesis outline and contributions

This thesis builds on the integration of shape memory polymers with the polymer actuators, namely pneumatic, dielectric elastomer, and electromagnetic soft actuators, and advances the field by developing and demonstrating practical applications in microfluidics and soft robotics. The thesis consists of four parts; the introductory chapter covers the fundamentals of commonly used soft actuators and the novel contributions of the thesis are categorized in the following three chapters.

Chapters 2: Fundamentals of soft actuators

This chapter covers the fundamentals of commonly used soft actuators, qualitatively and quantitatively compares their performance. Special attention is given to the pneumatic, dielectric elastomer, and electromagnetic soft actuators, which are the actuation mechanisms used in this thesis. The chapter is followed with a discussion on how to improve the mechanical functionalities of the soft actuators by integrating them with shape memory polymers and highlight the challenges of this integration.

Chapter 3: Individually addressable and latchable arrays of SMP valves

This chapter introduces the microfluidic platforms consisting of matrix of densely-packed latchable valves driven by a single pneumatic source, as a promising approach to develop microfluidic large-scale integration systems. The chapter covers the design, fabrication, and the testing of the SMP microfluidic valves. The performance of the valves is investigated under the extended cyclic as well as the long-term latching operations. A peristaltic pump and a reagent mixer that use the same working principle are presented.

As large arrays of microfluidics valves can be individually controlled by a single pneumatic source, our approach offers a promising alternative to the microfluidic multiplexing for large scale integration. Microfluidic multiplexing aims to address large numbers of valves with fewer controller units, e.g. the binary multiplexer developed by Thorsen et al. addresses up to $2^{n/2}$ using n pneumatic control lines. [13] Although the multiplexing method reduces the number of the pneumatic controllers, it still requires multiple pneumatic pressure sources and regulators, especially when the large numbers of valves are needed. Our approach eliminates the need for multiplexing and replaces the cumbersome pressure controllers with the electronic drivers to individually address each valve. This enables downscaling of the device footprint while accommodating multiple arrays of valve units, an important step towards a simple and compact high-density microfluidic chips.

Chapter 4: Reconfigurable and latchable dielectric elastomer actuators (DEAs)

This chapter demonstrates two different dielectric elastomer based devices that can be dynamically reconfigured to obtain different actuation shapes and have ability to lock their deformed shapes into place. The first device is a prestretched planar DEA that enables a selective deformation in two in-plane directions. The second device is a multimorph soft DEA sheet with ability to deform in various distinct configurations and has an increased blocking force at its latched state.

The chapter is divided into three sections: Section 1 explains the constraints and the theory of combining dielectric elastomer with the thermo-responsive shape memory polymers.

Section 2 explains the design, fabrication, and testing of the planar DEA, which can deform in preferential in-plane directions and can be latched in the deformed shape.

Section 3 demonstrates the multimorph soft DEA and pick-and-place demonstrations of the objects with different shapes. The section also details the optimization of the design parameters and provides a design guide for large deformation and high blocking force/

These hybrid actuators will enable us to morph planar membranes into more complex 3D structures and to keep the deformed shapes with zero-power. Since this method allows a dynamic and spatial stiffness tuning, any desired topology can be constructed. These reconfigurable surfaces can physically augment graphical contents through shape transformations and such displays could be used to physically explore data or for navigating on shape-changing maps. [14] The surface change ability can be adapted in numerous applications for different purposes such as

camouflaging: changing their appearance in order to hide or integrate with the surrounding environment

adaptation: adjusting their shape in interactive human-computer interfaces to fulfil the users' needs or adapt to specific situations.

physicalization: extruding shapes from planar surfaces to physicalize digital information or to ultimately generate physical matter.

Chapter 5: Latchable soft electromagnetic actuators with multi-degree of freedom

This chapter covers the shape programmable electromagnetic soft beams that can twist and bend through their narrow sections and can latch into multiple complex shapes. The chapter covers the working principle of the beams that uses liquid metal coils in a silicone structure with SMP joints. The chapter details the thermal constraint of electromagnetic actuation and the approaches to overcome this limitation.

Our technique provides versatile movements of soft electromagnetic devices with increased load-bearing ability using adjustable stiffness materials. This would find use for different applications in robotics where more degrees of freedom are needed. The developed electromagnetic beam, very similar to the human finger in terms of the design and motions, makes use of SMP composites at the joints. By independently heating different SMP joints of the beam, the user is able to control the configuration of these soft robotic arms.

With three different devices, we have shown that the hybrid actuators combining shape memory polymers and polymer based actuators improves the ability and functionality of soft actuators. This integration produces more robust soft actuators that can withstand higher blocking forces thanks to drastic stiffness change of the shape memory polymers (>1000 times) with the temperature sweep. Depending on the device configuration, the holding force of these actuators can be significantly increased. For example, the soft electromagnetic beam that we developed can hold an object that is 125 times heavier (252 g) than its own weight (2 g). Different designs can be employed to further improve this load-bearing capacity. Compared to holding force of other soft actuators, our devices outperforms most of the available techniques. Still, there are some methods, i.e. dielectric elastomer actuators with electroadhesion, can perform better than our devices and can hold over 1000 times its own weight [15]. However, these actuators don't have a latching ability and a continuous high voltage needs to be applied to keep holding the weight.

2 Fundamentals of soft actuators

2.1 Summary

In this chapter, I first briefly explain soft actuation mechanisms and classify them into seven groups. The scope of this thesis covers the integration of shape memory polymers with pneumatic, dielectric elastomer, and electromagnetic soft actuators, therefore these actuation mechanisms are explained in detail and a few examples are selected for each group to demonstrate their versatility and key benefits. I then compare all types of soft actuators and highlight their advantages and disadvantages. Finally, I discuss how we can improve the functionalities of the soft actuators by integrating them shape memory polymers and highlight the challenges of this integration.

2.2 Overview of soft actuators

Soft actuators are classified into seven main groups based on their working mechanism and their fundamental response to external stimuli. The soft actuators and fundamentals of their responses are summarized in Figure 2.1. Each group offers different performance trade-offs that must be considered in functional implementations. The detailed discussion on the comparison is carried out in the following sections of this chapter. Although this categorization covers a wide range of soft actuators, there are examples that do not completely fit into one of these groups and some devices utilize two or more different actuation mechanisms, e.g. hydraulically amplified electrostatic actuators or shape memory polymers integrated pneumatic actuators.

Liquid crystal elastomers (LCEs) are anisotropic materials that exhibit shape transformations by changing the direction of their molecular order, known as the director field (\mathbf{n}). [4] The director field can be spatially programmed during the fabrication, allowing complex shape changes when subjected to various stimuli such as heat, light, or solvent. [7] When actuated,

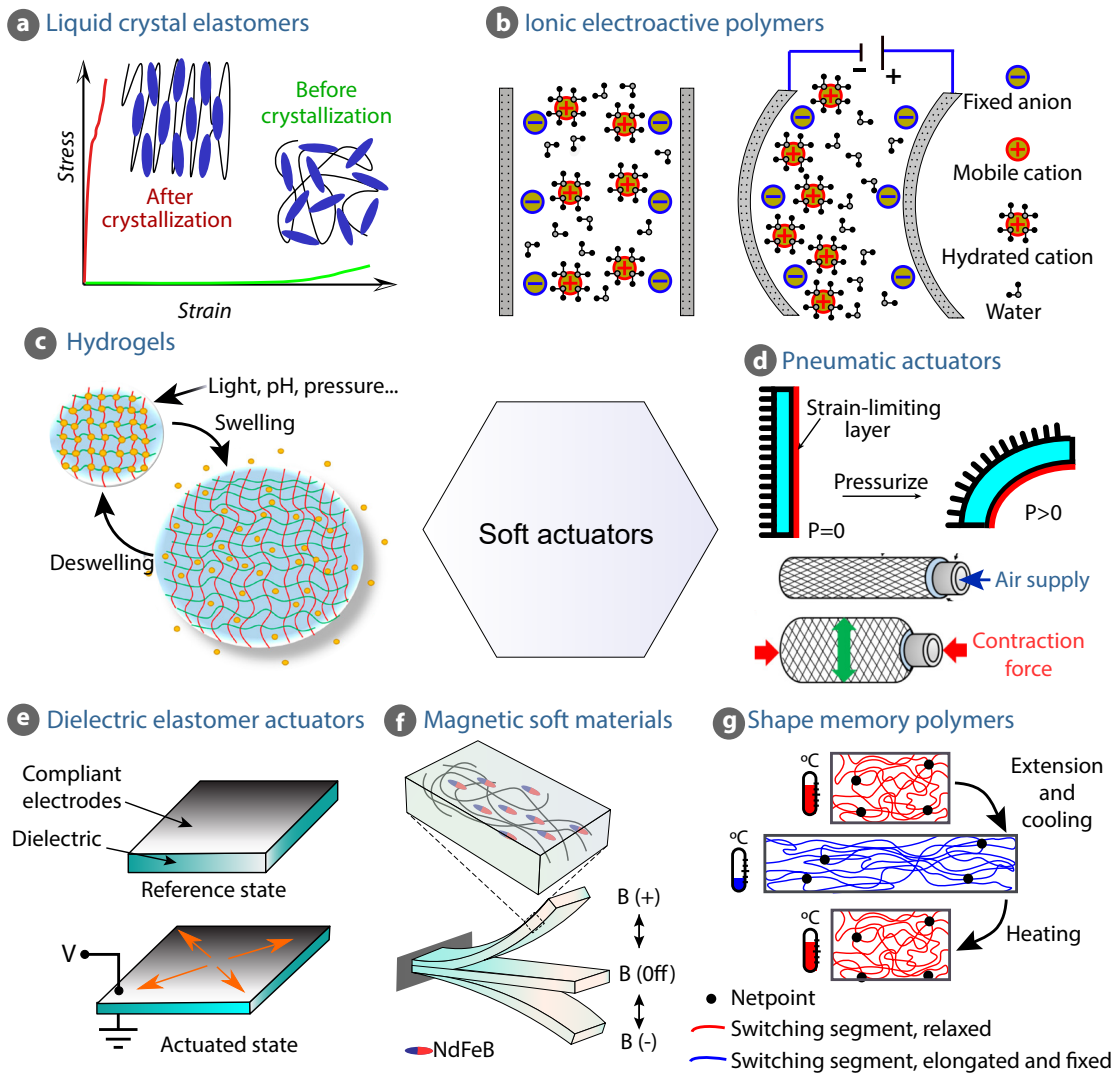


Figure 2.1: Classification of soft actuators. a) LCEs have considerably larger Young's modulus along the director axis when oriented under external stimuli. [16] b) IEAPs bends in response to an applied electrical field as a result of cations transport in the polymer membrane. [17] c) Swelling of a drug delivery hydrogel in response to various chemical and physical stimuli. [18] d) Asymmetric soft devices containing a void deforms when the chamber is inflated (pressurized). [19]. e) The electrostatic attraction of opposite charges of the electrodes (Coulomb force) squeezes the dielectric membrane, resulting in area expansion due to its incompressibility. f) The aligned magnetic particles embedded in the soft materials generate torque and deformation when subjected to an external magnetic field. [20] g) Molecular mechanism of thermally induced shape-memory effect SMPs, showing the shape fixation and shape recovery. [21]. The figures are modified from original publications.

LCEs become oriented and therefore mechanically anisotropic, e.g. the Young's modulus measured along the director axis is significantly larger than the modulus in the perpendicular axis (see Figure 2.1a). They can reach large reversible deformations with directional strains of up to 400%. [22] The LCEs based devices find use in diverse fields ranges from microactuators and sensor to cell mechanics. [23, 24]

The force generated by LCEs is generally limited by the film thickness; the thicker the film, the higher the force. [25] Increasing the thickness, on the other hand, reduces the achievable deformation and increases the fabrication complexity of localizing the alignment of these materials, a requirement to achieve complex deformations.

Ionic electroactive polymers (IEAPs) contain an ion exchange film coated with two electrodes. When an electric field is applied to these electrodes, it drives mobile cations to diffuse through stationary anion side groups. [26] The movement of the cations and the water due to the electric field causes a shape change (see Figure 2.1b). Similarly, when they are mechanically bent, they generate a low voltage between the two electrodes due to the non-uniform concentration of ions in the membranes. [17] Their reduced power requirements have lead to applications in wearable and medical devices, and implementation in robotics. [27]

The drawbacks of IEAPs include slow response time, strong hysteresis effects, low coupling efficiency(k^2 , energy converted into mechanical work per cycle/electrical energy applied), and fast device degradation due to the electrochemical nature of the working mechanism.

Hydrogels are hydrophilic, three-dimensional polymeric matrices that are able to absorb and swell with water without dissolving. [18, 28] They can exhibit large volumetric changes of up to several times of their initial volumes in response to a wide range of chemical and physical stimuli. Their aqueous nature, sensitivity to biologically relevant stimuli, and similarities to living organisms make hydrogels attractive for various biomimetic applications, including drug delivery and tissue engineering. [29] For example, they can be used as vehicles for drug delivery, thanks to their highly porous nature that allows the loading and releasing of drugs (see Figure 2.1c).

The factors limiting the broad application of hydrogels are their relatively long response time, requirement of mass transportation of the solvents, operational only in aqueous environments, and their brittleness. [30] Their actuation performance also depends on the diffusion rate and the ambient temperature. These limitations make them poorly suited for dynamic robotic applications.

Pneumatic soft actuators are intrinsically soft devices with void or chamber that utilize pressurized liquids to induce deformation. They are typically constructed from a combination of elastomer and inextensible but flexible materials. Upon pressurization, the embedded chambers in the soft actuator expand in directions that have lower stiffness and lead to linear, bending, and twisting motions depending on the device geometry (see Figure 2.7d).

Pneumatically stimulated soft robots requires external compressor and pressure regulating components, which are generally bulky. This makes it difficult to miniaturize, to array, or to untether them as they need to be connected to rigid control and power systems to provide adequate forces required for locomotion. [31]

Dielectric elastomer actuators (DEAs) consist of an incompressible dielectric elastomer membrane sandwiched between two compliant electrodes. When a voltage difference is applied between these electrodes, it generates an electrostatic pressure that compresses the dielectric, causing thickness reduction and area expansion. The different actuator geometries and the boundary conditions allow in-plane, bending, and out-of-plane expansions. [32–34] In addition to their simple structure, DEAs are highly compliant, can provide large actuation strains at high frequencies. [35]

The overall performance of DEAs strongly depends on the elastomer stiffness, the dielectric constant, and the breakdown voltage. They require high electric fields ($>70 \text{ V}\mu\text{m}^{-1}$) to generate high elastic energy densities ($>0.1 \text{ J cm}^{-3}$). [36] When actuated for long periods of time, DEAs are prone to fail due to leakage current and the need for driving voltages on the order of kilovolts increases the risk of the electrical breakdown. [37]

Electromagnetic soft actuators (EMSAs) are usually composed of soft compounds filled with discrete magnetic particles. These particles create a magnetization profile with variable magnitude and direction. When exposed to a magnetic field, the magnetic fillers seek alignment with the field resulting in generation of different deformation types such as bending, elongation, and contraction. [31] By spatially aligning the magnetic particles in the soft mater, complex actuation shapes can be programmed. [38] These magnetically responsive devices allow a remote control in different mediums as the magnetic field can penetrate through a wide range of materials. This ability makes them appealing for applications restricted to enclosed areas such as drug delivery, microfluidics, and microsurgery. [39, 40]

External magnetic coils are used to create magnetic field for actuation. These coils consume a lot of power, therefore they make energy inefficient systems if used for long-term actuations. Usually the region where the magnetic field is strong enough and controllable are usually small, which makes it difficult to size-scale these actuators.

Shape memory polymers (SMPs) are a set of materials that have an ability to undergo substantial shape deformation and fixation, and subsequently recover their original shape when exposed to an external stimulus such as heat or light. [41, 42] As the SMPs can fix their shape after the deformation is achieved, they allow energy efficient systems where long-term actuation is needed. The other benefits of SMPs include chemical stability, biocompatibility, damping, and transparency. [43]

The applications of SMPs are mostly limited by their one-way character, e.g. SMPs do not return to their initial shape upon cooling. [44] The drawbacks of SMPs includes long time response in the order of a few seconds, and large hysteresis.

As the scope of this thesis covers the integration of shape memory polymers with pneumatic, dielectric elastomer, and electromagnetic soft actuators, these actuation mechanisms are discussed in more detail in the following sections.

2.3 Pneumatic soft actuators (PSA)

2.3.1 Working mechanism

This class of soft actuators is based on fluid (gas or liquid) transport within engineered material constructs. They convert pneumatic energy (pressurized gas) to mechanical motion and force. They are essentially made of an asymmetric flexible structure around an internal void (inflatable channel) so that the device bends when the void is pressurized. [2] The asymmetry can be created using materials that have different elastic moduli on each side of the channel, or using an asymmetric geometry of the cross section referred to as bellows-type actuators (see Figure 2.1d).

Another possible approach to program the deformation of these inflatable tubes is to integrate them with flexible but inextensible threads. McKibben actuators are the most common types composed of tubes surrounded by woven threads. When inflated with pressurized air, the tubes expand radially and contract axially, generating tensile forces. [45] Different types of motions such as axial extension, radial expansion, bending, or twisting can be obtained by varying the angle of these fibers. [46]

2.3.2 Fabrication

The pneumatic actuators are usually made of elastomers with an asymmetry and are fabricated via traditional manufacturing approaches such as molding and soft lithography. [47] Differently, in some cases the need of fluidic pathways in the soft body may introduce additional design constraints to their fabrication. The popular process is molding elastomers to include a central fluid channel and then bonding it to other parts, i.e. stiffer elastomer or fabric. For McKibben, for example, the stiffening process (which usually defines the actuation profiles) is carried out by weaving the inextensible fibers into the elastomer, trading off extension for lateral expansion to allow significant force production upon pressurization.

The morphological complexity of the actuators is limited by the fabrication method, which makes it difficult to fabricate robots that are more sophisticated than simple two-dimensional extrusions. [48] 3D printing and digital additive manufacturing, as emerging fabrication approaches for soft systems, can enable complex 3D pneumatic actuators. With these techniques, for example, robots containing functionally graded materials and active sensing elements can be produced.

2.3.3 Applications

Considerable research has been carrying out to demonstrate advanced soft robotics functions derived from pneumatic actuators. Currently, the most of soft machines are driven by this types of actuation. Soft fluidic grippers, for instance, are the most common type of grippers. they are being explored to grasp fragile objects with unknown shapes. Pneumatic based grippers have already found use in industry to usually pick-and-place delicate materials.

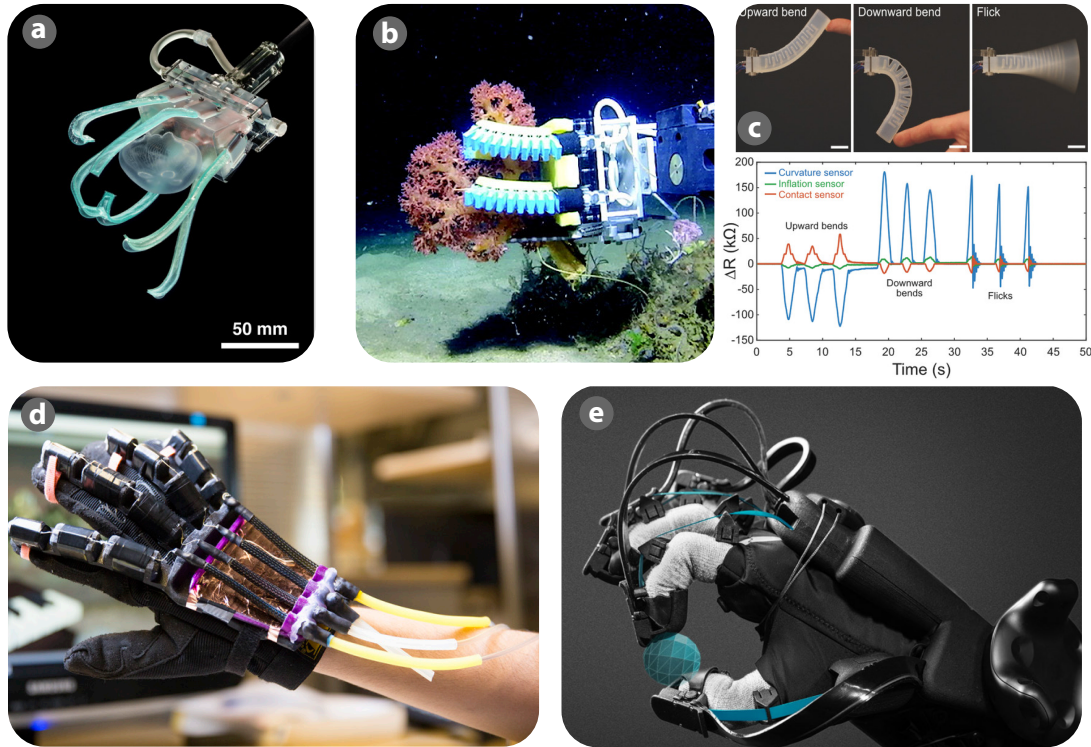


Figure 2.2: Pneumatic actuation based soft grippers and haptic gloves. a) A very gentle soft gripper grasping a jellyfish. [2] b) A bellows-type gripper collecting soft red coral (*Dendronephthya sp.*) [49]. c) Still images of a sensor-integrated gripper holding nothing, a smooth ball, and a spiked ball, and the plot showing the resistance change for each sensor action. [50] d-e) Haptic gloves using pneumatic pressure to provide force feedback. [51, 52] The figures are modified from original publications.

Sinatra et al. and Galloway et al. developed very gentle soft grippers capable of manipulating fragile tissue samples and of grasping delicate marine species, e.g. jellyfish and coral. (see Figure 2.2a-b). [2]. The soft deformable bodies can be easily equipped with a network of sensor, providing information about the force and deformation (strain). With multimaterial fabrication platforms, the mechanical sensors can be integrated seamlessly. [50] The feedback from the sensors makes these devices more smart, e.g. functioning as the receptors on our fingers. This way, the soft grippers are capable of understand if the object is picked up and also of controlling the position and force. The gripper shown in Figure 2.2c has a set of resistive strain gauges and can provide haptic, proprioceptive, and thermoceptive feedback. [50]

Pneumatic actuators now have promising results in replacing rigid virtual reality (VR) interfaces. The glove developed by the researchers at UC San Diego has a soft exoskeleton equipped with McKibben muscles. [51] These muscles respond like springs to apply force when the user moves their fingers. The force is generated by inflating and deflating of McKibben actuators to mimic the forces that the user would encounter in the VR environment (see Figure 2.2d). Similar application ideas have already gained recognition in industry. The HaptX glove shown in Figure 2.2e has a similar force feedback exoskeleton powered by pneumatics actuators and microfluidic air channels. [52] The resistive forces and the haptic feedback in these pneumatic systems enhance the perception of size and weight of virtual objects.

2.3.4 Discussion

Among the soft actuators, pneumatic based devices and robots are particularly suited for end users as they offer reliable repeatability over long time period. Comparatively, they have high force-to-weight ratios ($>9 \text{ kN kg}^{-1}$), maintain compliance at cold temperatures, and are potentially low cost. [53–55] However, requiring external compressors and pressure regulators limit their miniaturization (scaling down the size of the components) and practicality for portable applications. [56] They generally show a slower time response compared to electrical drives and they are characterised by dominant nonlinearities, namely the force characteristic and the volume characteristic.

2.4 Dielectric elastomer actuators (DEAs)

2.4.1 Working mechanism

DEAs are electrostatically driven soft capacitors that deform when a voltage is applied. [57] They consist of a dielectric elastomer membrane sandwiched between two compliant electrodes, very soft and thin conductive layers. When a potential difference is applied to these electrodes, Coulombic attraction between the opposite charges on the electrodes compresses the dielectric membrane, resulting in thickness reduction. Due to incompressibility ($\nu = 0.5$), the thickness reduction is accompanied by the area expansion. The stress generated due to applied voltage is referred as Maxwell stress and is proportional to the permittivity of the dielectric membranes and to the squared of the electric field.

DEAs are promising for applications in soft robotics as they offer a unique combination of numerous advantages with a simple structure. They achieve large deformations (1000%), have high energy density ($> 3.4 \text{ MJ m}^{-3}$), actuate very fast (on the order of millisecond), and are lightweight. [57] In terms of the performance, i.e. force density and deformation, they resemble natural muscle of humans. [58] Due to their large strain capability, they are usually referred as artificial muscles.

2.4.2 Fabrication

To fabricate a DEA, a dielectric film is first produced and then the electrodes are patterned on the both sides. The dielectric membrane is usually desired to be very uniform, defect free, and ideally with very high dielectric breakdown strength. The thickness of the dielectric film defines the voltage needed to drive the actuator, thicker films requires higher voltage to obtain the same electric field. [10]

For the dielectric membrane, either commercially available materials such as VHB 4910 (from 3M) and Elastosil (from Wacker Chemie AG) or in-house synthesized membranes can be used. Two main material group of the dielectric are acrylics and silicones. Acrylics achieve larger deformations but they are highly viscoelastic. Silicones, on the other hand, do not reach as high strains as acrylics but they have very low viscoelasticity. This makes them well suited for high frequency applications.

A critical design consideration of DEAs is the compliance of the electrodes. The electrodes should not obstruct the expansion and should follow the dielectric deformation without losing their conductivity. Carbon grease and powders, and graphite are commonly used materials as electrodes. Carbon grease is easy to apply and highly compliance but is not robust and requires encapsulation. Graphite and other metal based electrodes are comparatively robust but they are prone to lose the electrical contact for large strains.

2.4.3 Applications

Recent studies on DEAs has rapidly broadened to diverse applications. Here, a few examples are selected to demonstrate their versatility and also the key benefits. Figure 2.3a shows an electrically tunable silicone lens. [35] The lens consists of an encapsulated transparent fluid in the center and surrounded by a planar DE actuator, forming a biconvex lens. The actuator controls the tension on the fluid filled lens thus changing its shape and focal length. The tunable lens is very fast at adjusting its focal length thanks to low viscoelastic silicone materials.

The operating voltage of the DEAs, which is usually around a few kilovolts, can be lowered by reducing the dielectric thickness. This way, the control electronics to drive them can be downsized to make autonomous untethered robots. A insect-like DEA robot (called DEAnsect) is shown in Figure 2.3b weights less than 1 gram including the electronics for actuation and sensing. The stacked DEAs can operate at voltage lower than 450 V. [59] The robot can move at a speed of 30 mm/s at a frequency of up to 1 kHz.

A single DEA generate high force but low displacement in out-of-plane direction. A method to increase the displacement while maintaining high force is to stack the actuators in series. [60,61] Figure 2.3c shows a dielectric elastomer stack actuator. [62] This actuator can contract 10% under a weight of 1 kg. The gripper shown in Figure 2.3d uses another techniques called electroadhesion to lift heavy and unprecedented objects. [6] The device employs an

interdigitated electrode geometry that increases the adhesion force between the actuator and grasped object.

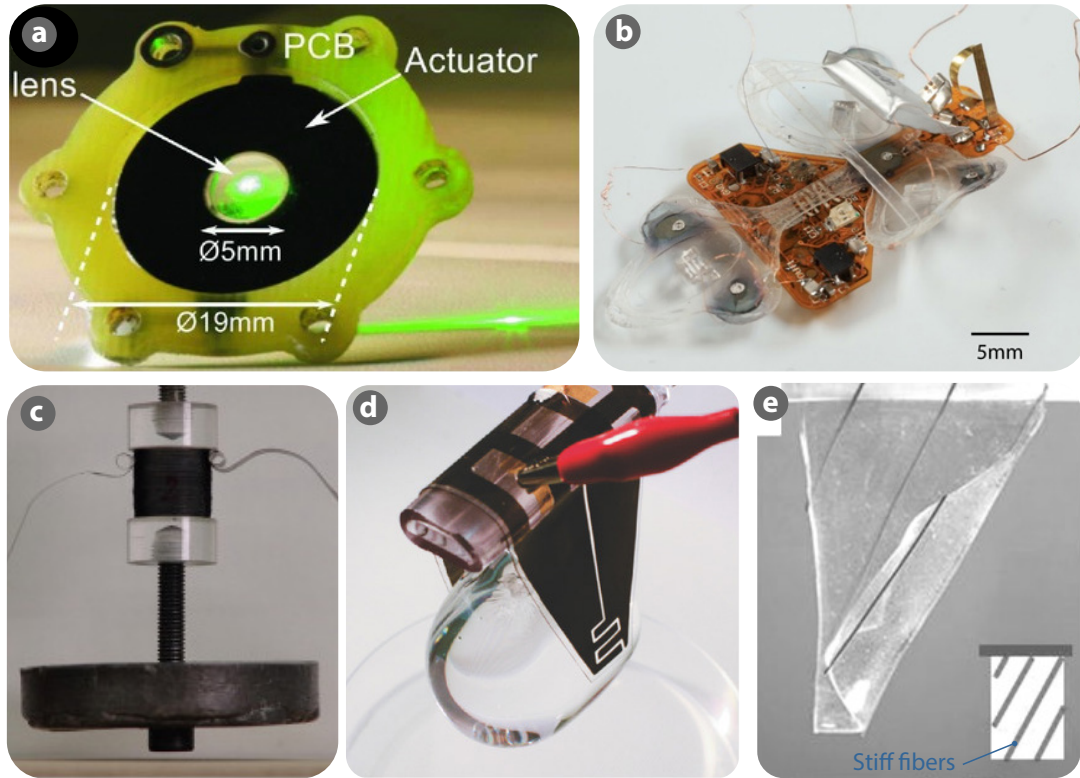


Figure 2.3: Dielectric elastomer based devices. a) A tunable silicone lens consisting of a liquid filled core surrounded by a planar DEA. [35] b) An autonomous untethered robot driven by three low-voltage stacked DEAs carrying its control and power circuit and weighing less than 1 gram. [59] c) A stacked DE device lifting 1 kg of weight. [62] d) An interdigitated electrode design enables both DEA actuation and high adhesion force. The gripper can manipulate very soft objects, i.e. highly deformable water-filled thin membrane balloon. [6] e) Attaching stiff fiber with orientation of 60° , changes the bending axis of the structure, forming a cylinder with the same orientation as the fiber. [5] The figures are modified from original publications.

Similar to the McKibben actuators where the deformation shape is programmed by the alignment of the stiff threads, DEA can be reinforced with the stiff strips to achieve various distinct actuation shapes. When a stiff strip or fiber is attached to the DEA, it prevents the elastomer expanding along the strip and since the volume of the elastomer sheet cannot change with applied voltage, the elastomer stretches in a direction perpendicular to the strips instead. [63] The DEA based device shown in Figure 2.3e utilizes a set of Vinyl fibers oriented with 60° to control the actuation direction. The integrated fibers are used to break the symmetry of the electric field induced deformation and therefore to predetermine the direction of shape changes. [5]

2.4.4 Discussion

DEAs usually requires operating voltages in the kV ranges, which limits potential applications, due to possible safety concerns but mostly due to the cost and size of the control electronics. Although autonomous untethered DEA robots have been developed, they are far from being used for any load bearing application. Silicone based DEAs were shown to be operational at frequency up to kHz range. However, making them working at higher frequency is a real challenge mostly due to the viscoelasticity of the components but also charge and discharge of the capacitor (due to capacitance and resistance of the electrodes). In order to increase their life time, DEAs are not operated at full performance. The reason for this is to keep device away from several failure mechanisms such as electromechanical instability, leakage current, loss of tension for prestretched devices, and dielectric breakdown.

2.5 Electromagnetic soft actuators (EMSAs)

2.5.1 Working mechanism

These magnetically responsive soft actuators are soft compound that incorporate magnetic particles with a programmed magnetization profile (direction and magnitude). [64] When an external magnetic field is applied to these actuators, the embedded magnetic particles align themselves along the field. This alignment generates a torque, which depending on the design creates different deformations, i.e. contraction, elongation, and bending. The deformation pattern of these actuators can be designed by varying the magnetization profile, by changing the actuating magnetic field, or by spatially tuning the material stiffness or shape. [65]

Another way of making soft material magnetically responsive is to suspend the magnetic particles in a encapsulated liquid. These types of liquids are called ferrofluidics if the particle size is less than 20 nm and magnetorheological fluids for particle in the range of a few micrometers. [64] When exposed to a magnetic field, the particles align and form columns along the direction of the field, forming a gel of dipoles. This alters the viscosity of the liquid, an effective transformation from liquid to solid-like gel. This method is usually preferred in microfluidics, e.g. for locomotion of small ferrofluid droplet and microassembly. [66]

Liquid metal coils have shown to be emerging type of soft electromagnetic actuators. These actuators replace the conventional rigid coils with a conductive liquid coil in a flexible polymer microchannels. Typically, the liquid metal based devices are electrically and mechanically stable under large deformations and high cycles. [67]

2.5.2 Fabrication

The most commonly used technique to fabricate electromagnetic soft actuators is to mix the particles into uncured material, align them in a high magnetic field and cure the material. Alternative ways include the porous materials absorbing the magnetic-particle mixed fluids or

precipitating particles onto nanofibril network. [64] After the particles are embedded, they can be magnetized by a large applied field. A continuous but non-uniform magnetization profile is achievable by spatially deforming the particle-embedded polymer before the magnetization step. [38] A discrete magnetization profile can be obtained by simply attaching small permanent magnets. Discrete magnetization has limited shape complexity but it generally enables very easy manufacturing.

2.5.3 Applications

Magnetic soft actuators have been used for creating a variety of small-scale swimmers, crawling robots, and micropumps. Figure 2.4a shows a millimeter-scale untethered swimmer propelled by a continuous undulatory deformation. The propulsion is enabled by the distributed magnetization profile of a flexible membrane. This 5.9 mm size robot can swim with a speed up to 17 body-lengths per second. Figure 2.4b shows a stretchable acoustic device incorporating liquid metal coil of Galinstan. The device is driven by the dynamic interaction between the liquid metal coil and a permanent Neodymium magnet. It maintains the sound pressure after repetitive uniaxial (50%) and biaxial (30%) strains. A miniature soft magnetic gripper is shown in Figure 2.4c. The arms of the gripper have aligned magnetic particles embedded in silicone layers. The gripper is actuated using soft helical coils filled with liquid metal (eutectic gallium indium, EGaln).

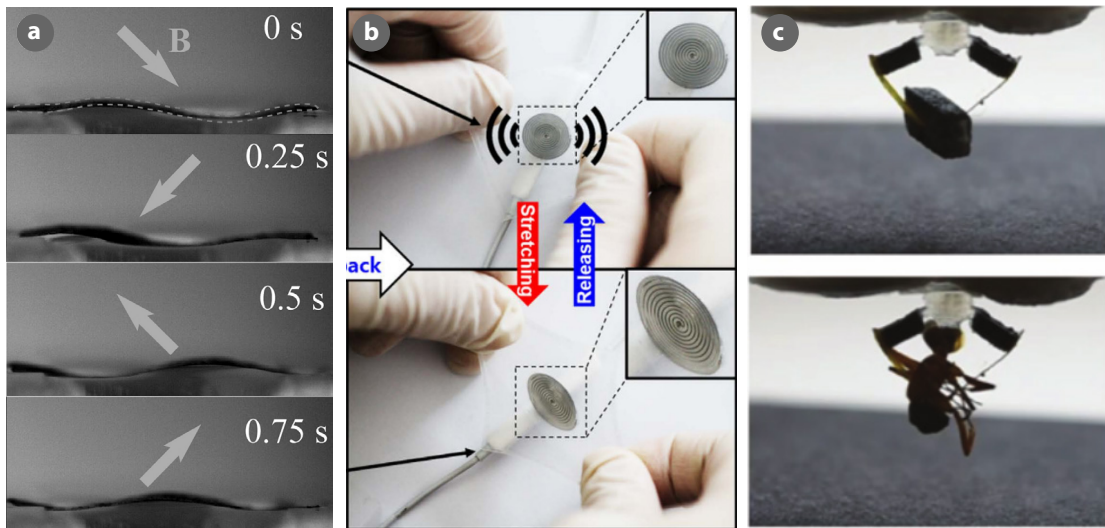


Figure 2.4: Magnetically responsive soft devices. a) The side views of a mm-scale robot showing the wave propagation as the magnetic field rotates clockwise. [65] b) A stretchable acoustic device records using liquid metal coil and and playbacks sound. [67] c) A miniaturized gripper lifting a soft foam cube and an ant. [68] The figures modified from original publications.

2.5.4 Discussion

Magnetic actuators can be controlled remotely and therefore they are well-suited for applications in enclosed spaces such as drug delivery, microsurgery, and in-situ operations. They can operate at high frequencies. However, these devices are generally in small-scale mostly due to mostly the poor scaling of magnetic forces, challenging to generate high magnetic field over large volume. Workspaces where the magnetic field and gradient are well-controlled tend to be small. The electronics for the control and actuation are usually large and have high power consumption.

2.6 Shape memory polymers (SMPs)

2.6.1 Working mechanism

Among the soft actuators, SMPs are the sole material group with shape memory effect. Shape memory is the capability of a material to be deformed and fixed into a temporary shape, and to recovery its initial shape. These materials can memorize a permanent shape, can be deformed and fixed to a temporary shape under specific conditions of the temperature and stress, and can be recovered to the original shape upon application of a particular stimulus. [69] All polymers intrinsically show a certain degree of shape memory effects under specific conditions. [70] However, the characteristics of strain recovery rate, work capability during recovery, and retracted state stability vary for each polymer material. The shape-memory term is usually used for those having very high strain fixation and strain recovery rates.

The underlying mechanism in shape memory is the dual segments system, one being elastic (always hard) and the other one transition segment, the stiffness of which depends on the presence of the stimulus (see Figure 2.5a). [71] The transition segment changes its mechanical stiffness according to the applied stimulus while the elastic segments always remains hard. SMPs (both segments) are stiff in their glassy states and become very soft in the rubbery states due to softening of transition segment. SMPs are usually deformed to a temporary shape in the rubbery state, allowing an easy transformation. The deformation achieved at the rubbery state can be fixed by cooling. This way the work done on the material can be stored as latent strain energy if the recovery of the polymer chains is restricted by vitrification or crystallization. [69] This fixation is stable for long period of time, and the initial permanent shape can be recovered by reapplying the stimulus.

The important quantities describing shape memory properties of a material are the strain recovery (R_r) and strain fixity rates (R_f). The strain recovery rate quantifies the ability of the material to memorize its permanent shape, whereas strain fixity rate describes the ability of the switching segment to fix the mechanical deformation. A description of a thermomechanical test with loading at high temperature is shown in Figure 2.5b. A sample is deformed to a constant strain ϵ_m at a constant strain rate. While maintaining the strain at ϵ_m , the samples were cooled to a low temperature and unloaded. Upon removing the constraint, a substantial

amount of strain is stored in the material ϵ_u . The sample was subsequently heated above T_g and kept at that temperature allowing the recovery to take place. This completes a thermo-mechanical cycle leaving a residual strain ϵ_p . The R_r and R_f for N^{th} cycle can be formulated as:

$$R_r(N) = \frac{\epsilon_m - \epsilon_p(N)}{\epsilon_m - \epsilon_p(N-1)} \quad (2.1)$$

$$R_f(N) = \frac{\epsilon_u(N)}{\epsilon_m} \quad (2.2)$$

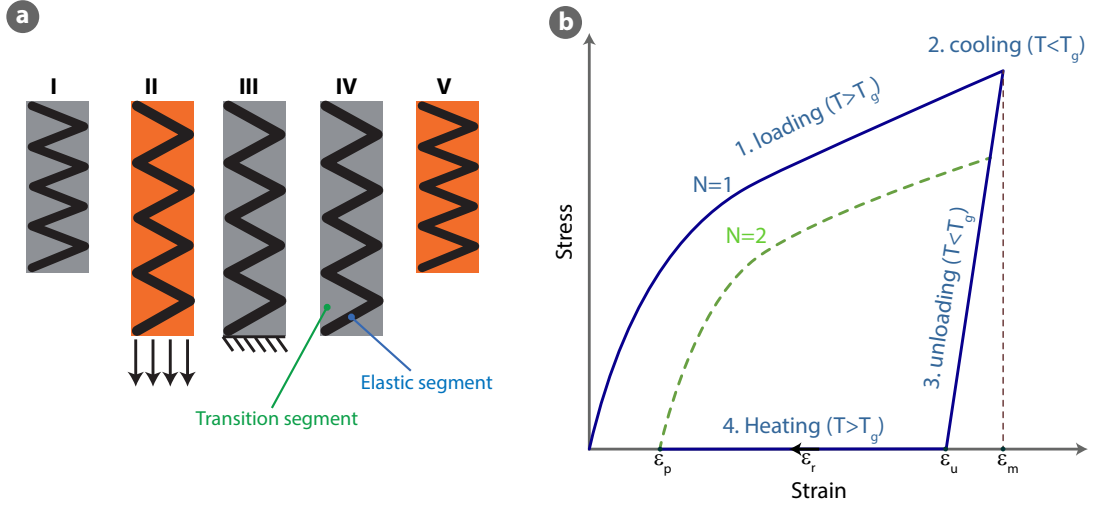


Figure 2.5: Working principle of thermo-responsive SMPs. a) Illustrations of the mechanism of the shape memory effect: (I) Initially stiff material at low temperature ($T < T_g$); (II) easily deformable at high temperature ($T > T_g$); (III) stiff again after cooling; (IV) temporary (deformed) shape after load is removed; (V) shape recovery upon re-heating (adapted from [71]). The dual-segment systems (elastic and transition) allows for shape fixation and shape recovery in SMPs. b) A thermo-mechanical cycle for a one-way shape-memory polymer. The dashed green line indicates the second loading cycle. ϵ_p , ϵ_r , ϵ_u , and ϵ_m stand for the permanent strain after unloading, the recovered strain during reheating, the stored strain when the material is fixed at the deformed state, and the applied mechanical strain, respectively (adapted from [72]).

2.6.2 Applications

Thermally triggered shape memory effect is more common where the recovery takes place with respect to a certain critical temperature of switching phase: glass transition temperature for (T_g) for amorphous materials and melting temperature (T_m) for crystalline polymers. [73] To demonstrate the process of programming and recovery in thermo-responsive SMPs, a few

examples are selected. Figure 2.6a shows a preprogrammed single-stroke swimmer. This untethered robot can achieve a propulsion using bistable shape memory polymer muscles connected to paddles that amplify the actuation forces. [74] The SMP material is prestrained and fixed in the deformed state. When the robot is submerged in hot water, the SMP relaxes to initial state which applies a force to the bistable element. This in return actuates the robots fins. As there is no on-board control and power, this robot can achieve only one stroke of propulsion. 3D printing technology have enabled the fabrication of complex shape memory structures. The miniaturized Eiffel Tower shown Figure 2.6b is 3D printed using micro-stereolithography based additive manufacturing. [75] It can follow the typical shape memory cycles; a temporary bend shape is achieved by external force at 60 °C and is fixed by cooling down under the applied force. The bent Eiffel tower gradually recovered its original straight shape when heated above 60 °C.

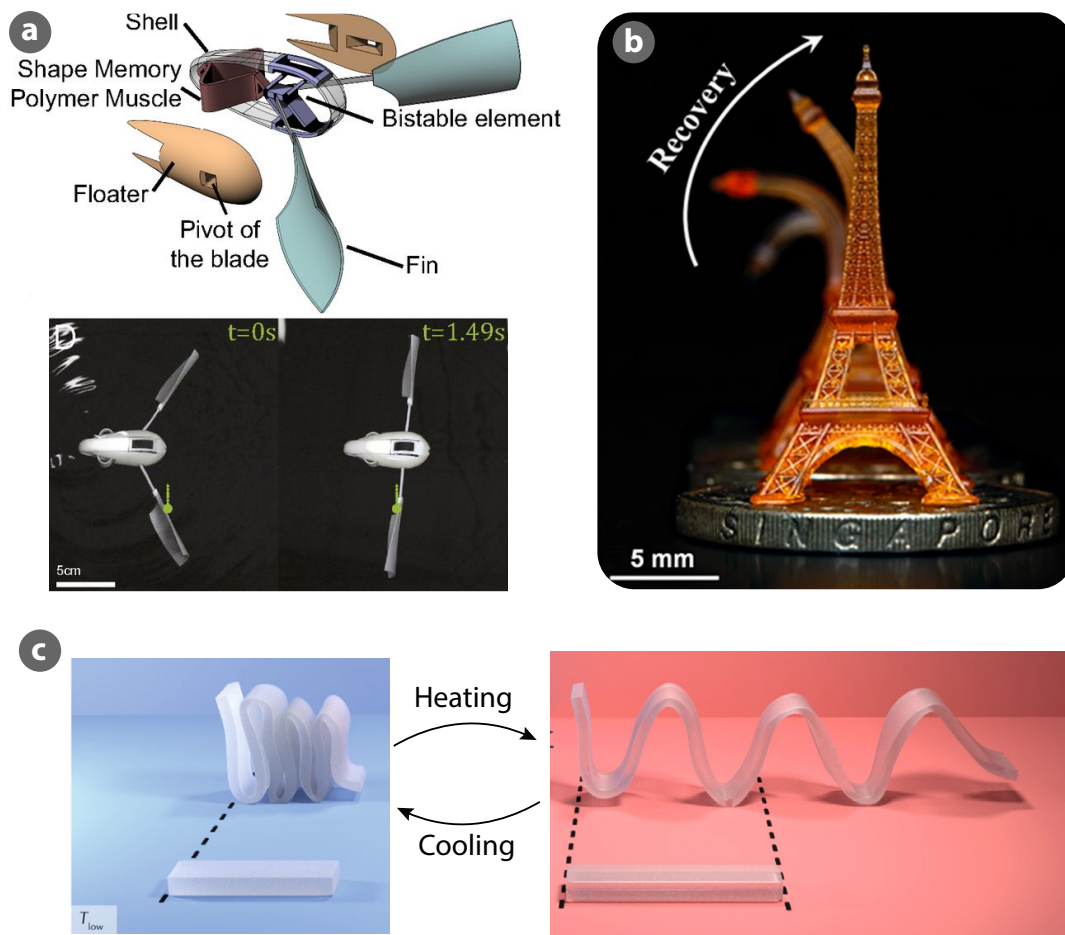


Figure 2.6: Shape memory polymer devices. a) An untethered swimmer using the bistability of shape memory effect as propulsion mechanism. [74] b) 3D printed shape memory Eiffel Tower recovering from a deformed state upon heat treatment. [75] c) A two-way reversible shape memory device that shrinks upon cooling and stretches when heated. [76] The figures are modified from original publications.

2.6.3 Discussion

Shape-memory polymers have shown good shape transformation ability when stimulated. However, their applications are restricted by their one-way actuation, thus they need to be reprogrammed through external loading for each deformation, e.g. after the original shape is fully recovered, a conventional shape memory polymer cannot return to its temporary form. [77] Recently, two-way shape memory materials capable of transforming between two programmable states have been developed. [76] The design of such a movement requires the incorporation of at least two different chain segments (transition segments) associated with crystallites with distinctly different melting temperatures. [76] The folded structure shown in Figure 2.6c has two-way reversible shape memory effect where it shrink upon cooling and stretches when heated. The transition between these two shapes is achieved using only a thermal stimulus.

2.7 Comparison of soft actuators

There are a number of key features that merit careful attention in both the design and the selection of soft actuators. Table 2.1 lists some of these factors that play important roles in choosing the appropriate actuator for a specific application.

Table 2.1: Critical factors that determine the choice of soft actuation mechanism for specific applications (adapted from [64]).

Actuation strain and force/stress production	Operating environment (in solution, air, etc.)
Size scale & arraying	Resistance to other stimuli
Power consumption	Actuation speed and response time
Biocompatibility & biodegradability	Durability and fatigue resistance
Multifunctionality & anisotropy	Remote or tethered power source
Self-healing properties	Hysteresis & material viscoelasticity
Manufacturability	

Among these listed metrics, the commonly used ones are actuation (generated) stress and strain, response time, energy, work, power, and force densities. [64]. Here, I choose actuation stress, actuation strain, work density, and response time for the quantitative comparison. In addition to being critical performance indicators, these factors also offers a trade-off which facilitates the calculation of the suitable operational range of the chosen actuator.

The definitions for these metrics:

- **Actuation strain** (ϵ) is the percentage elongation in the length upon actuation. The formula used to find the actuation strain is $\epsilon = (L - L_0)/(L_0)$, where L_0 is the initial length and L is the length after the actuation.
- **Actuation stress** (σ) is defined as the ratio of the output force to the cross-sectional area normal to the actuation direction.

- **Response time (t)** is the time it takes an actuator to shift from the rest position to actuated position upon a given input.
- **Work density (w)** is the output work done by the actuator upon excitation per the mass (or per the volume) of the actuator. Almost all of the published studies take the mass of the actuator into account when calculating the work density (not the mass of the whole system). Similarly, the work densities shown in Figure 2.7b are based on the mass of the actuator unit only.

As soft actuators consists of highly deformable materials, they can produce and withstand large strains. Figure 2.7a shows the range of the actuation stress and strain for the major classes of soft actuators. The actuation stress is proportional to the force that the actuator can produce, allowing it to do work. The higher actuation stress is desired for load-bearing applications. As depicted from the Figure 2.7a, pneumatics, hydrogels and IEAPs can generate high actuation stress. Among these soft actuators, LCEs and electromagnetic soft actuators have the lowest actuation stress values, indicating low force generation. There are different methods to increase the force output of these actuators, however they are either costly or they are creating fabrication complexity, e.g. building a set-up to generate very high magnetic field.

The actuation strain is another aspect referring to the deformation that can be achieved when actuated. All soft actuators can easily achieve high strains $> 20\%$, much higher than their rigid counterparts. Among them, hydrogels, pneumatics, LCEs, and DEAs can generate linear strain $> 100\%$. It should be noted that this graph covers the study where both actuation stress and strain are reported and that there are soft actuators can achieve larger strain than the ones shown here. Therefore, the studies reporting only one of these values (either stress or strain) are not included in this graph.

Figure 2.7b shows the work density versus the response time. Work energy density gives an approximation of volume needed of a given actuator technology to accomplish a given amount of work. The higher the energy density of the actuator the less volume needed to meet the design objective. DEAs, pneumatic, and SMPs are three classes with high work density. As a result of low actuation force, the electromagnetic actuators have the low energy density. Their work density depends on the external magnetic field strength, the stronger magnetic field the higher work density. As far as the speed is concerned, DEAs and electromagnetic soft actuators are the fastest two groups. They can operate at high frequencies ($> 100\text{Hz}$), whereas hydrogels, LCEs, and SMPs are the slow actuators with response time on the order of a few seconds up to several minutes.

Every actuator has its advantages and drawbacks, providing alternatives and also limitations for a specific application. Table 2.2 is provided at the end of this chapter to qualitatively compare the seven major classes of soft actuators.

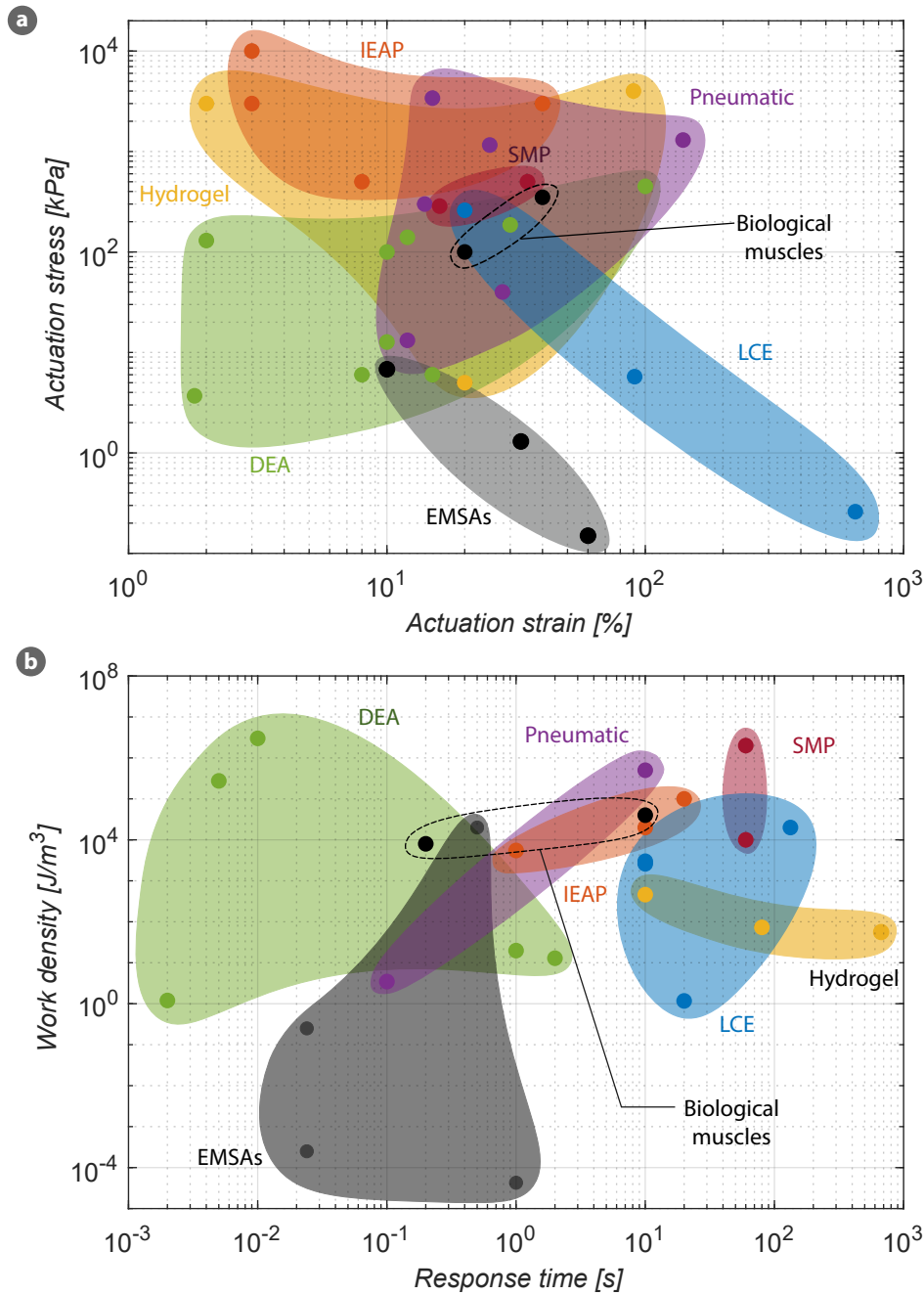


Figure 2.7: Performance comparison of soft actuators. The graphs are generated using data from the published studies where both variables are reported, e.g. actuation stress and strain for the first graph. a) All soft actuators can achieve strain $> 20\%$, higher than their rigid counterparts. In terms of actuation stress, all actuators, except soft electromagnetic actuators and LCEs, resemble the biological muscles. b) DEAs and EMSAs are the fastest actuator among the soft actuators. They can operate at frequencies $> 100\text{ Hz}$. Hydrogels, SMPs, and LCEs are among the slowest actuators. As far as work density is concerned, DEAs, pneumatics, and SMPs can provide higher values, surpassing the work density of the biological muscles. *References and abbreviations:* DEA: dielectric elastomer actuator [56, 62, 78–82]; IEAP: ionic electroactive polymer [83–85]; SMP: shape memory polymer [86, 87]; EMSA: electromagnetic soft actuator [64, 68, 88–90]; LCE: liquid crystal elastomer [79, 91]; Pneumatics [83, 92, 93]; Hydrogels [83, 93, 94].

2.8 Combining soft actuators with shape memory polymers

SMPs have been previously integrated with different soft actuators to advance their mechanical functionalities. This integration is an effective approach to enable a reversible and multi-stable shape effect. Previous studies were carried out with dielectric elastomers, [95,96] ionic electroactive polymers, [97] pneumatic, [98] and electromagnetic soft actuators. [20,98]

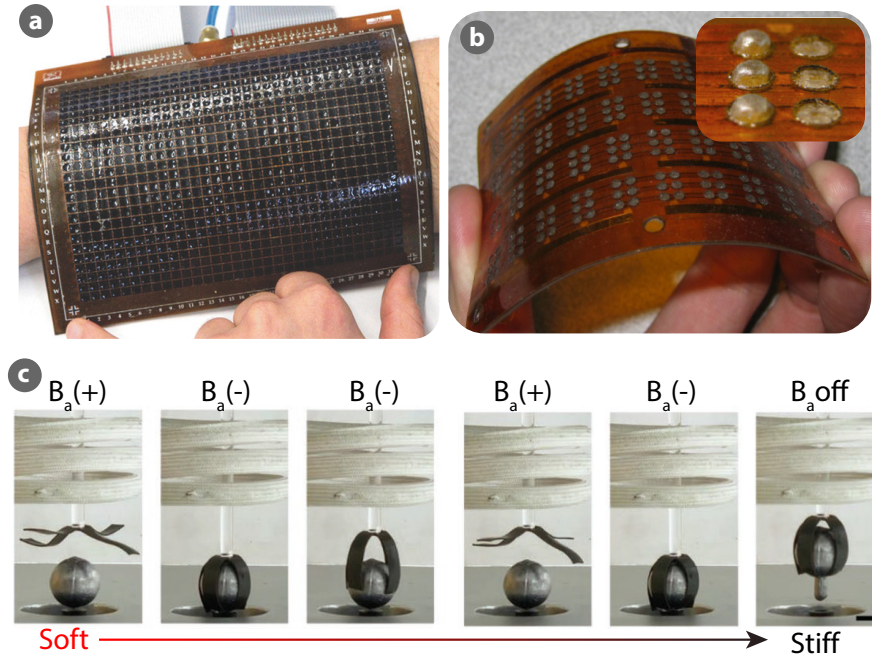


Figure 2.8: SMP integrated soft actuators. a) Photograph of the flexible active skin consisting of 32x24 multistable tactile actuators addressable by Joule heating of compliant heaters. [99] b) A refreshable Braille display device made of a layer of bistable electroactive polymer film and an array of heater elements. [100] c) A magnetic SMP gripper is lifting a 23 g lead ball with shape locking. [20] The figures are modified from original publications.

Besse et al. developed a large array of individually addressable shape memory polymer actuators. [99] The fabricated flexible device consists of 32x24 high force tactile pixel where each one is addressed by Joule heating through the stretchable electrodes (see Figure 2.8a). Niu et al. combined shape memory polymer with dielectric elastomer, named as bistable electroactive polymer (BSEP). [95] Similar to any SMP based device, their device can provide bistable deformations in a rigid structure through the use of glass transition temperature. Figure 2.8b shows flexible Braille display device of BSEP exhibiting the ability of SMPs, namely large deformation and high blocking force. [100]

The example shown in Figure 2.8c incorporates low-coercivity and high-remanence magnetic particles with the shape memory polymers to achieve locking and unlocking of multiple deformations. [20] Low-coercivity particles are used for heating and high-remanence for the actuation. To actuate the device, first an AC magnetic field is applied to heat the device

and when heated a DC magnetic field is applied to deformed the structure. The deformed structure is cooled down under constant DC magnetic field, allowing to lock the deformed shape. After the device is latched, the field is removed while keeping the shape deformed. The gripper shown in Figure 2.6f demonstrates that the remote shape transformation and latching can be used in soft robotic applications.

As these examples demonstrate, integration of SMPs with soft actuators can improve their functionalities with additional advantages:

- **Increased load-bearing ability:** Shape memory polymer can be very soft at temperature above T_g ($T > T_g$) and very rigid below $T < T_g$. When their deformation is fixed at a state and the temperature is cooled down, they mechanically improve the robustness of the actuators, becoming less sensitive to environmental variation and also can withstand larger external forces.
- **Zero-power actuated states:** The shape fixation ability of the SMPs can allow us to mechanically latch the device in the actuated position. This way we confine the energy consumption into the actuation step only and can remove the power source when the actuation is achieved. This allow more energy efficient systems where long-term actuation is required, e.g. it eliminate the need of applying continuous power to hold a position.
- **Arraying / scalability:** Sometimes its difficult to array soft actuators as their stimuli source or control unit does not allow an easy scaling. Pneumatic soft actuators, for instance, require pumps and pressure regulating units which are generally bulky. If we want to make a set of pneumatics actuators, then we need many of these pumps and regulators to individually control any actuator in an array, which is usually impractical. Integrating SMP with an array of soft actuators enables us to use different addressing systems for selective actuation, e.g. electrical addressing instead of pneumatic addressing.
- **Reconfigurability / tunable boundary conditions:** When a SMP is integrated with a soft actuator, the overall stiffness of this integration is generally determined by the stiffness of SMP. As we can tune their stiffness with a stimuli, we can change the mechanical stiffness of the integration. We can use SMP as a structural material for soft actuators and by adjusting their properties we can modify their of the boundaries, e.g. SMP can be used as a frame for prestretched DEAs.

Combining SMP with soft actuators introduces some challenges to be addressed:

- **Need for additional stimuli source:** Every SMP requires a stimulus source for its actuation. When it is combined with another soft actuator, the stimulus source for SMP needs to be integrated to the system and also needs to be synchronized with the other components. Therefore, these requirements should be analysed in detail and the type of SMP needs to chosen carefully.

- **Fabrication complexity:** Combining SMP with soft actuators usually requires a fabrication recipe of multilayered structures, i.e. layers for DEA + SMP layer + layer for heaters (SMP stimulus). Depending on the fabrication method, there are several challenges in multilayer fabrication, e.g. de-lamination between the layers, surface properties between the neighbour layers, solvent suitability of different layers, curing conditions.
- **Stiffening effect of SMP:** Most of the soft actuators generate limited forces. Attaching a SMP layer to these actuators induces a stiffening effect of the SMP on the device performance, reducing the achievable deformation. The stiffening effect due to any additional layer, therefore, should be taken into account. Since SMPs are usually stiffer than the materials used for soft actuators, a through-out analysis and calculation is required to minimize the performance loss.
- **Increasing time response:** This is a crucial aspect when combining SMP with fast soft actuators, i.e. SMP + DEAs. SMP integration increases the time response of these systems. How fast we can actuate them is now limited by the time constant of SMP. To make these devices fast enough, we need to design an efficient method to apply stimuli.

2.8.1 Size scaling of shape memory soft actuators

Shape memory polymer can be combined with different actuation mechanisms to make hybrid actuators. These hybrid actuators will have different aspects of scaling, depending on which type of the actuation mechanism is integrated with the SMP. To generalize the scaling discussion for the all types, we here mainly focus on the scaling aspects of the thermo-responsive SMPs which is the common in all types. The length (L) is used as the parameter for size scaling.

1. Scaling of heat transfer coefficients

An important factor for the thermo-responsive SMPs is the heat transfer between the heaters and the SMP material. The conductive and the convective heat transfer coefficients are inversely proportional (L^{-1}) to the size for dimensions smaller than 10 mm and constant for larger size. [101] Having smaller dimensions allows higher heat transfer coefficients, and therefore faster heating and cooling.

2. Scaling of time response

For the SMP integrated systems, the speed is mostly limited by cooling time. In case of Joule heating, applying higher current for shorter time can increase heating speed. As the cooling is proportional surface area, L^2 , mass is proportional to L^3 , and convective coefficient proportional to L^{-1} , it will take a time proportional to L^2 to cool the mass. Increasing the actuators size will significantly increases the time response of the systems.

3. Scaling of power consumptions of thermal stimulation

During the steady state actuation (the actuator temperature is constant), the energy loss is proportional with the surface (L^2) and the convection coefficient (L^{-1}). Normalizing this to the volume (L^3), the specific consumption is found proportional to L^{-1} . This means that smaller actuators will consume more heating power in comparison to their volume.

4. Scaling of recovery force density

The elastic segment of the SMPs generates a recovery force when exposed to an external stimulation. Assuming that this segment does not change its behaviour at different scales (recovery stress is the same), the recovery force will be proportional to its volume (L^3). Normalizing this force to the volume, we see that the recovery force density does not change with the size.

The SMP can be integrated with soft actuator at different scales. At the large scales, they have increased response time therefore become slower due to slower heat transfer (heating and cooling). Scaling down their sizes, on the other hand, shortens their response time and allows faster actuation and recovery.

Chapter 2. Fundamentals of soft actuators

Table 2.2: Performance comparison of soft actuators. Abbreviations: LCE: liquid crystal elastomer; IEAP: ionic electroactive polymer; DEA: dielectric elastomer actuator; PSA: pneumatic soft actuator; SMP: shape memory polymers, EMSA: electromagnetic soft actuator.

Actuator	Stimulus	Mechanism & Size	Advantages	Limitations
LCE	E-field, heat, light, chemical	Phase change [μm – cm]	Low driving voltage. High actuation strain. Remote control of actuation.	Low coupling efficiency. Require multilayers for high force. Heat and solvent based types are slow ($> 10\text{s}$). Not suitable for high-torque applications.
IEAP	E-field	motions of ions [μm – cm]	Low driving voltage [$1 - 5\text{V}$]. Generate moderate strain and force	Relatively slow ($> 1\text{s}$). More durable in high humidity. High cost.
Hydrogel	E-field, m-field, pH, Temperature, Solvent	Diffusion based swelling [nm – cm]	Biocompatible. Large deformations.	Actuation speed depends on diffusion rate. Slow actuation (up to several minutes). Temperature dependency. Requires aqueous environment. Mostly fragile/brittle
DEA	Electric field	Compression due to Coulomb force [μm – cm]	Large actuation strains. High energy density ($> 3\text{ MJ m}^{-3}$). Self-sensing Fast actuation response	Requires high Voltage ($0.5 - 10\text{kV}$). Failures associated with high E-field. Leakage current. Prestrain required for large deformations.
PSA	pressurized air	Deformation of void [mm – cm]	Generate high forces ($> 4\text{kN}$). High power-to-weight ratio. Maintain compliance at cold temperatures Potentially low cost.	Bulky components, i.e. compressors and pressure-regulating units. Difficult to array or miniaturize.
EMSA	m-field	Alignment of magnetic particles [nm – mm]	Enables remote actuation. M-field penetrate through different medium.	High power consumption. Difficult to obtain uniform m-field for large space. Scale down poorly.
SMP	Heat, light, solvent	Phase change [μm – cm]	Remote actuation. Multiple shape possible. Tunable stiffness. Deformation fixation with zero-power. High possible work densities.	Slow actuation ($> 10\text{s}$). Typically one-way motion. Low force.

3 Individually addressable and latchable arrays of SMP valves

3.1 Summary

In this chapter, I introduce a microfluidic platform that consists of an array of individually addressable and latchable valves, an alternative approach to microfluidic multiplexing. The microfluidic valves have shape memory effect, are addressable by Joule heating, and need a single pneumatic pressure source for selective actuation. I first explain the working principle of these SMP based valves and the design considerations. I then discuss the cyclic and latching performance of these valves, and their electromechanical degradation. Finally, the peristaltic pump and the reagent mixer that use the same working principle are presented.

The 4x4 microfluidic platform and the reagent mixer developed within this study are shown in Figure 3.1. This work was carried out in a collaboration between EPFL-LMTS (Switzerland) and Micronit Microtechnologies (the Netherlands). Robert Jan Boom, Bas-Jan Hoogenberg, Marko Blom from Micronit, and my colleagues Dr. Nadine Besse and Olexandr Gudozhnik from EPFL-LMTS have contributed to this work. Micronit fabricated the polystyrene microfluidic chip. Olexandr Gudozhnik designed, fabricated, and programmed the controller board for the experimental setup. The working principle of the SMP actuators was initially developed by Nadine Besse for the haptic taxels. She designed the PCBs and modified the software to control the valves. I adapted her fabrication process flow, modified it for an additional layer of Styrene-Ethylene-Butylene-Styrene (SEBS), and optimized it for different designs. I fabricated the devices, tested for cyclic and latching operations, and analysed the results. I developed the demonstrators, the reagent mixer and the peristaltic pump, and tested them.

This work was published in *Lab on a Chip* [102]¹ and presented at ACTUATOR 2018 [103]² and

¹B. Aksoy, N. Besse, R. J. Boom, B.-J. Hoogenberg, M. Blom, and H. Shea, "Latchable microfluidic valve arrays based on shape memory polymer actuators," *Lab on a Chip*, vol. 19, no. 4, pp. 608–617, 2019.

²N. Besse, B. Aksoy, and H. Shea, "Large arrays of microfabricated shape memory polymer actuators for haptics and microfluidics," in *ACTUATOR 2018; 16th International Conference on New Actuators*, VDE, 2018, pp. 1–4.

at MicroTAS 2017. [104]³

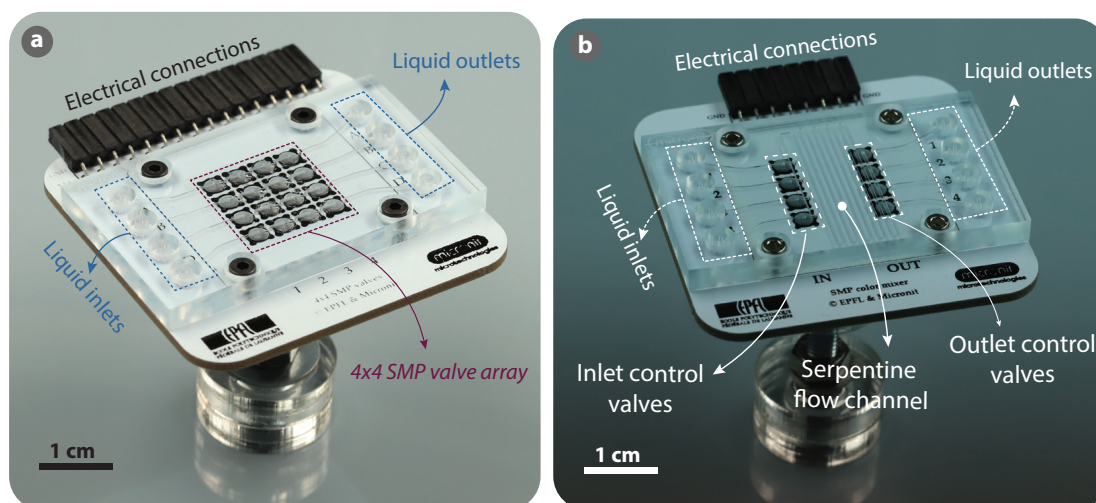


Figure 3.1: Microfluidic platform with 4x4 latching SMP valves and the reagent mixer accommodating 4X2 SMP valves. Each valve can be individually addressed by synchronizing the Joule heating with the pneumatic air pressure. The SMP layer embedded in the valves' diaphragm enables a permanent latching at a given state.

3.2 Introduction to microfluidic large scale integration (mLSI)

Microfluidic large scale integration (mLSI) systems are compact lab-on-a-chip devices that consist of a large number of functional units. With the advance in the fabrication technologies, mLSI systems have evolved into complex platforms, enabling various tasks such as parallel single cell analysis and high throughput screening assays. [105, 106] A single mLSI system can accommodate up to thousands of active elements such as micro-pump, reagent mixer, or multiplexer. [107, 108] These units are mostly actuated using a pressurized air and pressure controllers (i.e. pumps and regulators), which are generally bulky components. Increasing the number of the actuators therefore necessitates an efficient methods of addressing. [109]

Microfluidic multiplexing is now widely used in mLSI systems to address large numbers of flow channels with fewer control units. The binary multiplexer developed by Thorsen *et al.*, for instance, can address up to $2^{n/2}$ using n pneumatic control lines. [13] More efficient multiplexing techniques such as ternary and quaternary multiplexers take advantage of 3 or 4 threshold pressures to address $3^{n/2}$ and $4^{n/2}$ flow channels with only n control lines. [110]

Replacing pneumatic with electrical or optical addressing schemes can simplify the control units and therefore can miniaturize microfluidic platforms. [111] Bistable valves made of phase change materials are promising route to simplify the control of large arrays. Additionally, they

³N. Besse, R. J. Boom, B. J. Hoogenberg, B. Aksoy, M. Bloom, and H. Shea, "Array of independent microfluidic valves driven by shape memory polymer actuators using a single pneumatic supply," in *Miniaturized Systems for Chemistry and Life Sciences (Micro-TAS)*, October 2017, pp. 651–652.

offer lower power consumption thanks to their inherent latching capability and their control by Joule or radiative heating. [112, 113] The approach we developed here takes advantages of multistability and heat activation of SMPs. This method avoids any microfluidic multiplexing strategies, replacing all external pneumatics by an electronic control board and a single pressure source.

3.3 Working principle of SMP valves

The SMP valves are composed of three main components: 1) the micromachined polystyrene (PS) microfluidic chip accommodating fluid channels and valve seats, 2) the tri-layer valve diaphragm, and 3) the printed circuit board (PCB) attached on the pneumatic chamber made of poly-methyl methacrylate (PMMA). The heart of these valves is the diaphragm. It is composed of a shape memory polymer (SMP) membrane, stretchable carbon-loaded silicone (CB/PDMS) heaters, and an impermeable styrene ethylene butylene styrene (SEBS) film (see Figure 3.2).

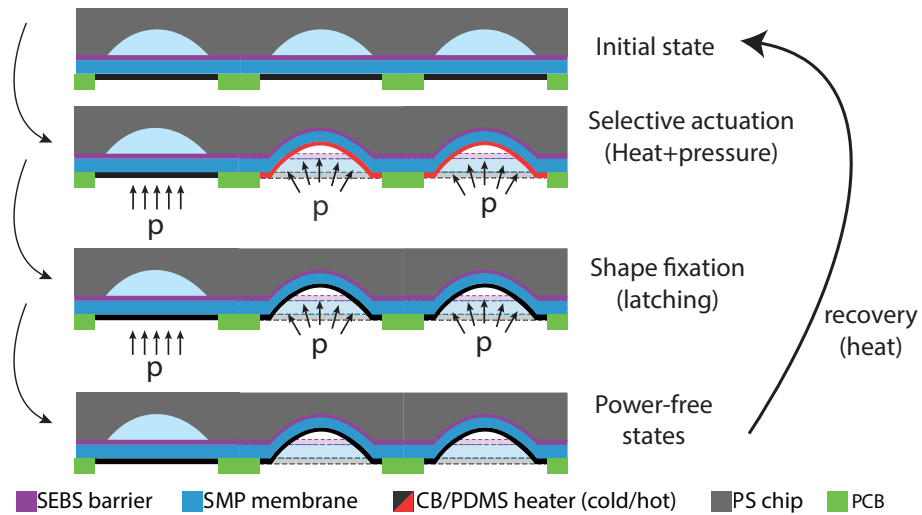


Figure 3.2: Working principle of SMP valves. The desired SMP valves are actuated by simultaneously applying Joule heating and positive pneumatic pressure. Although the pneumatic pressure is applied to all diaphragms, the only ones that are softened by Joule heating deform (2nd and 3rd valves). The displaced diaphragms are then latched in their new positions by cooling them under the pneumatic pressure. Latching allows us to lock them in either open or closed positions without consuming power. The initial positions of the valves are recovered by reheating them.

The valves are connected to the same PMMA chamber, allowing a single pneumatic source to actuate them selectively. When the chamber is inflated, it applies pressure to all diaphragms. However, the diaphragms that are softened by Joule heating are solely displaced. The un-addressed diaphragms are very stiff and therefore they do not exhibit significant motion, maintaining their position (see Figure 3.2). When the desired valves configuration is achieved, the diaphragms are cooled down under the air pressure. This locks the valves into place (usually referred as latching or shape fixation). After the pressure is removed, the valves stay in their

new positions until they are readdressed by Joule heating.

The schematics shown in Figure 3.2 demonstrate the selective actuation of the addressed valves and their latching ability after the pneumatic source is removed. The schematics are shown for normally-open design where the valves are open when the diaphragm is at rest. This configuration requires a positive pneumatic pressure to close the valves. Switching from closed state to open state, however, does not require a negative pressure as the SMP recovers its flat position upon Joule heating (more discussion in the next section).

3.4 Design and modeling of valve array

3.4.1 Valve design

Figure 3.3 compares the design and the operation of normally-open (NO) and normally-closed (NC) valves. In NO design, the microfluidic chip has an indentation (valve depth) and therefore the valve is in the open state when the diaphragm is at rest (see Figure 3.3a). NO valves work on positive air pressure, where the pressure moves the diaphragm in upward direction to close the valve. In NC valve design, on the other hand, the microfluidic chip has no indentation. The valves have a stable closed position when the diaphragm is at rest. A negative pressure is used to open the NC valves.

We used the same fabrication process flow for both NO and NC valves. The challenge we faced during the fabrication of NC valves was the undesired bonding between the microfluidic (PS) chip and the SEBS layer beneath the valve's seat. During this bonding process, we had to apply a negative pressure to the diaphragm to keep it away from the PS chip. This prevents the bonding of diaphragm beneath the valves' seat. Elsewhere outside the valves' seat, a good bonding between the PS chip and the diaphragm is required to prevent any leakage. Increasing the depth of the valve prevents the undesired bonding between the PS chip and SEBS layer beneath the valve's location. Increasing valve's depth, however, increase the air pressure needed to close it and also the SMP needs to lock their shape at higher deformation. Based on our fabrication experience and the finite element modeling (FEM) of valve diaphragm, a NO valve design with depth of 200 μm was found suitable for our application. More discussion on the optimization is included in the modeling section.

3.4.2 Operating cycles of normally-open valves

A complete valving cycle to switch a valve, from initially stable open to stable closed and finally to stable open position, takes places in 6 consecutive steps, as illustrated in Figure 3.4c:

1. As the design of valve seat has a cavity, the assembled valves has stable (latched) open state (the first step in Figure 3.3.
2. To close the valve, a positive air pressure and a local Joule heating are applied simultaneously. This moves the valve's diaphragm up and closes it. This steps is usually referred

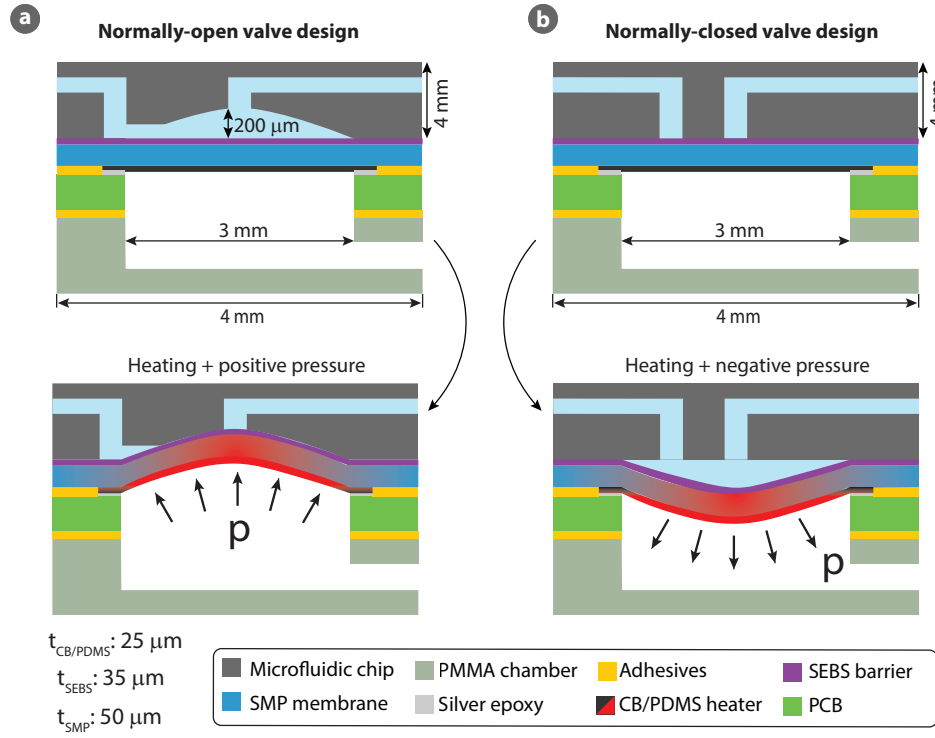


Figure 3.3: Design and operation of normally-open (NO) and normally-closed (NC) valves. The cross-sectional views highlight the critical dimensions which are the depth of the valve seat, the diameter of the valve, the height of the PS chip, and the thickness of each layer in the diaphragm. a) NO valves have a depth of 200 μm and are open when SMP layer is at rest. A positive pressure is applied to close these valves. b) NC valves are at closed state when the valve diaphragm is flat and require a negative pressure to open.

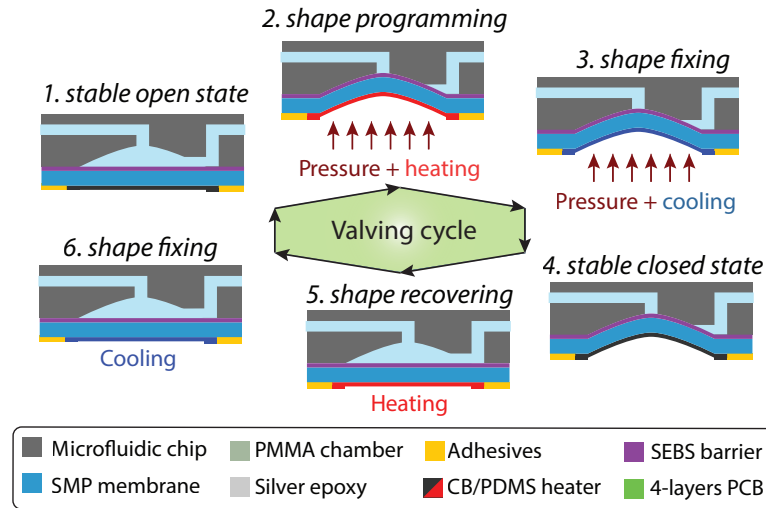


Figure 3.4: Schematic illustration of the valving cycles (open -> closed -> open): The diaphragm is displaced by synchronizing the pneumatic pressure and Joule heating. Once the valve is closed, the diaphragm is cooled down under the pressure, allowing to lock the valve in the closed position. Reheating the diaphragm recovers the initial open state.

as shape programming where the SMP layer is deformed by an external load.

3. To fix the deformed shape of SMP, the air pressure is maintained while the SMP actuator is allowed to cool down (shape fixation).
4. Once the SMP is fixed in its deformed shape, the air pressure is removed. The valve is now latched in its stable closed state.
5. To switch on the valve, a local Joule heating is applied (shape recovery). Although the initial shape can be recovered only by heating, we usually apply a small negative air pressure to assist and to accelerate the shape recovery.
6. The valve's diaphragm is then cooled down, allowing to lock in the valve in open state.

After the recovery step, the valve is ready for anew valving cycle.

3.4.3 Heater design

The heater design is adapted from Nadine Besse's previous studies on SMP haptic taxels. [99]. The heater design is shown in Figure 3.1. This heater shape can generate a homogeneous heat distribution over the active area. The heater has a circular shape with 4 pads where opposite pads have the same voltage. One set of the pads are grounded whereas the other set is applied with positive voltage. The uniformity of the temperature distribution is crucial as only the regions with temperature higher than the glass transition temperature will be significantly deformed under pneumatic pressure. The heater with a thickness of $25\mu\text{m}$ can provide a power of 350 mW which can increase the temperature of the diaphragm from 25°C to 70°C in less than 1.5 s.

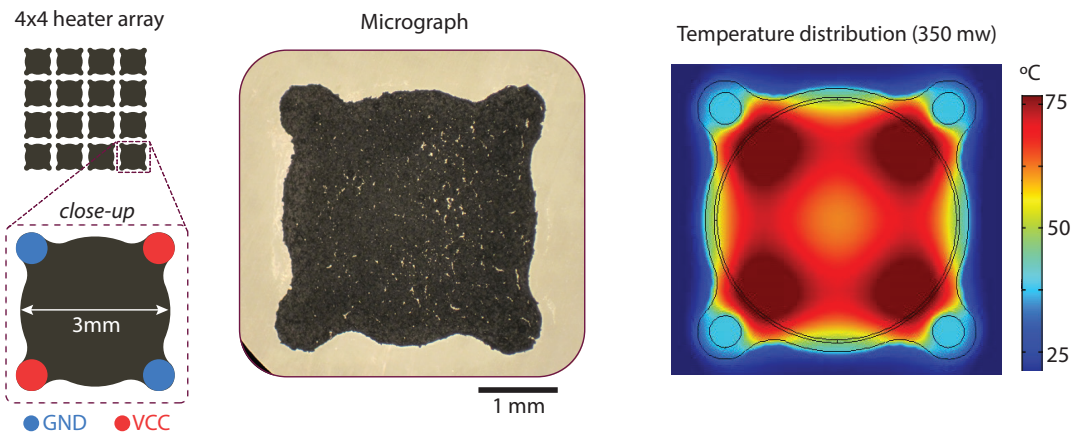


Figure 3.5: Design of stretchable CB/PDMS heaters. 4x4 heaters array is patterned on the SMP membrane. Each heater has 4 pads where two pads are connected to the ground and the remained two pads are connected to the VCC (blue pads: GND and red pads: VCC). The middle image shows the micrograph of a fabricated CB/PDMS heater. A simulated temperature distribution of the heaters when powered with 375 mW.

3.4.4 Thermo-mechanical characterization of valves diaphragm

The reciprocating diaphragm consists of three layers: shape memory polymer (SMP), stretchable heater (CB/PDMS), and water impermeable membrane (SEBS). The diaphragm is displaced at an elevated temperature and is fixed at the room temperature. Designing these valves, therefore, requires knowing of the stiffness of composed layers at different temperatures. We carried out dynamic mechanical analysis (DMA) on the bare SMP and as well as on the stacked tri-layers (DMA Q800 from TA instruments). The tests were carried out in the tensile mode with a strain amplitude of 0.1%. The temperature was swept from 0 °C to 120 °C with a ramp of 3 °C min⁻¹.

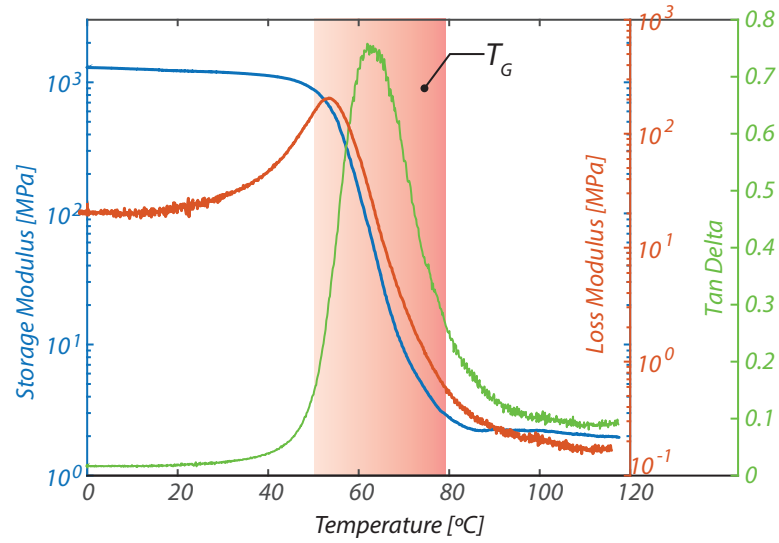


Figure 3.6: Dynamic mechanical analysis of the SMP: the change of the storage (E') and loss (E'') moduli, and phase angle (δ) of bare SMP as functions of the temperature.

The bare SMP and the tri-layer membranes (SMP+SEBS+CB/PDMS) exhibit similar mechanical behaviour at different temperatures. The Young's modulus of the SMP is very high compared to the other membranes and it dominates the overall stiffness of the diaphragm (see Appendix B: Thermo-mechanical analysis of SMP and SMP+SEBS+CB/PDMS). Figure A.1a shows the storage (E'), loss moduli (E''), and phase angle (δ) of the bare SMP membrane as functions of the temperature. The stiffness of the membranes drops from 1.2 GPa to a few MPa when the temperature is changed from the room temperature to 80 °C. A sharp transition in stiffness occurs between 55 °C and 75 °C. The shape recovery occurs on the basis of this region and it is referred as the glass transition region. Although the transition takes places in a temperature range, usually a single temperature value is used to define the glass transition (T_G) of polymers. The most commonly used way to find the T_G is to use the maximum value of the phase angle (green curve in Figure A.1a). The T_G of the SMP material we used (MM4520 from SMP Technologies) is around 65 °C, which is relatively higher than the value reported by the producer. This value varies depending on how the T_G is calculated and also it's also influenced by the treatments during the fabrication.

3.4.5 Optimization of SMP thickness

The diameter of the valves is chosen as 3 mm based on the previous experimental results obtained for haptics applications in LMTS. [99] The valves with a depth of 200 μm is chosen as this thickness enables an easy fabrication and the valve diaphragm can achieve adequate deformation to completely close this depth. The shape of the valves was then designed to allow for good sealing between the PS chip and valve diaphragm when the diaphragm is deformed. For the optimization purpose, we used the valve diameter of 3 mm and a depth of 200 μm . Among the tri-layers in the diaphragm, the stiffness of the SMP layer is much higher than the other two (even at the soft state). Therefore, we chose the SMP thickness as the main optimization parameter. Plots shown in Figure 3.7a-b were obtained using COMSOL multiphysics.

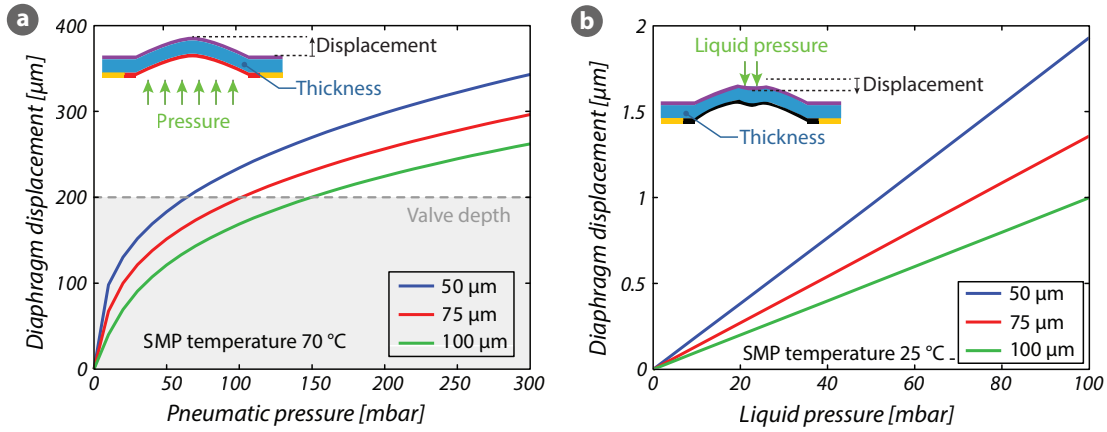


Figure 3.7: Thickness optimization of the SMP layer. a) The center diaphragm displacement as a function of pneumatic pressure for different SMP thicknesses. The thicker SMP requires the higher pressures to close the valve. b) Displacement of the center of the membrane under the liquid pressure in the cold state, predicting how much the membrane moves due to liquid pressure at the latched state.

The SMP thickness has influence on the actuation displacement, the blocked liquid pressure, and the power consumption. The thinner SMP membranes, for example, allows larger diaphragm displacement and shorter the switching time. However, thin SMP cannot resist high liquid pressure. Contrarily, the thick SMP membranes enable higher holding pressure and easy fabrication, but this increases the thermal time constant.

Increasing the SMP thickness allows us to keep the valve in closed-latched position under higher liquid pressure. However, it requires more pneumatic pressure to close the valve (see Figure 3.7a), increases the time thermal time constant (longer switching time) and also requires more heating power. Figure 3.7b shows the displacement of the center of the diaphragm (where the working liquid is acting on) in the closed latched state. The graph predicts that the valves remain closed until a liquid pressure of 100 mbar, as the resulting displacement is negligible ($<2 \mu\text{m}$). Based on the FEM simulations and the experimental results, we chose SMP thickness as 50 μm for this study.

3.5 Diaphragm fabrication and device assembly

The fabrication process flow of the valve diaphragm is illustrated in Figure 3.8. To fabricate the diaphragm, a polyethylene terephthalate (PET) sheet is first cut into A4 size to serve as a substrate. A sacrificial layer of Teflon is blade-casted on PET for easy removal of the layers from the PET sheet after curing. SEBS pellets (from HEXPOL TPE AB) are dissolved in toluene with a ratio of 50:50 in a centrifugal mixer for 10 minutes. The mixture is cast on Teflon and toluene is evaporated at room temperature for 12 h. For lower SEBS/toluene ratios, an oxygen plasma treatment can be applied to Teflon to adjust the surface wetting of Teflon for a uniform SEBS casting. SMP pellets (SMP MM4520 from SMP Technologies Inc.) are mixed with dimethylformamide (DMF) at a weight ratio of 20:80, then dissolved at 80 °C for 12 h. This mixture is cast on top of the SEBS layer. As DMF is hazardous compound, the casting and the curing is carried out in a ventilated fumehood.

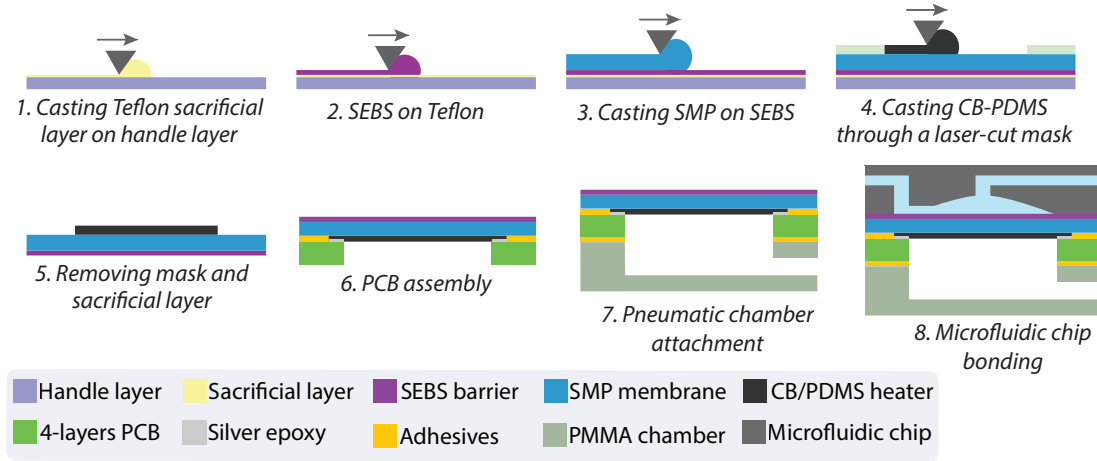


Figure 3.8: Fabrication process flow of SMP valves. The device assembly starts with the fabrication of the valve diaphragm by blade casting of SEBS, SMP, and CB-PDMS layers. The valve diaphragm is then attached to a PCB and a PMMA pneumatic chamber. The whole stack is finally bonded to PS chip.

DMF is then evaporated using a programmable hot plate (for 4 h with positive and negative ramps of 60 °C/h from 25 °C to 80 °C and a plateau of 4 h at 80 °C). A compliant electrode layer based on a mixture of carbon-black (Ketjenblack EC-600JD from Akzo Nobel N.V.) and polydimethylsiloxane (Silbione LSR 4305 from Elkem Silicones) is cast on the SMP membrane using a mask for patterning. The stack is finally put in an oven to cure the electrode layer at 80 °C for 2 h. After the fabrication of the diaphragm is completed, we have an active trilayer with a 50 µm thick SMP membrane, a 25 µm thick CB/PDMS layer with an electrical conductivity of 38.3 S/m, and a 35 µm thick SEBS barrier.

The valve diaphragm is then mechanically and electrically bonded to a PCB using acrylic adhesive with silver epoxy in the vias for the electrical interconnects. The PMMA pneumatic chamber is attached to the bottom of the PCB using an acrylic adhesive (VHB4905 from 3M). Finally, this stack is hermetically sealed under pressure to the microfluidic chip at 80 °C for 2 h.

3.6 Experimental setup for testing SMP valves

The valves are controlled by a custom circuit that synchronizes the individual Joule heating with the common pneumatic pressure. The experimental setup used for the valve characterization is shown in Figure 3.9.

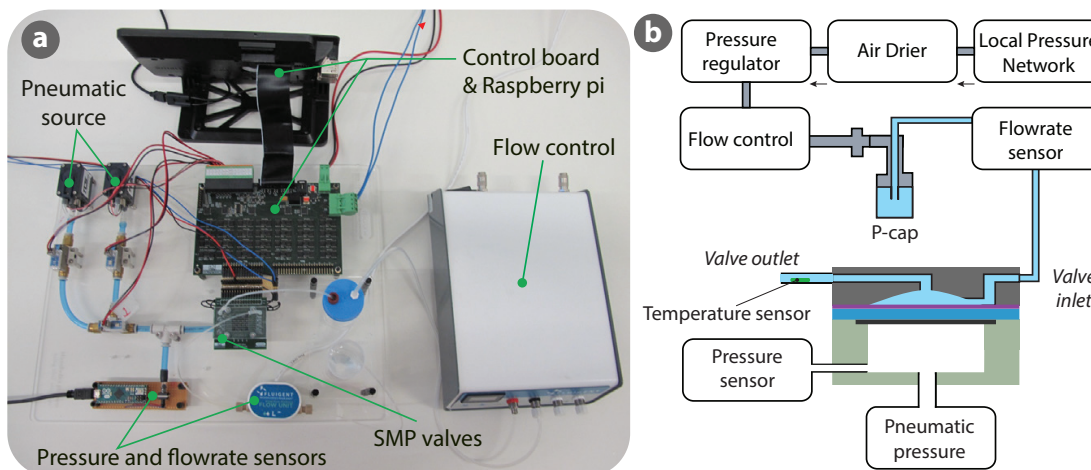


Figure 3.9: a) Photograph and b) schematics of the experimental setup showing the components used for the characterization of SMP valves.

The setup is composed of a commercial pressure regulator driving the liquid through the microfluidic chip (MFCS-EZ from Fluigent Inc.), a flow-rate sensor evaluating in real-time the liquid flow rate (FLOW UNIT M connected to FLOWBOARD from Fluigent Inc.), a platinum resistance temperature detector (RTD) sensing the liquid temperature (PPG101C1 from US Sensor Corp.), and digital multimeters measuring the heater resistance and Joule heating power (Model 2000 from Keithley Inc.). All the instruments are controlled using a LabVIEW subroutine from National Instruments Corp.

3.7 Performance of SMP valves under cyclic and latching operations

The performance of SMP valves are first tested under extended cyclic and long-term latching operations. Then, the electromechanical behaviour of the valve diaphragm is evaluated at a constant heating voltage.

The flowrate, the temperature change in the liquid, and the heating power are plotted as a functions of the time for a valving cycle (see Figure 3.10a). When the valve is switched from the open to closed state, the fluid present in the valve chamber is pushed through the outlet, causing a brief flow surge. Similarly, when the valve is opened, the membrane is pulled down and this pulls a small amount of liquid in, creating a brief backflow. This flow behaviour may generate negative and positive spikes in the flowrate graph. The flowrate at the closed states is around $0 \mu\text{L}\cdot\text{min}^{-1}$, indicating a good sealing between the diaphragm and the valve

3.7 Performance of SMP valves under cyclic and latching operations

chamber. The sealing in the closed state depends on several parameters: the uniformity of heat distribution in the hot state, the adequate pneumatic pressure, the shape fixation of SMP membrane in the cold state, and the match between the deformed valve diaphragm and the profile of valve's seat. The flow rate at the open state shows a small drift. This is possibly due to the relaxation of SMP when the pneumatic pressure is removed.

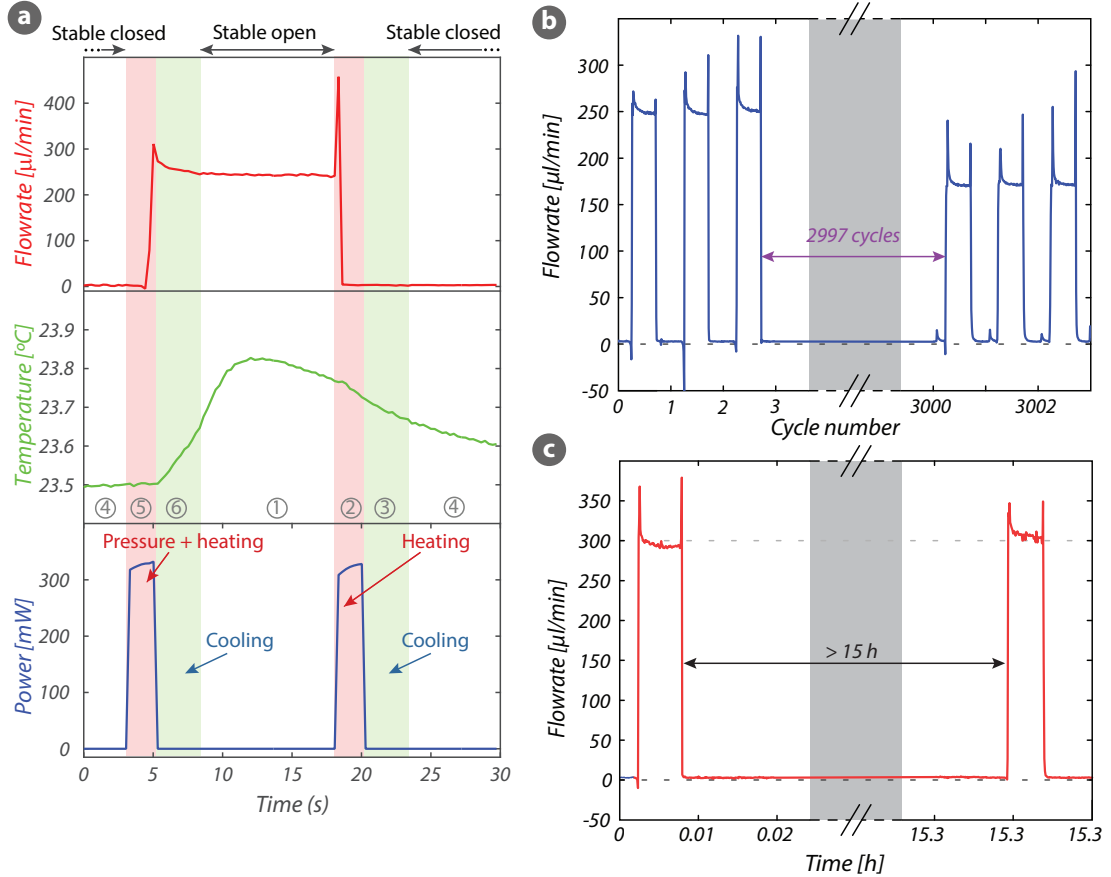


Figure 3.10: The performance of SMP valves under extended cyclic and long-term latching operations. a) Flowrate, temperature change, and heating power plotted as functions of time for a valving cycle with an applied liquid pressure of 50 mbar. b) Flow rate versus time for 3003 open/closed cycles showing only the first 3 and the last 3 cycles. c) Measured flowrate versus time for a latched valve in closed position for over 15 h.

To investigate the lifetime of SMP valves, a valve in the array is randomly selected and it is periodically switched under a fluid pressure of 50 mbar. A constant heating voltage of 19.5 V is applied in order to initially generate 375 mW of heating power. Using a constant voltage simplifies the control. However this control scheme does not compensate the power drop due to heater ageing. This phenomenon will be discussed in detail in the next section.

For cyclic test, the positive air pressure to close the valve is set to 200 mbar, the negative air pressure to open the valve to 100 mbar. The heating duration is 2 s where as the cooling time is 3 s. Between two states the valve is latched for 10 s. The complete valving cycle therefore

lasts 30 s. Figure 3.10b captures the flowrate of the first and last 3 valving cycles out of the 3003 cycles. The flow rate at the open state decreases by 30% (from $250\ \mu\text{L}\cdot\text{min}^{-1}$ to $175\ \mu\text{L}\cdot\text{min}^{-1}$) over the thousands of cycles. This is mainly related to the electrical degradation (resistance increase) of the carbon-based electrodes. [114]

SMP-based valves can intrinsically latch in any position, allowing stable prolonged continuous use in either open or closed states. To demonstrate this latching capability, a valve is operated for several cycles at 50 mbar of liquid pressure, then it is latched at the closed state for 15 h. After 15h of latching it is intentionally reopened and cycled to control its behavior. The flowrate measured during this long-term latching is shown in Figure 3.10c. The flowrates at the open states before and after latching are closed to each other, which is around $300\ \mu\text{L}\cdot\text{min}^{-1}$. As we used NO valve, we latched the valve at the closed state, the critical steps for NO valve. The reason why this step is critical is that the valve diaphragm has to maintain its deformed state under the liquid pressure. If the liquid pressure at the closed-latched state is higher than the internal holding pressure of the diaphragm, the valve is no longer functional and the liquid will flow. The latching experiment was not repeated for the closed-state as the open-latched state in the NO valve is not a critical state (the liquid pressure always helps to keep the valve open).

3.8 Electromechanical degradation of the valve diaphragm

Figure 3.11 shows the electrical resistance of the heaters, the heating power, the temperature changes of the liquid, and the flowrate as functions of the valving cycles. The electrical resistance of the silicone based electrodes have the utmost importance on the cyclic lifetime. As the resistance increases with the number of deformation cycles, the heating power at fixed voltage decreases. This leads to less heating and hence less softening of the SMP membrane. If the SMP membrane is not sufficiently heated to above their glass transition region, the displacement of the diaphragm will be limited due to stiff SMP membrane (see the diaphragm displacement for different temperature in Figure 3.7b). Due to insufficient heating, the valve is no longer fully functional, e.g. if the diaphragm does not fully recovery its flat shape during open state, the flowrate decreases due to partially open state.

The electrical degradation of the electrode occurs much faster than the mechanical deterioration of the SMP. After 3000 cycles of valving, the SMP retains its mechanical properties and can still latch the valve at the closed state up to 70 mbar of liquid pressure. The rate of the electrode degradation depends on the deformation amplitude that the electrode undergoes at each cycle. Lower deformation per cycle usually enables a longer lifetime. As the SMP membranes maintains its properties after thousands of cycles, the valves can achieve their initial performance by increasing the heating voltage at a value that corresponds to the initial heating power of 375 mW. A setup with constant power will enable higher cyclic operation and a constant flowrate over high cycles.

Microfluidic platforms are often used in cell mechanics studies to stimulate the living cells.

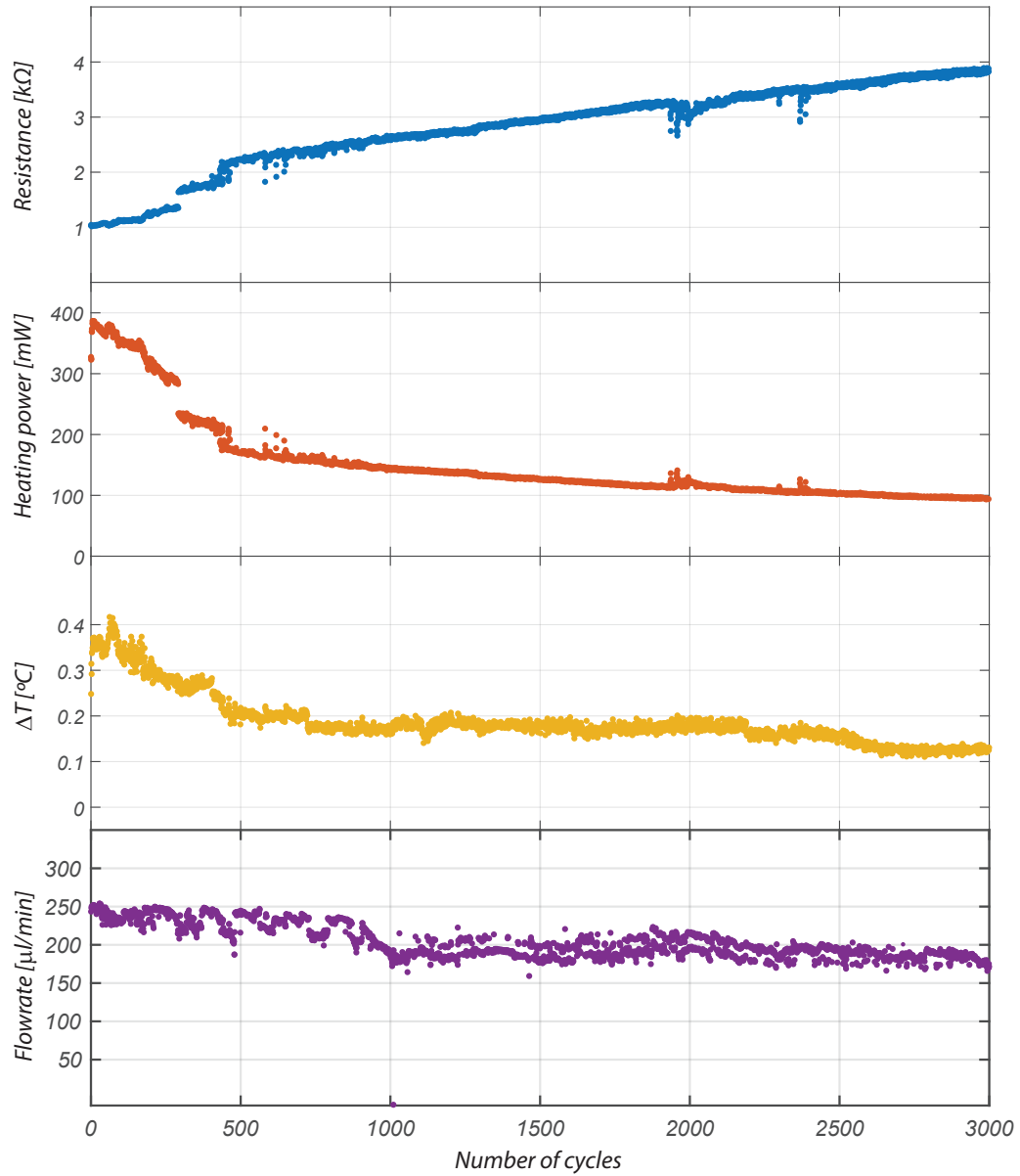


Figure 3.11: Electromechanical characterization of the valve diaphragm. Evolution of electrical resistance of the heaters, Joule heating power, temperature increase of working liquid, and flowrate is shown for over 3000 switching cycles. The electrical resistance decreases due to cyclic mechanical deformation of the heaters. Since a constant voltage source is used to provide Joule heating, the resistance increase causes a decrease in the heating power. The lower heating power the less temperature variation. The ability of the diaphragm to fully close and open the valve depends on the SMP softness during switching; the decrease in heating power leads to a less soft membranes (more stiff SMP) which limits the valve's displacement and eventually cause flowrate decrease.

[115]. Therefore, the heating power used to soften the SMP membranes should not have meaningfully temperature change of the liquid flowing through it. [116]. A temperature sensor was inserted in the tubing at the microfluidic channel outlet, which locates at 30 mm from the active valve. The maximum temperature change per cycles is plotted in Figure 3.11. The highest temperature change of 0.4 °C was observed when a heating power was 375 mW. As the heating power decreases, the temperature change decreases accordingly. Since the heating is confined into a small region of the valves (to heat the only moving region of the diaphragm), the temperature increase was observed to be less than 1 °C, despite the heating of the diaphragm at >70 °C.

3.9 Demonstration of SMP valves as reagent mixer and peristaltic pump

An array of SMP valves are used to demonstrate as a reagent mixer and a peristaltic pump.

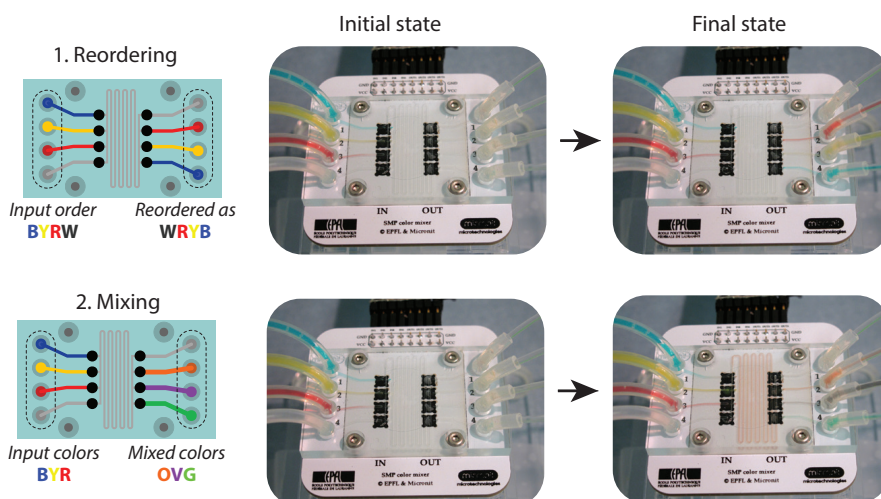


Figure 3.12: Demonstration of SMP valves as reagent mixer. a) Schematics of the reagent mixer having 4 inlets and 4 outlets. The inlets and outlets were controlled using SMP valves and the serpentine flow channel allowed mixing the reagents. The mixer was first used to reorder the different inputs. The BRYW colors at the inlets were reordered as WRYB at the outlet. Then, it was used to mix the input colors where BYR were mixed to obtain OVG.

The reagent mixer has 4 inlets and 4 outlets with a laminar flow mixing channel in the middle. The device was first used to reorder the inputs, as an illustration of the ability to control multiple valves simultaneously. Food dyes with different color were dissolved in water to represent different input reagents. Water (W), blue (B), yellow (Y), and red (R) were the four inputs used in this experiment. Water was used for rinsing. First, the input reagents were reordered at the device outlets without mixing them as shown in Figure 3.12. The color sequence of **BYRW** at the inlet was then reordered as **WRYB** at the outlet channels. By switching simultaneously one inlet valve and one outlet valve, a single color was transferred

3.9 Demonstration of SMP valves as reagent mixer and peristaltic pump

at a time. When color transfer was done, both open inlet and outlet valves were closed, both valves located at the extremities of the device were opened, and the mixing channel was rinsed to the waste container. This procedure is applied to all inlet colors so as to obtain RYB at the device outlet.

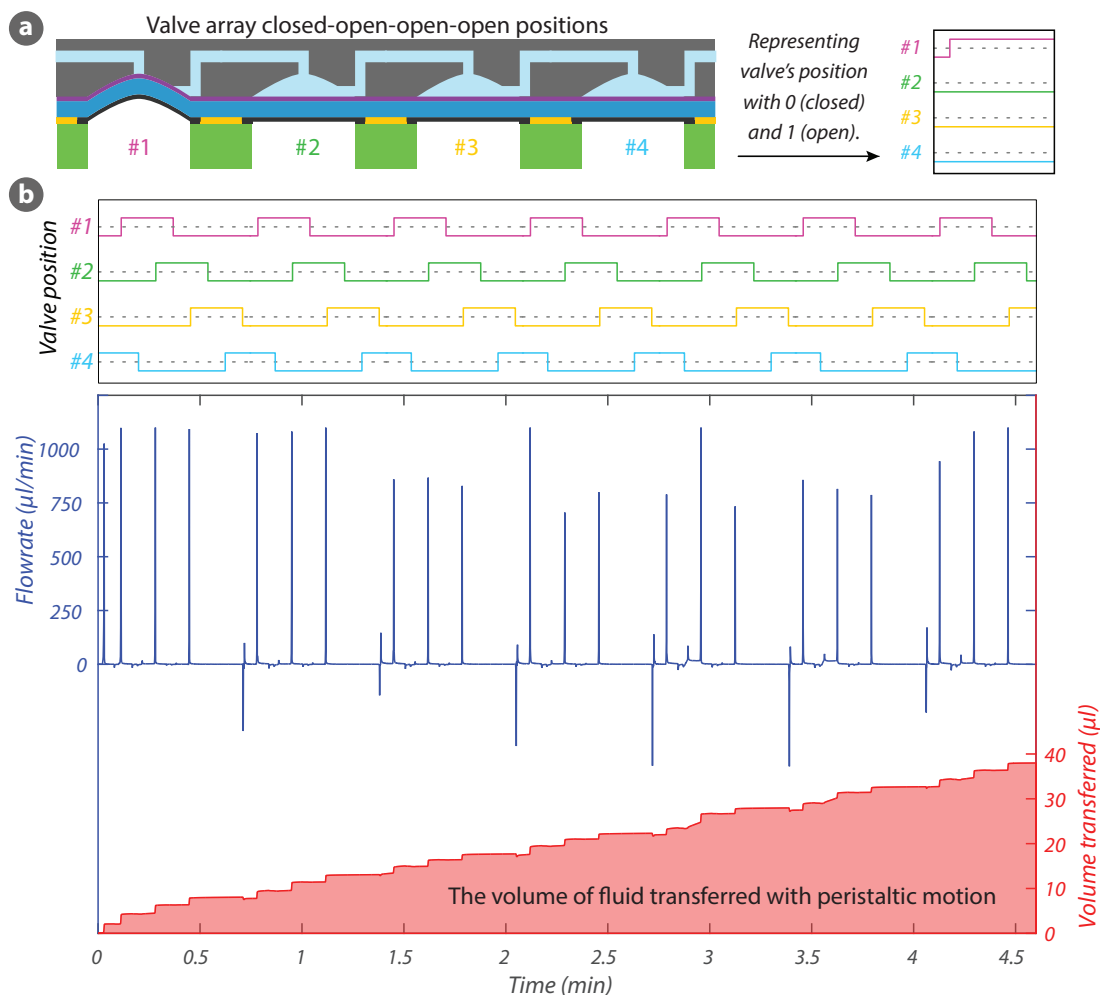


Figure 3.13: Demonstration of SMP valve array as peristaltic pump. a) The cross-section view of valve array used for peristaltic motion. By sequentially opening and closing the valves, the liquid was pushed from left to right to create a net flow. b) The close and open position of valves, the flowrate, and the volume of fluid transferred with peristaltic motion.

This microfluidic platform was then used to mix the three inlet colors. For this, two inlet valves and one outlet valve were simultaneously actuated, resulting in three sets of two mixed colors at the outlet: green ($G = B + Y$), violet ($V = B + R$), and orange ($O = Y + R$) colors. Here, the inlet channel reagents ordered as **BYR** were mixed as **OVG** at the device outlet. Although the applied liquid pressure is the same for all inlets, a variation in the flow rate between channels may occur if either the displacement of each SMP actuator or the hydraulic resistance of each tubing slightly varies. In this mixing application, both the latching and cyclic capabilities of the SMP valves were beneficial to minimize power consumption and device footprint (since

only one pneumatic control line is used). This application shows that a set of SMP valves can be simultaneously actuated.

Traditional PDMS-based peristaltic pumps require at least three pneumatic supplies to actuate each valve in a sequence. [117, 118] Thanks to the intrinsic latching ability of SMPs, a single pressure supply is sufficient for peristaltic motion. To make the pump, we used one row of 4 SMP valves in a series as shown in Figure 3.13a. By opening and closing the valves in sequence, the liquid was pulled into and pushed out of the valves to create a net flow. The actuation frequency of our peristaltic pump is limited by the heating and cooling time of each valve (approximately 2.5 s). Figure 3.13b plots the instantaneous flow rate as a function of time. The repeating peristaltic pump cycle has three large positive peaks corresponding to the closing of the first three valves and one negative peak when opening the fourth valve.

During peristaltic motion neither the inlet nor outlet was pressurized: both sides were at atmospheric pressure. The only driving force to create a flow was the opening and closing of the valves. When a valve is switched from open to closed, the fluid in this chamber exits through either the inlet or outlet. For valves 2, 3, and 4, closing creates a forward flow (at the outlet) because the valves on the inlet of each valve are closed and the valves on the outlet side are open. For valve 1, however, this process creates a backward flow, meaning the fluid in this chamber exits from the inlet channel. This backward motion is not seen in the flow-rate graph because the flow-rate sensor is placed at the outlet of valve 4. The volume transferred with the peristaltic motion is shown in Figure 3.13b. As depicted from this graph, the transferred volume has upward and downward steps. The average volume of upward strokes is $1.87\ \mu\text{L}$ (there are 3 per pump cycle) and downward strokes is $0.56\ \mu\text{L min}^{-1}$ (only 1 per pump cycle).

The sequential timing and the valve design can be optimized to improve the performance of peristaltic pumps. [119] For example, the average flowrate can be increased by using larger valves, or by implementing additional valves. Our approach enables a straightforward step for implementing additional valves as the number of addressable valves can be increased without the need for additional pressure supplies.

3.10 Conclusion

A microfluidic platform based on latchable SMP valves was developed and demonstrated as reagent mixer and peristaltic pump. Having SMP in the valve diaphragm enabled a permanent latching (>15h) as well as extended cyclic (>3000) operations. The SMP membrane was stimulated using patterned stretchable CB-PDMS heaters, allowing a local softening and therefore selective electrical addressing. The SMP layer and the heaters were protected from the working fluid using a thin layer of SEBS.

Thanks to the local heaters and drastic stiffness change of SMP, the synchronization of Joule heating with a global pneumatic air supply allows a selective actuation of each valve in an array without altering the neighbour valves. This approach enable downscaling of the device

footprint by eliminating the need for multiplexing and by replacing the pressure controllers with electronic drivers to individually address each valve.

The reagent mixer and peristaltic pump were shown to demonstrate simultaneous control of different valves, which can be further improved to obtain a simple and compact mLSI system based uniquely on SMP-based latching valves.

The small heat transfer between the active valve diaphragm and the working fluid (with temperature $<1\text{ }^{\circ}\text{C}$) allows this approach to be used in biological applications, i.e. organ-on-chips, drug delivery, and reagent mixers. [120, 121]

The current design can be further improved for faster actuation and larger scaling. Below, we list the critical aspects of scaling down the size and scaling up the number of valves are discussed below. To provide some quantified results, we use the example of scaling the diameter down from 3 mm to 1 mm and scaling up the number of valves from 16 to 256.

Electrical addressing of individual valves

Joule heating is used to locally soften the SMP membrane using integrated compliant heaters. All electrical connections to these heaters are through a single PCB. When the number of valves is increased from 16 (4×4) to 256 (16×16), row/column addressing can be used to reduce the number of control lines, then only 32 ($16 + 16$) control lines will be sufficient to actuate 256 SMP valves.

Size scaling of the valve's dimensions

For reciprocating valves, the active diaphragm needs to be designed with a free displacement greater than the valve depth to fully block the flow. In the devices reported here, a net pressure of 100 mbar is sufficient to completely close a 200 μm deep valve with a diameter of 3 mm. The parameters that most affect the pressure needed to switch the SMP valves are: the valve depth, the actuator diameter, and the mechanical properties of the SMP membrane.

To investigate the effects of these parameters on the required net pressure, FEM simulations were carried out to evaluate the net pressure required to close the valve as a function of the actuator diameter, for different valve depths. Computed pneumatic pressure required to close a valve is plotted as a function of actuator diameter for different valve depths in Figure 3.14. The SMP thickness and its mechanical properties are taken to be constant for these simulations. Reducing the actuator diameter exponentially increases the pressure required, while reducing the valve depth calls for lower required pressures. In other words, the footprint of the SMP valves can be reduced as long as the valve depth is decreased along with diameter reduction. As an example, 25 mbar of pressure can close a valve having a diameter of 3 mm and a depth of 100 μm .

However, a valve with a similar depth but with a diameter of 1 mm requires 775 mbar of net pressure to fully close. If we reduce the depth of this valve from 100 μm to 50 μm (keeping the same diameter of 1 mm), then the net pressure needed drops to 225 mbar. If soft lithography

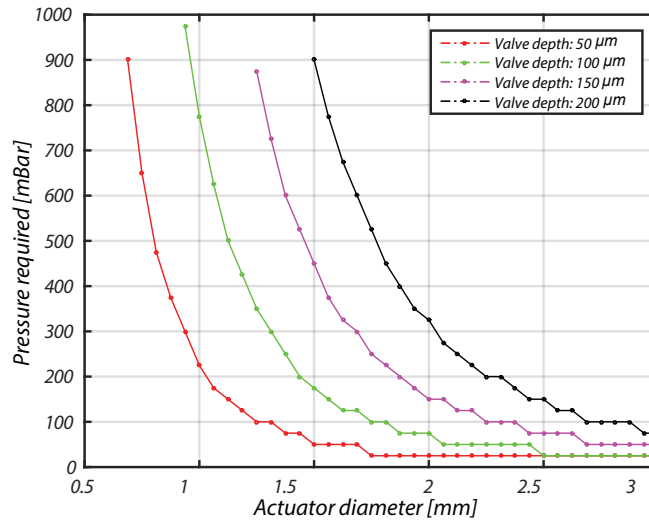


Figure 3.14: Computed pneumatic pressure required to close a valve plotted as a function of actuator diameter for different valve depths.

methods are used for the SMP material, the dimensions of the valves can be further reduced to $100\text{ }\mu\text{m} \times 100\text{ }\mu\text{m} \times 10\text{ }\mu\text{m}$ (typical dimensions for PDMS based valves). [117]

Heating requirements and thermal actuation speed

We reported here a circular SMP valve with a diameter of 3 mm (area of 7 mm^2) that requires 350 mW of power to heat above the glass transition temperature. When this diameter is reduced to 1 mm (0.8 mm^2 area), only 39 mW is needed (9 times less). This significantly reduces the contribution of individual SMP valves to the temperature increase of the entire chip. The thermal time constant is proportional to the actuator size. The smaller the SMP valve, the faster the actuation speed. The SMP valves scale down favorably in terms of power requirement and thermal speed.

Fabrication related challenges

Fabrication techniques play a role in scaling. For example, we use stencil printing to pattern the CB/PDMS electrode on the SMP layer and the feature size of printed electrodes is $500\text{ }\mu\text{m}$. This introduces a practical limitation on the size scaling of electrodes. Using soft lithography or other methods, the fabrication of microfluidic components with much smaller sizes is achievable.

4 Development and modeling of reconfigurable and latchable DEAs

4.1 Summary

In this chapter, I introduce two devices that can be dynamically reconfigured to obtain different actuation shapes and have ability to lock their deformed shapes into place (see Figure 4.1). The first device is a prestretched planar DEA that enables a selective deformation in two in-plane directions. The second device is a multimorph soft DEA sheet with ability to deform in various distinct configurations and has an increased blocking force at its latched state.

This chapter first gives a brief introduction to shape morphing in DEAs and continues with a discussion on the main challenges of combining shape memory polymers with DEAs to achieve multiple shape transformations. It then explains the actuation mechanisms of both devices. The analytical models for optimization of the actuation and latching performances is detailed. Finally, the experimental results and the comparison with the models are discussed. The results presented in this chapter were published in *Advanced Functional Materials* [122]¹ and in the SPIE proceedings of the *Electroactive Polymer Actuators and Devices* [123]², [124]³ and in MRS conference⁴.

The chapter is outlined as follow:

section 4.1: gives a brief summary of the chapter.

section 4.2 briefly explain how different shape transformations can be achieved in dielectric

¹B. Aksoy and H. Shea, "Reconfigurable and latchable shape-morphing dielectric elastomers based on local stiffness modulation," *Advanced Functional Materials*, p. 2001597, 2020.

²B. Aksoy and H. Shea, "Dynamically reconfigurable DEAs incorporating shape memory polymer fibers," in *Electroactive Polymer Actuators and Devices (EAPAD) XXI*, vol. 10966. International Society for Optics and Photonics, 2019, p. 109661Y.

³B. Aksoy and H. Shea, "An analytical model and its validation for the design of multistable dielectric elastomer actuators with high-blocking forces (conference presentation)," in *Electroactive Polymer Actuators and Devices (EAPAD) XXII*, vol. 11375. International Society for Optics and Photonics, 2020, p. 113751N.

⁴B. Aksoy and H. Shea, "Modeling Shape-Programmable and Reconfigurable Dielectric Elastomer Actuator Sheets", 2020 MRS Spring and Fall Meeting.

elastomer actuator using stiff or variable stiffness fibers.

section 4.3 explains the constraints and the challenges of combining the dielectric elastomers with the thermo-responsive shape memory polymers. This section also explains the fundamentals of the analytical models that are used to find the actuation and latched deformations. **section 4.4** explains the design, fabrication, and experimental results of the planar DEA, which can deform in preferential in-plane directions and can be latched in the deformed shape.

section 4.5 demonstrates the multimorph soft DEAs. The working principle, fabrication, experimental results, and pick-and-place demonstrations with different objects are presented. This section also details the optimization of the design parameters and provides a design guide for large deformation and high blocking force.

section 4.6 summarizes the outcomes of the study.

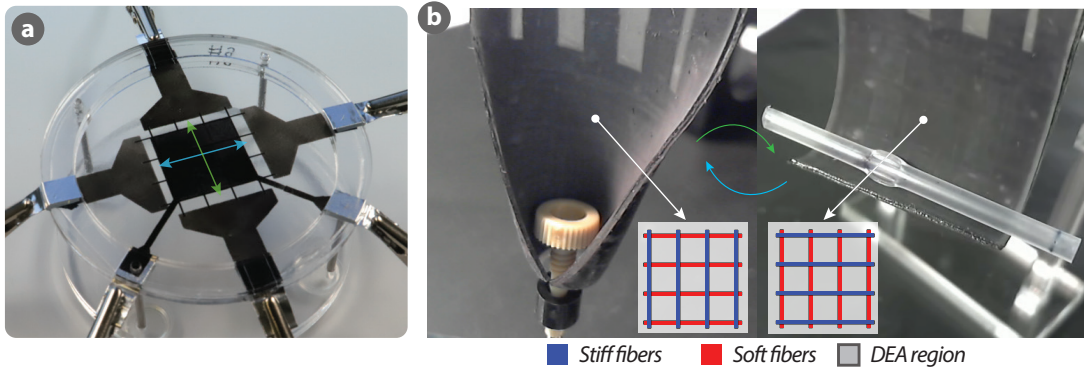


Figure 4.1: Dynamically reconfigurable and latchable DEAs. a) A planar DEA with ability to deform and latch in two in-plane directions. b) A multimorph DEA sheet picking and placing objects with different shapes. The orientation of the stiff and soft fibers determines the actuation shape.

4.2 Introduction to shape morphing in DEAs

DEAs consist of a soft dielectric elastomer membrane sandwiched between two compliant electrodes as shown in Figure 4.2a. They reduce in thickness and expand in area when a voltage difference is applied to the electrodes. [57] With different boundary conditions and design configurations, this in-plane expansion can be transformed into out-of-plane deformations. [5] Attaching a passive layer to the dielectric elastomer, for instance, results in a bending actuation (see Figure 4.2b). The embedded stiff fibers constrain the deformation along their longitudinal direction and enhance the deformation in the transverse direction (see Figure 4.2c). These boundary conditions are imposed during the device fabrication and cannot be modified after the device is fabricated. The fixed boundary conditions, therefore, limit the number of deformation shapes.

Dynamically controlling the deformation of DEAs (usually referred to as shape-programming or shape-shifting) allows a broad range of functional mechanisms such as grippers, mobile robots, or drug delivery systems. [125] For example, origami-inspired surface morphing was used

for crawling robots that can fold themselves, tactile displays capable of controlling both the geometry and the mechanical properties allowed more realistic haptic sensations, self-folding mechanism in micro-scale was utilized for encapsulation and delivery of drugs. [126–128]

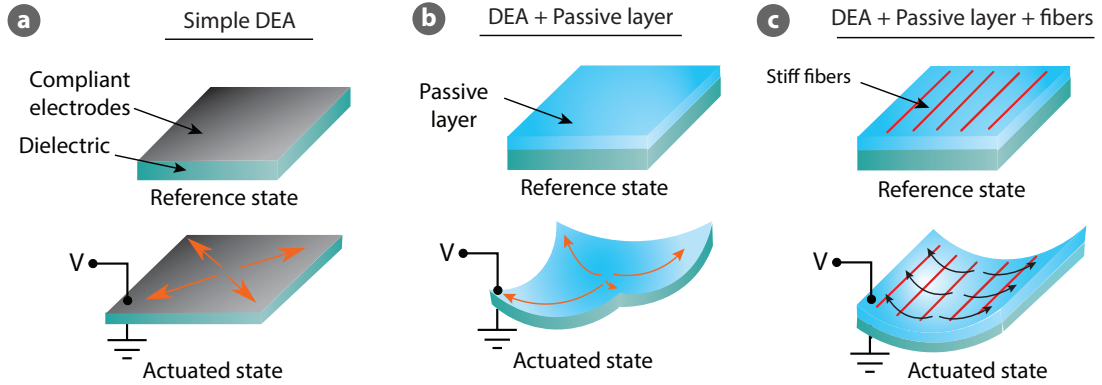


Figure 4.2: Shape programming of DEAs using passive layer and stiff fibers. a) A simple DEA expands in area and reduces in thickness upon electrostatic actuation. b) Having an additional passive layer bends the device and generates out of plane deformation. c) The stiff fibers constraint the deformation along their longitudinal directions.

Combining shape reconfigurability, reversibility, speed, and latching in a single soft system would enable complex functional mechanisms. However, developing such a system needs addressing numerous requirements which are usually difficult to integrate with the soft actuators, influence the actuator performance, and induce trade-off between the latching and actuation. Typical requirements for such a system are:

- I) an integrated addressing system for stiffness or actuation control,
- II) spatial stiffness tuning to reconfigure soft actuators for multiple distinct shapes,
- III) suitable active materials,
- IV) appropriate design method to reach simultaneously large deformation and high load-bearing capacity.

Here, we developed dielectric elastomer actuator sheets that can achieve multiple distinct deformations and also can lock their deformed shapes into place. The shape transformations were achieved by spatially tuning the stiffness of embedded shape memory polymer fibers. By preferentially softening the SMP fibers while keeping the unaddressed fibers stiff, we can determine the actuation direction (see Figure 4.3). The stiff fibers constraint the deformation along their longitudinal direction, thus the electrostatic actuation deforms (or bends) the dielectric elastomer along the direction of the soft fibers. When the DEA is actuated, it bends preferentially along the soft axis, enabling the device to morph into multiple distinct configurations. By locally softening different regions or fibers segments, various deformations can be achieved.

The SMP fibers were used as a latching mechanism, allowing holding a given actuated position without any power and therefore leading to much longer lifetime in stationary conditions. Once the desired deformation is achieved, the device can be locked in their actuated state by

cooling the SMP fibers. This way, the devices maintain their deformed shapes even after the high voltage is removed.

The working mechanism of two devices developed in this chapter was based on spatially tuning the stiffness the shape memory polymer fibers (by Joule heating) as shown in Figure 4.3. The planar DEA has two fibers sets oriented perpendicularly and one fiber set is softened at a time to control the direction of the DE motion. The DEA deforms along the direction of the soft fibers whereas the stiff fibers block the DEA expansion along their longitudinal directions. The multi-morphing DEA has asymmetrical structure which bends upon the electrostatic actuation of the DEA. Depending on which fiber set is soft during the actuation, the device deforms accordingly. Once the deformation is achieved, the device can be latched in the deformed state thanks to the shape memory effect of the fibers.

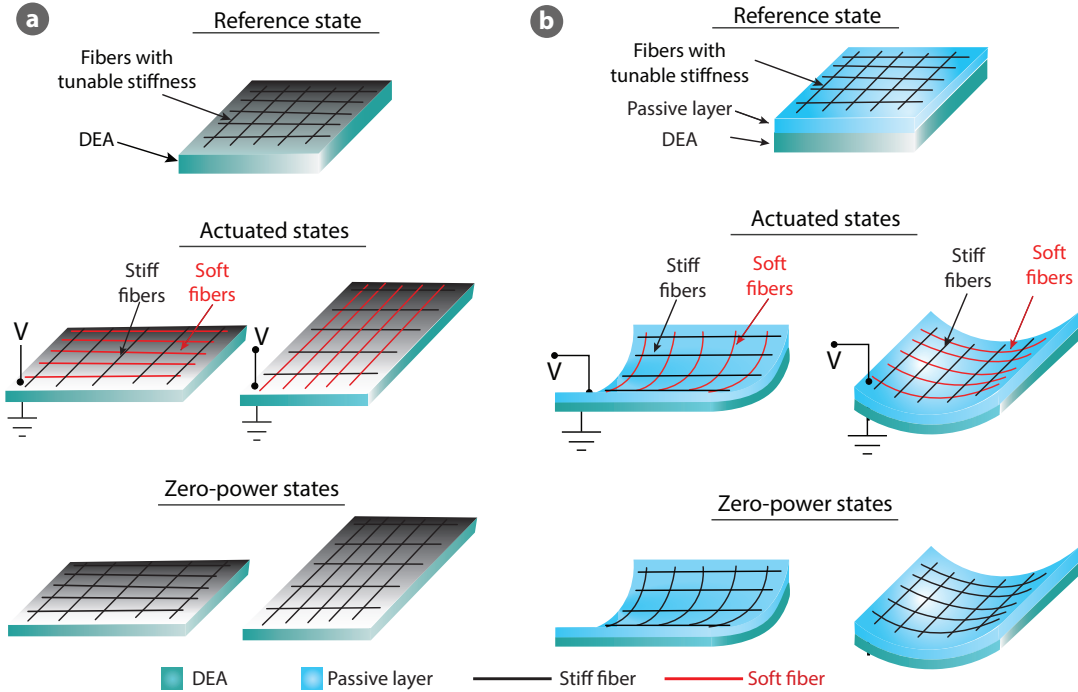


Figure 4.3: Shape programming and shape latching in DEAs using variable stiffness SMP fibers. a) The DEA deformation can be controlled in in-plane directions by tuning the stiffness of the SMP fibers: the DEA expands along the direction of the soft fibers whereas the actuation deformation is blocked in the transverse direction by the stiff fibers. b) Attaching a passive layer to the DEA generates a bending motion due to its asymmetrical design. Similar to the planar DEAs, the stiff fibers in this design constrain the bending along their longitudinal direction. The soft fibers, on the other hand, cannot resist this bending and undergo deformation. In both devices, the deformed shapes can be locked into place thanks to shape memory effect of the SMP fibers.

The fabricated planar device accommodates two conductive SMP fiber sets oriented perpendicularly on the both sides of the DEA. The SMP fibers are made conductive by mixing thermoplastic polyurethane fibers with carbon particles. This way, we can directly soften the fibers by applying voltage through the desired SMP fibers. This reduces the number of layers

in the device.

The second device combines a single DEA with 2 layers of SMP fibers and an array of stretchable heaters. Since the SMP fibers are not conductive in this device, a set of stretchable heaters were utilized to soften a portion of the fibers.

4.3 Main challenges of combining DEAs with thermo-responsive SMPs

Combining SMP with DEAs brings numerous aspects to be taken into consideration while designing and developing latchable soft systems. The following sections list and briefly discuss these aspects.

4.3.1 The effect of temperature on DEA actuation

We used thermo-responsive SMP in our devices. These material has very high stiffness at the room temperature and significantly soften when heated above their glass transition temperature. Therefore we have to soften them by Joule heating to achieve large actuation deformation. When we heat the SMP, we unintentionally increase the temperature of the other layers such as the dielectric membrane.

To investigate the affect of the temperature on the actuation deformation, we tested DEAs at different temperatures. We fabricated a simple DEA using 500 μm thick acrylic elastomer from 3M (VHB 4905) and 32 μm acrylic electrodes from Adhesives Research (AR-care 90366). The acrylic elastomer was biaxially prestretched by 2.8 and was fixed to the rigid PMMA frame. The VHB thickness after the prestretch was 63 μm . The circular acrylic electrodes were then placed on the both sides of the dielectric without prestretch. As we used climatic chamber to set the ambient temperature, we didn't use stretchable heaters and the SMP layer in this device.

The active region of the device had a circular shape with a diameter of 5 mm (see Figure 4.4a). The DEA was actuated with 3.5 kV at a frequency of 0.1 Hz. A video of the active region was captured during the electrostatic actuation. The actuation was repeated at different temperatures, from 25 $^{\circ}\text{C}$ to 50 $^{\circ}\text{C}$ with a step of approximately 5 $^{\circ}\text{C}$. The experiments were carried out in a climatic chamber, where the whole device was at the same temperature (the effect of the local heating is discussed in the next section). The frames of the videos were processed using Digital Image Correlation (DIC) method. [129] DIC is an optical method that employs image registration and tracking techniques for displacement and strain measurements. [129]

Two processed images shown on the left-hand side of Figure 4.4 depicts the spatial distribution of strain over the active region before and after the actuation. The graphs shows the average linear strain of this region at different temperatures. As seen from the graph, increasing the temperature during actuation, significantly increase the actuation strain: the actuation strain

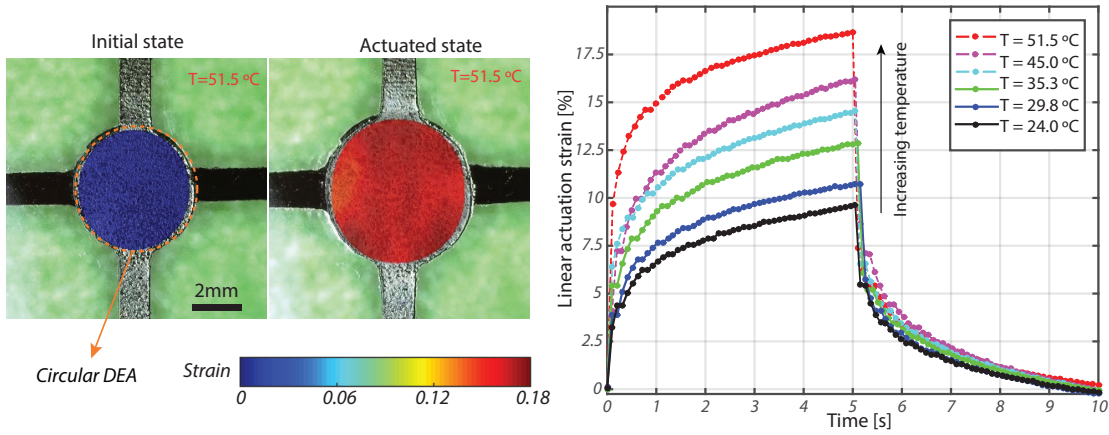


Figure 4.4: The effects of ambient temperature on the DEA actuation. The DEA is made of a pre-stretched acrylic elastomer as dielectric and two circular acrylic electrodes. The strain is spatially mapped on the captured micrographs at the reference (initial) state and at the actuated state. DIC is used to extract the in-plane strains from the captured images. [129] Time evolution of the linear strain at various temperatures: increasing the temperature results in higher actuation strain.

strongly depends on the ambient temperature. Increasing ambient temperature from $24\text{ }^{\circ}\text{C}$ to $51.5\text{ }^{\circ}\text{C}$ increased the actuation strain.

At the constant electric field, the actuation strain depends on the permittivity of the dielectric and the Young's moduli of the layers. As the permittivity of the dielectric layer (VHB 4905) remains almost constant within this temperature range, [130] the strain increased due the fact that both the dielectric and electrode layers get softer by increasing the temperature.

4.3.2 Stiffening effect of the electrodes on the actuation strain

One of the critical design considerations in DEAs is the compliance of additional layers, i.e. the electrodes and passive layers. These layers need to be very soft and compliant so that they do not obstruct the expansion. To demonstrate the effect of non-zero stiffness layers on the actuation strain, we prepared two DEAs using two different electrode types. Carbon-grease and AR-care electrodes were patterned on two identical acrylic elastomers. Carbon-grease electrodes are very soft whereas AR-care electrodes have a Young's modulus of 1.2 MPa at the room temperature.

Figure 4.5 compares the effect of the electrode types on the actuation strain. Images on the left-hand side show the reference and actuated states of the DEAs. The strain at these states are mapped on the active regions. The graph shows the evolution of strain when the DEAs are actuated at 2 kV and 2.5 kV at the room temperature. As seen from the strain maps and strain-time plots, the DEA with carbon-grease electrodes has higher actuation deformation. The stiffening effect of the AR-care electrodes significantly reduces the achievable deformation. As our devices consists of several layers of SMP, electrodes, and insulators, the contribution each

4.3 Main challenges of combining DEAs with thermo-responsive SMPs

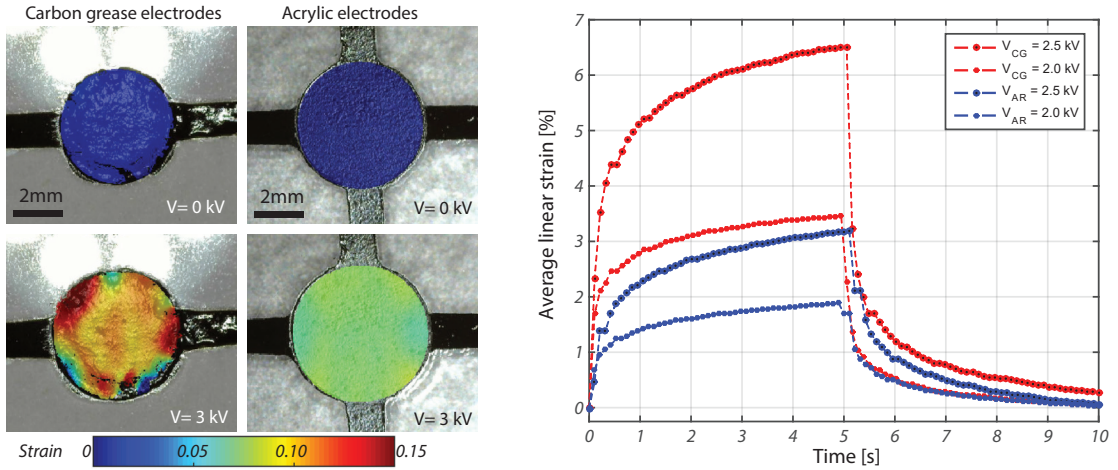


Figure 4.5: The effects of the electrode stiffening on the actuation strain: strain maps and strain graph showing the effect of relatively stiff and soft electrodes on actuation deformation: the stiffer electrodes the lower deformation.

layer on the overall device stiffness is utmost crucial and needs to be taken into consideration.

4.3.3 Asymmetrical deformation due to fiber stiffening

When a fiber is attached to the dielectric elastomer, it reinforces the membrane along the fiber's direction, and thus prevents the expansion in this direction. [5] Contrarily, the electrically-induced deformation in the transverse direction is generally enhanced. Since the volume of the elastomer sheet cannot change with applied voltage, the elastomer stretches in a direction perpendicular to the fibers. [63] The effect of the stiff fibers on the deformation shape of the DEA is shown in Figure 4.3.

To demonstrate how the embedded stiff fibers generate an anisotropic deformation, we fabricated two square DEAs with an active area of $5\text{mm} \times 5\text{mm}$: one with a set of stiff fibers having a Young's modulus of 200 MPa and the other one without any fiber. Both DEAs were actuated at the same voltage of 3.5 kV and the in-plane components of the actuation strain are compared.

Figure 4.6a and b compares the in-plane strain components of the DEAs with and without fibers. Figure 4.6a depicts the strain mapping of ϵ_{xx} and ϵ_{yy} of the square DEA (no fibers) at the actuation state. The strain maps show a uniform deformation in the in-plane directions. The average strain components shown Figure 4.6a confirm these uniform strain maps. As expected, the DEA without fiber set has uniform stiffness in in-plane directions and the DEA actuation generates a uniform deformation in x and y directions.

Attaching a stiff fiber set to the biaxially prestretched DEA causes an asymmetrical actuation deformation. The actuation strain components shown in Figure 4.6b belongs to the fiber-

constrained DEA. As the fibers are aligned in the horizontal direction, the deformation due to electrostatic actuation is limited by the fibers. This causes a small deformation in the fibers' direction. On the other hand, the strain in the lateral direction is enhanced by these fibers: under the same applied voltage the fiber constrained DEA has 15% and 5% strains in vertical and horizontal directions, respectively whereas the fiber-free DEA has strain of 11% in both directions.

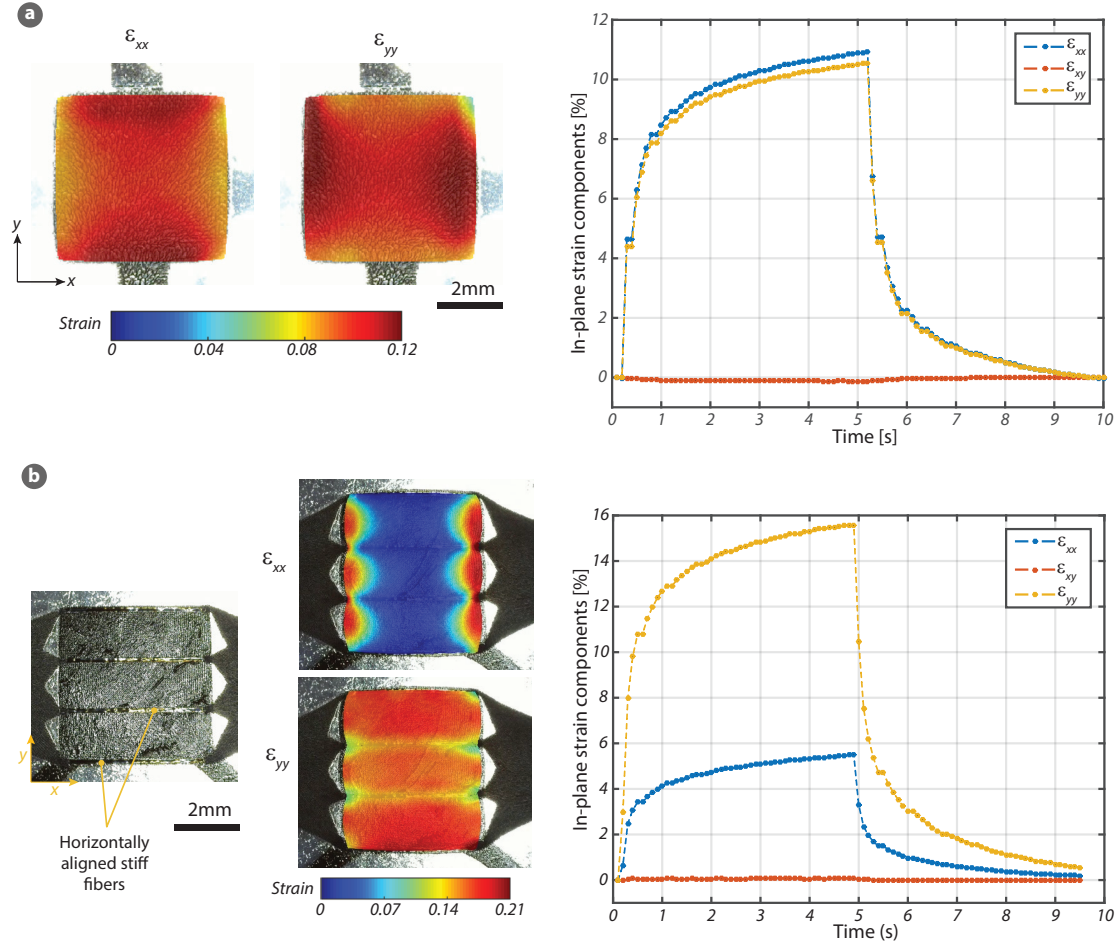


Figure 4.6: The effect of fiber stiffening on the actuation strain. a) The biaxially prestretch DEA has a uniform deformation in x and y directions. Strain maps of ϵ_{xx} and ϵ_{yy} shows a uniform deformation in both directions. b) The DEA with horizontally aligned fibers has larger deformation in y (transverse) direction than in the x (longitudinal) direction. The fibers constraint the actuation deformation along their longitudinal direction and therefore enhance the deformation in the transverse direction. The effect of fibers can be observed in the strain maps and well as in the average strain graph.

By implementing stiff fibers to DEAs, we can obtain high unidirectional actuation strain and also can control the actuation direction.

4.3.4 Effect of dielectric prestretch on voltage-stretch behaviour

The dielectric prestretch has been shown to eliminate the pull-in instability and to improve electric breakdown strength. [63] The actuation deformation in DEAs depends on an interplay between the highly nonlinear hyperelastic stress–strain behaviour and the electrostatic Maxwell’s stress. [131] Here, we briefly discuss how the prestretch changes the voltage-stretch curve of dielectric elastomers.

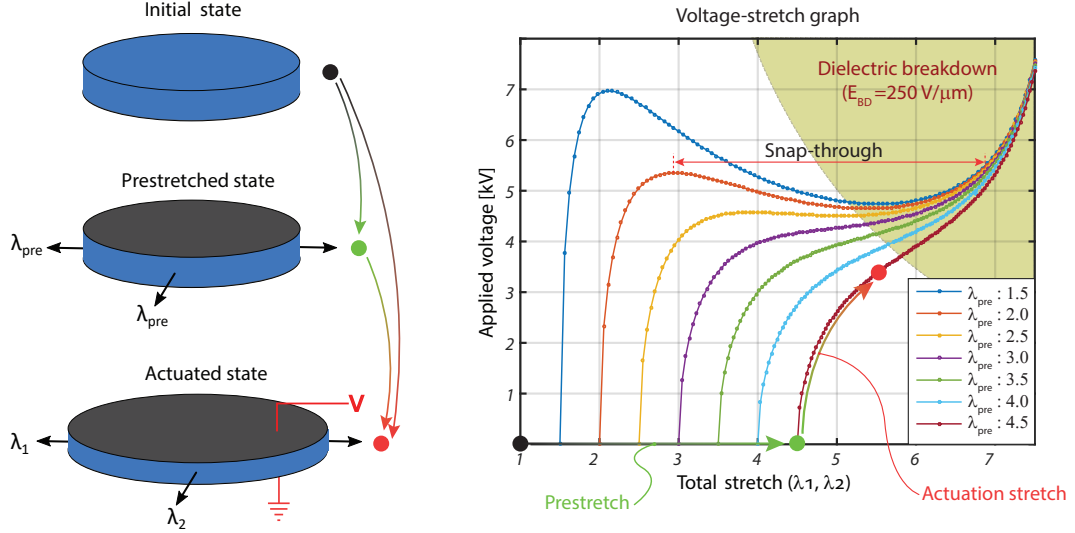


Figure 4.7: Schematics showing the three states of a prestretched actuator: initial, prestretched, and actuated states. A plot of applied voltage vs. total elastomer stretch, showing dielectric breakdown and snap-through regions.

Three states of the actuation of a prestretched DEA is shown in Figure 4.7: the initial, pre-stretched, and actuated states. In the initial state, the dielectric elastomer is at rest. In the prestretched state, the dielectric is prestretched and the electrodes are usually placed on the dielectric without prestretch. In the actuated state, the prestretched dielectric is subjected to a voltage across its thickness. The graph in Figure 4.8 shows the voltage as a function of total stretch, λ_{total} , under the biaxial forces. The total stretch equals to the product of the prestretch and the actuation stretch ($\lambda_{total} = \lambda_{pre}\lambda_{act}$). The three states of the actuator are shown on the graph with black, green, and red circles. The value of λ_{pre} for each curve can be read from the intersection between the curve and the horizontal axis.

The graph is computed using the model of ideal dielectric elastomer [132] and Gent model of strain energy density. [133]. The dielectric elastomer model assumes that the membrane is incompressible and the permittivity is independent of deformation. The model states that sum of the stress due to mechanical prestretch and voltage-induced (Maxwell) stress equals to the Helmholtz free energy ($W_{stretch}(\lambda_1, \lambda_2)$) associated with the stretching of the elastomer. This model is explained in more detail in the section of reconfigurable prestretched DEAs. The Gent hyperelastic material model describes the stretch-stress behaviour of elastomers. The

graph in Figure 4.7 is plotted for acrylic elastomer of VHB 4905 (from 3M) which has a shear modulus of 50 kPa and a limiting stretch of 120. [63] The dielectric breakdown field of this material is assumed constant ($250 \text{ V}\mu\text{m}^{-1}$).

For a given prestretch, the DEA has a unique voltage-stretch curve (see Figure 4.7. At high prestretch, the curve is monotonic. The voltage can be increased to achieve higher deformation until the electric field in the elastomer reaches up to the dielectric strength of the material. The dielectric strength of VHB is taken as $250 \text{ V}\mu\text{m}^{-1}$. At low prestretch values, the curve is N-shaped, the membrane is prone to pull-in instability. When the electric field in the dielectric elastomer increases, it gets thinner so that the same voltage induces even higher electric field. This positive feedback between the thinning of membrane and the increasing of electric field is known as the electromechanical instability.

4.3.5 The effect of local temperature change on prestretched DEAs

When an elastic materials is first stretched and then heated, it shrinks rather than expand. This effect is known as Gough-Joule effect in the literature: it was first observed by John Gough in 1802 and then was investigated further by James Joule. [134] When polymers are stretched, their entropy decreases due to alignment of their chains along the stretching direction (the chains line up in an order). By heating these polymers, we favor the entropy increase which increases the amount of disorder of chains.

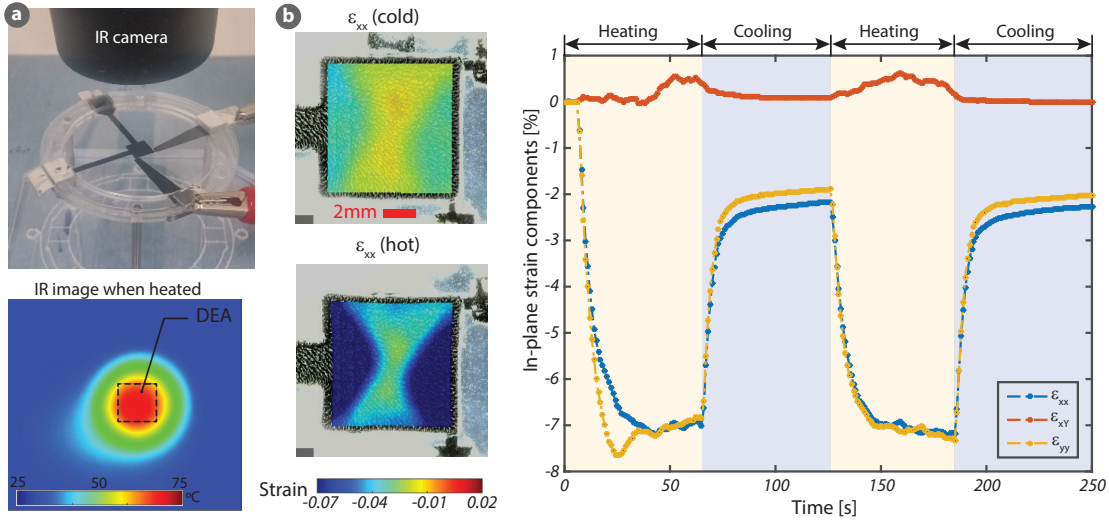


Figure 4.8: The effects of the prestretch and the local heating on the actuation strain. a) Schematics showing the three states of a prestretched actuator: initial, prestretched, and actuated states. A plot of applied voltage vs. total elastomer stretch, showing dielectric breakdown and snap-through regions. b) The experimental setup and the IR image showing the local heating of a prestretched membrane. b) The strain maps demonstration local shrink when the prestched membrane is heated. The graph of strain of the center region when the device is periodically heated and cooled.

When we locally heat the active region on the prestretched DEA, this region shrinks down. When

the heating is turned off it recovers its initial position. Figure 4.8a shows a prestretched DEA, where its center is heated and cooled down periodically. The IR image shows the temperature distribution, reaching 75 °C at the center. A video of this region was recorded while it was subject to a cyclic heating and cooling. Figure 4.8b shows two images captured at the hot and cold states. The strain distribution of the field of view is mapped on the images. The graphs shows the evolution of in-plane strains of the center region while it undergoes heating and cooling cycles. When heated up to 75 °C the area shrinks by 7%. The effect was observed during the actuation and latching of prestretched plane DEAs, which will be discussed in the relevant sections.

4.3.6 Stress-Strain-Temperature behavior of SMP and non-SMP materials

Materials with and without shape memory effect behave differently to the stress, strain, and temperature. Understanding how these materials act under various conditions enables us to design high performance and efficient actuators. In this section, we briefly discuss the difference between these materials and explain the basic concepts of how we quantify the deformation of these materials for building an analytical model.

To model shape memory polymers is tricky as they have different stress-strain-temperature behavior than the materials without shape memory effect. Figure 4.9a schematically represents the loading - shape fixing - unloading cycles of a SMP material (in orange) and a material that does not exhibit shape memory behavior (in blue). The main difference is that the SMP fixes its deformed shape when it is cooled down and it maintains its deformed state after the load is removed. The other material, on the other hand, goes back to its initial (undeformed) position as soon as the external force is removed.

The last column of panel a shows the evolution of the stress and the strain of a mechanically coupled membranes. The structure consists of an SMP layer and two other layers that do not exhibit shape memory effect. For the simplification, the deformation is applied in the longitudinal direction and the structure is chosen symmetric. As the membranes are coupled, both membranes always have the same longitudinal strain. The tensile stress in these membranes, however, depends on their shape memory properties and their Young's moduli. [123] For linear elastic membranes, the stress is related to their instant strain and their Young's moduli at that temperature. However, the stress in the SMP depends on not only their instant strain but also the strain at which they fix their deformation.

The states that are shown in panel a are represented on a stress-strain-temperature diagram in Figure 4.9b-c. The diagram in panel b shows the behaviors of SMP and non-SMP materials when they undergo different states separately. The diagram in panel c shows how these two membranes behave when they are mechanically coupled. This simplified stress-strain-temperature approach is adapted for our analytical model of the multistable dielectric elastomers. The strains ϵ_m , ϵ_f , and ϵ_p are the mechanically applied strain, the fixed (stored) strain after unloading, and the permanent (unrecoverable) strain, respectively. to simplify the

calculation, we assume that the SMP has a shape fixity ratio of 100% ($\epsilon_f = \epsilon_m$) and completely recover its initial state ($\epsilon_p = 0$). In reality, the shape fixity ratio of the SMP membranes is about 97% and the permanent strain is close to 0 (the SMPs are attached with the other elastic materials which force SMPs to go to the initial configuration during the shape recovery).

4.4 Reconfigurable and latchable planar DEAs

This section of this chapter explains how we used the fiber-stiffening technique to achieve actuation deformation in different directions in a planar DEA.

The section covers the design, fabrication, modeling, and experimental results of the planar DEAs that can be deformed in the preferential in-plane directions and can be latched in the deformed state after the high voltage is removed (see Figure 4.10a). These devices accommodate two conductive SMP fiber sets oriented perpendicularly on both sides of the DEA, allowing a selective deformation in two different directions. During the electrostatic actuation, one of the fiber sets is softened by Joule heating while the unaddressed fibers remains stiff. The stiff fibers determine the actuation direction by blocking deformation along their longitudinal direction. The SMP fibers also allow an integrated latching mechanism by holding a given actuated position without consuming power. This leads to much longer lifetime in static (DC) conditions.

4.4.1 Working principle of planar DEAs

These planar actuators combine a single DEA with two perpendicular conductive SMP fiber sets (see Figure 4.10b). They have 6 electrical connections, two of which are used for electrostatic actuation of the DEA and the remained 4 connections are used to apply voltage for Joule heating of the top and bottom fibers. During actuation, one of these fiber sets is softened by Joule heating, while the other one remains stiff and determines the direction of voltage-induced deformation. Fibers are made of conductive SMPs and the electrical connections to them are made by pad-printed silicone electrodes. Two passive elastomer layers are placed between the fiber sets and the DEA electrodes for electrical insulation. These layers also serve as thermal insulation between addressed (hot) and unaddressed (cold) fibers.

Figure 4.11 shows the steps for actuation and latching along the y-axis. The first step is to soften fibers that are aligned in y-direction by applying voltage (V_{JH}) through the top electrodes. This increases the temperature of the fibers above their glass transition region, thus they become very soft. Once the fibers are heated, a high voltage is applied to the DEA electrodes for the electrostatic actuation. Once the deformation is achieved in the preferential direction (in y-direction in this case), the DEA can be locked in this actuated state by first removing the heating voltage and then removing the DEA voltage (V_{DEA}). Keeping the DEA voltage on during the cooling enables us to fix the deformed shape of the SMP fibers. This shape fixation, thanks to the shape memory ability of the polyurethane, can keep the device in the

4.4 Reconfigurable and latchable planar DEAs

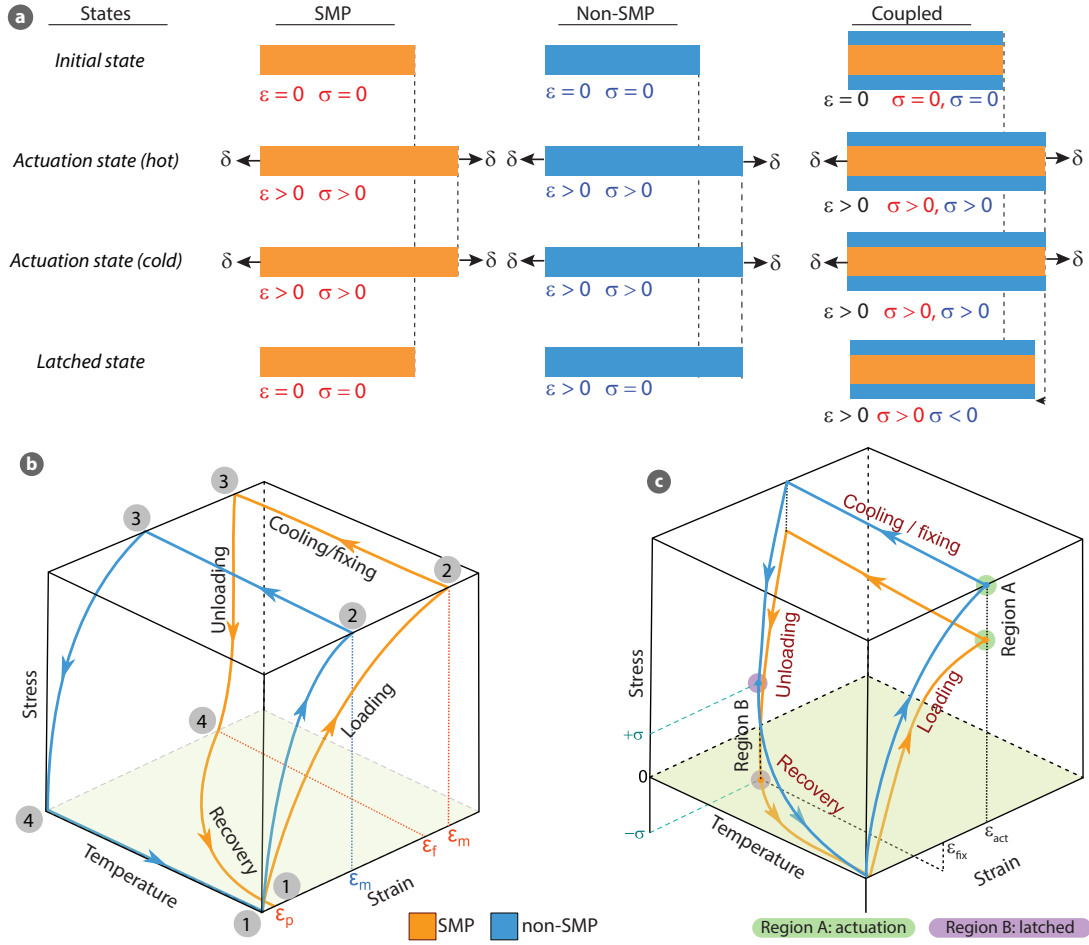


Figure 4.9: a) The stress-strain-temperature behaviors of a thermo-responsive SMP material (in orange) and a material without shape memory effect (in blue) are schematically represented as they are heated, loaded, cooled, unloaded, and finally recovered. a) The SMP materials can fix their deformed shape upon cooling whereas the other materials (non-SMP) do not exhibit this behavior. The evolution of stress and strain in a mechanically coupled structure (1 SMP layer + 2 materials with no shape memory) as it undergoes different temperature and loading states. Since both materials are bonded together, they have the same longitudinal strain in all states. The red and the blue stress values correspond to stress in the SMP material and in the material that does not have shape memory ability, respectively. b-c) The states that are shown in panel a are represented on a stress-strain-temperature diagram. The diagram in panel a shows the behaviors of SMP and non-SMP materials when they undergo different states separately. The diagram in panel c shows how these two behave when they are mechanically coupled. This simplified stress-strain-temperature approach is adapted for our analytical model of the bistable dielectric elastomers.

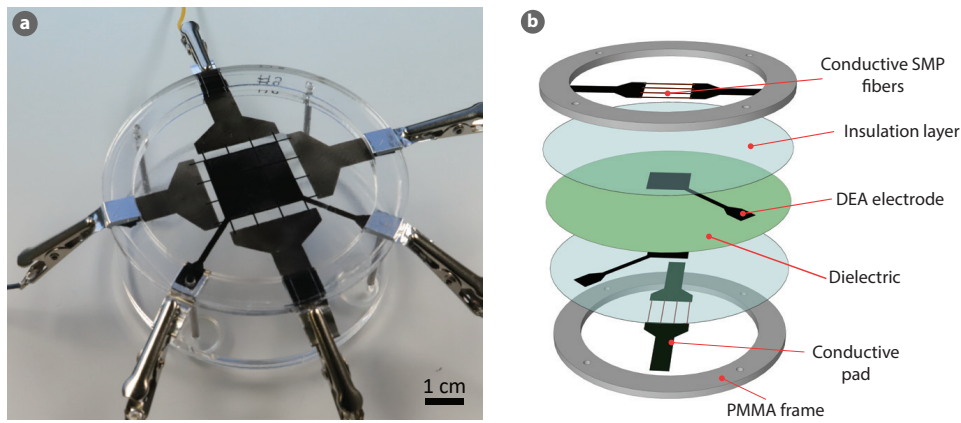


Figure 4.10: The image and exploded view of the reconfigurable and latchable planar DEA. a) Photograph of an assembled plane DEA showing electrical connections to the DEA and to the conductive SMP fibers. b) Exploded view of a DEA with 2 perpendicular sets of conductive SMP fibers. b) Steps to actuate and to latch the DEA in the y-direction.

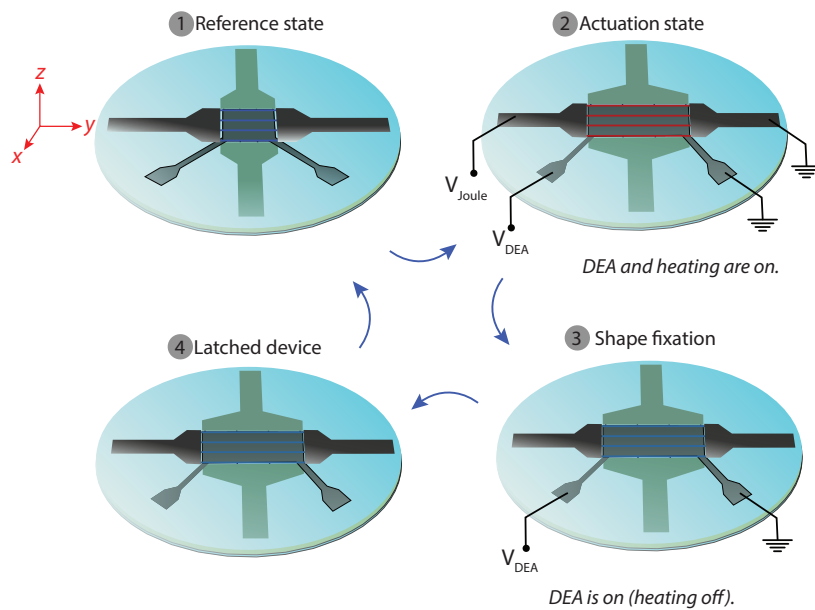


Figure 4.11: Steps to actuate and to latch the DEA in the y-direction. The actuation direction is determined by bottom SMP fibers which remain stiff during the electrostatic actuation.

actuated state even after the high voltage is removed. To recover the initial undeformed shape we simply reheat the same fibers. A similar approach can be repeated to actuate and to lock the device in x-direction by electrically addressing the fibers in x-axis.

4.4.2 Dynamic mechanical analysis of carbon-loaded SMP fibers

We take advantage of the large stiffness change of SMPs to soften the fibers by sweeping the temperature around its glass transition temperature. Soft SMPs enable us to achieve large actuation strain and stiff SMPs to lock in this actuation deformation into place. Therefore the temperature and similarly the stiffness during the actuation and latching are utmost important.

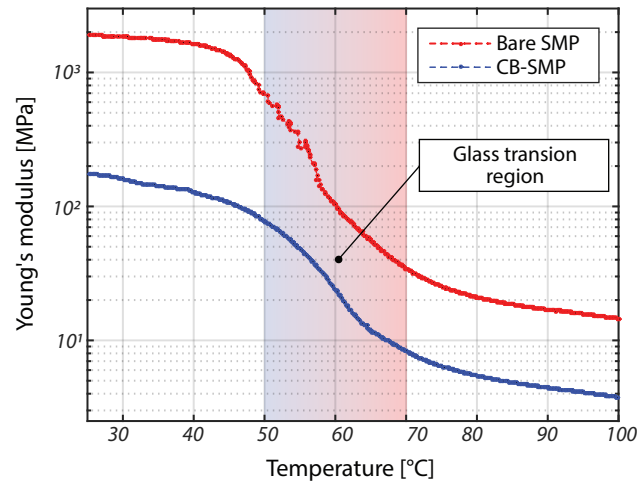


Figure 4.12: The Young's moduli of bare and carbon-loaded SMPs as functions of the temperature. Both samples have the same glass transition region, but carbon-loaded SMP has lower Young's modulus.

We made the SMP fibers conductive by adding carbon particles. This reduced the number of layers in the device and simplified the fabrication process. The temperature dependence of the Young's moduli of the bare SMP and the carbon-loaded SMP was measured by dynamic mechanical analysis (DMA). Figure 4.12 shows the Young's modulus of bare and carbon-loaded SMPs as functions of the temperature. Bare SMP samples, for example, has a Young's modulus of 2 GPa at the room temperature and above 75 °C this decreases to 20 MPa. Compared to Bare SMP, carbon-mixed samples have lower stiffness. the young's modulus of carbon-loaded SMP was used in our finite element modeling for thermal analysis (the following section) and in analytical modeling for the actuation and latched deformations.

4.4.3 Finite element model for thermal optimization

To achieve high deformation in one direction and to block the deformation in other direction, the heated (hot) and unheated (cold) fibers need to be thermally isolated. A finite element

model was used to design a device that minimizes the amount of the heat transferred between the fiber sets. The parameters that we optimized in these models are the thickness of the passive layers and the number of the SMP fibers.

FEM simulations were used to investigate the effect of the insulation layer thickness and the number of fibers on the cross-heating between the fiber sets. The model included all components that are shown in Figure 4.11a. The dielectric membrane constructed in the model had a diameter of 60 mm and a thickness of 35 μm . The DEA electrodes had thicknesses of 5 μm with a square area of 20 mm x 20 mm and they were placed on the top and bottom of the dielectric membrane. Insulation layers covered these electrodes and their initial thickness was 25 μm . In this simulation, we used 2 fiber sets each of which consisted of 4 fibers (75 μm x 100 μm x 25 mm). They were aligned perpendicularly on the bottom and top of the insulation layers.

The thermal conductivity of the dielectric membrane and the passivation layers used in this model was 0.19 W/mK. The carbon-loaded membranes, SMP, and PDMS, are expected to have higher thermal conductivity; therefore we used 2 W/mK for those membranes. The heat capacities of the dielectric membrane and the passivation layer is taken to be 1460 J kg⁻¹ K⁻¹. The heat capacities of the PDMS and SMP membranes were 1380 J kg⁻¹ K⁻¹ and 1900 J kg⁻¹ K⁻¹, respectively. The heating voltage was applied to the top fibers. Then we compared the temperature distribution along the top (heated) fibers and the bottom fibers. This procedure was repeated for different insulation layer thicknesses, from 25 μm to 100 μm and for different numbers of fibers.

The FEM simulations suggested to use thin insulation layers and set of 4 fibers for optimized DEA design. Figure 4.13b plots the temperature across the heated and unheated fiber for the optimal design. The addressed fibers have a uniform temperature distribution, slightly decreasing at overlaps between the heated and unheated fibers. Unaddressed fibers, on the other hand, have a varying temperature profile; highest at the overlaps.

When the thickness of the insulation layer increases, the temperature of the unheated fibers at the overlaps slightly decreases. However, thicker membranes cannot dissipate heat into air as fast as thinner ones. This allows heat to transfer in lateral direction which increases the temperature of the unheated fibers in regions outside the overlaps. These simulations showed that 100 μm thick insulation layers do not efficiently prevent the heat transfer between fibers.

4.4.4 Analytical model of prestretched planar DEAs for high actuation and locked strains

Actuation and locked strains favour different SMP thickness: thin SMP layers have less stiffening impact on the actuation strain but they are weak to lock this strain. Thick layers, on the other hand, significantly reduce actuation strain but they can lock most of the actuation deformation. An analytical model was developed to find best trade-off between the SMP thickness and the dielectric prestretched for maximizing actuation and locked strains.

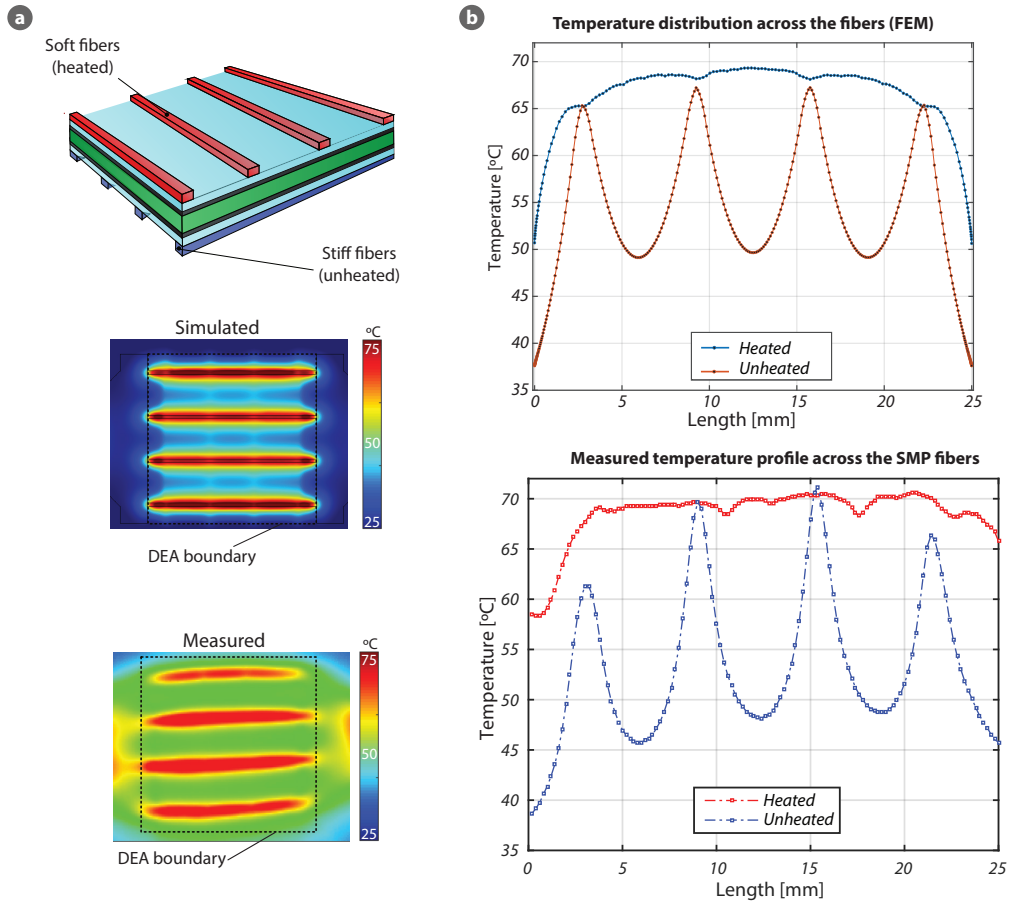


Figure 4.13: Finite element model for thermal optimization. a) The schematic of the DEA illustrating the heated (top) and the unheated (bottom) fibers. The simulated and measured temperature distributions when the horizontal fibers are heated. b) The simulated temperature distribution across the length of the heated and the unheated fibers. Due to the heat transfer between hot and cold fibers, the unheated fibers have high temperature at the overlapped regions. Measured temperature profiles (by IR camera) of the heated and unheated fibers confirm the FEM predictions.

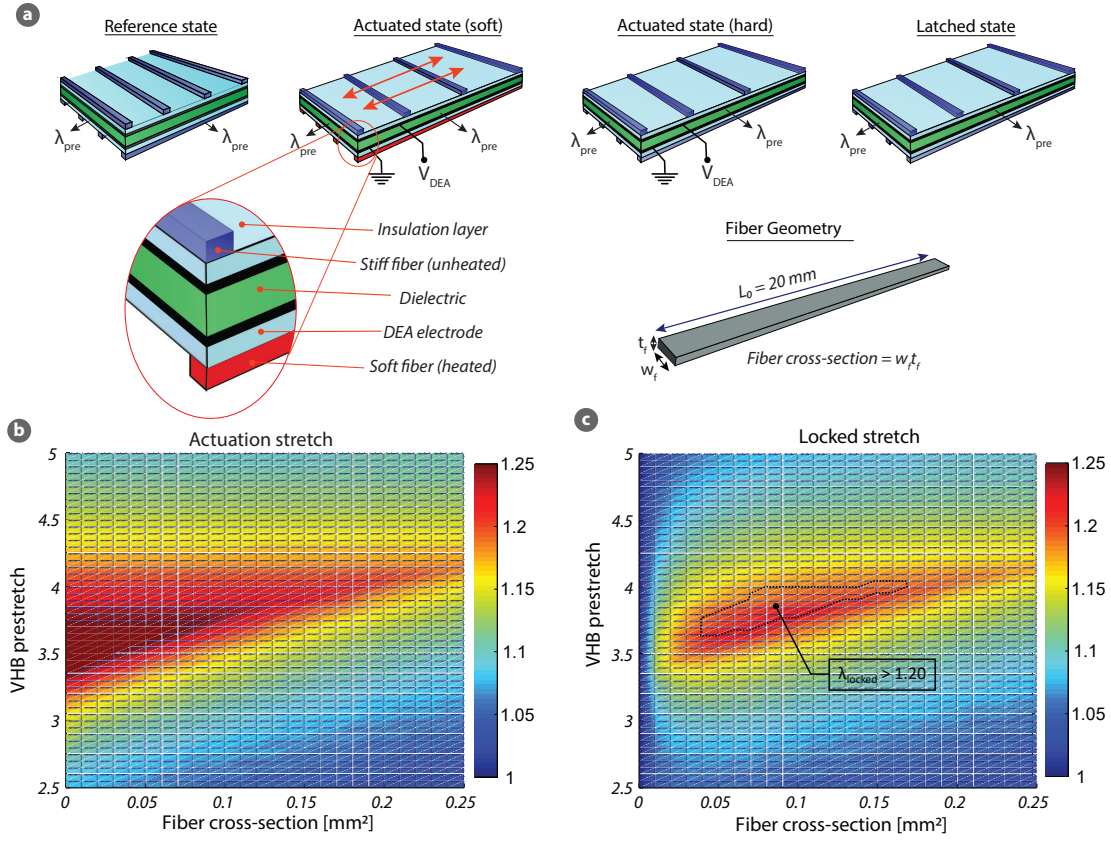


Figure 4.14: Optimization of SMP fiber cross-section and dielectric prestretch. a) Schematic illustrations showing the different states of the device. b-c) Surface plots of the actuation and the locked stretches as functions of the SMP fiber cross-section and the dielectric prestretch. The region with $L_{\text{locked}} > 1.20$ is enclosed with dashed lines.

DEAs are generally modeled based on the stress equilibrium of the dielectric membrane and the stiffening impact of the electrodes are neglected. The scale of electrode stiffening depends on the Young's modulus of electrodes and their thickness. If both the elastic modulus and the thickness are lower than the dielectric elastomer, this stiffening effect can be ignored. Otherwise, the stiffening of the electrodes should be taken into account. [10] Our design had multiple layers and each layer had a comparable thickness and stiffness. We therefore considered this effect in our calculation. We used equations of the force equilibrium instead of stress equilibrium. The stress generated in the membranes is converted into force by multiplying the stress value with cross-sectional area on which it acts.

Table 4.1 shows the stretch values and the cross-sectional areas of all membranes in the reference, actuated, and latched states. These values are for the actuation direction. We assume that there is no deformation in the transverse direction. This table helps us to understand how the membranes deform and also how the cross-section areas change in the aforementioned states. As seen from the table, each membrane has different stretch values. This is due to the fact that VHB is prestretched and the SMP fibers fix their shape upon cooling. Upon cooling, for instance, the stretch values of the VHB and the insulation layers remain the same whereas the stretch value of the SMP fibers goes from λ_{act} to 1. This indicates the shape fixation of SMP, which enables us to lock in the actuation strain.

Table 4.1: Stretch values and cross-sectional area of membranes for different states.

	Reference state		Actuation state (hot)		Actuation state (cold)		Latched state	
	Stretch	CS area	Stretch	CS area	Stretch	CS area	Stretch	CS area
VHB 4905	λ_{pre}	$\frac{L_0 T_v}{\lambda_{pre}^2}$	$\lambda_{pre} \lambda_{act}$	$\frac{L_0 T_v}{\lambda_{pre}^2 \lambda_{act}}$	$\lambda_{pre} \lambda_{act}$	$\frac{L_0 T_v}{\lambda_{pre}^2 \lambda_{act}}$	$\lambda_{pre} \lambda_{act} \lambda_{cont}$	$\frac{L_0 T_v}{\lambda_{pre}^2 \lambda_{act} \lambda_{cont}}$
467MP	1	$L_0 T_i$	λ_{act}	$\frac{L_0 T_i}{\lambda_{act}}$	λ_{act}	$\frac{L_0 T_i}{\lambda_{act}}$	$\lambda_{act} \lambda_{cont}$	$\frac{L_0 T_i}{\lambda_{act} \lambda_{cont}}$
SMP fibers	1	$W_f T_f$	λ_{act}	$\frac{W_f T_f}{\lambda_{act}}$	1	$\frac{W_f T_f}{\lambda_{act}}$	λ_{cont}	$\frac{W_f T_f}{\lambda_{act} \lambda_{cont}}$

The initial thickness of all membranes and their cross-sectional areas are known. As the membranes undergo different states, their thickness and their cross-section change. Although there are many parameters listed in the table, the only unknowns are λ_{act} and λ_{cont} which stand for the actuation stretch and the contraction value. Thus, we need two equations of two different states: one from the actuation state and the other one from the latched state.

Figure 4.14a shows the reference state, where only the dielectric is biaxially prestretched while all other components are at rest. The DEA is then actuated simultaneously by applying Joule heating and electrostatic actuation (see the 2nd state in Figure 4.14a). In the actuated state, the elasticity of the elastomers is balanced by the stress due to mechanical prestretch and by

the Maxwell stress of the electrostatic interaction. We used the Gent hyperelastic material model for strain energy density function. [133] We assumed that the deformation is completely uniaxial. The equilibrium of the forces in the direction of the elongation can be written as follow [63]:

$$A_p \sigma_p + A_v \epsilon E^2 = A_v \frac{\mu_v (\lambda_{1v}^2 - \lambda_{1v}^{-2} \lambda_{2v}^{-2})}{1 - (\lambda_{1v}^2 + \lambda_{2v}^2 + \lambda_{1v}^{-2} \lambda_{2v}^{-2} - 3)/J_v} + 2A_i \frac{\mu_i (\lambda_{1i}^2 - \lambda_{1i}^{-2} \lambda_{2i}^{-2})}{1 - (\lambda_{1i}^2 + \lambda_{2i}^2 + \lambda_{1i}^{-2} \lambda_{2i}^{-2} - 3)/J_i} + N_s A_s \frac{\mu_s (\lambda_{1s}^2 - \lambda_{1s}^{-2} \lambda_{2s}^{-2})}{1 - (\lambda_{1s}^2 + \lambda_{2s}^2 + \lambda_{1s}^{-2} \lambda_{2s}^{-2} - 3)/J_s} \quad (4.1)$$

where λ_1 , λ_2 , μ , J , E , A , N , and ϵ are the principle stretches in the directions of the heated and the unheated fibers, the shear modulus, the limiting stretch of membranes, the applied electric field, the cross-sectional area, the number of fibers in one set, and the dielectric constant, respectively. Subscripts p, a, v, i, s stand for prestretch, actuation, VHB, insulation layer, and SMP fibers. The first term of the left-hand side is the force generated by the mechanical prestretch, which assumed to be constant for all states. The second term of the left-hand side is the force caused by electrostatic actuation of dielectric membrane. Three terms on the right-hand side of the equation represent the forces generated due to deformations of the dielectric (VHB 4905), the insulators (MP467), and the SMP fibers. As we assumed that the deformation was completely constrained in the direction of the stiff fibers (direction 2 in our case), we substituted the following equations in Equation 4.1: $\lambda_{2v} = \lambda_{pre}$, $\lambda_{2i} = 1$, and $\lambda_{2s} = 1$. By substituting the stretch values in the actuation direction that are listed in Table 1, Equation 4.1 was simplified as:

$$A_p \sigma_p + A_v \epsilon E^2 = A_v \frac{\mu_v (\lambda_p^2 \lambda_a^2 - \lambda_p^{-4} \lambda_a^{-2})}{1 - (\lambda_p^2 \lambda_a^2 + \lambda_p^2 + \lambda_p^{-4} \lambda_a^{-2} - 3)/J_v} + 2A_i \frac{\mu_i (\lambda_a^2 - \lambda_a^{-2})}{1 - (\lambda_a^2 + 1 + \lambda_a^{-2} - 3)/J_i} + N_s A_s \frac{\mu_s (\lambda_a^2 - \lambda_a^{-2})}{1 - (\lambda_a^2 + 1 + \lambda_a^{-2} - 3)/J_s} \quad (4.2)$$

The shear moduli of the VHB and the insulation layers (467MP) were found using $\mu = E/2(1 + \nu)$, where E is the Young's modulus and μ is the Poisson's ratio. The Young's moduli of VHB and 467MP were found to be 63 kPa and 44 kPa from uniaxial tensile tests. The limiting stretch of the membranes was taken as 120. For the conductive SMP fibers, DMA was carried out to measure the Young's modulus as a function of the temperature. For the actuation step, we used shear modulus of the SMP in the rubbery state (see Figure 4.12). The initial thicknesses of VHB 4905 and MP467 are 500 μm and 60 μm , respectively.

The model includes two failure modes of DEA: dielectric breakdown and electromechanical instability (see Figure 4.7). [37, 135] The dielectric strength of VHB was taken as 250 $\text{V}\mu\text{m}^{-1}$. As

the electric field in the dielectric elastomer increases, it gets thinner so that the same voltage induces even higher electric field. This positive feedback between the thinning of membrane and the increasing of electric field is known as the electromechanical instability. Figure 4.7 plots the applied voltage as a function of the total stretch of VHB and shows the regions where failures occur.

Using Equation 4.2 with the aforementioned constraints, we plotted the actuation stretch as a function of the VHB prestretch and the fiber cross-section (see Figure 4.14b). For a given VHB prestretch, the actuation strain (stretch) is at its maximum where the cross-sectional area of SMP is zero (no fibers). As the cross-section of the fibers increases, the actuation stretch decreases.

To find the optimum cross-section that enables maximum locked strain, we developed an analytical model for the latching part as well. In the latched state, the deformation is locked by the SMP fibers. The VHB and the insulation layers want to shrink down as they do not have a shape memory effect. The SMP fibers, on the other hand, keep their deformed shapes and oppose this contraction. Therefore, there is a force balance between the SMP fibers and the other layers. The equilibrium of these layers in the latched state can be written as follow:

$$A_p \sigma_p = A_v \frac{\mu_v(\lambda_{1fv}^2 - \lambda_{1fv}^{-2} \lambda_{2fv}^{-2})}{1 - (\lambda_{1fv}^2 + \lambda_{2fv}^2 + \lambda_{1fv}^{-2} \lambda_{2fv}^{-2} - 3)/J_v} + 2A_i \frac{\mu_i(\lambda_{1fi}^2 - \lambda_{1fi}^{-2} \lambda_{2fi}^{-2})}{1 - (\lambda_{1fi}^2 + \lambda_{2fi}^2 + \lambda_{1fi}^{-2} \lambda_{2fi}^{-2} - 3)/J_i} + N_s A_s \frac{\mu_s(\lambda_{1fs}^2 - \lambda_{1fs}^{-2} \lambda_{2fs}^{-2})}{1 - (\lambda_{1fs}^2 + \lambda_{2fs}^2 + \lambda_{1fs}^{-2} \lambda_{2fs}^{-2} - 3)/J_s} \quad (4.3)$$

where subscript f stands for the final stretch of the membranes. When we plugged in the final stretch values listed in the last column of Table 4.1, we reduced the number of the unknowns in Equation 4.3 as:

$$A_p \sigma_p = A_v \frac{\mu_v(\lambda_p^2 \lambda_a^2 \lambda_c^2 - \lambda_p^{-4} \lambda_a^{-2} \lambda_c^{-2})}{1 - (\lambda_p^2 \lambda_a^2 \lambda_c^2 + \lambda_p^2 \lambda_c^{-2} + \lambda_p^{-4} \lambda_a^{-2} \lambda_c^{-2} - 3)/J_v} + 2A_i \frac{\mu_i(\lambda_a^2 \lambda_c^2 - \lambda_a^{-2} \lambda_c^{-2})}{1 - (\lambda_a^2 \lambda_c^2 + \lambda_c^2 + \lambda_a^{-2} \lambda_c^{-2} - 3)/J_i} + N_s A_s \frac{\mu_s(\lambda_c^2 - \lambda_c^{-2})}{1 - (\lambda_c^2 + 1 + \lambda_c^{-2} - 3)/J_s} \quad (4.4)$$

where λ_c is the percentage of the the shrink when the DEA voltage is removed. λ_c can be quantified as the ratio of the final stretch to the actuation stretch. Figure 4.14c shows the surface plot of the latched stretch. Depicted from this plot, one can observe the effect of the cross-section of the SMP on the actuation and the latched (fixed) stretches. If the cross-section

of the SMP fibers are too small or too big then the latched stretch is lower. This is because very small cross-sections do not resist to membranes contraction upon cooling and very large cross-sections introduce more stiffening effect on the actuation which eventually reduces the final stretch. A region with $\lambda_{locked} > 1.20$ is outlined in Figure 4.14c. This region gives us a range of prestretch values and fiber cross-sectional areas where we can achieve locked strain greater than 20% and we selected our design parameters accordingly.

4.4.5 Device fabrication and experimental procedure

The devices were fabricated by prestretching of acrylic elastomer (VHB 4905 from 3M) and fixing it to a rigid PMMA frame. Compliant electrodes based on the carbon-black (Ketjenblack EC-600JD from Akzo Nobel N.V.) and polydimethylsiloxane (Silbione LSR 4305 from Elkem Silicones) mixture were then pad-printed on the prestretched membrane using a mask for patterning. This stack was put in an oven at 80 °C for 1 hour to cure the electrodes. After curing, two insulation layers of thickness 40 μm (467MP from 3M) were placed on both sides.

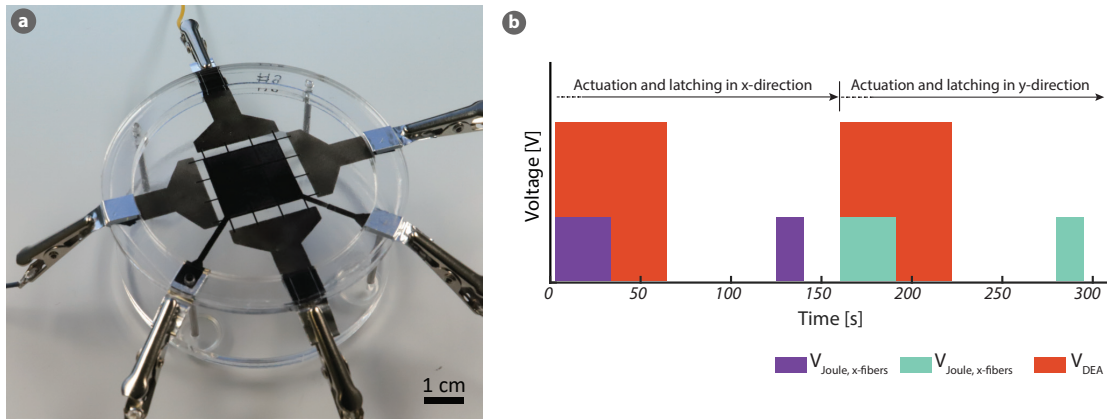


Figure 4.15: a) Photograph of an assembled plane DEA showing electrical connections to the DEA and to the conductive SMP fibers. The DEA has an active area of 20mm x 20mm. b) Time sequence of the actuation (HV) and Joule heating voltages for actuating and latching the DEA in x and y directions.

For conductive SMP fibers, we used thermoplastic polyurethane, SMP MM4520 from SMP Technologies Inc. They were fabricated separately and then assembled on the DEA. SMP MM4520 comes in pellets form. These pellets were dissolved in a container with dimethylformamide (DMF) at a weight ratio of 1 : 4 at 80 °C for 12 h. In another container, carbon-black is ball-mixed with DMF at a weight ratio of 1 : 20 at 2000 rpm for 5 min. The solutions in these two containers were then ball-mixed together for 5 min at 2000 rpm. This mixture was blade-casted on a PET sheet that was covered with a sacrificial layer of Teflon. To evaporate the DMF, a programmable hot plate was used (for 4 h with positive and negative ramps of 60 °C h⁻¹ from 20 °C to 80 °C and a plateau of 4 h at 80 °C). After curing the conductive SMP membrane, it was shaped in fiber form using a laser cutter. The SMP fibers were transferred onto the insulation layers with 90° of alignment between the top and bottom fibers. Thanks to stickiness of 467MP, no further surface treatment was required for this process. For electrical

connection between these fibers and metal contacts, polydimethylsiloxane mixed with carbon particle was pad-printed on both sides. Finally, the whole stack was cured at 80 °C for 1 h. The photograph of an assembled device is shown in Figure 4.15a.

Figure 4.15b shows the time sequence of the Joule heating and the DEA voltages that were applied to achieve the actuation and latching in the x and then in the y-directions. To actuate the device, the DEA and the heaters are simultaneously addressed using a 5 kV and 240 V power supply. After the DEA and the SMP fibers were actuated for 30 s, the heating voltage was removed while the DEA actuation was kept on for additional 30 s to provide time to cool down the membrane and thus to lock in the deformed shape. The device was then held latched for 1 min with no applied voltage. To go back to the reference state, we applied a heating voltage to the SMP fibers for 15 s. The same procedure was then followed to get actuation in the perpendicular direction by softening the other SMP fibers. To measure the evolution of in-plane strain components, images of deformed membranes were captured at a frequency of 1 Hz. The deformed images were processed using digital image correlation (DIC) method. [129]

4.4.6 Experimental results of in-plane deformations and latching

Figure 4.16a shows the evolution of the in-plane strains as the DEA is actuated and latched in y and then in x directions. The highest strain was achieved in the direction of the softened SMP fibers. However, a significant amount of deformation takes place in the transverse direction due to cross-heating between the addressed and the unaddressed SMP fibers. Panel b shows strain mapping of the in-plane components at $t = 280$ s. The warmer colors represent higher strain amplitudes whereas the cooler colors show lower strain values. As shown in the figure, the strain distribution was not completely uniform. This was mostly due to non-uniform heating and fabrication imperfections. The fibers heated the most will have the highest actuation strain.

As explained previously, a polymer under a constant tensile force shrinks upon heating and expands upon cooling. This is due to the elasticity increase through entropic straightening of polymer chains, followed by recoiling into a conformation of maximum entropy. This phenomenon is called the Gough-Joule effect [25]. Per actuation cycle, we observe this twice: first when we remove the heating voltage, and second when we apply heating to go back to the reference state. When the membrane is cooled down at $t = 30$ s, the strains increase. During heating we observe an opposite trend in the strains. The duration of the heating voltage in the recovery step is 15 s, just long enough to go back to reference state. When we increase this duration, we observe slightly negative ϵ_{xx} and ϵ_{yy} .

After one minute of latching, the ratio of the locked strains ($\epsilon_{xx}/\epsilon_{yy}$ or $\epsilon_{yy}/\epsilon_{xx}$) is 1.80. Compared to nylon or carbon fibers, SMP fibers perform poorly due undesired softening of unaddressed fiber set.

To improve this ratio, we designed a cross-shape DEA. We used only two SMP fibers that are

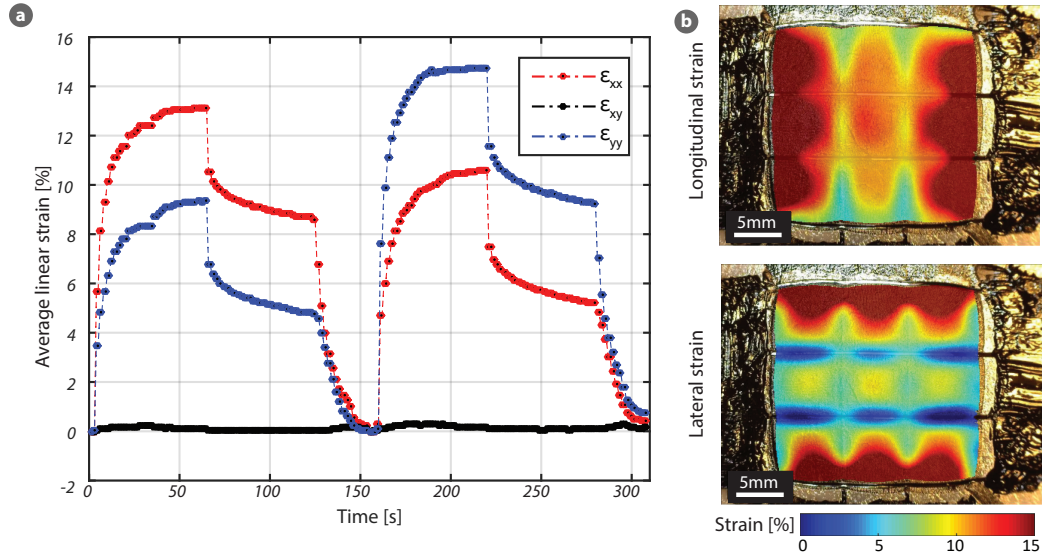


Figure 4.16: a) The evolution of the measured in-plane strains when different fiber sets are sequentially heated and actuated. b) Mapping of strain components on active region at $t = 280$ s.

oriented perpendicularly. The fibers have a uniform thickness of $75\text{ }\mu\text{m}$. Their widths vary across their lengths: wider at the intersection (4.5 mm) and narrower at the outside of the overlap ($750\text{ }\mu\text{m}$). A micrograph and a schematic of this design are shown in the insets of Figure 4.17a. The wider section of the fibers locally reduces the electrical resistance, thus reduces the heating power at this location. The inset of Figure 4.17b shows the IR image when the horizontal fiber was heated. As seen in Figure 4.17b, the temperature of the heated fibers drops from $70\text{ }^{\circ}\text{C}$ to $42\text{ }^{\circ}\text{C}$ at the center where the temperature of the unaddressed fiber increases from $24\text{ }^{\circ}\text{C}$ to $42\text{ }^{\circ}\text{C}$.

To actuate the device in the horizontal direction, we applied a heating voltage of 240 V to the horizontal fiber and actuate the DEA with a voltage of 3 kV . After 30 s , we removed the heating voltage and allowed the membranes to cool for 30 s . After the deformed shape was fixed by the SMP fiber, we removed the DEA voltage. The device was then kept latched for 1 min . Finally, we heated the SMP fiber again to recover the locked strain. Figure 4.17c shows how ϵ_{xx} and ϵ_{yy} evolve during these processes. As we partially solved the cross-heating issue, we are able to significantly increase the strain ratio. Figure 4.17d shows the strain ratio of $\epsilon_{xx}/\epsilon_{yy}$ during the DEA actuation in the x-direction. After 1 minute of latching, the strain ratio is approximately 8 .

4.4 Reconfigurable and latchable planar DEAs

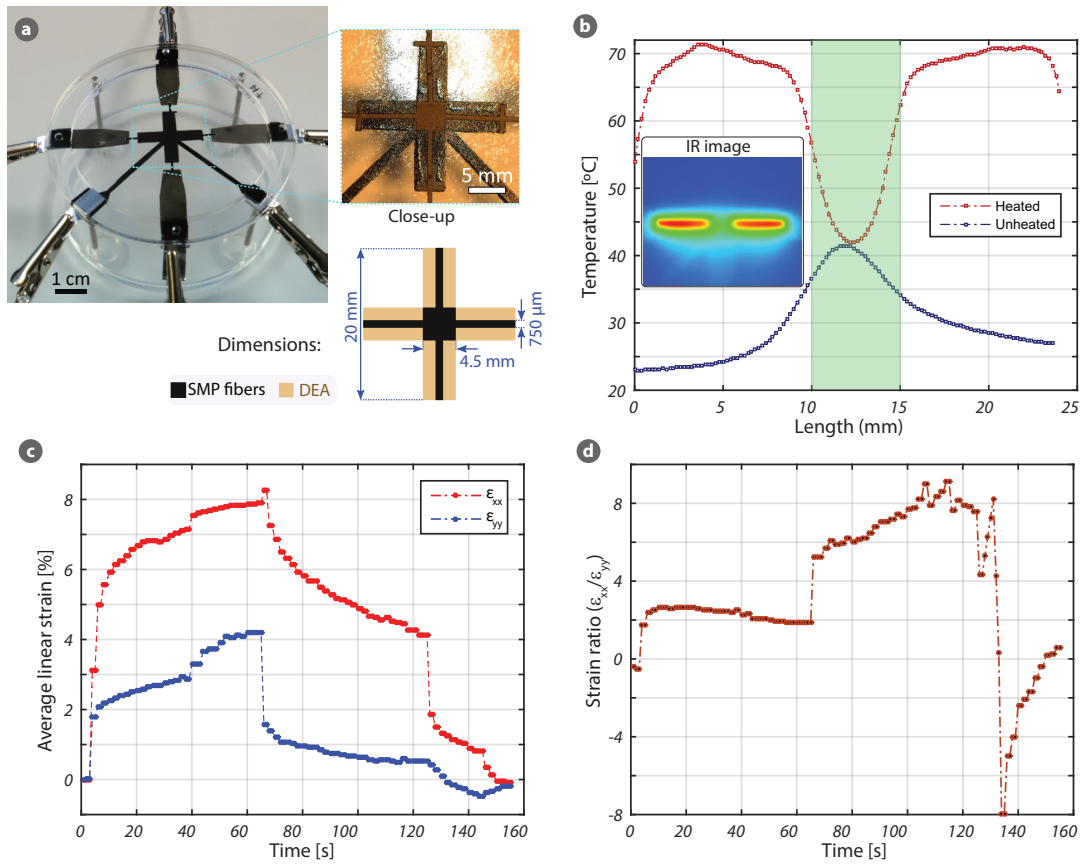


Figure 4.17: a) A photograph of a plus shape DEA with 2 embedded SMP fibers. b) The temperature distribution along the lengths of the heated (red) and the unheated (blue) fibers. The inset captures an IR image when the horizontal fiber is heated. c) The strains along the longitudinal direction of the heated and the unheated fibers. d) Evolution of the strain ratio for actuation in the x-direction, reaching a peak of over 8.

4.5 Reconfigurable and latchable shape-morphing DEAs

This section of the chapter presents complex shape morphing of thin dielectric elastomer sheets. The devices using one DEA and two antagonistic DEAs are demonstrated. An analytical model was developed and experimentally validated for maximizing the actuation deformation and the holding force.

The multistable shape morphing DEA introduced in this part of the chapter is based on a similar working mechanism as previously illustrated for the planar DEAs (see Figure 4.18). The difference between them is the prestretch and the deformation shapes. The first device is prestretched and fixed to PMMA frames whereas the second device is suspended freely (not prestretched). Due to these different boundary conditions, the planar DEA can deform in in-plane directions whereas the second DEA has out-of-plane deformations. Sample shape deformation of these devices are shown in Figure 4.3.

4.5.1 Design concept and working mechanism

This multi-morph device consists of a dielectric elastomer actuator (a dielectric membrane and two compliant electrodes), two sets of vertical and horizontal heaters, two SMP grids, and electrical insulation layers (see Figure 4.18a). The heaters provide the thermal stimulus needed for the softening of the SMP grids and the shape recovery. The orientation of the heaters defines the soft axis of bending, and thus ultimately the possible deformed configurations.

The multistable shape morphing mechanism is illustrated in Figure 4.18b. When a specific segment of the SMP grid is softened by the Joule heating, a temporary soft axis is created, about which the voltage-induced bending occurs upon the DEA actuation. When the voltage is applied to the DEA electrodes, only the region in the vicinity of the addressed heater bends as the dielectric sheet gets soften in this region. The DEA cannot significantly deform the unheated regions; this regions are very stiff. To visualize the soft and stiff regions in the device in Figure 4.18b, the addressed (hot) and the unaddressed (cold) heaters are coloured red and black.

When the desired deformation is achieved, the SMPs are allowed to cool down. This locks the device into a stable deformed configuration (referred as temporary shape). The permanent flat shape can be simply recovered by reheating. The device can be reconfigured for another shape transformation by addressing different heaters. Figure 4.18b shows the layers of the structure, with heater configured for six possible shape transformations. With a different patterning of the heaters, we can introduce different regions of deformations within the elastomer sheet for additional morphological transformations. Appendix E shows the deformations around two diagonal axes when the diagonally-oriented heaters are used.

4.5 Reconfigurable and latchable shape-morphing DEAs

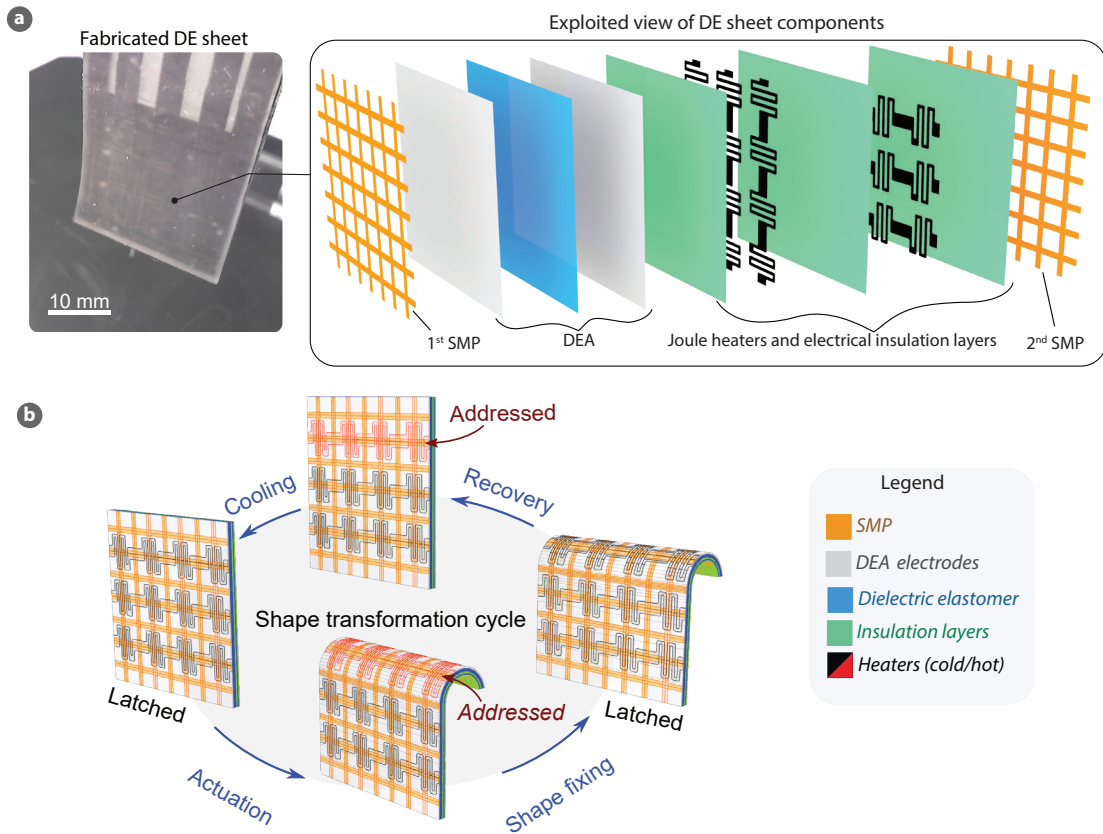


Figure 4.18: The working mechanism and the layers of the multistable reconfigurable dielectric elastomer sheets. a) A photograph of a fabricated device. The device consists of a DEA, two sets of vertical and horizontal heaters separated by the insulation layers, and two SMP grids. Total thickness these layers is 560 μm . b) The shape transformation cycle showing bending about a Joule-heated soft axis. The hot and cold heaters are coloured red and black.

4.5.2 Design optimization for large deformation and high holding force

The devices consist of up to 11 layers of the dielectric elastomer, the compliant electrodes, the insulators, and the SMP layers. The thickness of each layer and the order of the layers (e.g., SMP at center or at outer layer, one or two SMP layers, heaters inside or outside, etc.) plays a central role in obtaining both high bending angles and high holding force. Thicker SMP layers enable higher bending stiffness in the cold state, and thus higher load carrying ability. However, due to their non-zero stiffness in the hot state, thicker SMP layers reduce the actuation deformation.

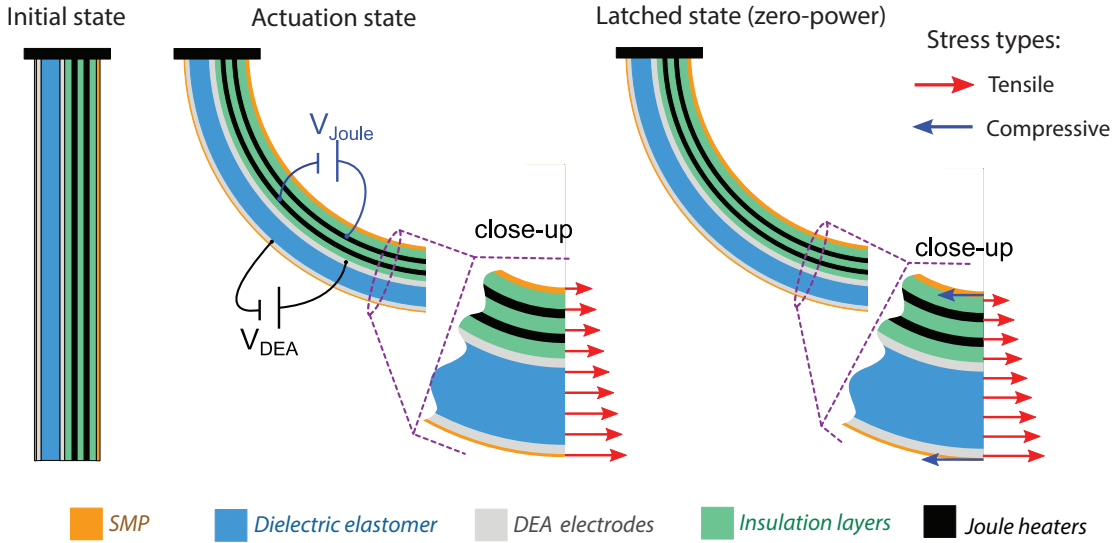


Figure 4.19: Modeling multistable dielectric elastomer sheets for large actuation and latched deformations. The cross-sections show the deflection of the elastomer sheet at three different states. The close-ups show the stress distribution on the cross-sections. In the actuation state, the DEA is on and the SMP is soft. To latch the device, the DEA is turned off and the SMP is cooled down. In the latched state, the SMPs have compressive stress whereas the other layers are under a tensile stress.

We developed an analytical model to quantify the trade-off between large actuation bending and high holding force. The model helps us to determine the optimum design parameters of the sheets, i.e. SMP and DEA film thicknesses and layer order. The model computes bending angle in three different states: i) the actuation state with the DEA voltage on and the selected heaters on, ii) the latched state where the deformation is held by the cold SMPs (DEA is off), and iii) the load-bearing state where an external force is applied to the latched device, i.e. the latched state under an external load.

When a voltage is applied across the dielectric layer, it expands laterally, thus applying a bending moment to all layers and generating curvature in the sheet. The beam bending was analyzed using Stoney's equations for the mechanical equilibrium. [136] We assumed that the Maxwell stress was uniform and remained constant during the deformation. The strain generated was small enough (< 0.10) to use a linear elasticity model. We used the force equilibrium in the tangential direction and moment equilibrium about the z-axis (see

Figure 4.19a). The elastic force due to the deformation of all layers is equal to the force generated by the voltage applied to the dielectric membrane. Adopting the ideal dielectric elastomer model, we can write the equation of the force equilibrium in the tangential direction as: [63, 136]

$$\int_{A_{all}} \left(-Y_i \frac{r - r_0}{\rho_0}\right) dA = \int_{A_{die}} (\epsilon E^2) dA \quad (4.5)$$

where Y_i is the Young's modulus of i^{th} membrane, r_0 is the neutral axis, ρ_0 is the radius of the curvature, ϵ is the permittivity of the dielectric membrane, and E is the applied electric field. Subscripts *all* and *die* stand for all layers and the dielectric membrane, respectively. Similarly, the equation of the moment equilibrium about the z-axis can be written as:

$$\int_{A_{all}} \left(-Y_i \frac{r - r_0}{\rho_0}\right) y dA = \int_{A_{die}} (\epsilon E^2) y dA \quad (4.6)$$

The thickness of the films, the positions, the stiffness (as a function of the temperature) and the geometries are used as inputs. We solve for y_0 and ρ_0 . The tip deflection angle can be computed as: $\theta_{tip} = L\rho_0^{-1}$, where L is the initial length of the device.

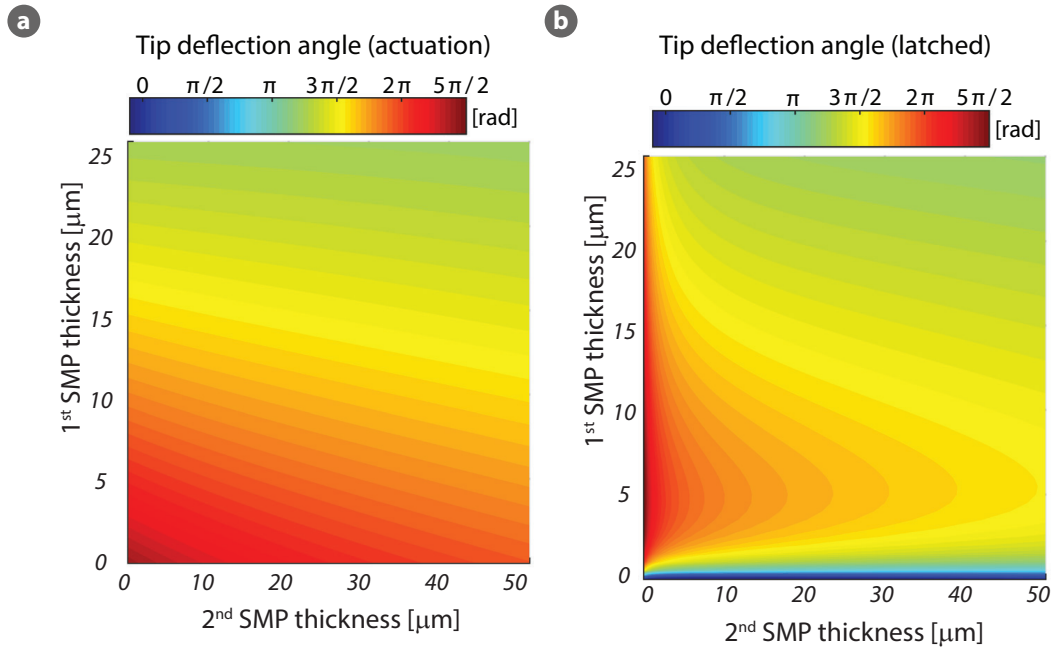


Figure 4.20: The tip deflection angle plotted as a function of two SMP thickness for the actuated and latched states. The SMP layers have different effects on the actuation and latching performances.

Figure 4.20a shows as a color plot the tip deflection angle at the actuated state (for an electric field of $20 \text{ V}\mu\text{m}^{-1}$ where the SMPs are in the soft state. The tip deflection angle is plotted as a function of the thickness of both SMP layers for the device shown in Figure 4.18a. The dimensions and the Young's moduli of the materials are listed in Table 4.2. When the device bends, the 1st SMP layer (the layer closest to the DEA) is on the outside (highest tensile stress) and the 2nd SMP is at the inside of the curve. As the structure is asymmetric, the two SMP layers have drastically different effects on tip deflection: the 1st SMP layer has a higher stiffening effect on the bending than the 2nd SMP. Increasing the thickness of either SMP layer decreases the actuation deformation.

Table 4.2: The dimensions and the Young's moduli of the materials used in the analytical model for the tip deflection angle. *Abbreviations: SMP: shape memory polymer, A.E.: acrylic electrode, D.E.: dielectric elastomer, I.L.: insulation layer. Y at 30 °C and 85 °C is the Young's modulus at the specified temperatures.*

Parameter	Unit	SMP	A.E.	D.E.	A.E.	I.L.	A.E.	I.L.	A.E.	I.L.	SMP
Thickness	μm	1:25	32	250	32	50	32	50	32	50	1-50
Length	mm	25	25	25	25	25	25	25	25	25	25
Width	mm	4x1	25	25	25	25	25	25	25	25	4X1
Y at 30 °C	MPa	1192	1.1	0.81	1.1	0.41	1.1	0.41	1.1	0.41	1192
Y at 85 °C	MPa	2.83	0.26	0.15	0.26	0.05	0.26	0.05	0.26	0.05	2.83

Cooling down the SMPs fixes the actuation deformation into place, with a slight relaxation when the DEA voltage is removed. The sheet finds a new mechanical equilibrium for which we can write similar equilibrium equations of the force and the moment as we did for the actuation phase. In this equilibrium state, the compressive stress of the SMP layers is balanced by the tensile stress of the other membranes (see Figure 4.19a). Appendix F gives the details of this modeling steps and explains the derivation of the equations.

Figure 4.20b plots the tip deflection angle in the latched state as a function of the two SMP thicknesses. Comparing panels a and b, we see a reduction in tip deflection. The SMP layers have markedly different effects on the actuation and latching performances. A thicker 1st SMP layer decreases the actuation deformation but enables latching with higher tip deflection. The 2nd SMP layer alone is insufficient to lock the device, we need the 1st SMP layer for a better latching.

Finally, we computed the effective bending stiffness of the curved beam in the latched state as a proxy for the holding force. Both SMP layers play key role in determining this bending stiffness. We employed the usual form of Castigliano's first theorem [137] to the curved device with a tip deflection angle of 270°). The displacement of the curved beam (Δ_y) due to an external force of P can be expressed as:

$$\Delta = \int_0^{\theta_{tip}} \left(\frac{M_\theta}{Y_i I_i} \frac{\partial M}{\partial P} \right) ds \quad (4.7)$$

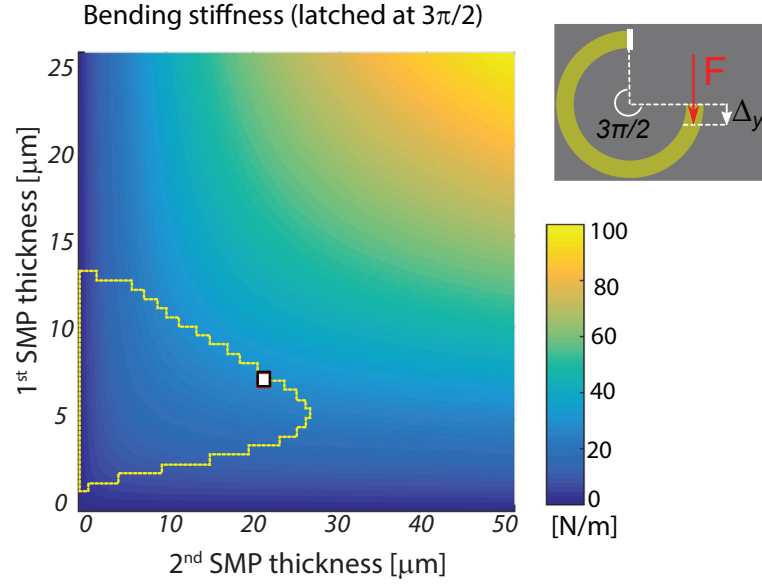


Figure 4.21: Color plot of bending stiffness of a curved dielectric elastomer sheet (latched at 270°) vs. SMP thicknesses. The inset shows the configuration used to determine the bending stiffness. The yellow line delimits the regions of SMP thicknesses where both the actuated and latched states have a deflection greater than 300° . The SMP thicknesses of the device shown in Figure 4.22 is highlighted in red square.

where M is the moment due to force P , $Y_i I_i$ is the equivalent stiffness of the all layers with Y_i and I_i being the Young's modulus and the area moment of inertia of i^{th} membrane, respectively. The bending stiffness of this curved beam is then found as $K_{bending} = P/\Delta_y$. The dimensions and the Young's moduli of the materials at 30°C are listed in Table 4.3. Figure 4.21 shows the 2D plot of the bending stiffness vs. the thickness of two SMP layers. The bending stiffness increases with the increase of both SMP thicknesses; high holding forces are in the top right of Figure 4.21, but high deflections are obtained in a region near the bottom left.

Table 4.3: The dimensions and the Young's moduli of the materials used in the analytical model for the calculation of the bending stiffness. *Abbreviations: SMP: shape memory polymer, A.E.: acrylic electrode, D.E.: dielectric elastomer, I.L.: insulation layer. Y at 30°C is the Young's modulus at 30°C .*

Parameter	Unit	SMP	A.E.	D.E.	A.E.	I.L.	A.E.	I.L.	A.E.	I.L.	SMP
Thickness	μm	1:25	32	250	32	50	32	50	32	50	1-50
Length	mm	25	25	25	25	25	25	25	25	25	25
Width	mm	4x1	25	25	25	25	25	25	25	25	4X1
Y at 30°C	MPa	1192	1.1	0.81	1.1	0.41	1.1	0.41	1.1	0.41	1192

To find a reasonable operating region, we first computed the SMP thicknesses for which the device can achieve a tip deflection angle $> 300^\circ$. The region fulfilling this requirement is enclosed by the yellow curve in Figure 4.21. The SMP thicknesses for our devices are selected by the pair of values that give the highest bending stiffness within this region. The fabricated

Chapter 4. Development and modeling of reconfigurable and latchable DEAs

device shown in Figure 4.18a has 7 μm and 22 μm thick SMP layers, corresponding the red square in Figure 4.21. The dimensions of the layers of the final geometry is summarized in Table 4.4.

Table 4.4: The dimensions of the final geometry. *Abbreviations: SMP: shape memory polymer, A.E.: acrylic electrode, D.E.: dielectric elastomer, I.L.: insulation layer.*

Parameter	Unit	SMP	A.E.	D.E.	A.E.	I.L.	A.E.	I.L.	A.E.	I.L.	SMP
Thickness	μm	7	32	250	32	50	32	50	32	50	22
Length	mm	25	25	25	25	25	25	25	25	25	25
Width	mm	4x1	25	25	25	25	25	25	25	25	4X1

4.5.3 Device fabrication

The multistable dielectric elastomer sheets were made of stacked layers of acrylic elastomer, acrylic conductive elastomer, and shape memory polymer. The dielectric membranes were 250 μm thick acrylic elastomer (VHB 9473PC from 3M) and they were cut into 30mmx50mm sheets. For the DEA and Joule heating electrodes, we used conductive acrylic materials (AR-care 90366 from Adhesives Research). The thickness of conductive acrylic was 32 μm . The DEA electrodes were cut into 28mmx28mm and placed on the opposite sides of the dielectric membranes, forming the active DEA region. The fabricated device a buffer (passive) region located between the DEA region and the clamps. As this region is soft, it reduces the clamping effect on the DEA performance. The heating electrodes had a length of 28 μm and a varying width of a 5 μm and 0.5 μm . The narrow regions of the heaters were overlapped with the SMP segments. The electrodes are patterned using a laser cutter (8011 Speedy 300, from Trotec).

To electrically insulate the heating electrodes, we used 50 μm thick acrylic elastomers (F9460PC from 3M) and they were cut into 30mmx50mm sheets. As for the SMP material, we used thermoplastic shape memory polyurethane (MM4520 from SMP technologies). For fabrication of SMP membranes, we first mixed SMP pellets with Dimethyl sulfoxide (DMSO, from Sigma-Aldrich) at a weight ratio of 1:4, then dissolved at 80 $^{\circ}\text{C}$ for 12 h. This mixture was casted on the top of a Teflon sacrificial layer. The DMSO was then evaporated at 80 $^{\circ}\text{C}$ in an oven for 1 h. The cured SMP membranes was patterned into grids using the laser cutter. Once all membranes were ready, we laminated them to assemble our devices. Thanks to tackiness of the acrylic elastomers we did not need any surface treatment to bond the membranes.

Once assembled, we put markers at the bottom edge of the device which were tracked to measure the radius of the curvature. Some devices were coated with thermal dust (131F, from Solarcolordust.com), which helped us to get rid of the tackiness and image the hot region without the need of a thermal camera. For the validation experiments, we used a thermal camera (FLIR A50 from FLIR Systems, Inc.) to measure the temperature of the device.

To measure the radius of curvature, we first tracked the markers on the deformed images and then fitted a circle to them using a custom Matlab code.

4.5.4 Multiple latched shapes in a single device

To morph the dielectric elastomer sheet, a vertical or a horizontal segment of the device is heated to 85 °C, followed by applying 6.25 kV across the dielectric membrane to bend this soft segment (a lower voltage could be applied if less bending is desired). Once bent, the applied voltage was maintained at 6.25 kV while the device was allowed to cool for 30 s. This is the shape fixing (or shape programming) step where the device is locked in the actuated state. We turned off the high voltage after the shape fixation, yielding the zero-power actuated position. All possible shape morphs are showing in a Figure 4.22.

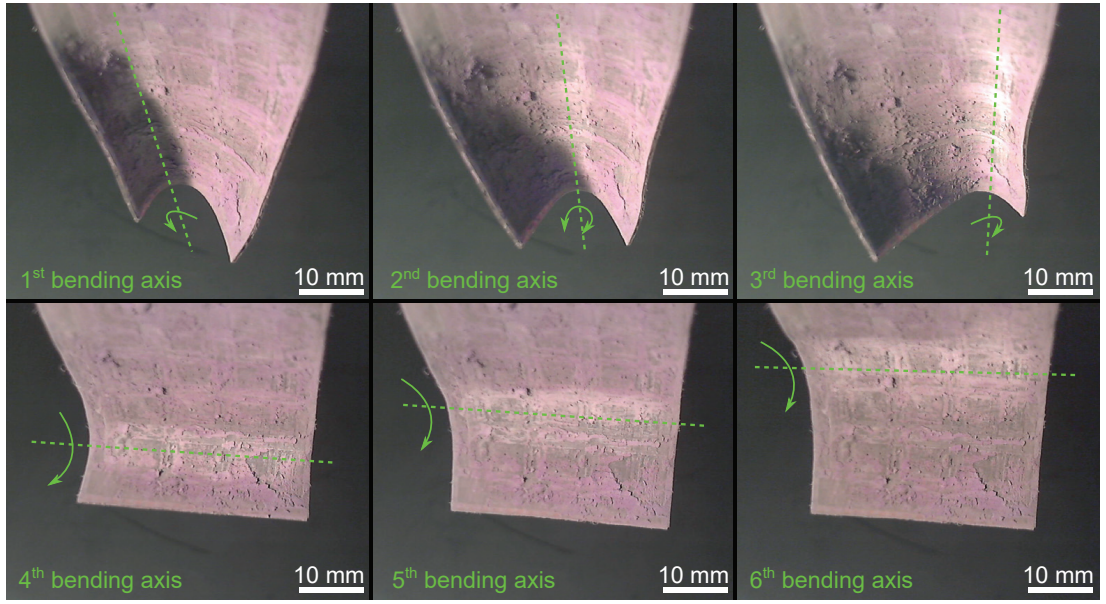


Figure 4.22: Photographs of a device latched at six different configurations. The device bends around the soft axis that is created by addressing the Joule heater. The heaters are located at different regions and different orientations to create distinct shape changes. The integrated SMP layers allows to freeze these achieved deformations.

The latched shape is stable as long as the temperature remains below the TG of the SMP. The permanent (i.e. initial as fabricated) flat shape was then recovered by heating the device to 85 °C for 30 s. By combining spatial stiffness tuning technique with the shape memory effect in the dielectric elastomer sheets, one can achieve a continuous deformation in various directions without the need of complex joint mechanisms and can hold a given actuated position with zero-power.

The orientation of the Joule heaters can define the axis of bending. Therefore, we can introduce additional regions of deformations within the elastomer sheet for various morphological transformations by patterning different heaters. Figure 4.23 shows five latched configurations of a DEA sheet which obtained by bending the structure about two diagonal and three vertical axes. Figure 4.23a shows the device layers of a sheet that can bend about three vertical and two diagonal axes.

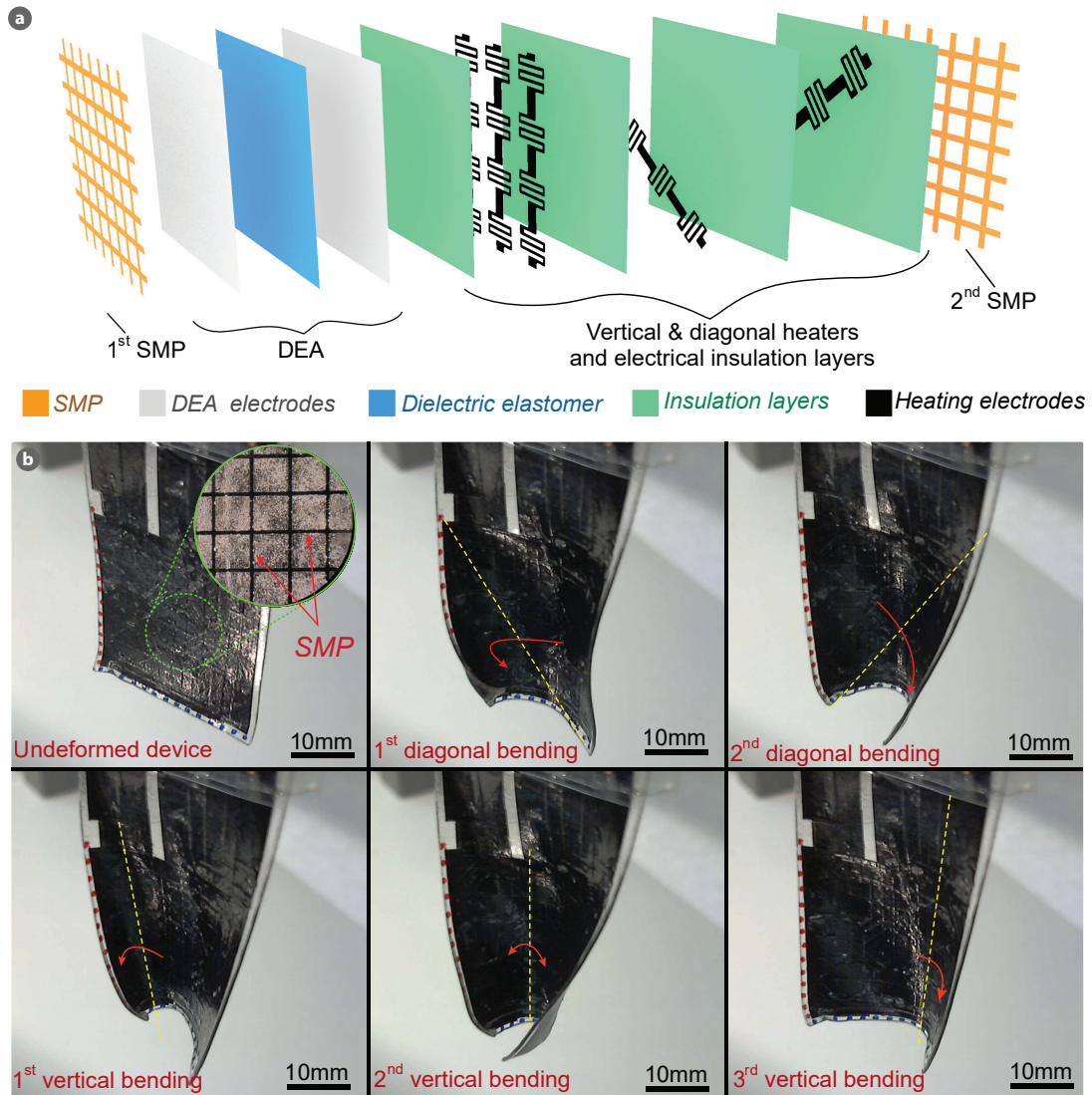


Figure 4.23: Deforming and latching a DEA around its vertical and diagonal axes. a) Schematic diagram showing the device layers of a sheet that can bend about three vertical and two diagonal axes. b) Photographs of the sheet morphed into five latched configurations.

To illustrate the versatility enabled by the shape reconfigurability, we first used the gripper to pick and place objects with two very different shapes (a circular screw and a horizontal tube), as shown in Figure 4.24. The device was first actuated in a vertical bending shape to grip a circular plastic screw by softening the horizontal fibers. When the horizontal SMP fibers were softened, the stiff vertical SMP fibers (the effective stiff fibers) set the deformation mode. In Figure 4.24, the soft fibers are shown in red and stiff fibers are in blue. After releasing the screw, the gripper was configured to pick a plastic tube by heating the vertical fibers, leaving the horizontal ones stiff. The gripper can thus alternate between different deformed shapes to easily grasp a range of objects.

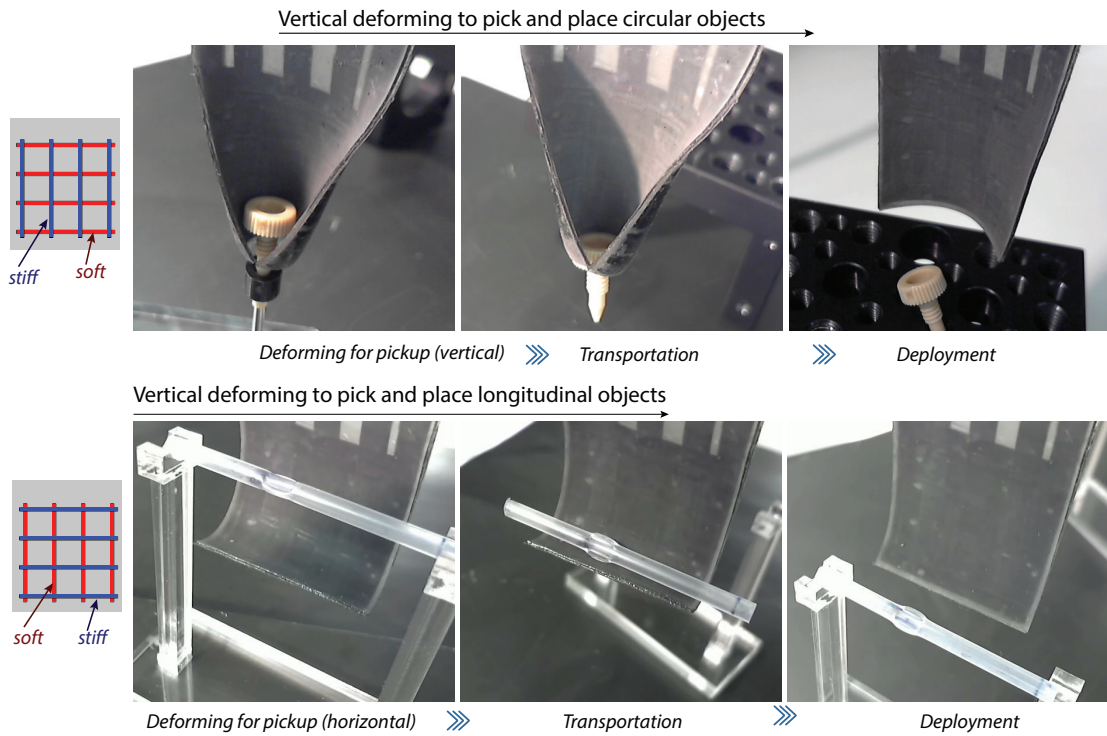


Figure 4.24: a) Gripping objects with very different shapes by heating either horizontal or vertical fibers to enable DEA actuation in vertical or horizontal axes. The horizontal SMP fibers are softened during actuation to wrap around a circular screw. The vertical fibers then are softened to pick-and-place a plastic tube.

4.5.5 Mirror shapes with antagonistic DEAs

A second DEA was integrated in an antagonistic configuration to enable more complex shape transformations, with both positive and negative curvature, using a sequence of deform-and-hold operations of different segments (Figure 4.25a). A dielectric elastomer sheet that can morph, amongst other configurations, into S and its mirror SS shapes is presented here. The operating cycle is schematically demonstrated in Figure 4.25b. First, the right-hand side of the device is deformed with a forward bending and locked in place. Then, the flat left-hand side of the device is bent in the opposite direction of the first bending (backward bending) and

Chapter 4. Development and modeling of reconfigurable and latchable DEAs

subsequently latched. The deformation of the right segment is preserved during the second shape transformation thanks to the cold SMPs in this region. This way, we can decouple the deformations of two neighbour segments and therefore can achieve a deformed S-shape with the left and the right parts having the opposite shapes.

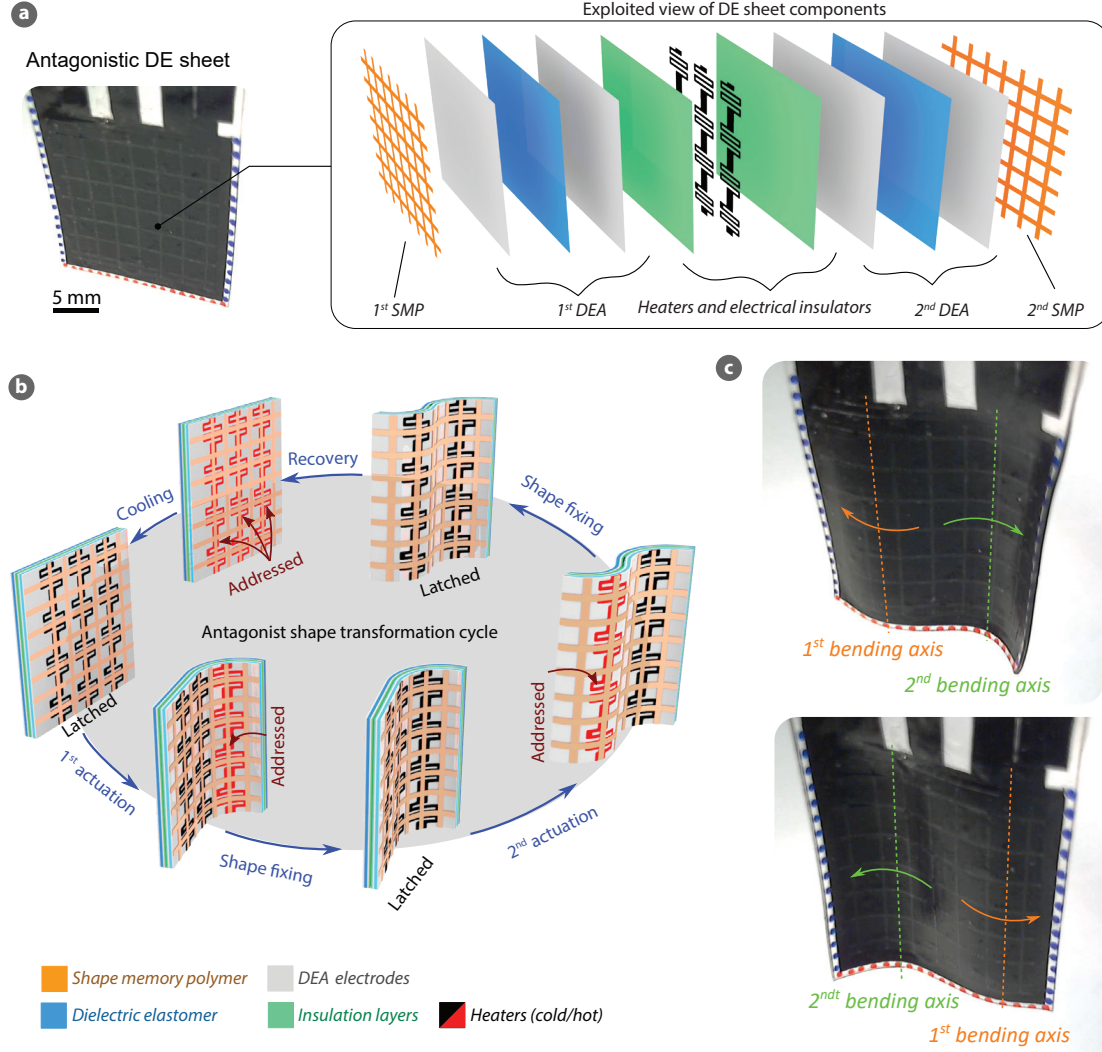


Figure 4.25: Complex mirror deformations are achievable by synchronizing the electrostatic actuation of the two antagonistic DEAs and the addressing of the Joule heaters. a) The antagonistic dielectric elastomer sheet consists of 2 DEAs placed on the opposite sides of a central set of vertical heaters, and two SMP grids on the outside. It has a thickness of 775 μm . b) The shape transformation cycle showing the sequence of the deform-and-hold operations to achieve S-shape deformation. c) Photographs showing the morphing of the flat sheet into two mirror shapes.

We implemented two DEAs in a dielectric elastomer sheet to adopt an antagonistic behavior. This was achieved by placing two identical DEAs on opposite sides of the stacked layers. The device had two SMP grids, a layer with three vertical heaters, and 2 antagonistic DEA layers, placed to enable forward and backward bending (see Figure 4.25b).

Figure 4.25c shows two complex mirror shapes obtained in a single dielectric elastomer sheet. We first softened the left-hand side of the device (75 °C) by addressing the left-column heater and applying a voltage of 5.5 kV to the 1st DEA, which in return only bent the left segment in the backward direction. This deformation was fixed by cooling the SMPs. Subsequently, we simultaneously softened the right segment and electrostatically actuated the second DEA. This generated a forward bending in the right-hand side of the device. Following another shape fixation after the second actuation, we latched the device in a S-shape configuration (see the first image in Figure 4.25c). The mirror shape of this deformation (SS-shape) was achieved by swapping the synchronization of the DEA actuation and the addressing of the Joule heaters. For this, the actuation of the first DEA is synchronized with the right-column Joule heater, and similarly the second DEA with the left-column heater. As these DEAs have antagonistic behavior, the Maxwell stress generated during the second actuation tries to unfold the deformation of the first segment. However, The SMPs in this region are cold (hence stiff) and they can resist this unfolding force. As depicted from the experimental photographs shown in Figure 4.25c), the cold SMPs hold the deformed shape under the Maxwell stress.

4.5.6 Model validation using the tip deflection angle and blocking force

We used the tip deflection angle and blocking force as the validation parameters for our model. Figure 4.26a compares the model predictions with the experimental results for the case when the dielectric elastomer sheet was actuated at an elevated temperature (70 °C) and latched at 29 °C. 178° tip deflection was measured at 5.5 kV at 70 °C where the model predicted a deflection of 197 °C. When the device was latched at the room temperature, it held most of its actuation deformation: following 5.5 kV actuation, 86% shape fixation was measured while the model predicted 83%.

Larger deformations can be obtained by further increasing the temperature, as the SMP becomes even softer. A tip deflection of 300° was obtained at 5 kV when the device was heated to 90 °C during actuation. Higher temperatures however increase heating and cooling times and increase the cross-heating between heater regions.

We measured the blocking force of the deformed dielectric elastomer sheet and compared with the analytical model. For the force measurement, the dielectric elastomer sheet was first actuated and locked at an angle of 180°. Two force measurements were carried out on this bent structure: one at the soft actuation state (the DEA and the SMP heating were on) and the other one at the latched state (both DEA and SMP heating were off). Figure 4.26b shows the measured blocking of a deformed dielectric elastomer sheet at the actuation and the latched states. The bending stiffness of a device at a latched zero-power state was 4.3 times higher than in the soft (hot) actuated state.

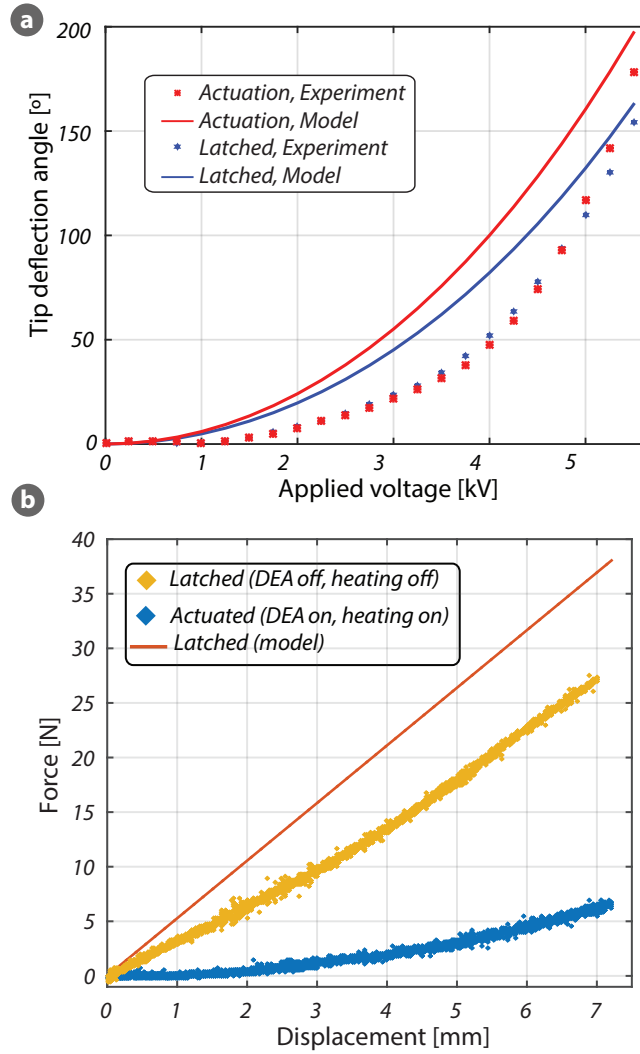


Figure 4.26: Experimental validation of the modeling using the tip deflection angle and blocking force. a) A good agreement between the model prediction and the measured results for the device actuated at 70 °C and latched at 29 °C. b) The model predictions and the measured blocking forces for a device bent at 180°. When the device is at cold state (latched) the blocking force is 4.3 times higher.

4.5.7 Using the model to improve the actuation and latching performances

Both the experimental results and the model predictions show that the thickness of the SMP layers, the locations of the DEAs, the distance between the SMP layers, and the relative position of the shape locking materials (SMPs) to the other materials have major roles in the actuation and latching performances.

Figure 4.27 shows the model results for three different designs in which the layer order was varied, highlighting the importance of neutral axis location and careful choice of film stack sequence. The location of the pink electrical insulator (the same material as other electrical insulators) is changed for each simulation. In the bent configurations, the 1st SMP layer is on the outside of the curved shape, and the 2nd SMP layer is on the inside. When the pink layer is placed on the outside of the 2nd SMP layer (1st design), it increases the actuation and the latching performances. When it is placed on the outer surface of the 1st SMP layer (3rd design), it has an opposite effect, decreasing both actuation and latched deformations. For the 1st and 3rd designs, the bending stiffness are quite similar. When this layer is placed in between two SMP layers, it increases the distance between two SMP layers (very stiff layers) and therefore increases the bending stiffness.

This analytical model can be easily adapted for the multistable bending actuators to optimize their actuation, latching, or load-bearing capacities. The actuation part of this modeling can be used for all bending DEAs. Here, we include qualitative outcomes of the model, to serve as a guide for designing multistable DEA sheets based on our architecture, and discusses the thermo-mechanical properties of shape memory polymers that can improve the device performance.

Based on the modeling and experimental results, the following mechanical design rules are suggested for obtaining simultaneously large deformation and high holding force:

The highest bending stiffness (blocked force) is achievable when 2 SMP layer are used (instead of one SMP layer) and they should locate at the outsides of the stacked layers so that the distance between them is greatest. This gives the highest area moment of inertia (as the cold SMP is the stiffest material).

Thicker SMP layers lead to higher blocked force. However, due to the limited force from the DEA, the thickness of the SMP layers and the location of the DEA should be chosen carefully. We found that the DEA can generate a high bending moment when the SMP layers have different thicknesses and when the DEA is placed close to the thinner one. The reason being that in this configuration, the neutral axis is close to the thicker SMP layer and the DEA is as far as possible from the neutral axis. Therefore, the bending moments (simply the DEA force times the distance between the DEA and the neutral axis) is maximum. This configuration results in the maximum strain in the thin SMP film and the minimum strain in the thick SMP layer. As deforming thinner layers is easier, this gives a higher deflection.

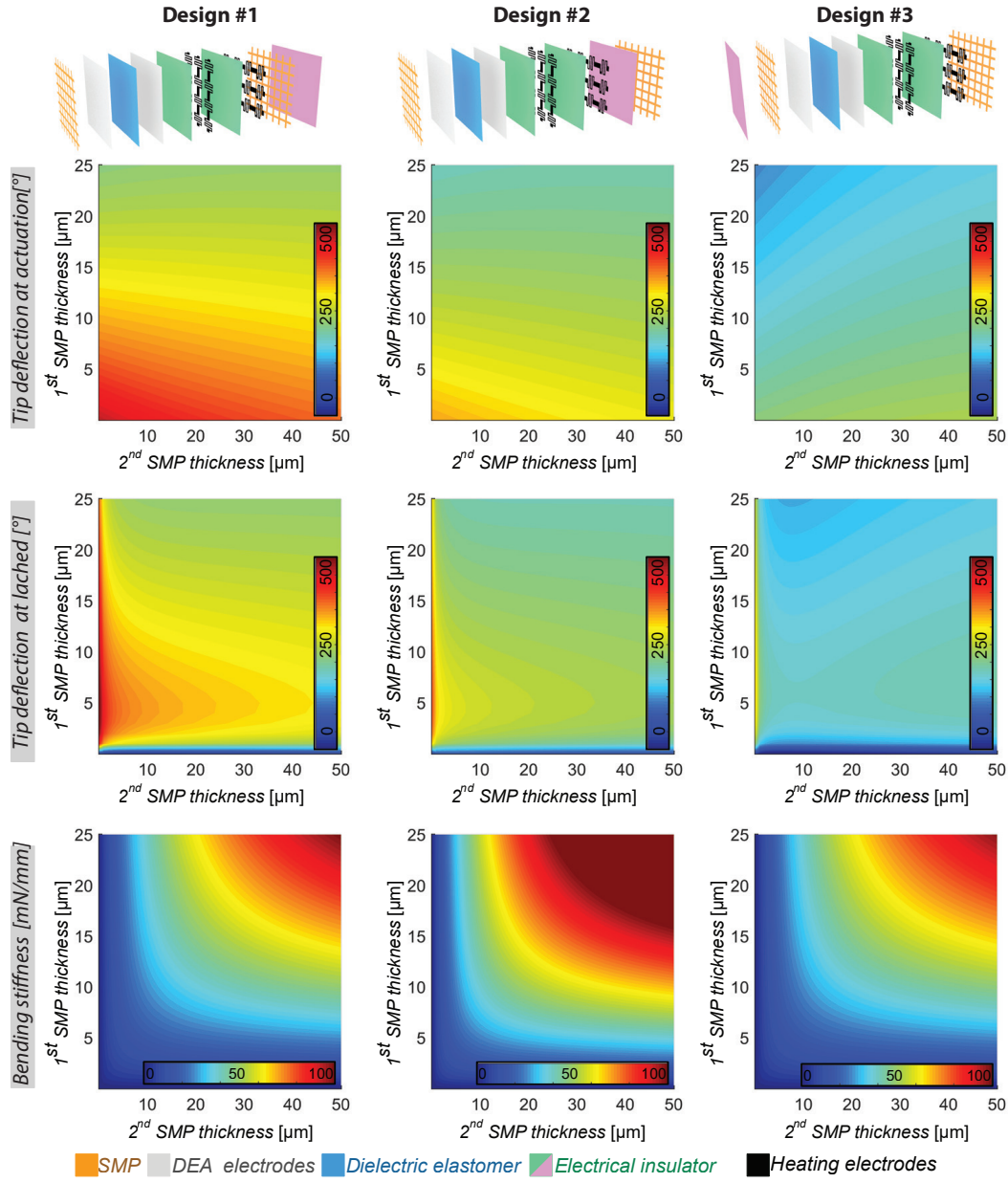


Figure 4.27: The location of the pink electrical insulator is changed for each simulation to investigate the effect of the layers order on the actuation, latching, and load-bearing ability of the devices. When this layer is placed on the outside of the 2nd SMP layer (1st design), it increases the actuation and the latching performances. It has an opposite effect when placed on the outer surface of the 1st SMP layer (3rd design). Placing this layer in between two SMPs, it increases the distance between two SMP layers and therefore increases the bending stiffness.

If higher bending angles are required, a thin additional passive layer can be bonded to the outer side of the thick SMP layer to shift the neutral further away from the DEA, increasing the bending moment. The thickness of this layer is crucial as thick layer significantly increases the area moment of inertia during the actuation, so a careful balance must be found.

In addition to, or instead of, changing mechanical designs such as the layers order and thickness, the thermo-mechanical properties of the shape memory polymers can be tuned to increase the device performance. Among many options, thermo-responsive SMPs are good candidate for this application not only due to their high shape fixation ratio and shape recovery but also due to the very large stiffness change around their T_g . Because the performance of our DEA + SMP devices relies on a very high ratio of modulus below and above T_G (or T_M for crystalline cases), glassy thermosets and thermoplastics are the best options, even though sharper transitions can be obtained from semi-crystalline SMPs.

Lowering the SMP stiffness above T_G by changing the cross-linking density or by material synthesis would lead to higher actuation deformation. However, these changes must not decrease the stiffness at temperatures below T_G because this would decrease the holding force. Simply stated, using SMPs that are very stiff at $T < T_G$ and very soft at $T > T_G$ will maximize device performance. Shape memory polymers with sharp glass transition region will increase the speed of the device because only a small temperature change (ΔT) would be sufficient to switch states, reducing heating and cooling times.

4.6 Conclusion

In this chapter, I present two different DEA based devices that can be reconfigured for various deformed shapes and can be latched in their actuated states.

In the first type of reconfigurable soft actuator, we combined conductive SMP fibers with DEAs to introduce on-demand bi-directional actuation with latching ability. This is achieved by using two fiber sets aligned perpendicularly. The selection is made by softening one of these SMP fiber sets, which change their stiffness drastically within a small range of temperature increase. By increasing number of fiber sets and changing their orientations, it is possible to increase the degrees of freedom.

The assembled devices are alternately actuated in two perpendicular directions; the deformation in the direction of softened fibers are higher than the deformation in the transverse direction. Due to cross-heating between SMP fibers, the deformation along the stiff fibers are not completely blocked. A finite element model was used to reduce the cross-heating between the fiber sets. Different design strategies can also be implemented to better decouple the fiber heating and therefore improve asymmetrical deformation, e.g. a cross-shape fiber design with varying width was shown to increase the strain ratio.

In the second-type device, we combined a single DEA with a grid of shape memory polymers

and an array of stretchable heaters to realise multistable and reconfigurable shape-morphing sheets. By addressing the integrated heaters, we can program local and temporary soft axes in different directions which allowed dynamic control of multiple distinct deformations when the dielectric elastomer sheet is globally electrostatically actuated. We demonstrated more complex shape transformations by sequentially deforming and latching different regions. The shape memory polymers enabled holding the devices in the actuated shape with good blocking force once all voltages are removed.

The devices reported here could be fabricated using additive manufacturing techniques to reach higher resolution or further improve performance, for example by local thickness control of SMP, or by local heating of smaller areas.

We used thermo-responsive SMPs which limits the actuation speed due to relatively long heating and cooling times. These devices can be made faster by using different types of SMPs, i.e. photo-sensitive SMPs, or by integrating with active cooling systems.

We developed analytical models for the planar and the multi-morph DEAs. The model gives the crucial information on the design parameters to achieve high actuation deformation and high blocking forces. The models can be easily adapted for the multistable bending actuators to optimize their actuation, latching, or load-bearing capacities. The actuation parts of models can be used for all types of DEAs, which also takes account the stiffening effect of the electrodes and the passive membranes.

5 Latchable soft electromagnetic actuators with multi-degree of freedom

In this chapter, I introduce the soft electromagnetic beams that can twist and bend through their narrow sections called joints. Each joint can individually deform in the magnetic field when its stiffness is reduced by the Joule heating. The wider sections of the device accommodate the liquid-metal coils, which generate the electromagnetic force when addressed. Once the desired deformation, either torsional or bending, is achieved, the joint is locked into place by the shape memory polymer layers, maintaining the deformed state with zero-power for long periods of time. A latched deformed configuration, among various shapes, of an initially flat beam is shown in Figure 5.1. The device is very robust in its latched state and can hold a weight of 252 g.

In this chapter, I first explain the working mechanism of the latchable multi-DoF soft electromagnetic actuators (SEMAs) and the thermal limitations of using thermo-responsive shape memory polymers with the electromagnetic actuation. I then derive a numerical model to overcome the trade-off between the stiffening and the shape fixation of shape memory polymers. After a brief explanation of the fabrication process flow and the experimental set-up, I share the experimental results obtained in the torsional and bending configurations and compare with the model predictions. I conclude the chapter with some design suggestions that can improve the device performance.

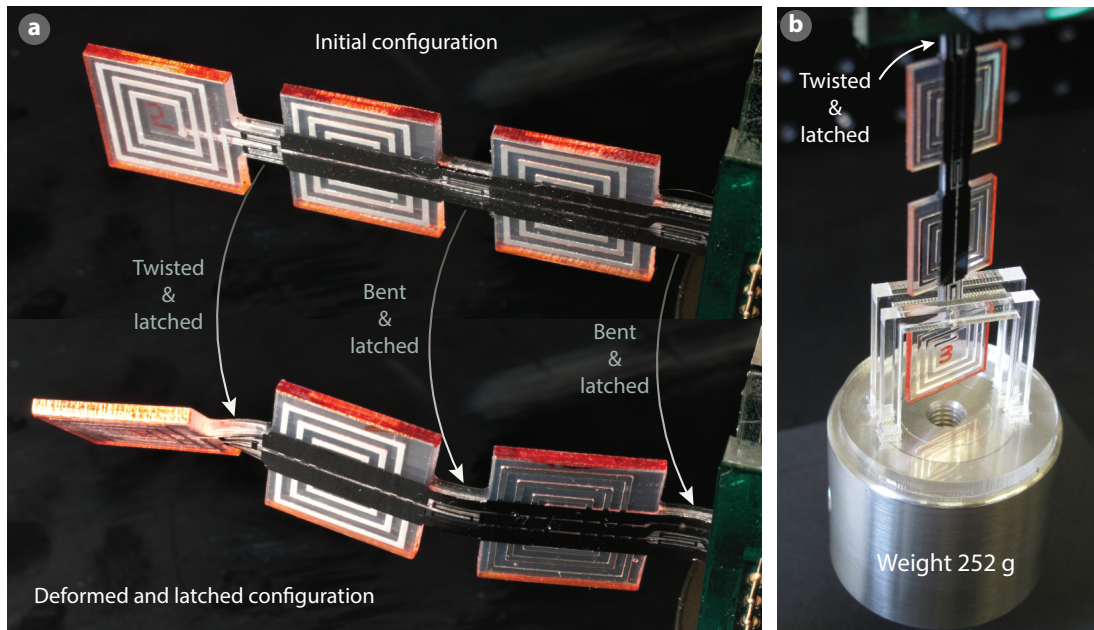


Figure 5.1: a) An electromagnetic soft beam morphing into a complex latched shape by twisting and bending through its narrow sections. Photographs show a complex shape transformation of an initially flat device that goes through a series of sequential bend-and-latch and twist-and-latch operations. b) A deformed and latched soft beam holding a weight of 252 g.

5.1 Introduction to soft electromagnetic actuators (SEMs)

The soft electromagnetic actuators follow the same working principle as the conventional electromagnetic motors. The electromagnetic motors are commonly composed of a magnet case (stator) and metal coils (rotor). The soft electromagnetic actuators replace these solid metal coils with liquid-metal channels encapsulated with silicone shells. [138] As they are made of soft materials, they deform under the electromagnetic force generated by the conductive coils in a magnetic field. The soft electromagnetic actuators have relatively simpler design, mostly made of a moulded silicone channels filled with the liquid-metals.

Liquid metal coils have shown to be emerging type of soft electromagnetic actuators. They have been utilized as sensors and actuators in many applications for developing robust and stretchable electronics. [139] Typically, the liquid metal based devices are electrically and mechanically stable under large deformations and high cycles. [67] They have high thermal and electrical conductivities, tunable mechanical properties, electrical/mechanical self-healing capabilities, making them strong candidate for various applications. [139]

Although the soft electromagnetic actuators can operate at very low operating voltages (less than a few volts), they requires high current to generate high force output. Therefore, they consume a lot of power during the actuation. To keep these soft actuators working for long periods of time requires high amount of energy. Using a latching mechanism would eliminate

this high power consumption and would allow more energy efficient systems. In our design, we overcome this limitation by integrating the soft electromagnetic actuators with the shape memory polymers. This integration allows numerous advantages:

- The actuator can be latched in the deformed state with zero-power consumption.
- The actuator stiffness can be tuned to achieve large deformation during the actuation and high blocking forces at the latched state.
- Using localized stimulation, the actuator can be reconfigured to achieve multiple distinct deformations.
- Local deformation can be individually controlled.

However, integrating shape memory polymers with soft actuators needs addressing of several requirements and challenges such as:

- A suitable fabrication flow process is necessary to allow multi-layer fabrication of different materials.
- An integrated stimuli source is needed to stimulate the shape memory polymers, i.e. heat or light source.
- Spatially varying stimuli source is required for the reconfiguration which is necessary to achieve complex shapes.
- The actuation has to be decoupled from the stimulation of shape memory polymer (The actuation should not affect the mechanical properties of the SMP).
- Efficient methods needed to overcome the trade-off the stiffening and the latching of shape memory polymers.

In this study, we developed a soft electromagnetic beam that can deform through its multiple sections with different deformation types and also can lock its deformed shapes into place. Therefore it can be frozen in the actuated state with zero-power over long periods of time. The localized deformations were achieved by spatially tuning the stiffness of integrated shape memory polymers. The deformation of the desired location was determined by preferentially softening the SMP in that location while keeping the rest of the device stiff. When the liquid-metal coils are actuated, the device deforms through the soft joint. By selectively softening the desired joints in the different directions (and with different deformation types), various complex shapes were achieved in a single device (see Figure 5.1).

5.2 Working mechanism of the latchable multi-DoF SEMAs

The latchable SEMAs are composed of three wide sections called segments, three narrow regions (joints), and one clamping section (see Figure 5.2). The clamping section accommodates the electrical connections to the liquid-metal coils (LMC) and to the Joule heaters. During the experiments, the device is clamped from this section. The segments are the wide sections of

the device and the liquid-metal coils are located here. The electromagnetic forces and the torques are generated in these sections. The joints are the narrow parts of the device. During the actuation, these joints are softened by Joule heaters and they undergo torsional or bending deformations.

The device consists of multiple layers of silicone (PDMS), shape memory polymers (SMP), and stretchable heaters (see Figure 5.2a). The silicone layer is fabricated with microfluidic channels which later on were filled with eutectic Gallium Indium (EGaIn). The silicone layer is sandwiched between two SMP layers. These SMP layers are used as the variable stiffness material and also as the latching element. The acrylic based stretchable heaters are located on the top of each SMP layer. The heaters are used to reduce the stiffness of the SMP layers by increasing their temperature above the glass transition temperature. The heaters are designed for localized heating of the joint sections only (see Figure 5.2b). Each joint has two heaters, both are addressed during the actuation. When the device is actuated, only the soft joints deform. The segments and the unaddressed joints do not deform during the actuation as they are relatively stiffer.

During the actuation, the soft joint undergoes either torsional or bending deformation. Two deformation types are schematically shown in Figure 5.2b-c. If the magnetic field is parallel to the surface normal of the segment, the generated electromagnetic force is parallel to the magnetic field lines. Therefore, the joint bends when a voltage is applied to the liquid-metal coil. Changing the direction of the LMC current still generates a bending motion but in the opposite direction. Therefore, an antagonistic motion can be easily achieved in these electromagnetic actuators by just reversing the coil current. If the magnetic field is perpendicular to the surface normal and in the lateral direction as shown in Figure 5.2c, applying voltage to the liquid metal coils creates the Lorentz forces in the upper and lower segments of the liquid-metal coils. Due to direction of the current in the coil segments, the electromagnetic force acts in the opposite directions in the upper and lower coil segments. This creates a torque and twists the soft joint. Reversing the polarity of the LMC current generates a torsional deformation in the opposite direction.

Having a segmented design and using local heaters allowed us to preferentially deform the device through any joint. Different strategies can be adapted to amplify the deformation of the joints. For example, to increase the bending deformation of a joint, the segment that is furthest to this joint can be actuated. This enables longer distance between the soft joint and the electromagnetic force which increases the bending moment and eventually increases the actuation deformation.

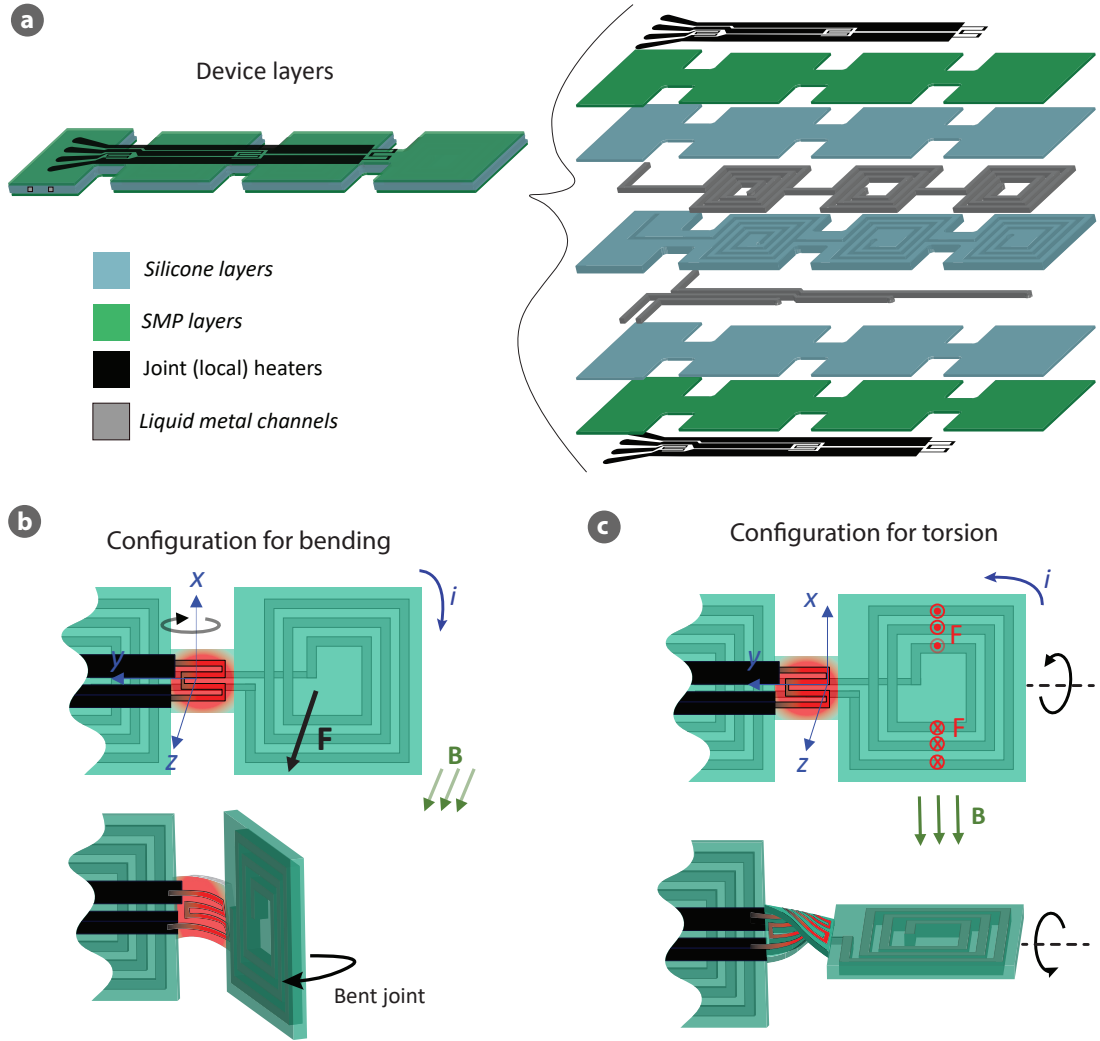


Figure 5.2: The device layers and the working mechanism of the multi-DoF soft electromagnetic beams. a) The device consists of three liquid metal coils (LMC) encapsulated with a silicone structure, two SMP layers located on both sides of the silicone layer, and two sets of stretchable heaters placed on each SMP layer. The heaters are designed to locally soften the narrow sections (joints) of the device. b) The device deforms through its joints where the selected joint is softened by Joule heating. If the magnetic field is parallel to the the device surface normal, the soft joint bends when the current is applied of the liquid-metal coils. c) If the magnetic field is perpendicular to the surface normal then the joint twists due to the torque created by the Lorentz forces on the top and bottom segments of the liquid-metal coils. Due to the opposite directions of the current in the top and the bottom coil segments, the Lorentz forces here are also in the opposite directions, resulting an electromagnetic torque.

5.3 Thermal limitation of LMC current on SMP material

As explained in the previous section, the device deforms through its soft joint where the joint softened by two dedicated heaters. However, the current of the liquid-metal channel also generates heat in the segment and this heat transfers to the adjacent joint. When the liquid-metal coil is actuated with a current of I_{LMC} , it produces Joule heating: $P_{LMC} = I_{LMC}^2 R_{LMC}$. Most of this resistive heating dissipates to the air through convection but a portion it transfers to the adjacent joint by conduction.

During the actuation, this cross-heating between the actuated segment and the adjacent joint can be used as a secondary heating source for the softening the joint. As seen in this specific scenario, the cross-heating can be useful if we need to heat the adjacent joint. However, this only applies to the actuation state and in the latching step this cross-heating has an adverse affect. To lock the deformed shape, the joint needs to be cooled down (ideally down to room temperature). In the latching process, the heaters are turned off while the LMC current is still on (if the heating and LMC currents are simultaneously removed, the device immediately goes back to its undeformed state and the latching is not possible). If the cross-heating between the actuated segment and the joints is too high during the latching process, the deformation cannot be fixed properly.

The following sections discuss how the cross-heating between the actuated segment and the joint induces a limitation on the choice of the SMP material and how we choose the SMP to withstand high temperatures while achieving large actuation and latched deformations.

5.3.1 Temperature effect of the LMC current on the choice of SMP material

As previously discussed, the LMC current produces resistive heat and this transfers to the joints through conduction. At high LMC currents, the thermal cross-heating becomes significant and it increases the joint temperature during the latching. The increased temperature adversely affects the latching performance. Figure 5.3 depicts the relationship between the electromagnetic force generated in a segment and the temperature of its adjacent joint as functions of the LMC current. Figure 5.3a shows the schematic of the segments and the joints. The electromagnetic force generated in the segment is linearly proportional to the LMC current whereas the joint temperature is proportional to the square of this current ($I_{LMC}^2 R_{LMC}$).

The glassy and rubbery states of a thermo-responsive SMP are shown on the force and temperature graph (see Figure 5.3). The SMP is stiff at the glassy region and becomes very soft at the rubbery state. For a given SMP material, the temperature of the joint should be kept below the glass transition temperature to allow a good latching. Therefore, the maximum current that we can put in the LMC is limited by the T_g of the selected SMP material. The device can be operated at any LMC current that allows a latching temperature below the glass transition temperature ($T < T_g$).

5.3 Thermal limitation of LMC current on SMP material

Although the latching is very good at low LMC current, the actuation deformation is small due to low electromagnetic force. At high LMC current, on the other hand, large deformations can be achieved. However, due to high latching temperature at this LMC current range, the shape fixation is poor. Using SMP materials with higher T_g allows higher LMC current and eventually high force and large deformation. However, using very high T_g SMP requires more heating power, increases the actuation and latching time, and can cause high temperature related mechanical or electrical failures.

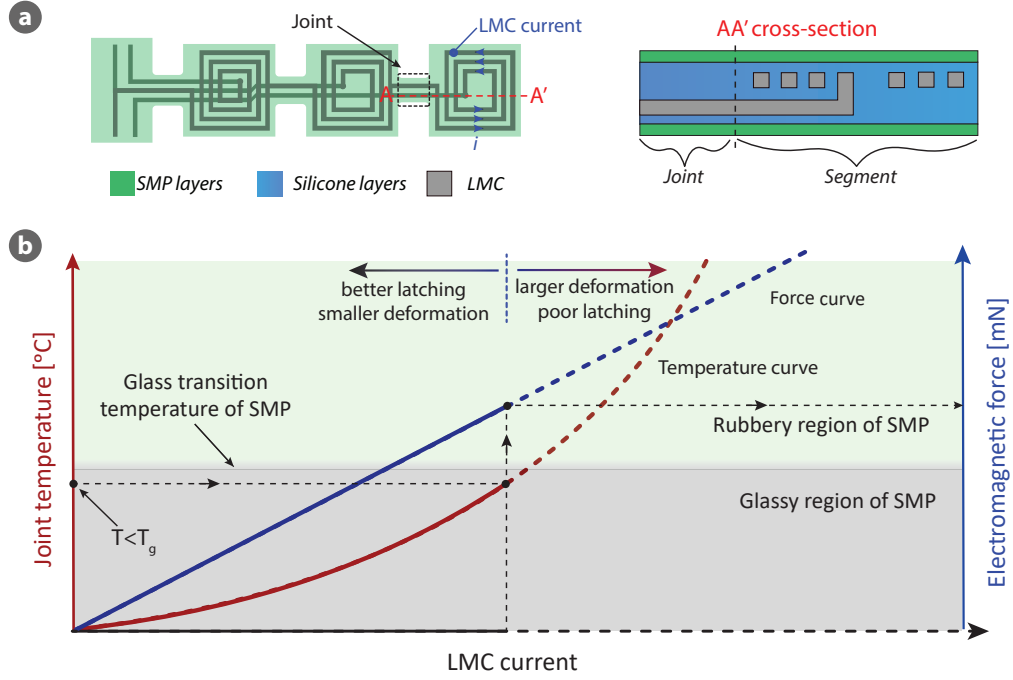


Figure 5.3: Thermal limitation of the LMC current on the choice of SMP material. Due to non-zero electrical resistance of liquid-metal coils, heat is produced when the current is on. A portion of the produced heat transfers to the adjacent joint by conduction. During the latching process, the temperature of the joint is increased by this cross-heating. The temperature increase due to coil current during latching process is therefore of the utmost importance. The electromagnetic force is linear to the LMC current whereas the temperature is proportional to the square of this current. Since the temperature of the SMP need to be kept below its glass transition to avoid undesired softening, the maximum magnetic force is limited by the glass transition temperature of the chosen SMP material. Using an SMP with higher glass transition temperature allows higher electromagnetic force.

5.3.2 The selection of the SMP material

In this section, I exemplify the thermal limitation of the LMC current on the electromagnetic force with two specific SMP materials: MM4520 and MM7520. These are thermoplastic polyurethanes from SMP technologies, Japan. MM4520 was used in the previous chapters of this thesis and has a glass transition temperature around 45 °C. The glass transition temperature of MM7520 is around 80 °C.

Figure 5.4 shows the dynamic mechanical analysis (DMA) of these materials. The DMA tests were carried out in the tensile mode with a strain amplitude of 0.1%. The temperature was swept from 0 °C to 120 °C with a ramp of 3 °C min⁻¹. The DMA results show that both materials are very stiff at room temperature with Young's moduli above > 1 GPa. As the temperature increases above $T > 45$ °C, the stiffness of the MM4520 drastically decreases while the MM7520 maintains its stiff structure until 80 °C. Increasing the temperature further above 80 °C sharply decreases the rigidity of the MM7520. The Young's moduli of both materials are around 10 MPa at temperature >100 °C.

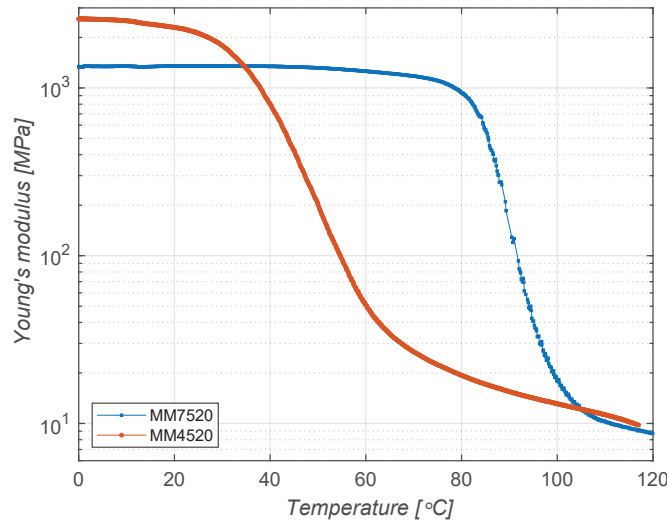


Figure 5.4: The Young's moduli of the low T_g (MM7520) and the high T_g (MM4520) SMP materials are plotted as functions of the temperature. MM4520 and MM7520 are thermoplastic polyurethanes with glass transition temperatures around 45 °C and 80 °C, respectively. Both materials have Young's moduli around 10 MPa at temperature >100 °C.

The glass transition of the SMP material plays a crucial role in both actuation and latching steps. To achieve large deformation during the actuation, the SMP needs to be softened in order to reduce their stiffening effect. To fix the actuation deformation, the SMP layers need to be cooled down below their glass transition temperature; the lower the SMP temperature the better latching. Since the LMC current is on during the latching process, the temperature of the joint is higher than room temperature due to the cross-heating between the segment and the joint. In order to lock the actuation deformation, the joint's temperature needs to be lower than the glass transition temperature of the SMP. Using high T_g SMP allows us to operate at higher latching temperature. The Young's modulus-temperature graphs in Figure 5.4 shows how much these materials can resist the temperature change before getting soft. This enables us to choose the suitable SMP materials for the desired applications.

To investigate how much force we can achieve in a segment before softening the adjacent joint, we used a finite element model (FEM) for the thermal analysis and a numerical model for the computation of the electromagnetic force. COMSOL software was used to compute the temperature of the joint as a function of the LMC current. The geometry of the device

5.3 Thermal limitation of LMC current on SMP material

was first constructed in the software and the parameters shown in Table 5.1 were assigned to the materials. As we considered the heat generation in the EGaln channels and the heat transfer between the materials and air (conduction and convection), we needed the thermal conductivity, the heat capacity, and the density of the materials, and the electrical conductivity of EGaln. Although the other materials parameters, e.g. the Young's moduli and Poisson's ratio, needed to run the simulation in COMSOL, they didn't affect the thermal analysis. Therefore they are not shown in the table. The heat produced in the LMC coil transfers to the other sections of the device through conduction and also dissipates to the air through convection (heat transfer coefficient of air: $h=10 \text{ W m}^{-2} \text{ K}^{-1}$).

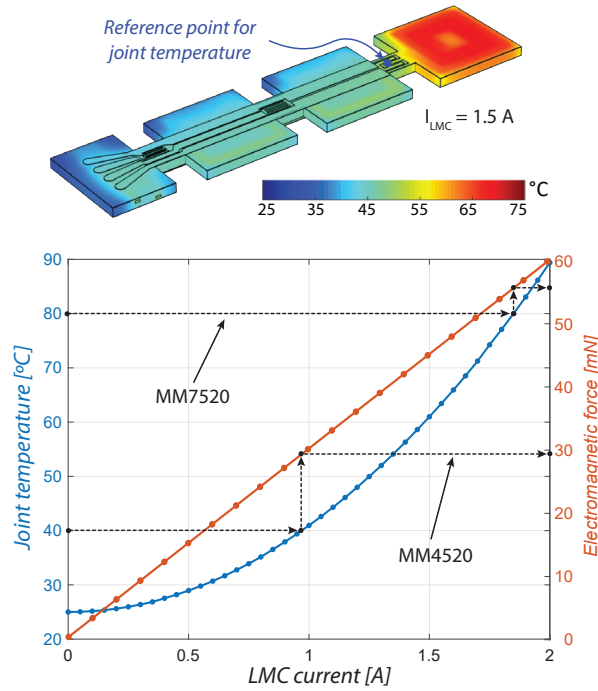


Figure 5.5: The electromagnetic force and the temperature of the joint as functions of the LMC current. The electromagnetic force is linear to the the LMC current whereas the temperature of the adjacent joint is proportional to the square of this current. The temperature is simulated using a finite element model (COMSOL) and the electromagnetic force is numerically calculated by assuming the magnet and the coil as two magnetic dipoles. Black dashed lines show how much force we can achieve for the specific examples of SMP materials (MM7520 and MM4520) before softening them. The dashed lines intersect with the temperature axis according to the T_g of the SMP materials. Horizontal lines are drawn from these points until they meet the temperature curve. Then the vertical lines are drawn until they hit the force curve. These points show how much force can be achieved for a given SMP material. As MM4520 gets soft at lower temperature, the maximum electromagnetic force of this materials is around 30 mN, whereas with high T_g SMP, which allows operation at higher LMC current, can achieve higher force.

In the simulations, the LMC (EGaln) current of the the furthest segment was swept from 0A to 2A with an increment of 0.1 A and the temperature of its adjacent joint was computed (see Figure 5.5). The surface plot shows the temperature distribution in the device at $I_{LMC} = 1.5 \text{ A}$. The blue curve shows how the joint temperature evolves as the LMC current increases. The

Table 5.1: The parameters of the materials used in FEM for thermal analysis.

Parameter	unit	SMP	PDMS	EGaIn
Thermal conductivity	$\text{Wm}^{-1}\text{K}^{-1}$	0.17	0.15	26.4
Electrical conductivity	Sm^{-1}	-	-	3.4×10^6
Heat capacity	$\text{Jkg}^{-1}\text{K}^{-1}$	1260	1460	305
Density	kgm^{-3}	1210	970	6250

joint temperature is correlated to the heating power of the LMC, which is proportional to the the square of the current and the electrical resistance of the LMC ($I_{LMC}^2 R_{LMC}$).

To compute the interaction force between the magnet and the liquid-metal coil, we assume them as two magnetic dipoles with $m_1 = (M_{mag} V_{mag})$ being the dipole of the plate magnet and $m_2 = NI\pi R_m^2$ being the magnetic moment of the coils. Assuming that the magnet and the coils are axis-aligned, the attraction force between them can be written as [140]

$$F = \left(\frac{3\mu_0}{2\pi}\right)(M_{mag} V_{mag})(NI\pi R_m^2) \frac{1}{z^4(1 + R_m^2/z^2)^{5/2}} \quad (5.1)$$

where M_{mag} and V_{mag} are the permanent magnetization and the volume of the magnet. N , I , and R_m are the number of turns, the LMC current, and the mean radius of the LMC coils. z is the distance between the dipoles, and μ_0 is magnetic permeability. This equation assumes that the distance between the magnet and coil is constant and the coils are in-axis with the magnet. In the next section, we modify this equation for the deformed structures where the distance and the angle between the LMC coil and the magnet varies. The parameters and the values used in the force calculation are listed in Table 5.2.

Table 5.2: Parameters used in electromagnetic force calculation.

Symbol	Parameter	Value
M_{mag}	Permanent magnetization	$1 \times 10^6 \text{ Am}^{-1}$
V_{mag}	Volume of the magnet	$1.35 \times 10^{-4} \text{ m}^3$
μ_0	Magnetic permeability	$1.26 \times 10^{-6} \text{ Nm}^{-2}$
N	Number of turns	3
I	Coil current	0-2A
z	Distance between the dipoles	30 mm
R	Mean radius of LMC	9 mm

The interaction force between the plate magnet and the LMC is plotted on the joint temperature vs. LMC current graph. The graph is interpreted for MM7520 and MM4520 materials. Black dashed lines show how much force can be achieved for these specific SMP materials before softening them. The dashed lines intersect with the temperature axis according to the T_g of the materials. Horizontal lines are drawn from these points until they meet the

temperature curve. Then the vertical lines are drawn until they hit the force curve. The intersections of black dashed lines with the force curve show how much force can be achieved for the given SMP materials. As MM4520 gets soft at relatively lower temperature, the maximum electromagnetic force of this materials is around 30 mN. MM7520 which allows operations at higher LMC current as it has high T_g and can achieve higher electromagnetic force before softening, e.g. 55 mN. We therefore chose MM7520 as our SMP material in this study.

5.4 The joints design and SMP thickness optimization

This section provides the details of the joints design and the thickness optimization of the shape memory polymer layers to achieve large torsional and bending deformations with a good latching performance.

5.4.1 Design of the joints and their torsional and bending stiffness

The beam is designed with narrow and wide sections. The wide section allows more number of turns of the liquid metal coils to produce high electromagnetic forces. The narrow sections, on the other hand, are designed to undergo very large torsional and bending deformations. Therefore, the deformable regions have much lower bending and torsional stiffness compared to wide sections.

Although the width of the device varies along its longitudinal direction, the thickness of the SMP and the PDMS layers is uniform everywhere in the device (see Figure 5.6a). The bending and torsional stiffness of the joints as function of the temperature was calculated using Equation 5.2 and Equation 5.3. In this section, the stiffness calculation is carried out for the predefined layer thickness: the SMP layers has a thickness of 65 μm and the thickness of the PDMS is 1.35 mm. The following section details the optimization procedure of the SMP thickness.

The joints have the same length of 5 mm and their widths vary from 4 mm to 5 mm. Assuming that the joints deforms under a pure bending deformation, the bending stiffness of the joints was calculated using the following equation:

$$k_{bending} = \frac{3(YI_{PDMS} + YI_{SMP})}{L_{joint}^3} \quad (5.2)$$

where Y is the Young's modulus and I is the area moment of inertia of the material. $L_{joint} = 5\text{ mm}$ for all joints. As seen from Figure 5.4, the Young's modulus of the SMP strongly depends on the temperature, therefore we used the measured Young's modulus of the MM7520 in the calculations. Although the Young's modulus of the PDMS layer also depends on the temperature, this dependency is small compared to the SMP and we assume it is constant. Figure 5.6b

shows the computed bending stiffness of three joints as functions of the temperature. As the temperature increases above 80 °C the stiffness of all joints drops sharply. Due to small variation in their widths, there is a small difference among their bending stiffness.

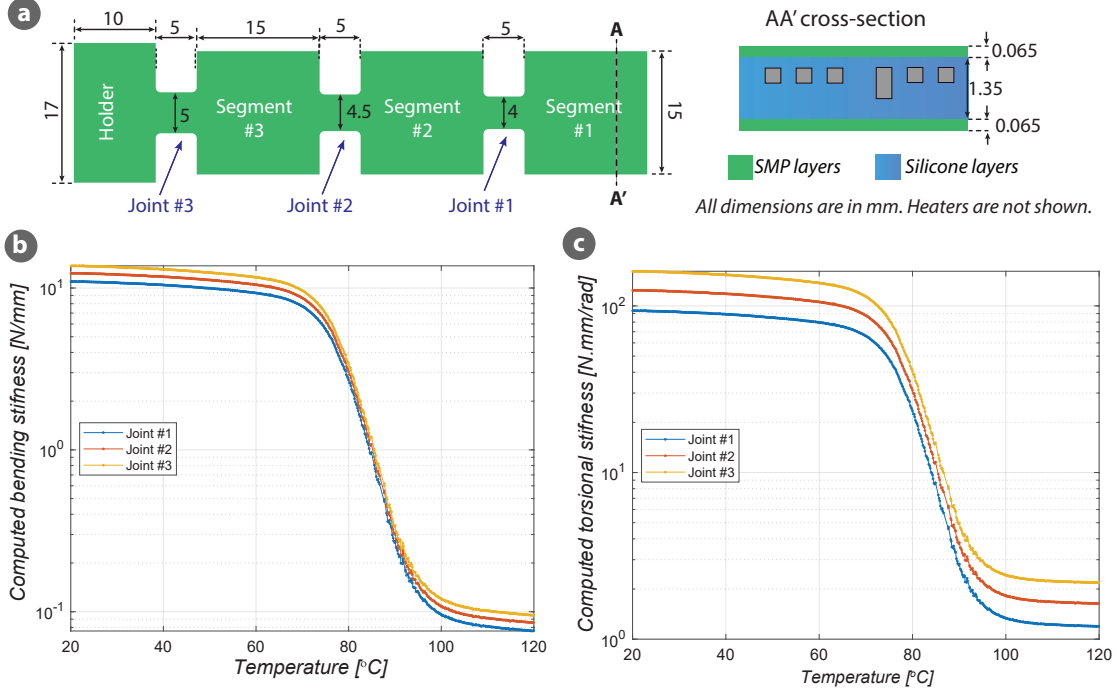


Figure 5.6: The joints design and their bending and torsional stiffness at different temperatures. a) The beam is composed of three identical segments accommodating liquid metal coils and three joints enabling mechanical connections between these segments. The segments are dimensionally identical with a surface area of 15 mm x 15 mm. The joints have the same length of 5 mm but varying widths. The joints are designed as narrow as possible while accommodating their dedicated heater and the leads for other joints' heaters. As the joints have different number of lead (electrical connections for the other joints), they have small thickness variations, changing from 4 mm to 5 mm. b-c) The bending and the torsional stiffness of the joints as functions of the temperature. The stiffness calculation is carried out for high T_g SMP material (MM7520). Both the bending and the torsional stiffness of the joints decrease significantly when the temperature increased above 80 °C. The variation in the widths of the joints causes small stiffness difference; the wider joints have higher stiffness.

The torsional stiffness of the joints was calculated using the following formula:

$$k_{torsion} = \frac{3(GJ_{PDMS} + GJ_{SMP})}{L_{joint}} \quad (5.3)$$

where the G is the shear modulus and J is the polar area moment of inertia. The shear modulus of the materials is calculated as $G = Y/2(1 + \nu)$, where ν is the Poisson's ratio of the material. The computed torsional stiffness of the joints is shown in Figure 5.6c. Similar to the trend observed in the bending stiffness, the torsional stiffness drops with a factor of 100 when the

temperature is swept from room temperature to above 80 °C. The torsional stiffness variation between the joints are more visible compared to their bending stiffness due to the cubic term of the widths. These stiffness calculations are used in the deformation analysis for the actuation (high temperature) and latched (cold temperature) states.

5.4.2 Optimization of the SMP thickness for large actuation and latched deformations

The following section quantify the deformation for bending and twisting scenarios. We derive the equations for the actuation and latched deformation to optimize the SMP thickness for the best trade-off between the SMP stiffening and shape fixation.

The torsional deformation of a soft joint is demonstrated in Figure 5.7. The liquid metal-coils are placed on a magnetic field that is perpendicular to the surface normal. When the current of these coils is switched on, the Lorentz forces is produced in the segments of the liquid-metal coils. Due to the direction of the current in the coil segments, the Lorentz forces act in the opposite directions. The cross-sections of the device segment at the initial and the deformed states are shown in Figure 5.7b. The initial distance between the coil segment and the magnet are represented with z_i with i being the number of i^{th} coil segment. When the device is twisted with a coil current of I , the distance between the coil segments and the magnet changes. The distance in the deformed states is shown with z'_i . As seen from the schematics, the Lorentz force on the left-hand side of the coil is downward whereas on the right-hand side of the coil the force acts in the upward direction. The torque created by the Lorentz forces can be quantified as:

$$T_{magnetic} = \sum B_{z(z'_i)} I L_i d'_i \quad (5.4)$$

where $B_{z(z'_i)}$ is the magnetic field in z direction at distance z'_i , I is the coil current, L_i is the length of the coil segment, d'_i is the distance between the coil segment and the center of the rotation. Here, we see that z'_i and d'_i depend on the angle of the twist θ_t . The general formula of the angle of the twist can be written as:

$$\theta_t = \frac{T_{magnetic} L_{joint}}{< GJ >} \quad (5.5)$$

where is $< GJ >$ the equivalent torsional rigidity of the joint. To find the angle of the twist, we

simply plug $T_{magnetic}$ (Equation 5.4) in Equation 5.5:

$$\theta_t = \frac{IL_{joint}}{\langle GJ \rangle} \sum B_{z(z'_i)} IL_i d'_i \quad (5.6)$$

where $d'_i = d_i \cos(\theta_t)$ and $z'_i = z_i + (1 - \cos(\theta_t))d_i$. z and z' are the distances between the magnet and the coil segment before and after the torsion. d and d' are the perpendicular distance between the Lorentz force of the coil segment and the center of the rotation before and after the torsion.

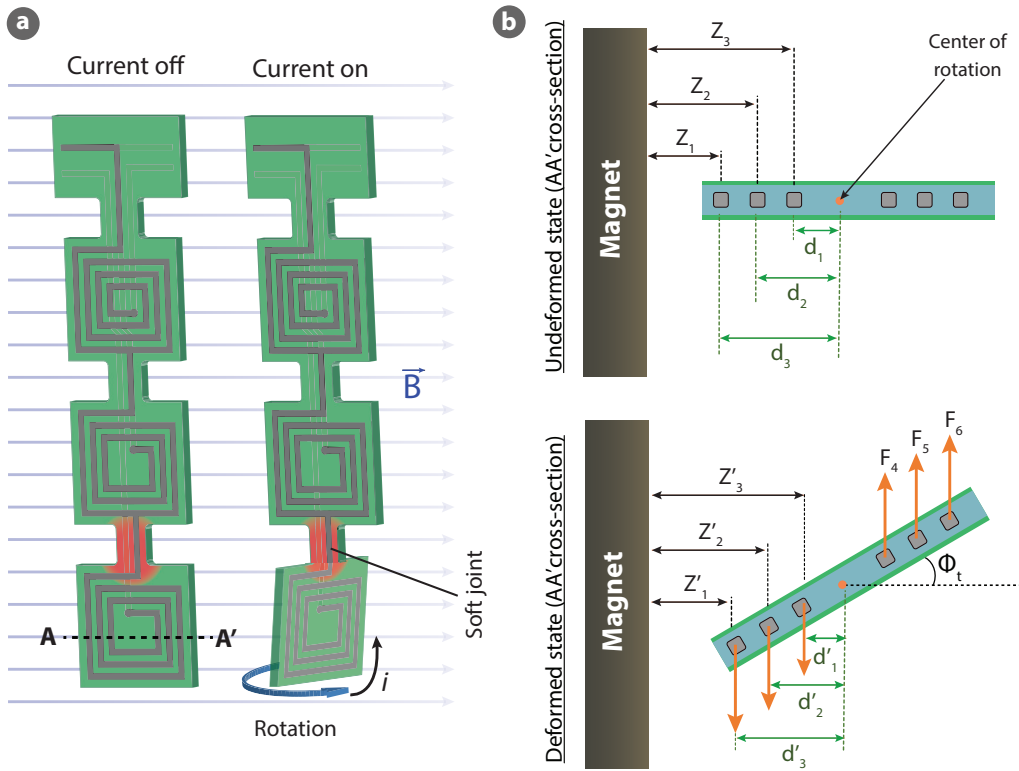


Figure 5.7: Calculation of the electromagnetic torque on the twisted segments. a) The schematics demonstrate the torsional deformation of the soft joint and the rotation of the adjacent segment when the LMC current is switched on in a magnetic field that is perpendicular to the surface normal. b) AA' cross-section views of the segment before and after the torsion. During twisting, the LMC segments that are closed to the magnet (z_1 , z_2 , and z_3) move away from it whereas the far-away LMC segments approach to the magnet. The Lorentz forces produced in these liquid-metal coil segments are in the opposite directions. This creates a torque and twists the joint.

We now can quantify the torsional deformation at any given temperature using Equation 5.6 and the torsional stiffness of the joints in Figure 5.6. The three states of the actuation and latched processes are shown in Figure 5.8a: initial, actuated, and the latched states (for easy visualization the cross-section is shown in circular shape). In the actuation state, the joint is

softened at an elevated temperature. We assume that the actuation temperature is 110 °C. The blue curve shown in Figure 5.8b show the angle of the twist during the actuation state as a function the SMP thickness. The angle of the twist that is obtained in this state is called θ_{act} where *act* stands for actuation.

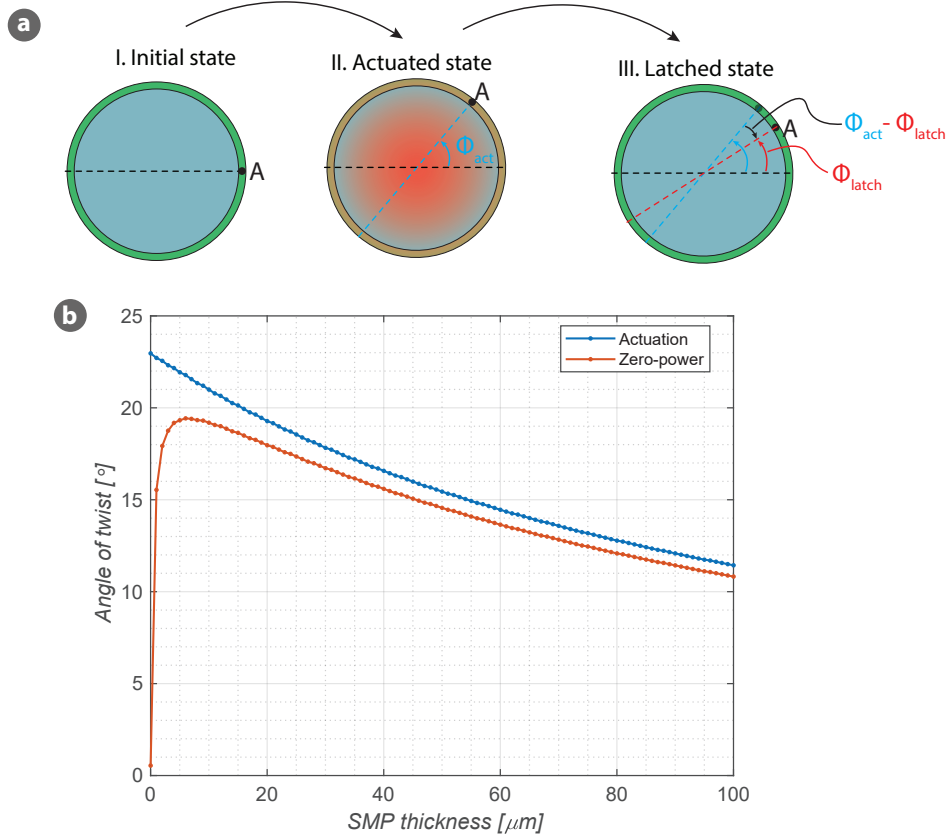


Figure 5.8: The optimization of the SMP thickness for large torsional deformation in the actuation and latched states. a) Schematics show the lateral cross-section of a joint in different states: the initial (undeformed), actuated, and latched (zero-power) states. The cross-section is shown in circular for easy visualization. In the actuation state, the joint is softened by the Joule heater and twisted by the torque (created by the Lorentz force in the upper and lower LMC segments). When the twisting is achieved, the joint is cooled down, allowing the SMP to fix the deformation. At the latched state, the PDMS want to recover its initial shape whereas the SMP opposes this recover and wants to stay in their deformed (actuated) state). The torques of these two layers are in balance in this state. b) The angle of the twist is computed and plotted as a function of the SMP thickness for the actuation and latched (zero-power) states. The actuation deformation is highest at $t_{SMP} = 0$. For zero SMP thickness, however, there is no latching. The maximum latched deformation is predicted for the SMP thickness around 10 μm . Above 10 μm , the latched deformation decreases as the SMP thickness increases due lower actuation deformation.

Once the actuation deformation is achieved, we turn off the heater and allow the SMP layer to lock this deformation (called latching). At the latched state the PDMS wants to recover its initial undeformed shape whereas the SMP opposes this recovery and wants to maintain its deformed shape. Therefore, there is an equilibrium between these materials. At this

equilibrium state, the torque generated by the PDMS to go back to its initial state is balanced by the torque of the SMP. The equation of the torque equilibrium for the final latched state can be written as:

$$\frac{\theta_{latch} G_{pdms} J_{pdms}}{L_{joint}} = \frac{(\theta_{act} - \theta_{latch}) G_{smp} J_{smp}}{L_{joint}} \quad (5.7)$$

where θ_{latch} is the angle of the twist in the final state. Recall that, since the SMP layer already fixes its actuation deformation during the latching step, the angle of the twist for this layer is $\theta_{act} - \theta_{latch}$ (not θ_{latch}). Isolating θ_{latch} from (5.6), we find:

$$\theta_{latch} = \frac{G_{smp} J_{smp}}{G_{smp} J_{smp} + G_{pdms} J_{pdms}} \theta_{act} \quad (5.8)$$

Figure 5.8b shows the actuation and the latched deformation as functions of the SMP thickness. The actuation deformation is highest at $t_{SMP} = 0$ and decreases as the SMP thickness increases. This is due to increased torsional rigidity. Although the actuation deformation is high in thinner SMP, the latching is small in this region. Because the thin SMP cannot resist the recovery of the PDMS layers, resulting lower latched deformation. The maximum latched deformation takes place at around $10 \mu\text{m}$ SMP thickness. Above $10 \mu\text{m}$, the latched deformation decreases as the SMP thickness increases due lower actuation deformation.

To decide the optimal SMP thickness where we can achieve large actuation and latched deformations, we carried out similar analysis for bending cases. Figure 5.9a shows the bending of the soft joint when actuated in a magnetic field parallel to the surface normal. To find the attraction force between the magnet and the liquid-metal coil, we can assumed the magnet and the coil as two magnetic dipoles, with $m_1 = (M_{mag} V_{mag})$ being the dipole of the plate magnet and $m_2 = NI\pi R_m^2$ being the magnetic moment of the coils.

Figure 5.9b-c show two deformed configurations of the device segment when actuated. During the actuation, the actuated segment either moves away from the magnet or approaches to the magnet as shown in panel c. When the segment moves away, the distance between the LMC increases whereas in the approaching scenario this distance decreases. In both cases, the angle between the segment surface normal and axial direction of the magnet changes, from 0 to θ_b .

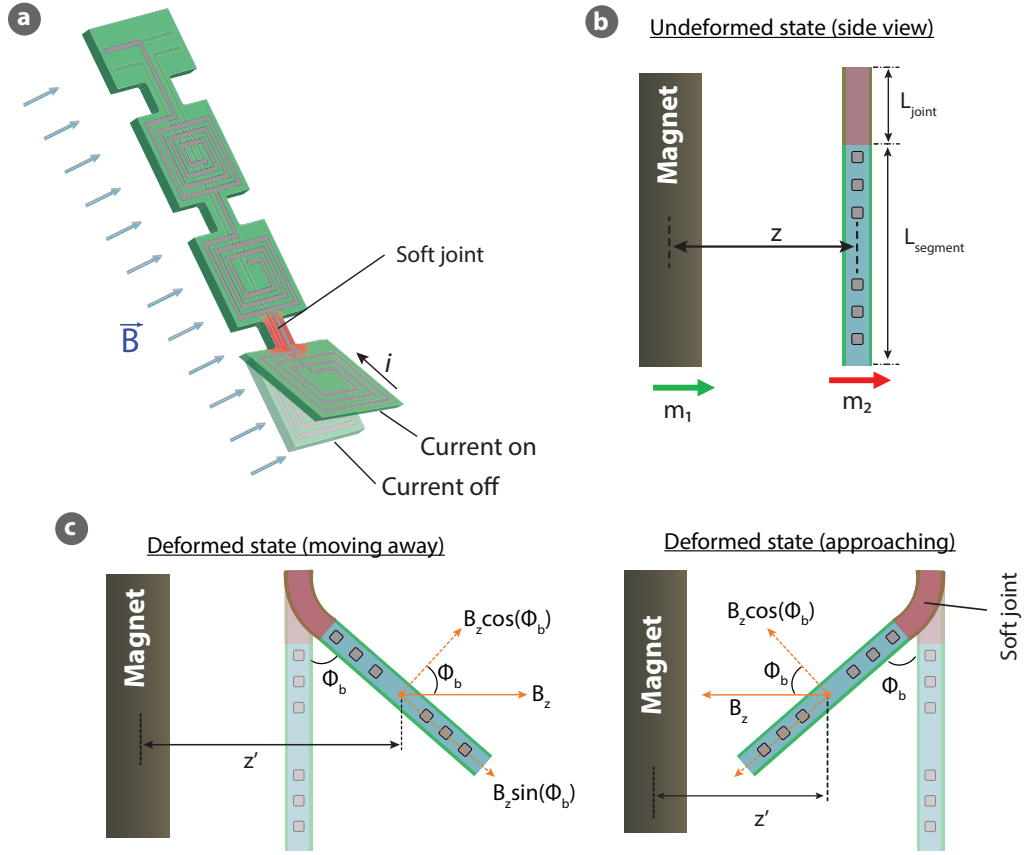


Figure 5.9: Calculation of the electromagnetic force for bent segments. a) The schematic shows the bending of the soft joints when the LMC current is on in a magnetic field parallel to the surface normal. b) To calculate the force between the magnet and the LMC, we assume that the magnet and the LMC are two magnetic dipoles (m_1 and m_2). c) When the joint is bent, the corresponding segment either approaches to the magnet or moves away from it. The electromagnetic force acting on the LMC is higher when approaching to the magnet than when it moves away from the magnet.

The attraction force between the current-carrying liquid-metal coils and the magnet is previously computed using Equation 5.1 for the fixed magnet-coil distance. This formula is valid for a fixed distance of z and aligned configuration as shown in Figure 5.9b. When the segment is actuated, this distance and the angle between surface normal of the magnet and the coil changes. The modified force equation for the deformed state can be written as:

$$F_{bend} = \left(\frac{3\mu_0}{2\pi}\right)(M_{mag} V_{mag})(N I \pi R_m^2) \left(\frac{1}{z'^4 (1 + R_m^2 / z'^2)^{5/2}}\right) \cos(\theta_b) \quad (5.9)$$

where z' is the distance between the magnetic dipoles at the deformed state and it is a function of θ_b . θ_b is the tip deflection angle of the joint which also equal to the angle between the surface normal of the segment and B_z . Knowing this electromagnetic force (acting on the center of the actuated segment), we can find the tip deflection of the joints at the actuation

state as:

$$\theta_b = \theta_{act} = \frac{F_{bend} L_{joint} (L_{joint} + L_{segment})}{6(Y I_{pdms} + Y I_{smp})} \quad (5.10)$$

The bending deformation during the actuation state are computed for both approaching and move-away cases and are shown Figure 5.10b. As seen from the graph, the deformation is higher at the approaching case due to shorter distance between the magnet and the LMC.

To find the latched deformation, we follow the same procedure as we did for the torsional deformation. Once the bending deformation is achieved, we cool down the joint, allowing the SMP layer to fix the deformation. When latched, the PDMS tries to go back to its undeformed configuration whereas the SMP resist this recovery of the PDMS. Therefore, there exists a balance of the moments between the SMP and PDMS layers, which can be written as follow using the Stoney's equation: [136],

$$\int_{A_{pdms}} -Y_{pdms} \epsilon_{latch} r dA = \int_{A_{smp}} -Y_{smp} \frac{\epsilon_{latch} - \epsilon_{act}}{1 + \epsilon_{act}} r dA = 0 \quad (5.11)$$

where ϵ_{act} and ϵ_{latch} are the strains at the actuation and the latched states, respectively. A_{smp} and A_{pdms} stands for the cross-section areas of the SMP and the PDMS layers. As we can see from this equation, the stress in the PDMS depends on its instant strain whereas the stress in the SMP depends not only on their instant strain but also the strain at which it fixes its deformation. The strain formulae for the actuation and the latching states are:

$$\epsilon_{act} = \frac{r - r_{act}}{\rho_{act}} \quad (5.12)$$

$$\epsilon_{latch} = \frac{r - r_{latch}}{\rho_{latch}} \quad (5.13)$$

where r and ρ are the neutral axis and the radius of curvature. We know that the neutral axis locates at the center of the device thickness due to symmetrical structure and pure bending configuration. We also know that $\rho_{act} = L_{joint} / \theta_{act}$. Therefore, Equation 5.11 is sufficient to find the latched deformation.

Figure 5.10b compares the angle of the tip deflection between the actuation and latched states. The actuation deformation is highest at $t_{smp} = 0$ and decreases with the increase of the SMP

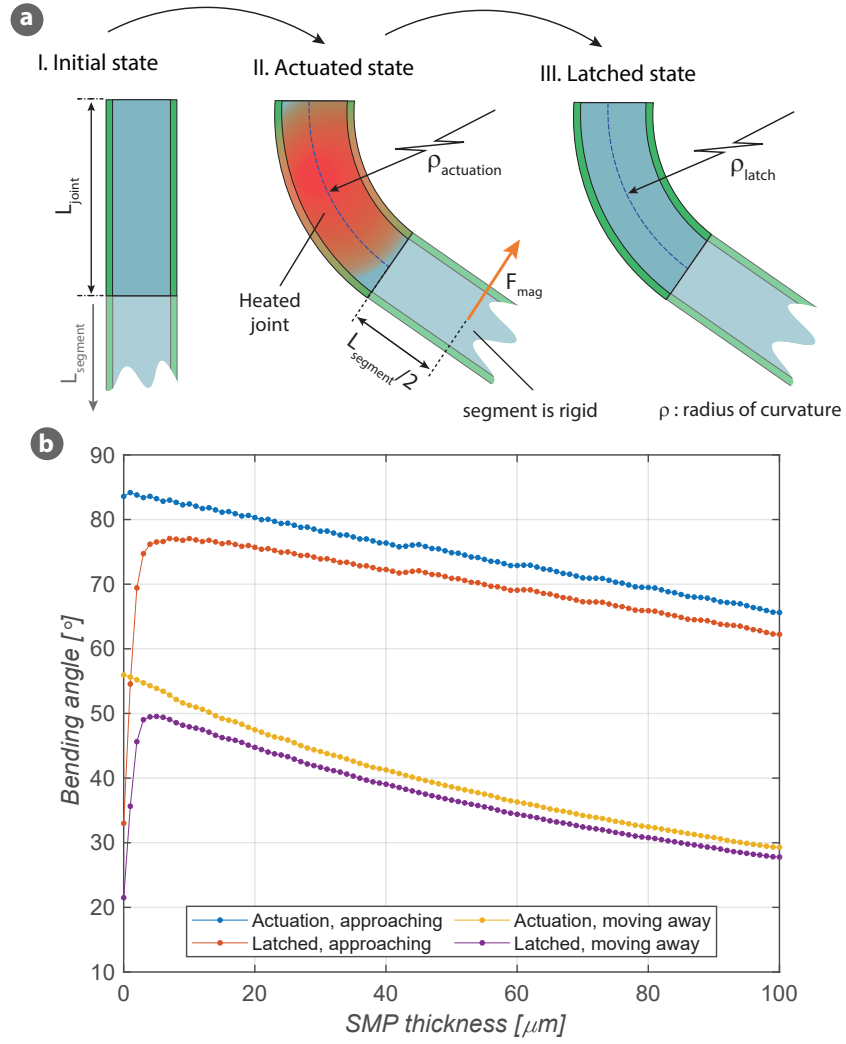


Figure 5.10: Optimization of the SMP thickness to achieve large bending deformation during the actuation and latched states. a) The schematics show the longitudinal cross-section of a joint in initial, actuated, and latched states. During the actuation state, the joint is soft and the electromagnetic force acts in the direction of the surface normal. Once the bending is achieved, the heater is turned off, allowing to fix the joint deformation into place. Depending on the SMP thickness, the radii of the curvature varies between the actuated and latched states. b) The actuation and latched deformations of the joint are plotted as functions of the SMP thickness. If there is no SMP layer (zero thickness) the joint has the highest deformation for both approaching and moving-away scenarios. However, all these deformations are recovered during latching process as there is no shape fixation. The model predicts the maximum latched deformation when the SMP thickness is around $10\mu\text{m}$.

thickness. The maximum latched deformation occurs at 10 μm thick SMP and then decreases as the SMP thickness creases due the lower actuation deformation. Although increasing the SMP thickness above 10 μm decreases the latched deformation, the device with thicker SMP greatly increases the stiffness of the device at the cold state. Therefore, we chose SMP thickness of 50 μm for our devices, where we sacrifice 14% of the maximum latched deformation in order to enhance the device rigidity at the cold state.

5.4.3 Heater design

In this section, we discuss the design of the heaters and compare the temperature distribution between one-heater and two-heaters designs. The heaters were designed to locally soften the joints and aimed to minimize the heating of the segments and unaddressed joints (see Figure 5.11a). The heater are confined to the small joint areas and are connected to the electrical pads through long and wide leads made of the same material of the heaters.

The total thickness of the devices is around 1.35 mm. This slightly varies between the fabricated devices due to small thickness variation in the PMMA molds. Each device has two SMP layers located at the opposite sides of the device. We soften both SMP layers during the actuation to achieve large deformation. When the joint is softened by one heater, very high temperature difference occurs between the SMP layers. The SMP layer closed to the heater has higher temperature than the far-away SMP layer. We used the finite element modeling to compare the temperature distribution of the one-heater and two-heaters designs. for one-heater design, we experimentally validated the temperature difference between the SMP layers using a PT100 temperature sensor.

Figure 5.11a compares the simulated temperature distribution between one-heater and two-heaters designs. In the two-heater design, an identical heater is placed the opposite side of the first heater. In the first simulation, the heater is powered with 400 mW whereas in the second design each heater is addressed with a power of 200 mW to have the same heating power. The parameters used in the simulation are listed in Table 5.3. The simulation is run in the stationary mode where the heater of the 3rd joint are addressed.

Table 5.3: The material parameters listed in this table were used in the FEM simulation. The heaters are AR-care 90366 from Adhesives Research

Parameter	unit	SMP	PDMS	EGaIn	Heater
Thermal conductivity	$\text{W m}^{-1} \text{K}^{-1}$	0.17	0.15	26.4	1.6
Electrical conductivity	S m^{-1}	-	-	3.4×10^6	0.644
Heat capacity	$\text{J kg}^{-1} \text{K}^{-1}$	1260	1460	305	1460
Density	kg m^{-3}	1210	970	6250	960

The close-up surface temperature shows the temperature gradient the joint area; the closer areas have higher temperature (see Figure 5.11a). The temperature across the device thickness are computed for two lines shown in panel a. One line passes through the liquid-metal chan-

nels whereas the other line passes through only PDMS layer. Figure 5.11b shows temperature across the device thickness in one-heater and two-heaters designs. A temperature difference of $>30^\circ\text{C}$ are predicted between the top and bottom SMP layers when one heater is used. Using two heaters overcomes this temperature difference and enable the same temperature of both SMP layers.

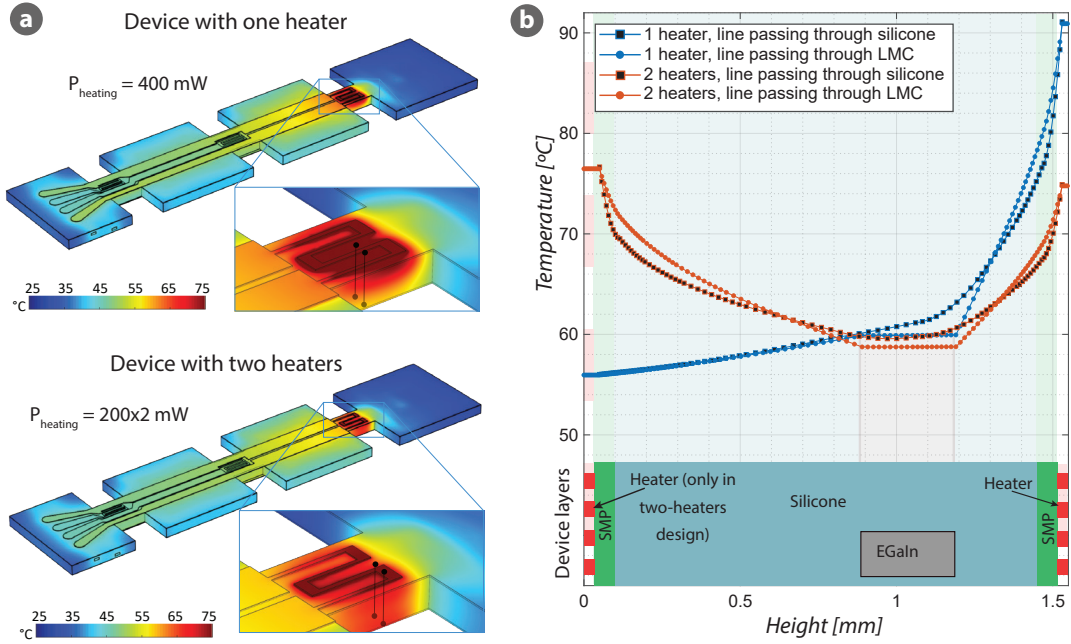


Figure 5.11: Temperature difference between the SMP layers in one-heater and two-heaters designs. a) Surface plots of temperature distribution for two identical devices having one heater (top) and two heaters (bottom). In the first simulation, the joints is heated with a power of 400 mW. In the second simulation, there are two heaters with each providing 200 mW of heating power. b) The temperatures across the device thickness are shown for one-heater and two-heaters designs. To show the temperature gradient across the device thickness, two line are selected where one line passes through liquid metal channels and the other one pass through only PDMS layer. When the joint is softened with one heater, a big temperature difference occurs between two SMP layers, more than $>30^\circ\text{C}$ (see the blue lines). when two heater are used to soften the same joint, similar temperature values are obtained for both SMPs (the red lines).

For one-heater design, the temperature difference between the SMP layers was experimentally validated. The joints temperature was measured using a PT100 temperature sensor. The joint was heated with a power of 375 mW for 5 min and cooled down for another 5 min. The temperature of the top SMP layer was first measured. Then the temperature measurement was repeated with the same power and this time the temperature of the bottom SMP layer was measured. The configuration of these experiments is shown in Figure 5.12a. The temperature profile of the SMP layers are shown in Figure 5.12a. For a heating power of 375 mW, we measured a temperature difference of 16°C . Both the simulation and the experimental data prove the necessity of using two heaters for softening a joint, which enables more efficient heating with less temperature difference.

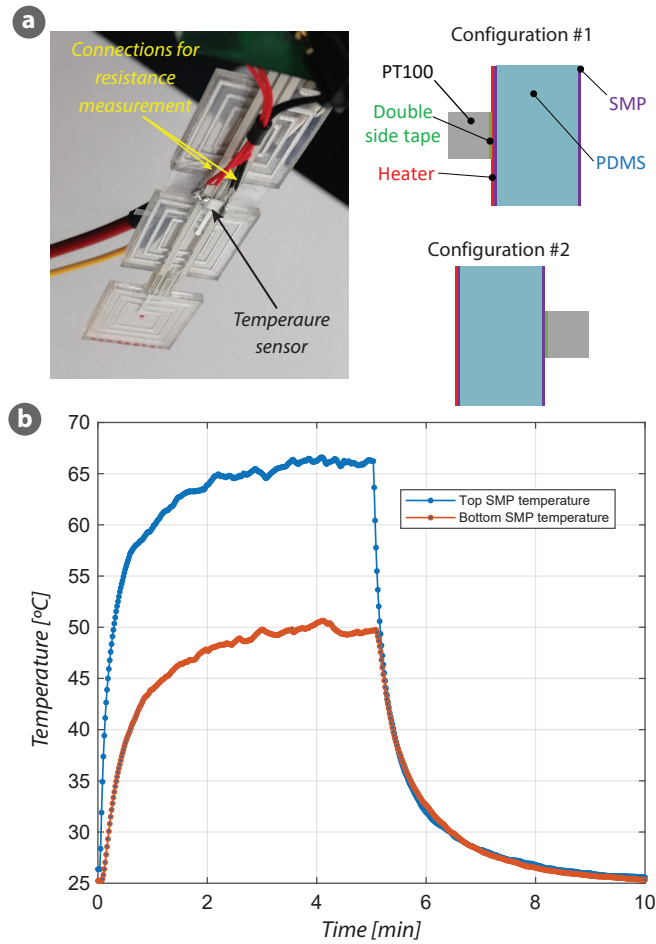


Figure 5.12: Measured temperature difference between the SMP layers in one-heater design. a) A PT100 temperature sensor was attached to the device using a double-sided tape. To measure the temperature of the bottom SMP layer, the temperature was placed to the bottom of the device where the joint is heated with the same power. b) The SMP layer closed to the heater has higher temperature than the far-away SMP. A temperature difference of 16 °C was measured when the joint was heated with a power of 375 mW. As we aim to obtain the same temperature for both SMP layers, it is necessary to use two heaters per joint.

5.5 Device fabrication and experimental setup

5.5.1 Device fabrication

The fabrication of the latchable soft electromagnetic beams starts with casting of multi-layers of SMP+PDMS; steps 1 to 5 in Figure 5.13. An A4-size PET sheet was used as the substrate layer. The surface of the PET was treated with oxygen plasma and followed by casting a thin layer of Teflon using the thin film applicator. The Teflon layer was used as sacrificial layer to easily release the device layers. Then the mixture of SMP and DMF with a weight ratio of 1:4 was casted on the Teflon. The DMF was evaporated on a hot plate at 80 °C for 4h. The mixture of Sylgard 186 (1:10 ratio) was then casted on the SMP layer and cured in the oven at 80 °C for 1h.

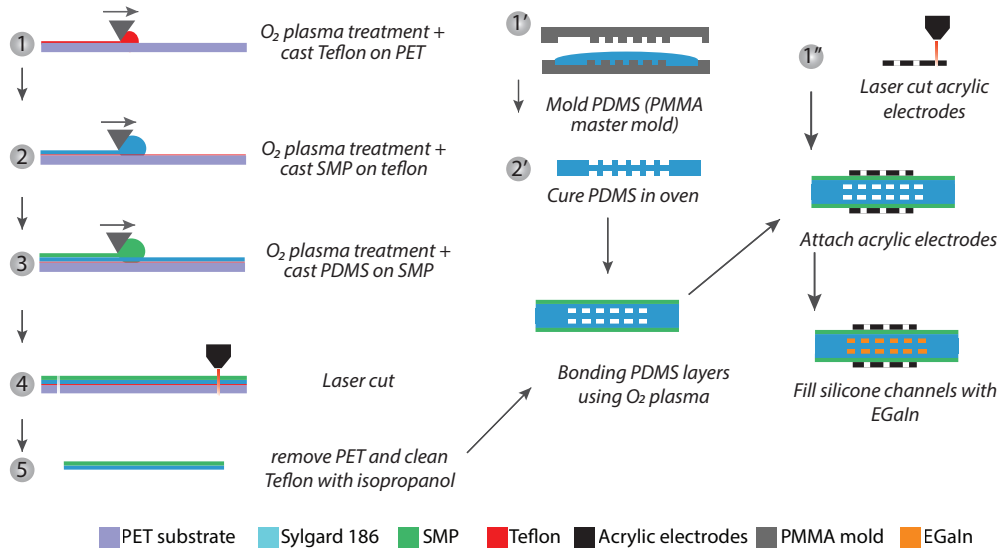


Figure 5.13: The fabrication flow process of the multi-layered SEMAs. The fabrication starts with casting of multilayer of SMP, PDMS, and Teflon on a PET substrate (steps from 1 to 5). Two PMMA master molds are used to fabricate silicone microfluidic channels. The PDMS solution is poured into the PMMA molds and clamped, and cured in the oven at 80 °C for 1 h. Two layers of PDMS+SMP composite are bonded on both sides of the molded PDMS using oxygen plasma treatment. An acrylic based conductive type is patterned with laser cutter and is placed on the top and on the bottom of the assembled structure. Finally, the PDMS channels are filled with EGaln using a syringe.

To fabricate PDMS structure with microfluidic channels, we used PMMA master molds. First the mixture of Sylgard 186 was poured in to the top and bottom PMMA molds. The air bubbles were removed using a desiccator. The bottom and the top were aligned and clamped. The PDMS solution was cured in the oven at 80 °C for 2h.

The molded PDMS were then bonded with two layers of PDMS+SMP composite to form SMP-PDMS-SMP structure. Having the SMP layers at the outer sides enable high stiffness at room temperature as the SMP is very stiff (>1 GPa). For heaters, we used an acrylic based conductive tape (AR-care 90366 from Adhesives Research). We shapes the electrodes using the laser cutter to define the heater shape. We attached the heaters to the both sides of the device. The final

step of the fabrication was to fill the silicone channels with the liquid metal. The channels were filled with EGaIn using a syringe. After the electrical connection were made, the channels were sealed with a silicone glue.

5.5.2 Magnetic field measurement of the plate magnet

We used plate magnets in our experiments. This simplified the experimental setup while providing high magnetic field. The magnetic field of the magnet was measured using a Teslameter (see Figure 5.14a). The sensor probe was placed on a XYZ motorized state and the magnetic fields in the radial and axial directions were measured as the stage was moved in the x , y , z directions.

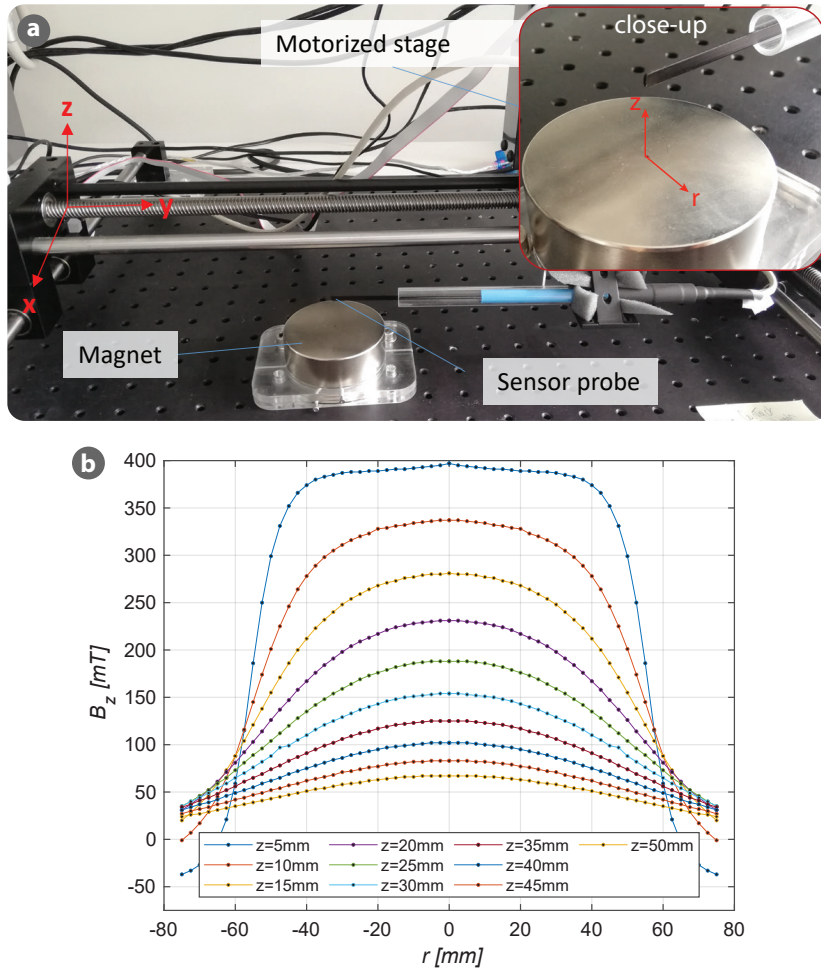


Figure 5.14: Magnetic field of the permanent magnet was measured using a Teslameter. a) The setup used for the magnetic field measurement. The sensor probe was attached to a motorized XYZ state. The magnetic field of the magnet in radial ($B_r(z, r)$) and axial ($B_z(z, r)$) directions were measured as functions of z and r . b) Measured magnetic field in the axial direction as function of the radius for different heights. The magnet has a radius of 35 mm and a height of 35 mm. This measured magnetic field was used in our calculations.

Figure 5.14b shows the measured magnetic field in the axial direction as a function of the radial distance for different height. On the surface very closed to the magnet, the magnetic field is around 400 mT and decreases as the height increases. The magnet has a diameter of 70 mm and a height of 35 mm. The length of our device is 60 mm and the maximum width of the device is 15 mm. During the experiments the device were placed close to the magnet to benefit from the high magnetic field.

5.5.3 Experimental setup for actuation and latching tests

The main components of the experimental setup are the magnet, the power supplies, the video cameras, and the infrared camera (see Figure 5.15). The power supplies and the cameras were controlled with a custom-written Python code. The video cameras were used for capturing the deformed images of the device to be image processed for the deformation analysis and for the visual inspection. The power supplies were used to provide the current for the liquid metal coils and the voltage for the Joule heaters. The IR camera was used to measure the temperature of the joint during the experiments.

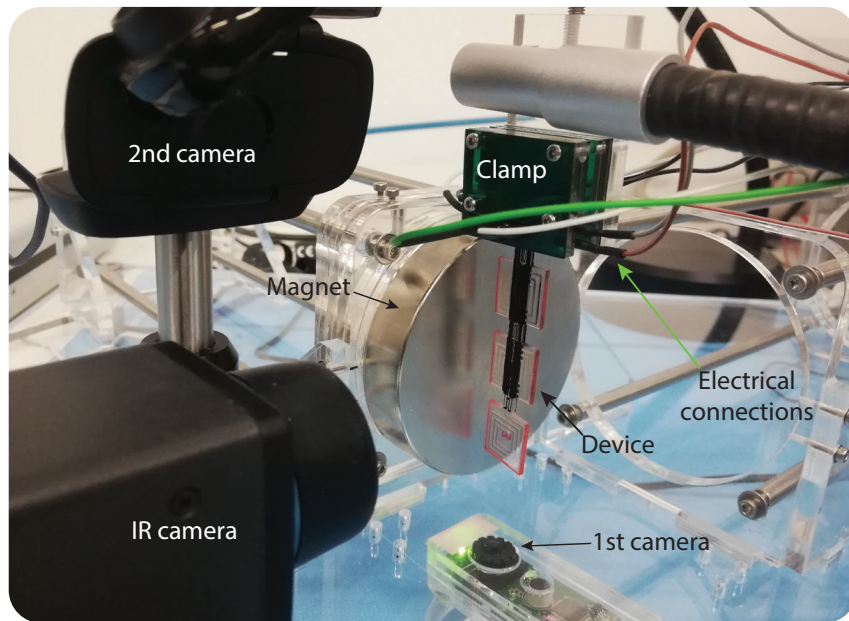


Figure 5.15: Photograph of the setup used for the actuation and latching experiments. In the experiments, the device is placed next to the magnet and clamped from its top edge where we also have electrical connections to the LMC coils and to the heaters. Using magnet simplifies the setup. The 1st camera is placed below the device to capture the deformed images. The edges of the device segments are painted red to easy the tracking of the segments. The 2nd camera captures the overall view of the device, used mostly for visual inspection. The IR camera is used to record the temperature of the joint during the experiments.

5.5.4 Experimental procedure to deform and latch operations

The four steps of a deform-and-latch cycle are shown in Figure 5.16. The cycle starts with the actuation step where the joint is softened by the Joule heaters and the current is applied to the liquid-metal coil. Once the actuation deformation is achieved, the heater are turned off while keeping the LMC on for a while to cool down the joints. Cooling down the joints allows the SMP layers to fix the deformed shape. This cooling steps is called shape fixation step. Once the device is fixed in the deformed state, the LMC current is removed (zero-power). In the zero-power step, neither the LMC current nor the Joule heaters is on. The device maintains its deformed shape in this state for long periods of time without consuming any power. To recovery the initial shape, the joint can be simply re-heated where both the SMP and the PDMS layers try to go back to their undeformed states.

The deformation in the device is recorded by two video cameras during the actuation and latching steps. The images shown in Figure 5.16b were captured by the 2nd camera and they show the overall view of the device. The images shown in panel c were captured by the 1st camera and these images were processed to extract the torsional or the bending deformations.

5.6 Experimental results and discussion

This section presents the experimental results obtained for different deform-and-latch scenarios.

5.6.1 Twist-and-latch experiments

In the twist-and-latch experiments, the selected soft joint was twisted during the actuation and subsequently latched. The experiments were carried out at different LMC currents to investigate how the torsional deformation change with the current and how much of this deformation can be fixed by the SMP layers.

The current of the liquid-metal coil was varied from 0A to 2A with an increment of 0.2A. For each increment, the device was actuated, latched, kept in zero-power, and finally recovered (see Figure 5.17). The deformed images at the end of the actuation and zero-power states were captured for the deformation analysis. The initial heating power was set to 550 mW. As the LMC increases, the electrical heating produced in the segment contributes to the joint temperature. To compensate this temperature increase due to the cross-heating, we formulated the power of the heaters as:

$$P_{heating} = P_{initial} - \frac{I_{LMC}^2 R_{LMC}}{10} \quad (5.14)$$

where I_{LMC} is the current applied to the LMC and R_{LMC} is the resistance of the coil. This

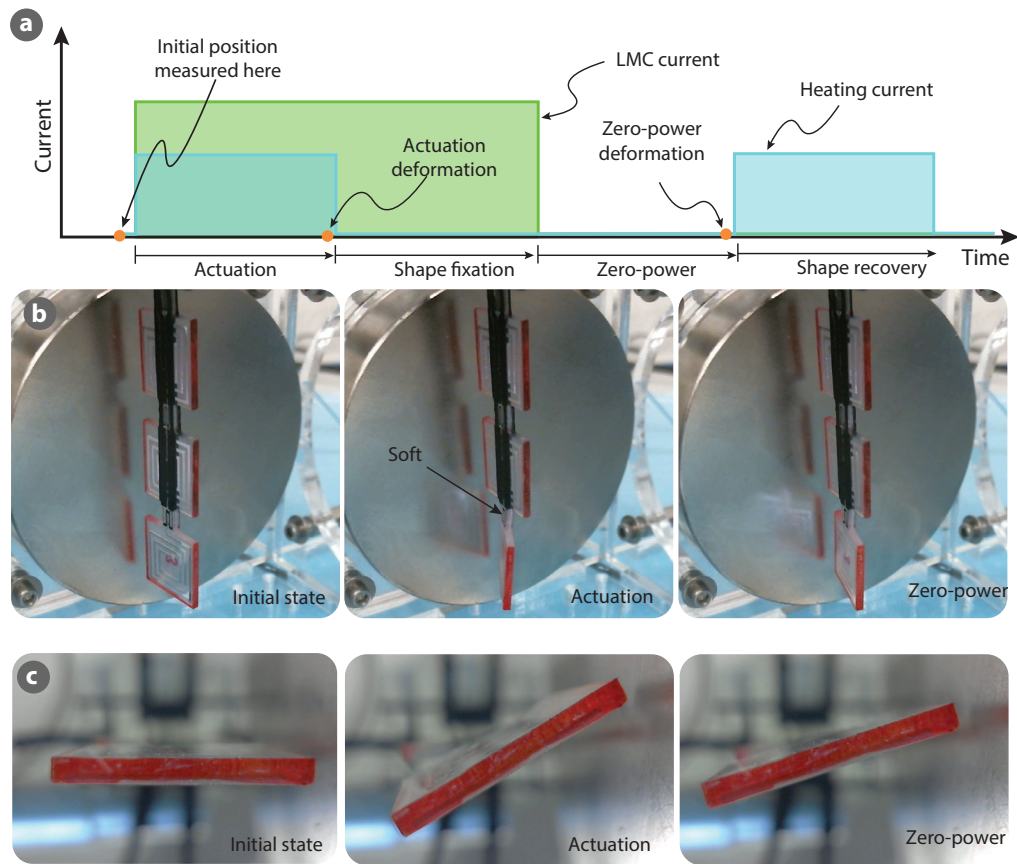


Figure 5.16: Experimental procedure to deform and latch the joints, and examples of deformed joints. a) To achieve a stable deformed shape, two steps need to be followed subsequently: actuation and shape fixation. During the actuation, both the heaters and the LMC currents are on. Once the deformation is achieved, the shape fixation steps is followed by turning off the heaters. This allows cooling down the SMP layers, therefore fixing the deformed shape. After this steps the LMC current can be turned off and the device now has a permanent deformed shape (zero-power). To recovery the initial shape, the joint is simply heated. b) The photographs show the deformation of a device at three states. During the actuation, the bottom joint is softened and therefore deformation occurs only in this joint. c) Images captured by the 1st camera show the close-up bottom view of the deformed segment. These images are processed to extract the deformation.

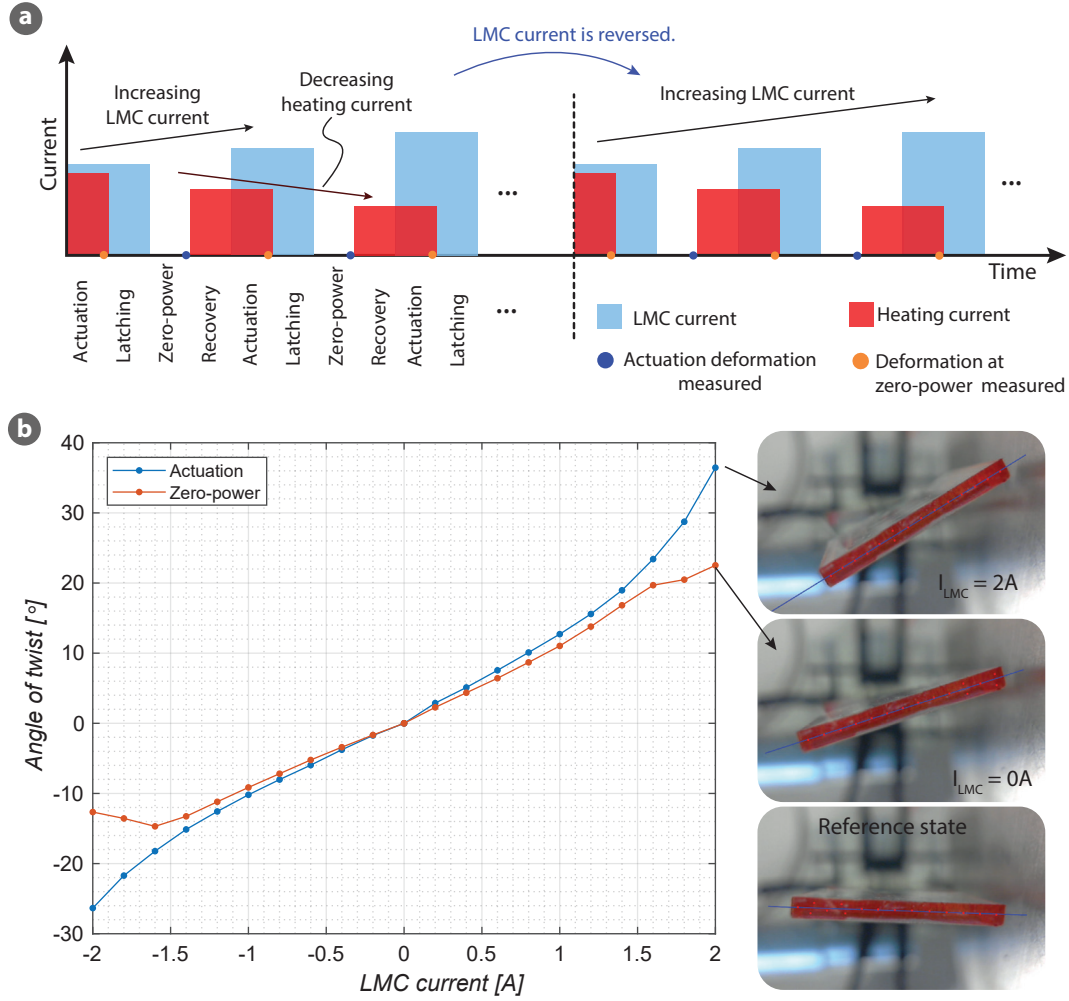


Figure 5.17: Twist-and-latch experiments at different LMC currents. a) The sequence of the LMC and heating currents. The LMC current was swept from 0A to 2A with a step of 0.2A. To compensate the temperature increase due to LMC current, the heating current is decreased accordingly. Once the steps were done for the positive LMC current, the same procedure was repeated for the negative coil current; from 0A to -2A with a decrement of 0.2A. b) The angle of the twist of the actuated segment in the actuation and zero-power states. Both deformations show similar trend for the positive and negative LMC currents. The device can fix its deformation with high ratio (actuation/latched) for the LMC current up to 1.5A. This ratio decreases as the LMC current increases from 1.5A due to increased latching temperature.

modified heating power provides a constant temperature during the actuation at different LMC currents. The formula also shows that a small portion of the LMC heating transfers to the joint (10%), most of the heat dissipates to the air. Once the steps are done for positive LMC current, then the same procedure was repeated for the negative coil current, from 0A to $-2A$ with a decrement of $0.2A$ (see Figure 5.17a).

Figure 5.17b shows the angle of the twist in the actuation and zero-power states at different LMC currents. In this test, the first joint was softened by the heaters and the first segment was actuated (see Figure 5.16). Both deformations show similar trend for the positive and negative LMC currents. At lower LMC current ($< 1.5A$) the actuation and latched deformation are very closed to each other. This indicates that the actuation deformation is fixed by the SMP layers with high shape fixation ratio. As the LMC increases above $1.5A$, the actuation deformation deviates from the zero-power deformation due to the increased joint temperature in the latching steps. As discussed previously, the SMP performs better at latching at the cold temperature. The increased latching temperature results in poor latching performance.

Figure 5.18 shows the measured temperature of the joints during the actuation and latching steps at the low ($I_{LMC} = 0.2A$) and high LMC currents ($I_{LMC} = 1.6A$). The temperature of the joints was measured using the IR camera. The maximum actuation temperature of the 1st joint (the heated joint) in both cases is around $110^{\circ}C$. Since the LMC current is on during the latching process, the temperature of the joints differs a lot between the low-current and high-current latching. At low LMC current, the joint temperature goes down to $35^{\circ}C$ whereas at high LMC current the temperature is around $60^{\circ}C$. Since the SMP layers fixes their deformation at this state, the higher latching temperature causes poor latching performance.

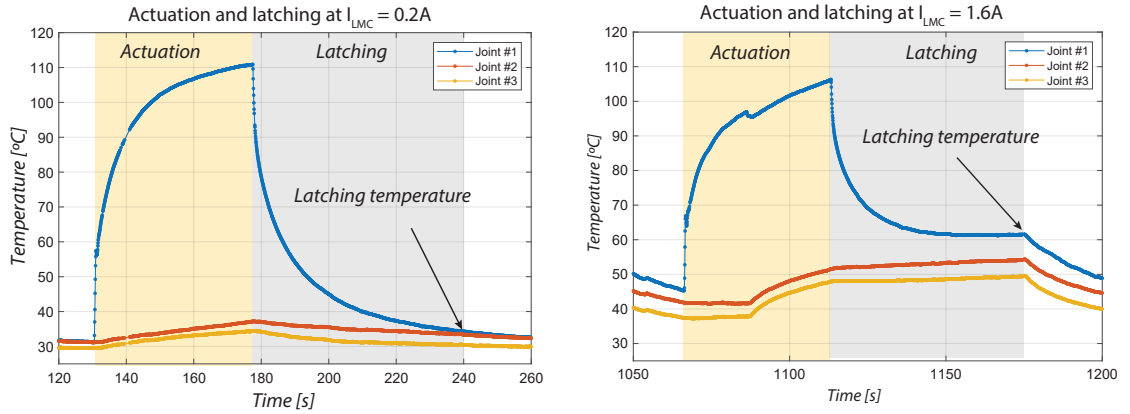


Figure 5.18: The temperature of the joints during the actuation and shape fixation steps. In the both experiments, the actuation temperature is around $110^{\circ}C$. However, the latching temperature is significantly different. It is around $35^{\circ}C$ for $I_{LMC} = 0.2A$ and $60^{\circ}C$ for $I_{LMC} = 1.6A$. The latching temperature has influence on the shape fixation ratio: having lower temperature during shape fixation step allows a better latching.

As each joint and segment can be individually addressed, we can sequentially deform-and-latch them to amplify the tip deflection of the beam. In this experiment, we consecutively

twisted and latched three joints. The schematic of the heating and LMC currents is shown in Figure 5.19a. In these experiments, the latched deformation of the joints was not recovered (no shape recovery step) and the deflection angle of the bottom segment was measured. Figure 5.19b plots the angle of the twist of the bottom segment as the joints were consecutively deformed and latched. Due to the voltage drops in the long leads, we slightly adjust the heating power for the joints: $P_{joint1} = 600mW$, $P_{joint2} = 550mW$, and $P_{joint3} = 500mW$. As depicted from the Figure 5.19b, the deformation of the bottom segment can be increased by a sequence of deform-and-latch operations.

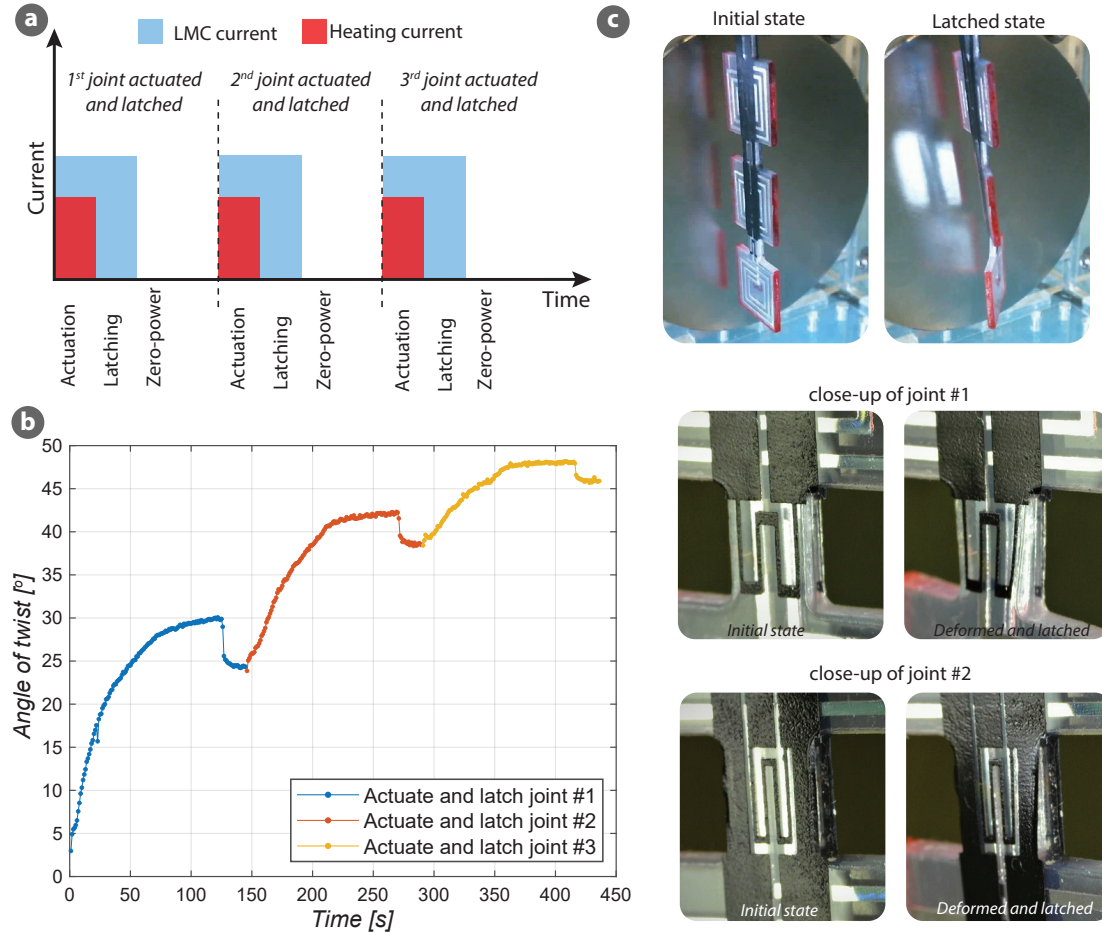


Figure 5.19: The joints are sequentially twisted and latched to increase the tip deflection of the device. a) The sequence of the LMC and heating currents for a consecutive twist-and-latch of the joints. b) The angle of the twist of the bottom segment is plotted as the joints are being deformed and latched. The narrow joint (joint 1) has the largest deformation whereas the widest joint has the smallest deformation. This is due to small variation in the joints widths ($w_{joint1} < w_{joint2} < w_{joint3}$) and the temperature uniformity of the joints during the actuation. By sequentially deforming and latching the joints, the twisting angle of the tip of the device is increased. c) Two images captured by the second camera show the device configuration in the initial and latched state where all joints are in a stable deformed state. Micrographs shows the close-up deformation of the first two joints.

The joints have different deformations: $\theta_{joint1} > \theta_{joint2} > \theta_{joint3}$. This is mostly due to

variation in the joints widths ($w_{joint1} < w_{joint2} < w_{joint3}$) and the temperature uniformity of the joints during the actuation, e.g. the heaters of the 1st joint provides more uniform heating compared to the 3rd joint heater. Figure 5.19c shows the deformation in the after three latching steps. The close-up images shows the deformation of the joints. The micrographs also show heater designs: the 1st heater is wider than the 2nd heater (and provides more uniform temperature distribution over the joint area during the actuation). The second heater is smaller in width due to region occupied by the conductive leads that goes to the other heater.

5.6.2 Bend-and-latch experiments

This section presents the experimental results obtained for the bending deformations of the joints. The same experimental procedure summarized in Figure 5.20a was adapted for the bending tests.

In the first test, the first joint was softened and the first segment was actuated (see Figure 5.20a). When the positive current was applied to the LMC, the segment approached to the magnet whereas for the negative LMC current the segment moved away from the magnet. The displacement of the segment in the approached configuration was higher due to the higher magnetic field. The unaddressed joints were very stiff and therefore they had very small deformation, e.g. the deflection angle of the 2nd and 3rd segments was around 0°. Almost all of the deformation achieved during the actuation was locked by the SMP layers for the LMC current up to 1.5A. Small relaxation during latching is observed at higher currents (> 1.5A) due to the increased latching temperature.

The same bend-and-latched experiment was carried out for the second joint. In this test the first segment was actuated. Actuating the first segment instead of the second segment increases the distance between the electromagnetic force and the soft joints, resulting higher bending moment and therefore higher deformation. Since the joint between the segments 1 and 2 are stiff, these segments move together with the same deflection angle (see Figure 5.20b). Similarly, when the third joint (the joint between the last segment and the clamps) was softened, the device acted as rigid beam with a deformable region closed to the clamps (see Figure 5.20c). All segments had the same deflection angle as the joints between them were very stiff. Due to the variation between their widths and the heat distribution during the actuation, the joints had different deflection angles, e.g. the wider width design and more localized temperature distribution caused smaller deformation in the third joint.

After each joint was independently deformed, latched, and recovered at different LMC currents. The device was tested in a sequential bend-and-latch experiment. Figure 5.21a shows the sequence of the LMC and the heating currents during the consecutive bend-and-latch deformation of the joints. During the test, the 3rd, 2nd, and 1st joints were softened in an order while the 1st segment was actuated in all cases. The current of this segment was positive when the first and the third joints were deformed and was negative when the second joint

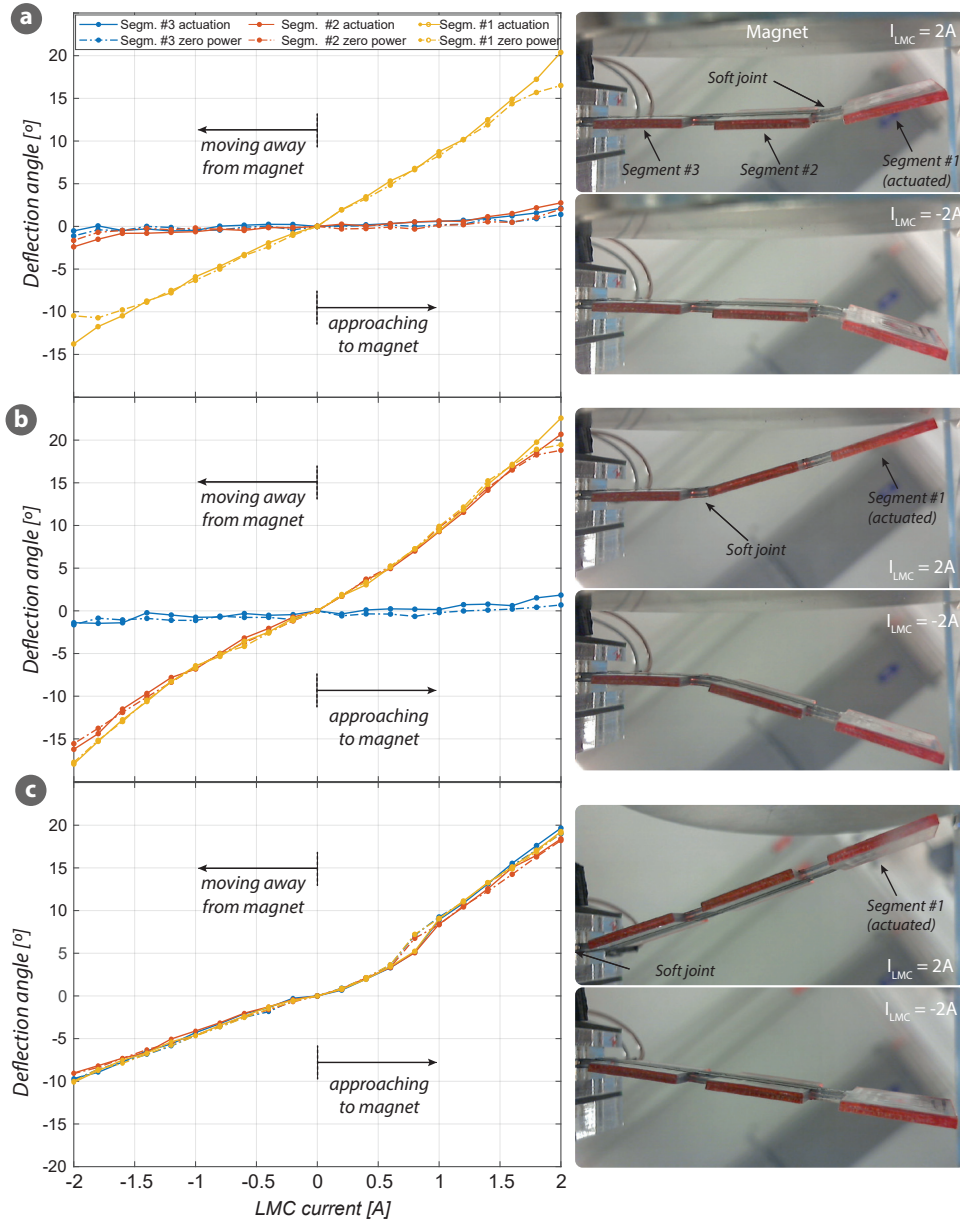


Figure 5.20: Experimental results showing the bending and latching of the joints. a) The deflection angle of the segments are plotted as function of the LMC current when the first joint was softened and the first segment was actuated. The segment approached to the magnet when a positive current is applied to the LMC and moved away from the magnet for the negative LMC current. The deformation in the approaching cases was higher due to the higher magnetic field. The unaddressed joints were very stiff and therefore had very small deformation. The joint had high shape fixation for LMC current $< 1.5A$ and slightly decreases above $1.5A$ of the LMC current. b) The graph shows the deflection angle of the segments when the second joint was softened and the first segment was actuated. Actuating the first segment instead of the second segment increases the distance between the electromagnetic force and the soft joints, resulting higher bending moment and therefore higher deformation. As the joint between the 1st and 2nd segments were stiff, they moved together with the same deflection angle. c) When the third joint (the joint between the last segment and the clamps) was softened, the device acted as a rigid beam with a deformable sections closed to the clamps. All segment had the same deflection angle as the joints between them are rigid. Due to the variation among their widths and the heat distribution during the actuation, the joints had different deformations.

was addressed. This current profile deformed the 1st and 3rd segments in the same directions while the 2nd segment moved in the opposite direction.

The initially flat device was first bent around the third joint in upward direction and subsequently latched (see the second image in Figure 5.21b). The joint was softened with 500 mW of heating power and the segment was actuated with 2A and latched. Then the second joint was softened with $P_{heating} = 550\text{ mW}$ and bent in the downward direction with $I_{LMC} = -2\text{ A}$. After latched in this position, the first joint was deformed in the upward direction ($P_{heating} = 500\text{ mW}$ and $I_{LMC} = 2\text{ A}$) and latched. Figure 5.21b shows the deformation profiles of the device after each step.

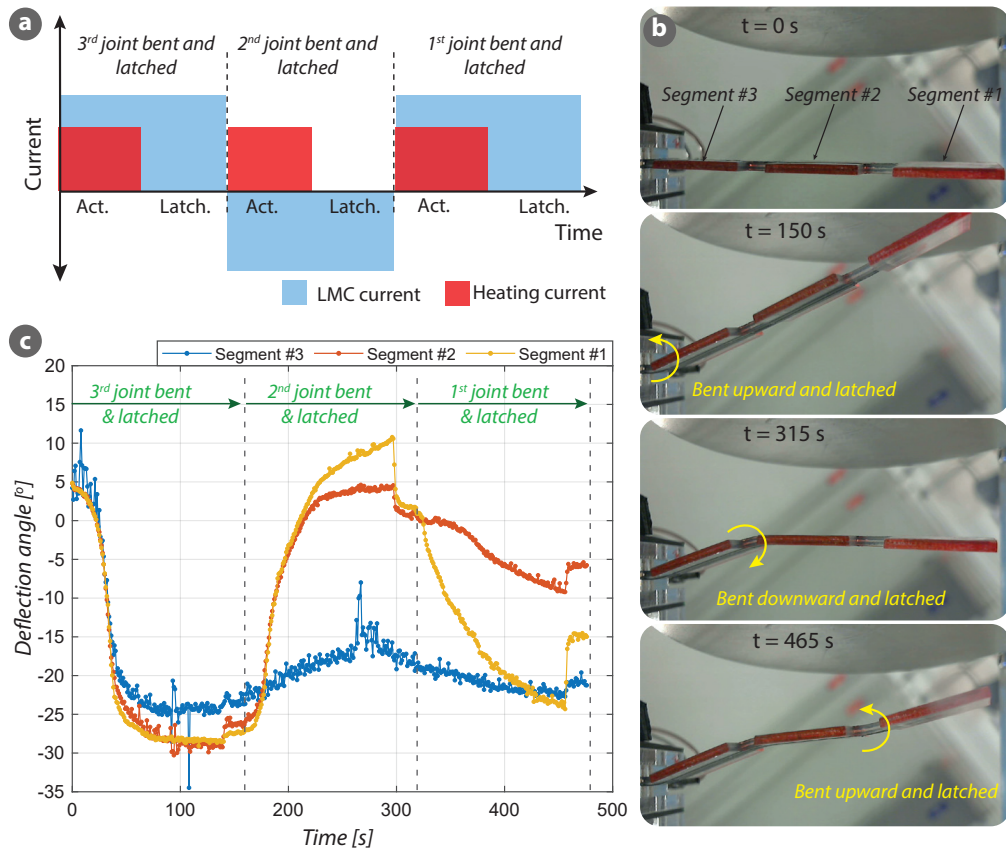


Figure 5.21: Three joints of the device were sequentially bent and latched. a) The sequence of the LMC and heating currents during the consecutive deform-and-latch operations. A positive LMC current was applied during the deformation of the first and the third joints whereas a negative LMC current was used to deform the second joint. This bent the 1st and 3rd segments in the same direction and the 2nd segment in the opposite direction. b) The initially flat device was first bent around the third joint in upward direction and subsequently latched. Then the second joint was softened and bent in the downward direction. After latched in this position, the first joint was deformed in the upward direction and latched. c) The deflection angle of the segments during these steps were extracted from the recorded videos. When the 3rd joint was softened, all segments deflected with the same angle as the joint between them were very stiff. Similarly, when the second joint was softened, the 1st and 2nd segments had the same deflection angle.

The deflection angle of the segments during these bend-and-latch operations were extracted from the recorded videos and shown in Figure 5.21c. When the 3rd joint was softened, all segments deflected with the same angle as the joint between the segments were stiff. All segment deflected with an angle between 25-30° and this deformed state was latched with a small relaxation. Similarly, when the second joint was softened, the 1st and 2nd segments moved with the same deflection angle, going from -30° to 5-10°.

Small difference in the latching performance of the joints was observed. As seen from Figure 5.21c, the 3rd joints has better latching than the other joints. This is due to long distance between the actuated segment and the soft joint. As this distance increases the heat transfer between the actuated segment and the joint decreases. The smaller the cross-heating the better latching of the joints.

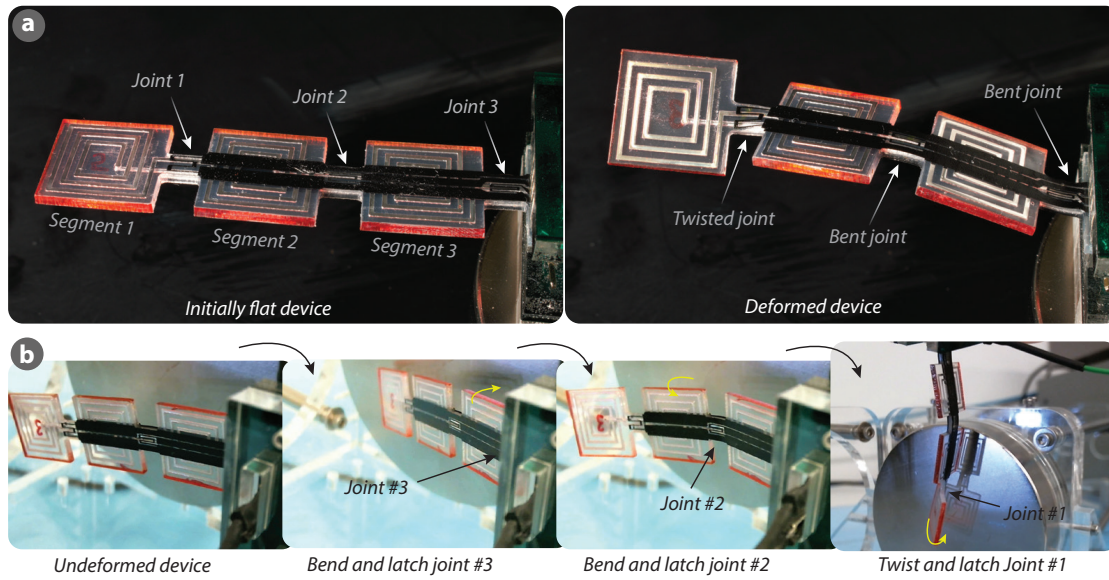


Figure 5.22: Various complex shapes can be achieved by combining the torsional and bending deformations. a) An initially flat device is deformed by two bend-and-latch and followed by a twist-and-latch operations. In the deformed shape, the first joint is twisted whereas the other joints are bent. b) Images captured by the second camera show the intermediate steps of these deformations. To achieve the torsion instead of bending, the device is repositioned.

As the type of the deformation can be individually controlled for each joint, complex shape transformations are achievable. The joints can bend or twist depending on the direction of the magnetic field. Figure 5.22a shows an initially flat device (the left image) which later on morphed into a complex shape by deforming and latching through its joints (right image). The deformed shape was achieved by two bend-and-latch and one bend-and-latch operations. A sequence of the captured images during this shape transformation is shown in Figure 5.22b. The device was first deformed bent through the 3rd joint and latched. Then the 2nd joint was bent in the opposite direction of the first bending and subsequently latched. The device was repositioned with respect to the magnet to allow the torsional deformation. The first joint was softened and twisted, and followed by a final latching. As the device allows independent

actuation and latching, the final deformed shape of the device includes both the bending and the torsional deformations.

5.7 Picking up objects by sequential deform and latch operations

The fabricated devices were used to pickup objects by sequentially deforming and latching through the different joints. This enabled both the alignment of the device with the objects orientation and also a firm holding. Figure 5.23a shows the pickup of an object with a weight of 37.5 g. To match the slit orientation of the object, the first segment the beam was twisted by 20° around z-axis and subsequently latched in this deformed configuration. After the latching, the device was manually lowered. Then the second joint was softened by the Joule heater and twisted in the opposite direction of the first rotation. Once the joint is latched in the desired deformed states, the device was pulled up to lift the weight. The latched state of the device is stable and robust enough to hold weights more than 250 g (see Figure 5.1b).

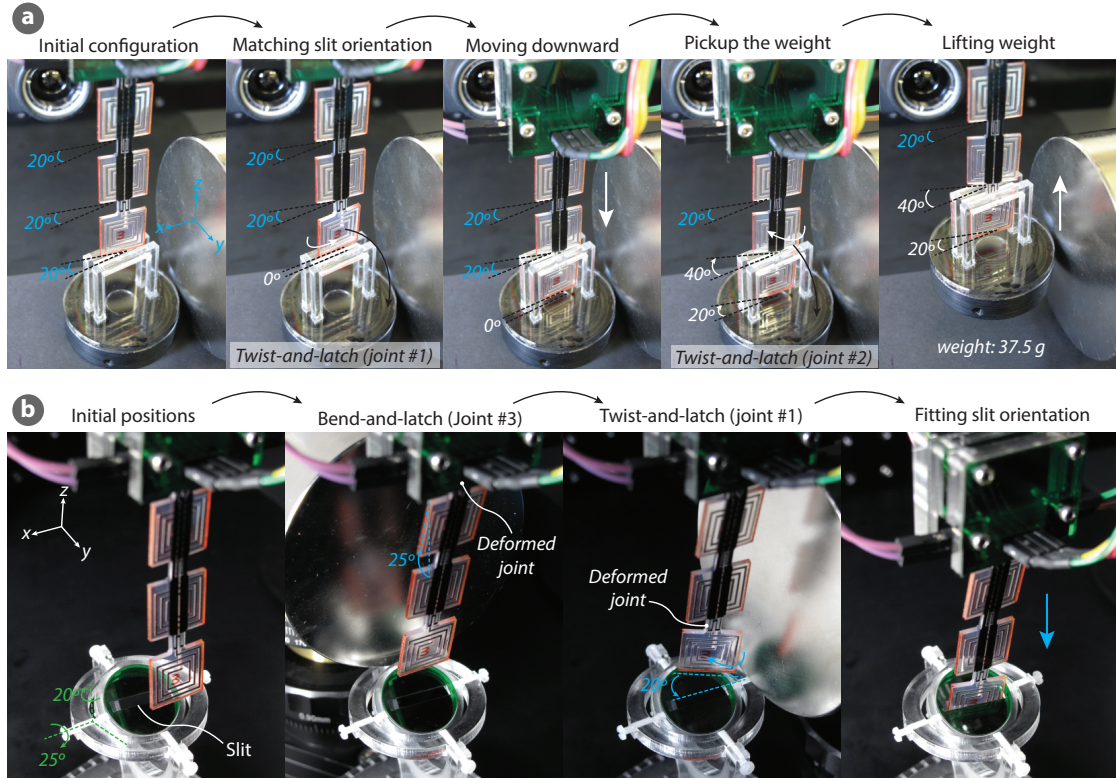


Figure 5.23: Picking up objects and matching the different orientations by complex deform and latch operations. a) An initially flat device deforms and latched through its different joints to match the orientation of the object and to securely lock it for grasping. b) The joints of a flat devices was sequentially bent and twisted to match a slit orientation of a PMMA piece.

Individually controlling the deformation of the joints allows more degrees of freedom to easily manipulate the objects with different orientations. A PMMA piece with a slit was placed on a

gyroscope-like structure and was rotated with an angle of 25° around x-axis and 20° around z-axis. The beam was initially flat and placed longitudinally along the z-axis (its surface normal is parallel to the y-axis). As the slit was orientated about 2 axes, a single deformation is insufficient for a perfect match. To do this, the device was first bent with an angle of 25° through its third joints and was latched. For a complete fitting, the device was twisted through another joint while the deformation of the first joints was locked throughout the second actuation. For the second deformation, the first joint where it was twisted with an angle of 20° . Once the device configuration matched with the slit orientation the device was lowered down manually to demonstrate the fitting. Here we have shown two sequential deform-and-latch operations using the first and the third joints. Multiple distinct deformations can be achieved by changing the sequence and the type of the deformation of each joint.

5.8 Experimental validation of the model

We compared the model predictions with the experimental data obtained from the torsion tests (see Figure 5.17). We compared both actuation and zero-power deformations. For the numerical model, we used the actuation temperature as 110°C and the latching temperature of 60°C . The shape fixation of the MM7520 at this temperature was assumed as 95%. The temperature during the experiments were measured by the IR camera. We used an average temperature value for the soft joint by averaging the temperature across the width of the joint. As the Young's modulus of the SMP material is not linearly proportional to the temperature, this averaging may induce some error in the calculation.

Figure 5.24 compares the model output with the experimental results. The model output and the experimental data overlap nicely for the LMC current $< 1.5\text{A}$. The joint latches the deformation with high shape fixation ratio in this region. As the LMC current increases, the latching temperature also increases. This temperature increase reduces the latching performance. As a result, the actuation deformation is latched with lower shape fixation ratio.

At high LMC current ($> 1.5\text{A}$), the experimental results show higher deformation than the model prediction. This is mainly due to undesired softening in the other joints. As we measure the deflection of the bottom segment, the small deformation in the other joints contributes to this deformation. Additionally, the averaging of non-uniform temperature distribution in the joints, the assumption we made in the modeling, i.e. a constant shape fixation of 95%, the accuracy of image process to extract the deformation may also contribute the deviation between the experimental data and the model prediction.

5.9 Stiffness measurement of the joints

When the device is latched at room temperature, the SMP layers become very stiff. Due to the location of the SMPs on the opposite sides of the device (SMP+PDMS+SMP), the device has high stiffness. This configuration enables high blocking force and therefore can withstand high

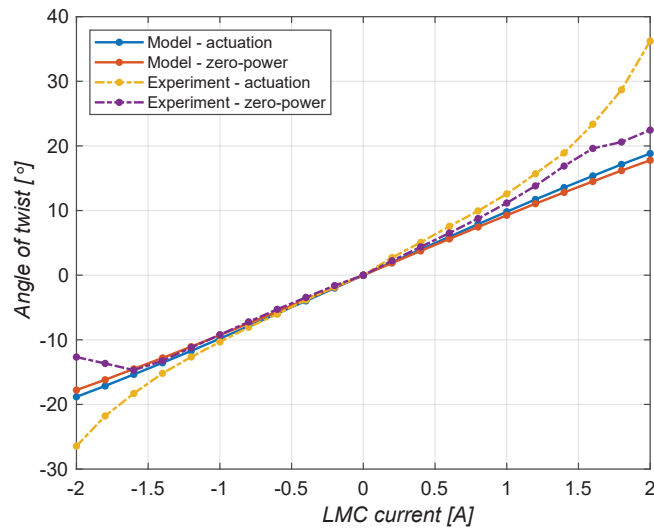


Figure 5.24: The model predictions are compared with the experimental results for the torsional deformation. The model prediction and the experimental data overlap for the LMC current smaller than 1.5A. Both data shows a good latching performance in this current range. As the LMC current increases, the latching temperature also increases which decreases the shape fixation ratio. At higher LMC current ($> 1.5A$), the experimental results are higher then the model prediction. This is mainly due to undesired of softening in the other joints at higher LMC current but also due to non-uniform temperature distribution in the joints, inaccuracy of the image process, and the assumptions of the modeling.

external loads. We measured the blocking force of the joints at the room temperature using a load cell attached to the motorized state. One end of the joint was clamped between two rigid PMMA plates. We applied the displacement to the free tip of the joint (in the direction of the surface normal) and measured the force.

Figure 5.25a shows the blocking force of the joints as a function of their tip deflection. The joints have blocking forces between 400-500mN while undergoing a tip displacement of 1 mm. The wider joints has higher forces; $F_{joint3} > F_{joint2} > F_{joint1}$. Having high blocking forces allows these devices to be used in load-bearing applications where they can withstand high external load without while maintaining their deformed shapes.

Figure 5.25b shows the deformation of the joint as it was deformed at the room temperature. The joint was clamped from its top edge and the force is applied at the bottom edge of the joint. The joint is composed of a thick PDMS layer (1.59 mm) and two SMP layers (each 65 μ m thick). The shear (ϵ_{xy}) and the longitudinal (ϵ_{yy}) components of the strain are mapped on the deformed joint. The strains in the PDMS layer are much higher than the strains in the SMP layers. The PDMS layer has both shear and normal strains around 10% whereas the strains in the SMP layers fluctuate around 0%. This is due to very high stiffness ratio (more than 1000) between the SMP and the PDMS layers.

When the SMP layers become very soft at the high temperature, the joint undergoes a bending deformation under the same loading conditions. Figure 5.25c shows the images of the deformed joint at 90 °C. Comparing with the cold-state deformation in the panel b, the joint has a significantly different deformation shape. Since the SMP layers are very soft, it becomes easy to deform them. The deformed images and the strain maps show the high deformation in the SMP layers. The maps of the longitudinal strain component (ϵ_{yy}) shows the tensile and the compressive sections of the joint where the SMP layers has the highest tensile and compressive strains as they are located at the outside of the device.

5.10 Conclusion and Outlook

In this chapter, I presented the soft electromagnetic beams capable of deforming in different directions and able latch in any given deformed state. This combines multiple degrees of freedom and latching ability in a single device. The fabricated device can morph into very complex shapes by large and distinct deformation of each joint. A shape transformation consisting of hybrid deformations of torsional and bending is shown in Figure 5.1. At the latched states, this device becomes very stiff and enables higher blocking forces, e.g. a joint can withstand a load of 400 mN while deforming less than 1 mm.

The multifunctional shape manipulations can be further exploited for applications including soft grippers with large grabbing force, reconfigurable antennas, and deployable biomedical devices. Soft electromagnetic materials composed of elastomer shell and liquid-metal have drawn great interest recently due to their operation at very low voltages, high conductivity, and

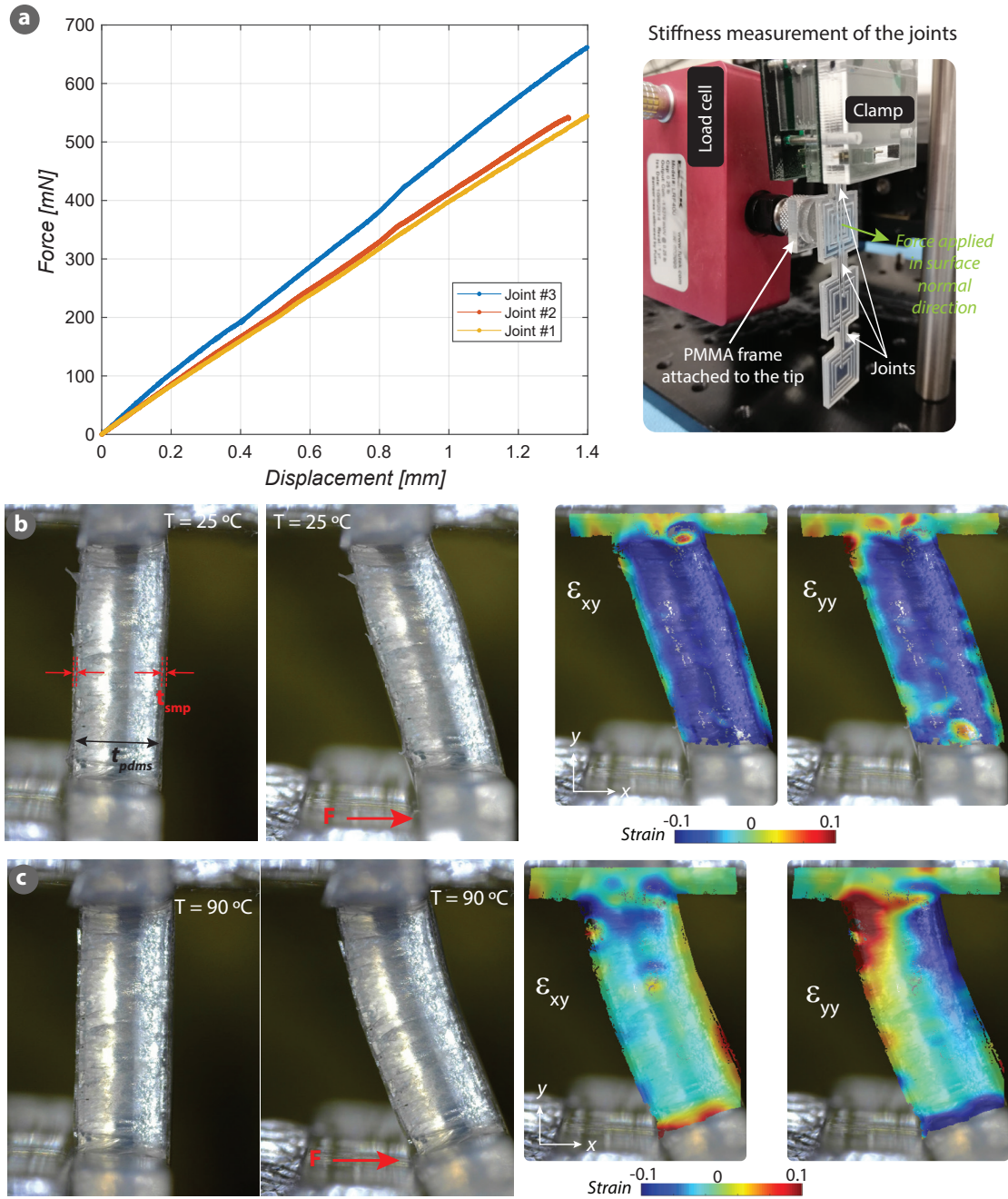


Figure 5.25: The stiffness measurement of the joints and their deformation analysis at room and elevated ($90\text{ }^{\circ}\text{C}$) temperatures. a) The blocking force of the joints is plotted as a function of the tip displacement. The joints have a blocking force between 400-500mN for the displacement of 1 mm. b) The micrographs shows the side view of the joint as it is deformed at the room temperature. The region in focus is the side view of the joint whereas the clamp and the tip of the load cell are not in the focus. The joint was clamped from the top edge and the displacement was applied to the bottom edge. At room temperature, the joint undergoes a shear deformation whereas at $90\text{ }^{\circ}\text{C}$ the joint has a bending deformation. The strain components are mapped on the deformed images to compare their deformation at different temperatures. At room temperature, the SMP layers has smaller strains (ϵ_{xy} and ϵ_{yy}) than the PDMS layers, indicating the large deformation occurs in the PDMS layer. c) At $90\text{ }^{\circ}\text{C}$, the SMP layers are very soft (easy to deform them) and the joint undergoes a bending deformation where the SMP layers has the highest tensile and compressive strains.

tunable electromechanical properties. However, these actuators cannot fix their deformation as they need a constantly applied current, which is highly energy inefficient. Additionally, the materials used in these actuators are very soft (with Young's modulus less than <1 MPa), which is very suitable for handling fragile and soft objects. In other hands, in many practical applications, such as soft robotic grippers and morphing antennas, it is highly desirable that the actuated shape can be locked with high enough stiffness so that the material can fulfil certain functions requiring high supporting or self-supporting force without the constant presence of external power. [20] In these scenarios, shape memory polymers with adjustable stiffness and with shape memory effect can greatly serve to meet the requirements.

The current version of the device demonstrates its main abilities such as selective actuation, latching, multiple deformations in each joint. There is still rooms for improvement. Here, I list a few design suggestions that will improve the deformation and increase the actuation speed.

Joint geometry

The current design has joints with variable widths (4-5mm) but a constant length (5 mm). Due to this variation in the widths, the joints have different deformation amplitudes for the same heating and actuation parameters. The length of these joints can be varied to compensate the width variation. For example, increasing the length of the wide joint decreases its bending and the torsional stiffness. This way, the deformation of the wider joints can be increased.

Identical heaters

Due to design restrictions, the heaters are not identical in the current design, e.g. the heaters of the 1st joint are wider than the others. Therefore, the first joint heaters provides more uniform temperature distribution over the joint area whereas the temperature of the other joints are more localized. Since the temperature of the outer regions are not high enough in the localized heating, the joints are relatively stiff and the deformation in these joints are small.

The heaters and the leads can be separated by putting an additional insulation layer between them. This way, the heater can be designed for more uniform heating without any design constraints due to leads. This however increases the complexity and the fabrication of the device.

Location of the heaters

In the current design, the heaters are placed on the top of the SMP layer. Since one side of the heaters is in contact with the air, a considerable amount of heat dissipated to the air through convection. This makes the heating less efficient. The heating efficiency can be improved by embedding the heaters in the SMP layer. Since the SMP covers the both side of the heater, the heating is more efficient and the temperature distribution is more uniform.

Carbon-based SMP heaters

We used acrylic based heaters in our devices. These heaters have low electrical conductivity around 0.644 Sm^{-1} . Therefore, we need to use high voltage for heating; between 0.5 to 1 kV. Carbon-black loaded SMP can be used for this purposes. By adjusting the carbon to SMP ratio

we can tune the conductivity of the heaters and can reduce the heating voltage. Using the SMP based heaters will also enables a good bonding between the heaters and the SMP layers. This can prevents any delamination problem related to difference between the thermal expansion coefficients of the materials.

6 Conclusion and Outlook

This chapter summarizes the contributions of this thesis to the field of soft actuators, and presents an outlook on future work.

6.1 Conclusion

6.1.1 SMP based latchable microfluidic valve arrays

We demonstrated that an array of microfluidic valves can be controlled using a pneumatic pressure source and a control board. The valves are addressable by Joule heating and can be latched in a given state. The joule heating allowed us to switch from pneumatic controller to electrical controller for addressing each unit in the array and this simplified the design for scaling. The technology is demonstrated with a reagent mixer and a peristaltic pump, where several valves were operated successfully at the same time.

The temperature of the working liquid is a critical aspect when combining these microfluidic valves with biological samples. We measured the fluid temperature using a PT100 temperature sensor inserted in the outlet tube when the valve was operated in a cyclic mode for more than >3000 cycles. A temperature less than $<1^{\circ}\text{C}$ was measured, indicating the suitability of this technique for high throughput screening of living cells.

6.1.2 Reprogramming the shape of the dielectric elastomer sheets

In this study, we developed dielectric elastomer actuator sheets that can achieve multiple distinct deformations and also can lock their deformed shapes into place using thermo-responsive shape memory polymers. The SMP fibers were used as a latching mechanism, allowing holding a given actuated position without consuming power and therefore leading to much longer lifetime in stationary conditions. The improved shape functionality of the dielec-

tric sheet is demonstrated by gripping objects with different shapes, which is challenging with just one shape transformation. This methodology can be implemented into bending structures, i.e. soft grippers, where multi-degrees of freedom enables more conformal wrapping of different objects.

A numerical model was developed to optimize the performance of the multi-morph DEAs. The model gives the crucial information on the design parameters to achieve high actuation deformation and high blocking forces. The models can be easily adapted for the multistable bending actuators to optimize their actuation, latching, or load-bearing capacities. Reconfigurable and latchable shape-morphing dielectric elastomers can be applied to soft robots to create to enable novel capabilities, e.g. reconfigurable wings and legs to adapt to different terrain or missions. The method developed here can augment the degrees of freedom of dielectric elastomer actuators without the need of multiple high power supplies.

6.2 Latchable multi-degree of freedom electromagnetic actuator

In this study, we present the soft electromagnetic beams capable of deforming in different directions and able latch in any given deformed state. This combines multiple degrees of freedom and latching ability in a single device.

The fabricated device can morph into very complex shapes by large and distinct deformation of each joint. Additionally, the actuated device can be latched in any given shape providing high energy efficient soft electromagnetic devices. These shape programming method can be used in conjunction with other soft robotics, such as pneumatic ones, where independent control multiple segments may be beneficial.

6.3 Outlook

6.3.1 Stretchable electromagnetic pump

The deformation of the soft electromagnetic actuators can be controlled by either the direction of the current or by the direction of the magnetic field. This makes it convenient to develop antagonistic actuators with very simple designs. This idea is illustrated with a conceptual design of a stretchable pump shown in Figure 6.1.

The pump consists of one chamber and two silicone diaphragms with embedded liquid-metal coils. The working principle of the pump is based on these reciprocating silicone membranes working in an antagonistic way (moving in the opposite direction under the same magnetic field and current). The diaphragms are made of liquid-metal coils buried in a silicone shell. These liquid-metal coils are connected in series with reverse polarity so that the current flows in the opposite directions in the coils. When these diaphragms are addressed with a current (I_{LMC}) in a magnetic field, they move in the opposite directions as shown in Figure 6.1b. The

inlet and the outlet can be designed to allow one-way fluid transfer to create net flow. When the pump chamber is inflated, the liquid is sucked into the chamber. Since the inlet valve deforms freely during this inflation, the liquid is transferred from the inlet. The valve at the outlet is mechanically blocked during this operation and therefore now flows from the outlet into the chamber. The inflation is then followed by the deflection by reversing the current. The liquid in the chamber is now pushed out through the outlet channel whereas the movement of the inlet valve is blocked this time. This inflation-deflation cycle can be repeated with high frequencies to generate high flowrates.

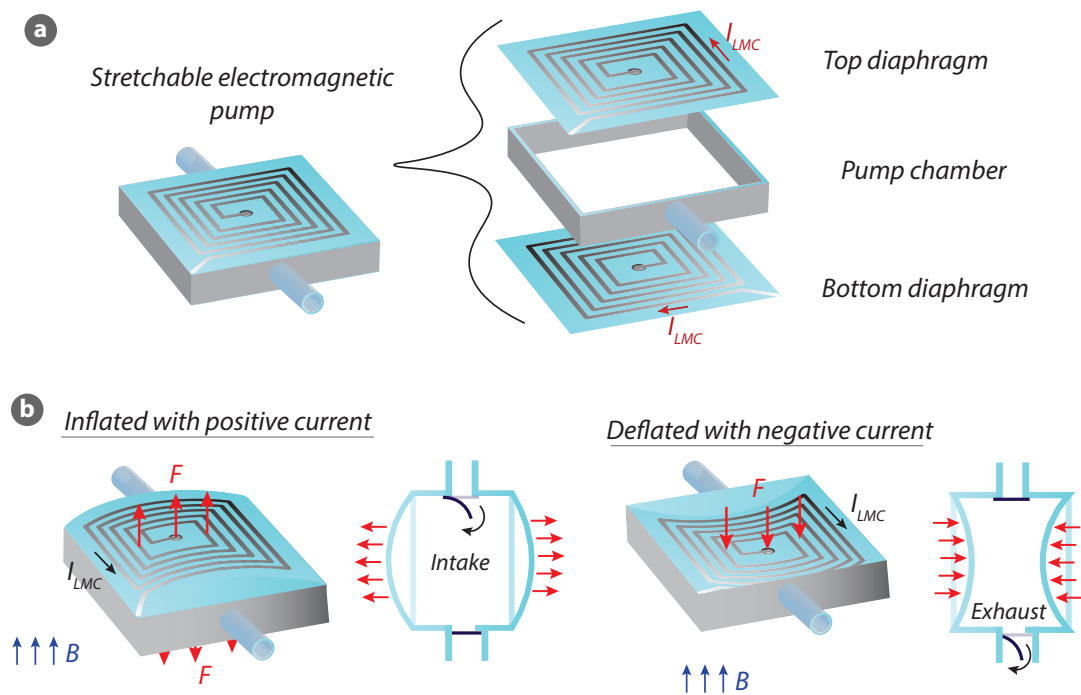


Figure 6.1: Stretchable electromagnetic pump made of liquid-metal coils and silicone structure. a) The pump consists of two antagonistic diaphragms and a silicone chamber. b) Due to the direction of the current in the top and bottom diaphragm, they move in the opposite direction when actuated in a magnetic field. The inlet and outlet valves allow one-way liquid transfer. Actuating these diaphragms at high frequency results in high flowrates.

The pumps can be completely made of stretchable materials. This would ease their integration with soft robotics applications. Two pumps connected in series, for example, can mimic the atrium and the ventricle of the heart which can perform the opposite intake and exhaust. They can be simply driven by single source of current, reducing the complexity of the fabrication and the experimentation.

6.3.2 SMP for tunable boundary conditions

Shape memory polymers generally have high shape fixation ability and they can withstand various loading and temperature conditions while maintaining their structural integrity. How-

ever, shape memory polymer actuators are relatively slower, having time constants of the order of seconds. This makes them less preferable in high speed applications. One way to take advantage of their shape programming ability without slowing down the actuation speed is to use them as a structural material for tuning the boundary condition rather than using them as a part of the actuation mechanism. Therefore, the actuation can be carried out independently of the SMP. This idea is conceptually illustrated with a reconfigurable buckling actuator (e.g. mirror) in Figure 6.2.

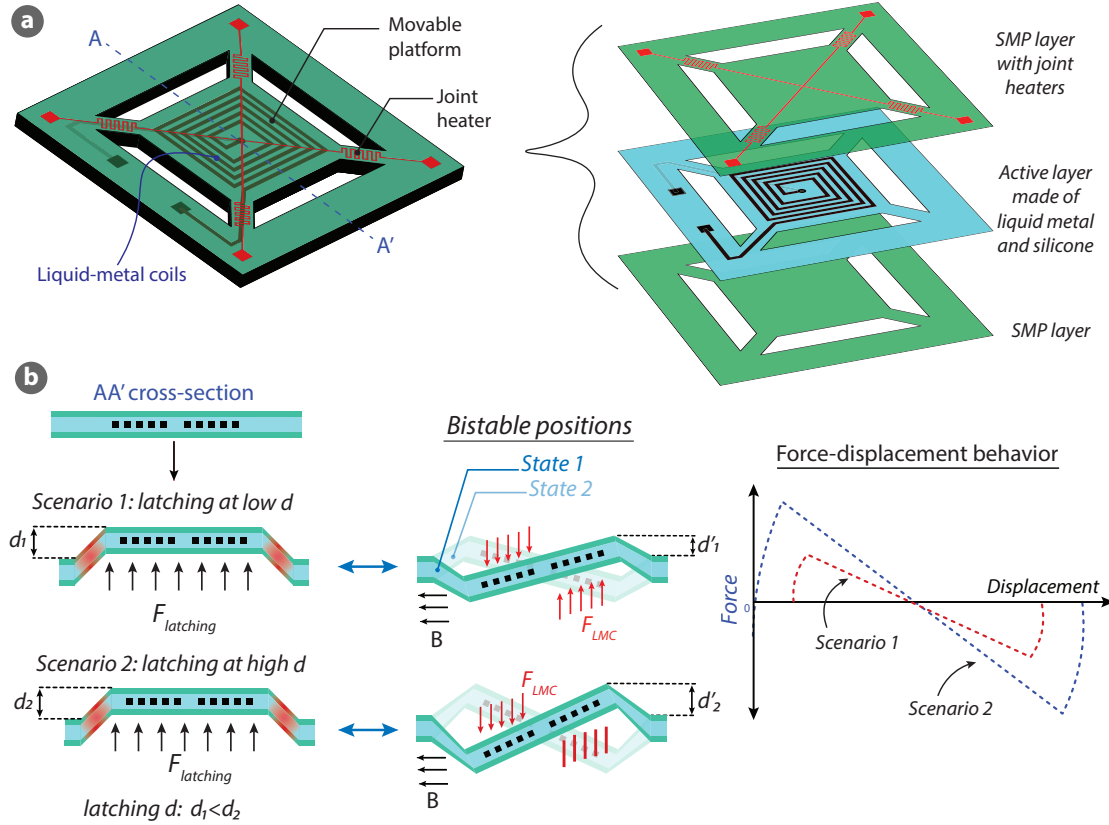


Figure 6.2: Reconfigurable buckled actuators using SMP and liquid-metal. a) A schematic of a buckling actuators with a movable platform and deformable (buckling) hinges. The platform accommodates the liquid-metal coils to generate electromagnetic force. The SMP layer with joint heaters allow to deform and fix the deformations in the joints to adjust the boundary conditions for the force and displacement behavior. b) The force-displacement behaviour of the buckling actuator can be tuned by deforming and latching the joints at different deformation amplitude. The buckling mode of the actuator is shown for the horizontal magnetic field.

The boundary conditions of this actuator can be modified after it is fabricated, allowing to

- 1) to change its the force-displacement behavior
- 2) to change the buckling modes (buckled shapes)

The actuator is composed of a movable platform connected to the rest of the device through the joints. The movable platform accommodates the liquid-metal coils and is stiffer than the joints to allow the force exerting on the platform to generate deformation in the hinges mostly

(negligible deformation in the platform). The joints have local heaters to locally soften the joint sections when programming their deformation. The deformation of the joints can be fixed at different amplitudes. This allows us to tune the force-displacement behavior of the device. Figure 6.2b schematically demonstrates the shape fixation of the joint at two different deformation amplitudes (d_1 and d_2) and their bistable deformation profiles for a horizontal magnetic field.

As the shape memory polymers are deformed and latched before the buckling actuation (they are not softened during the actuation), the actuator can operate at higher frequencies. Additionally, such a device can be fabricated monolithically (by deforming and latching of SMPs) without the need of the fixed or rigid frames. The buckling mode can be also controlled by changing the direction of the external magnetic field or the current in the liquid metal channels. The schematic in panel b shows the buckling mode for the horizontal magnetic field only.

A Thermo-mechanical analysis of SMP and SMP+SEBS+CB/PDMS

The bare SMP and the tri-layer of SMP+SEBS+CB/PDMS exhibit similar mechanical behaviour at different temperatures. The Young's modulus of the SMP is very high compared to the other membranes and it dominates the overall stiffness of the diaphragm (see Figure A.1).

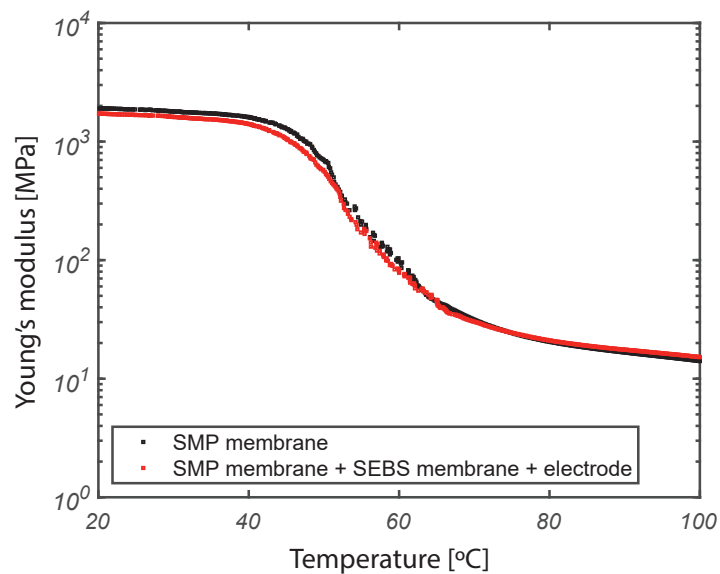


Figure A.1: Measured Young's moduli of a bare SMP layer and a layer of SMP+SEBS+CB/PDMS as functions of temperature.

Figure A.1 shows the dynamic mechanical analysis of a single layer SMP and a multi-layer of SMP+SEBS+CB/PDMS (DMA Q800 from TA instruments). The SMP material used here exhibits more than a hundred-fold change in Young's modulus between its cold glassy state ($<40^{\circ}\text{C}$) and its hot rubbery state ($>70^{\circ}\text{C}$), with a negligible influence from the SEBS and CB/PDMS layers.

B Latching planar DEAs at different time scales

Figure B.1 shows the latching performance of an SMP integrated DEA over different time scales, from a few minutes to several days. The device consists of 2 dielectric membranes, 2 high voltage electrodes (for DEA) and 1 ground electrode. The ground electrode made of conductive SMP materials and serves as 1) high ground terminal for DEA actuation and 2) Joule heating for SMP softening. The conductive SMP is softened by applying a small voltage across the ground electrode (the shape of the ground electrode is shown in the inset in Figure B.1 panel a). Once the SMP is soft, high voltage is applied to the HV electrodes and the DEA is actuated. Once the deformation is achieved the heating is turned off to enable the latching process and subsequently the high voltage is removed. Figure B.1 shows the evolution of strain over different period of time.

Appendix B. Latching planar DEAs at different time scales

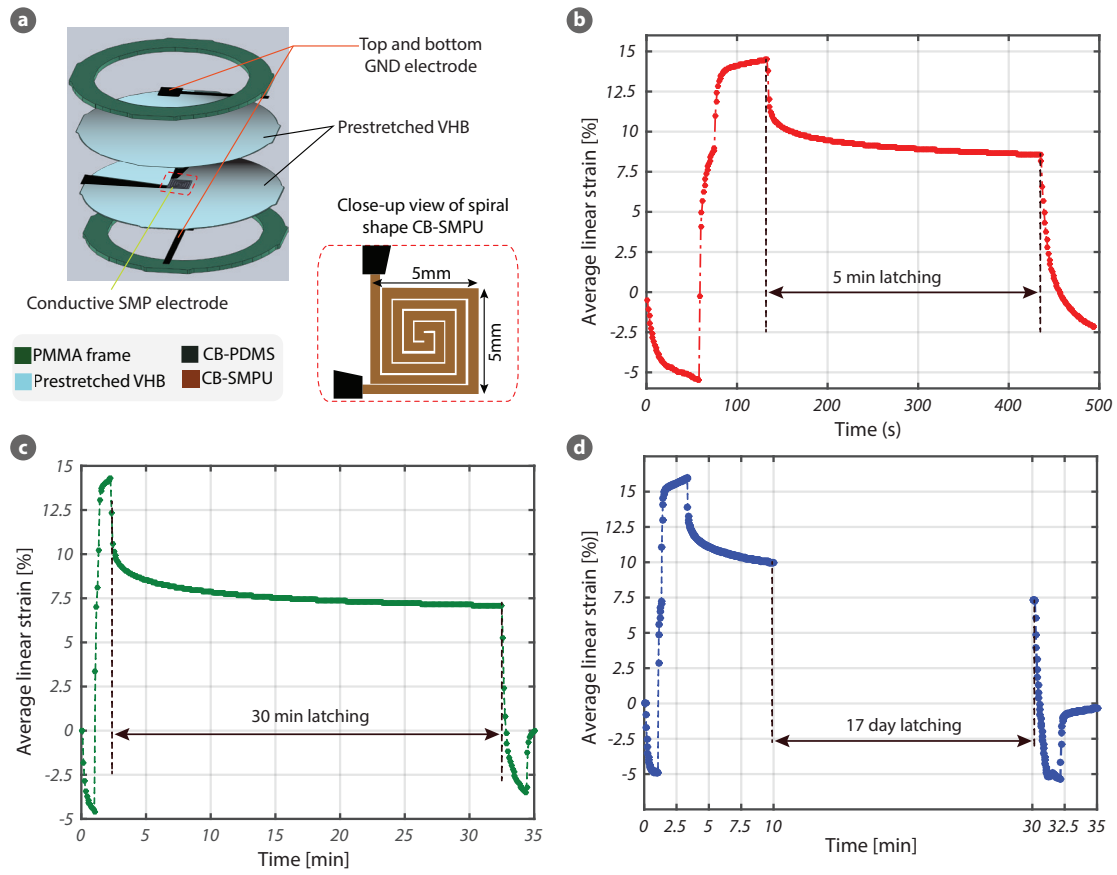


Figure B.1: Strain evolution in a latched DEA at different time scales.

C DMA of the membranes of the reconfigurable DEAs

The Young's moduli of the membranes at different temperatures were measured using a dynamic mechanical analyzer (DMA Q800 from T.A. Instruments). Figure C.1a shows the storage and loss moduli, and tangent delta of the SMP membranes (MM4520 from SMP Technologies) as functions of temperature. The Young's moduli of AR-care 90366 (used as DEA and Joule heating electrodes), VHB 9460PC (used as electrical insulators) and VHB 9473PC (used as dielectric membrane) are plotted vs. temperature in Figure C.1b. Sweeping the temperature from 25 °C to 70 °C reduces the stiffness of the SMP by more than 200 times while the stiffness of the other materials decreases by approximately three times.

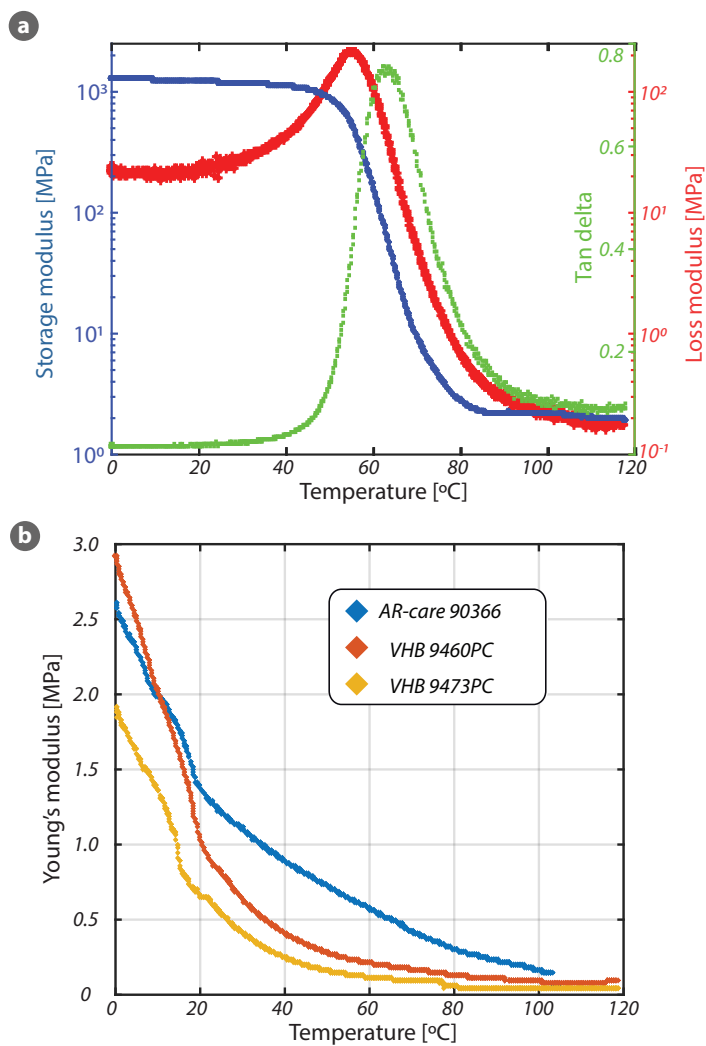


Figure C.1: Thermo-mechanical characterization of the membranes of the reconfigurable DEAs. a) The change of the storage and loss moduli, and tangent delta of SMPs vs. temperature. The stiffness of the SMP changes drastically with a small temperature change around its glass transition region. b) The Young's moduli of the AR-care 90366 (electrode material), VHB 9460PC (insulation layers), and VHB 9473PC (dielectric membrane) plotted as a function of temperature.

D Modeling the actuation and latching of SMP integrated DEAs

This appendix explains the basic concepts of modeling the multistable dielectric elastomers. The modeling idea of the actuation and latching deformations is first introduced for a simplified symmetric structure under uniaxial loading. I then go into detail about the multistable bending DEAs where I draw an analogy to beam deflection.

The critical part here is modeling the shape memory polymer (SMP) layers as they have different stress-strain-temperature behavior than the materials without shape memory effect. for simplification, we assume that the SMP we used has a shape fixity ratio of 100% and completely recover its initial state.

Figure 4.9 shows the evolution of the stress and the strain of mechanically coupled membranes. The structure consists of an SMP layer and two other layers that do not exhibit shape memory effect (a symmetric structure). For the simplification, the deformation is applied in the longitudinal direction (no bending). As the membranes are coupled, both membranes always have the same longitudinal strain (see the strain column). The tensile stress in these membranes, however, depends on their shape memory properties and their Young's moduli. For linear elastic membranes, the stress is related to their instant strain and their Young's moduli at that temperature (see the blue stress column). However, the stress in the SMP depends on not only their instant strain but also the strain at which they fix their deformation (see the red stress column).

The structure is in a mechanical equilibrium for the states shown in Figure 4.9b. The force equilibrium of the actuation state (hot) can be written as (using the linear elastic model):

$$\epsilon_{act} Y_{s,hot} + \epsilon_{act} Y_{o,hot} = F_{applied} \quad (D.1)$$

where ϵ_{act} is the actuation strain, Y is the Young's modulus, $F_{applied}$ is the force applied to the membranes in the longitudinal direction. Subscripts s and o stand for the SMP and for the other materials which do not have shape memory effect. We can find ϵ_{act} by substituting the

Appendix D. Modeling the actuation and latching of SMP integrated DEAs

force value and the material parameters at the elevated temperature (hot).

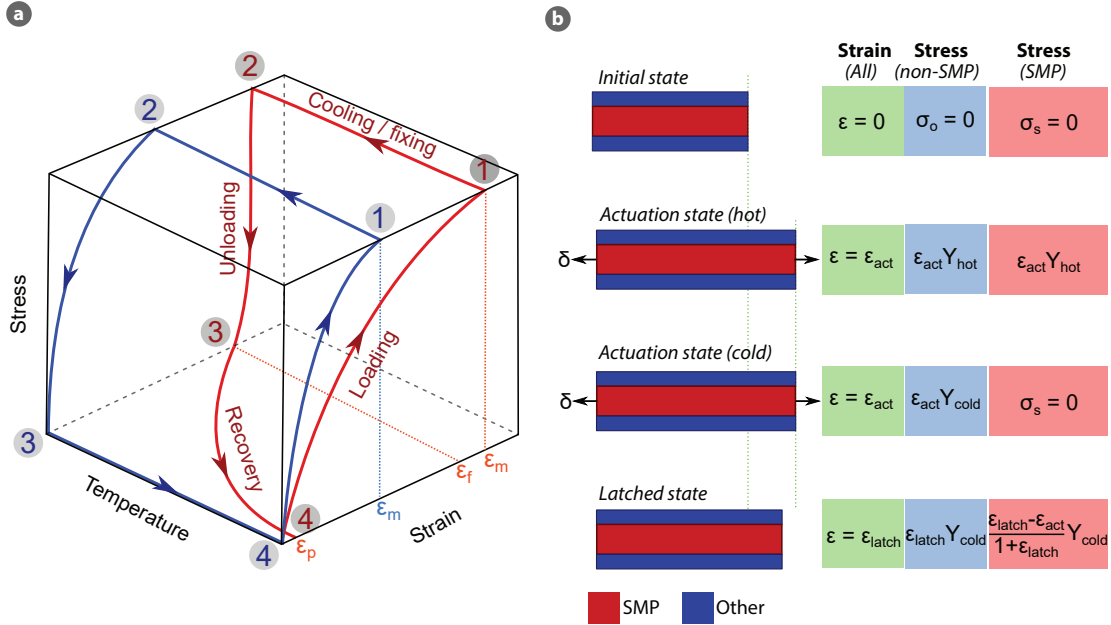


Figure D.1: a) The stress-strain-temperature behaviours of a thermo-responsive SMP material (in red) and a material without shape memory effect (in blue) are schematically represented as they are loaded, cooled, unloaded, and finally recover. The SMP materials can fix their deformed shape upon cooling whereas the other materials (non-SMP) do not exhibit this behavior. b) The evolution of stress and strain in a mechanically coupled structure (1 SMP layer + 2 materials with no shape memory) as it undergoes different temperature and loading states. Since both materials are bonded together, they have the same longitudinal strain in all states (see the green strain column). The red and the blue stress columns correspond to stress in the SMP material and in the material that does not have shape memory ability, respectively. This simplified stress-strain-temperature approach is adapted for our analytical model of the bistable dielectric elastomers.

When the structure is cooled down at a fixed deformation the stress in the SMP material approaches to 0 (assuming the shape fixity of 100%) whereas the other layers are still under a tensile stress. When the external constraint on the structure is removed, the structure finds a new equilibrium state where the SMP has compression stress and the other layers have tensile stress. In the equilibrium state, the sum of the forces due to these stresses is equal to 0 (no external force), so we can write the force equilibrium as:

$$\frac{\epsilon_{latch} - \epsilon_{act}}{1 + \epsilon_{latch}} Y_{s,cold} A_s + \epsilon_{latch} Y_{o,cold} A_o = 0 \quad (D.2)$$

where ϵ_{latch} is the strain stored in the device after the external constrain is removed (referred as latched strain). For this equation, we used the Young's moduli of the materials at the room temperature (cold) and ϵ_{act} here is the strain found in Equation D.1. ϵ_{latch} can be found by plugging in the material parameters and ϵ_{act} .

To find the deformation of the multistable DEA sheets at the actuation (hot) and latched

(cold) states, we followed the same approach as we discussed here for the simple uniaxial case. However, our DEA sheets does not have a symmetric structure and the force generated due to Maxwell stresses is eccentric. This creates both bending and extension of the membranes (it is not pure bending or pure extension). When a voltage is applied across the dielectric membrane, it bends the device with a radius of the curvature ρ_0 and a neutral axis r_0 .

The deflection of the DEA sheets was analyzed using the Stoney's equations for the mechanical equilibrium. Here, we assumed that the Maxwell stress was uniform and remains constant during the deformation and the strain generated was small enough (<0.10) to use linear-elasticity model. To quantify the deformation, we used the force equilibrium in the tangential direction and the moment equilibrium about the z-axis. The force due to the deformation of all layers is equal to the force generated by the voltage applied to the dielectric membrane (force due to Maxwell stress). Adopting the ideal dielectric elastomer model, we write the equation for the force equilibrium in the tangential direction as:

$$\int_{A_{all}} \left(-Y_i \frac{r - r_0}{\rho_0}\right) dA = \int_{A_{die}} (\epsilon E^2) dA \quad (D.3)$$

where Y_i is the Young's modulus of i^{th} membrane, r_0 is the neutral axis, ρ_0 is the radius of curvature, ϵ is the permittivity of the dielectric membrane, and E is the applied electric field. A_{all} and A_{die} in this equation stand for the cross-section areas of all layers and the cross-section of the dielectric membrane, respectively. As the SMP layers have a grid shape (two fibers sets one aligned vertically and the other horizontally), their cross-section area is different than the uniform membranes. For the actuation, we assume that only one of the SMP fiber sets is softened and the other one remains stiff, e.g. when the vertically aligned SMP fibers are softened (horizontal ones kept cold) the bending occurs about a horizontal axis. The cross-section area of the SMP layer corresponds to the total cross-section of the soft fibers: $A_{SMP} = nwt$, where n is the number of (soft) fibers, w is the width of each fiber, and t is the thickness of the fiber. Similarly, the equation of the moment equilibrium about the z-axis can be written as:

$$\int_{A_{all}} \left(-Y_i \frac{r - r_0}{\rho_0}\right) y dA = \int_{A_{die}} (\epsilon E^2) y dA \quad (D.4)$$

We solve the two equations for unknown y_0 and ρ_0 . The angle of the deflection at the free end, generally referred as tip deflection angle can be found as:

$$\theta_{tip} = L/\rho_0 \quad (D.5)$$

Appendix D. Modeling the actuation and latching of SMP integrated DEAs

where L is the initial length of the beam.

Cooling down the SMPs at the actuated position locks in the deformation. Once the DEA voltage is removed, all membranes want to recover their initial configurations whereas the SMPs want to keep their deformed positions as they already fixed their deformations. Thus, the SMP layers oppose to the recovery of the other membranes. The dielectric elastomer sheet finds a new mechanical equilibrium where the tension in the layers is balanced by the contraction of the SMPs. The equation of the force equilibrium at this new state can be written as:

$$\int_{A_{other}} (-Y_i \epsilon_{latch}) dA = \int_{A_{SMP}} -Y_i \frac{\epsilon_{latch} - \epsilon_{act}}{1 + \epsilon_{act}} dA = 0 \quad (D.6)$$

where ϵ_{act} and ϵ_{latch} are the strains at the actuation and the latched states, respectively. A_{SMP} and A_{other} stands for the cross-section areas of the SMP layers and the other layers. As we can see from this equation, the stress in the materials without shape memory ability depends on their instant strain whereas the stress in the SMPs depends not only on their instant strain but also the strain at which they fix their deformations. The strain formulae for the actuation and the latching are:

$$\epsilon_{act} = \frac{r - r_0}{\rho_0} \quad (D.7)$$

$$\epsilon_{latch} = \frac{r - r_1}{\rho_1} \quad (D.8)$$

where r_1 and ρ_1 are the neutral axis and the radius of curvature at the latched state. Similar to the force equilibrium, the equation for the moment equilibrium can be written as:

$$\int_{A_{other}} (-Y_i \epsilon_{latch}) r dA = \int_{A_{SMP}} -Y_i \frac{\epsilon_{latch} - \epsilon_{act}}{1 + \epsilon_{act}} r dA = 0 \quad (D.9)$$

To find the bending stiffness of a latched curved device, we employed the usual form of Castigliano's first theorem. We applied this formula to the curved device that has a tip deflection angle of 270° . The displacement of the curved beam (Δ_y) due to an external force of P can be

expressed as:

$$\Delta_y = \int_{A_0}^{\theta_{tip}} \frac{M(\Theta)}{Y_i I_i} \frac{\partial M}{\partial P} ds \quad (D.10)$$

where M is the moment due to P, $Y_i I_i$ is the equivalent stiffness of the all layers with Y_i and I_i being the Young's modulus and the area moment of inertia of i^{th} membrane. The bending stiffness of this curved beam is then found as:

$$K_{bending} = \frac{P}{\Delta_y} \quad (D.11)$$

Bibliography

- [1] X. Ji, X. Liu, V. Cacucciolo, Y. Civet, A. El Haitami, S. Cantin, Y. Perriard, and H. Shea, “Untethered feel-through haptics using 18- μ m thick dielectric elastomer actuators,” *Advanced Functional Materials*, p. 2006639.
- [2] N. R. Sinatra, C. B. Teeple, D. M. Vogt, K. K. Parker, D. F. Gruber, and R. J. Wood, “Ultra-gentle manipulation of delicate structures using a soft robotic gripper,” *Science Robotics*, vol. 4, p. eaax5425, 2019.
- [3] T. van Manen, S. Janbaz, and A. A. Zadpoor, “Programming the shape-shifting of flat soft matter,” *Materials Today*, vol. 21, no. 2, pp. 144–163, 2018.
- [4] T. H. Ware, M. E. McConney¹, J. J. Wie¹, V. P. Tondiglia¹, and T. J. White¹, “Voxelated liquid crystal elastomers,” *Science*, vol. 347, p. 982, 2015.
- [5] S. Shian, K. Bertoldi, and D. R. Clarke, “Dielectric elastomer based “grippers” for soft robotics,” *Advanced Materials*, vol. 27, no. 43, pp. 6814–6819, 2015.
- [6] J. Shintake, S. Rosset, B. Schubert, D. Floreano, and H. Shea, “Versatile soft grippers with intrinsic electroadhesion based on multifunctional polymer actuators,” *Advanced Materials*, vol. 28, p. 231, 2016.
- [7] Z. S. Davidson¹, H. Shahsavan, A. Aghakhani, Y. Guo, L. Hines, Y. Xia, S. Yang, and M. Sitti, “Monolithic shape-programmable dielectric liquid crystal elastomer actuators,” *Science Advances*, vol. 5, p. eaay0855, 2019.
- [8] M. J. Ford, C. P. Ambulo, T. A. Kent, E. J. Markvicka, C. Pan, J. Malen, T. H. Ware, and C. Majidi, “A multifunctional shape-morphing elastomer with liquid metal inclusions,” *Proceedings of the National Academy of Sciences*, vol. 116, no. 43, pp. 21 438–21 444, 2019.
- [9] N. Besse, “Large array of shape memory polymer actuators for haptics and microfluidics,” EPFL, Tech. Rep., 2018.
- [10] A. Poulin, S. Rosset, and H. R. Shea, “Printing low-voltage dielectric elastomer actuators,” *Applied Physics Letters*, vol. 107, p. 244104, 2015.

Bibliography

- [11] M. A. Robertson, M. Murakami, W. Felt, and J. Paik, "A compact modular soft surface with reconfigurable shape and stiffness," *IEEE/ASME Transactions on Mechatronics*, vol. 24, no. 1, pp. 16–24, 2018.
- [12] S. Follmer, D. Leithinger, A. Olwal, A. Hogge, and H. Ishii, "inform: dynamic physical affordances and constraints through shape and object actuation." in *Uist*, vol. 13, no. 10.1145, 2013, pp. 2 501 988–2 502 032.
- [13] T. Thorsen, S. J. Maerkl, and S. R. Quake, "Microfluidic large-scale integration," *Science*, vol. 298, no. 5593, pp. 580–584, 2002.
- [14] G. M. Troiano, J. Tiab, and Y.-K. Lim, "Sci-fi: Shape-changing interfaces, future interactions," in *Proceedings of the 9th Nordic Conference on Human-Computer Interaction*, 2016, pp. 1–10.
- [15] V. Cacucciolo, J. Shintake, and H. Shea, "Delicate yet strong: Characterizing the electro-adhesion lifting force with a soft gripper," in *2019 2nd IEEE International Conference on Soft Robotics (RoboSoft)*. IEEE, 2019, pp. 108–113.
- [16] H. Kim, J. M. Boothby, S. Ramachandran, C. D. Lee, and T. H. Ware, "Tough, shape-changing materials: Crystallized liquid crystal elastomers," *Macromolecules*, vol. 50, p. 4267, 2017.
- [17] D. N. C. Nam and K. Ahn, "Identification of an ionic polymer metal composite actuator employing preisach type fuzzy narx model and particle swarm optimization," *Sensors and Actuators A: Physical*, vol. 183, p. 105, 2012.
- [18] I. P. Harrison and F. Spada, "Hydrogels for atopic dermatitis and wound management: A superior drug delivery vehicle," *Pharmaceutics*, vol. 10, 2018.
- [19] Example, "Proposal of flexible robotic arm with thin mckibben actuators mimicking octopus arm structure," *2016 IEEE/RSJ International Conference on Intelligent Robots and Systems (IROS)*, 2016.
- [20] Q. Ze, X. Kuang, S. Wu, J. Wong, S. M. Montgomery, R. Zhang, J. M. Kovitz, F. Yang, H. J. Qi, and R. Zhao, "Magnetic shape memory polymers with integrated multifunctional shape manipulation," *Advanced Materials*, vol. 32, p. 1906657, 2019.
- [21] M. Behl and A. Lendlein, "Shape-memory polymers," *Materials Today*, vol. 10, p. 20, 2007.
- [22] B. A. Kowalski, V. P. Tondiglia, T. Guin, and T. J. White, "Voxel resolution in the directed self-assembly of liquid crystal polymer networks and elastomers," *Soft Matter*, vol. 13, p. 4335, 2017.
- [23] J. E. Marshall, S. Gallagher, E. M. Terentjev, and S. K. Smoukov, "Anisotropic colloidal micromuscles from liquid crystal elastomers," *Journal of the American Chemical Society*, vol. 13, p. 474, 2014.

- [24] A. Sharma, A. Neshat, C. J. Mahnen, A. d. Nielsen, J. Snyder, T. L. Stankovich, B. G. Daum, E. M. LaSpina, G. Beltrano, Y. Gao, S. Li, B. Park, R. J. Clements, E. J. Freeman, C. Malcuit, J. A. McDonough, L. T. J. Korley, T. Hegmann, and E. Hegmann, "Biocompatible, biodegradable and porous liquid crystal elastomer scaffolds for spatial cell cultures," *Macromolecular Bioscience*, vol. 15, p. 200, 2015.
- [25] T. Guin, M. J. Settle, B. A. Kowalski, A. D. Auguste, R. V. Beblo, G. W. Reich, and T. J. White, "Layered liquid crystal elastomer actuators," *Nature Communications*, vol. 9, 2018.
- [26] I. Park, K. Jung, D. Kim, S. Kim, and K. J. Kim, "Physical principles of ionic polymer-metal composites as electroactive actuators and sensors," *MRS Bulletin*, vol. 33, p. 190, 2008.
- [27] M. Shahinpoor and K. J. Kim¹, "Ionic polymer-metal composites i. fundamentals," *Smart Materials and Structures*, vol. 10, p. 819, 2001.
- [28] S. Jeon, A. W. Hauser, and R. C. Hayward, "Shape-morphing materials from stimuli-responsive hydrogel hybrids," *Accounts of Chemical Research*, vol. 50, p. 161, 2017.
- [29] X. X. Le, W. Lu, J. W. Zhang, and T. Chen, "Recent progress in biomimetic anisotropic hydrogel actuators," *Advanced Science*, vol. 6, 2019.
- [30] J. Kopecek, "Polymer chemistry - swell gels," *Nature*, vol. 417, pp. 388–+, 2002.
- [31] N. El-Atab, R. B. Mishra, F. Al-Modaf, L. Joharji, A. A. Alsharif, H. Alamoudi, M. Diaz, N. Qaiser, and M. M. Hussain, "Soft actuators for soft robotic applications: A review," *Advanced Intelligent Systems*, p. 2000128, 2020.
- [32] I. A. Anderson, T. Hale, T. Gisby, T. Inamura, T. McKay, B. O'Brien, S. Walbran, and E. P. Calius, "A thin membrane artificial muscle rotary motor," *Applied Physics A*, vol. 98, no. 1, p. 75, 2010.
- [33] G. Kofod, M. Paaanen, and S. Bauer, "Self-organized minimum-energy structures for dielectric elastomer actuators," *Applied Physics A*, vol. 85, no. 2, pp. 141–143, 2006.
- [34] C. Keplinger, T. Li, R. Baumgartner, Z. Suo, and S. Bauer, "Harnessing snap-through instability in soft dielectrics to achieve giant voltage-triggered deformation," *Soft Matter*, vol. 8, no. 2, pp. 285–288, 2012.
- [35] L. Maffli, S. Rosset, M. Ghilardi, F. Carpi, and H. Shea, "Ultrafast all-polymer electrically tunable silicone lenses," *Advanced Functional Materials*, vol. 25, p. 1656, 2015.
- [36] Q. Zhang, H. Li, M. Poh, F. Xia, Z.-Y. Cheng, H. Xu, and C. Huang, "An all-organic composite actuator material with a high dielectric constant," *Nature*, vol. 419, no. 6904, pp. 284–287, 2002.
- [37] J.-S. Plante and S. Dubowsky, "Large-scale failure modes of dielectric elastomer actuators," *International journal of solids and structures*, vol. 43, no. 25-26, pp. 7727–7751, 2006.

- [38] G. Z. Lum, Z. Ye, X. Dong, H. Marvi, O. Erin, W. Hu, and M. Sitti, "Shape-programmable magnetic soft matter," *Proceedings of the National Academy of Sciences*, vol. 113, p. E6007, 2016.
- [39] M. Sitti, H. Ceylan, W. Hu, J. Giltinan, M. Turan, S. Yim, and E. Diller, "Biomedical applications of untethered mobile milli microrobots," *Proceedings of the IEEE*, vol. 103, no. 2, pp. 205–224, 2015.
- [40] S. Fusco, H.-W. Huang, K. E. Peyer, C. Peters, M. Haberli, A. Ulbers, A. Spyrogianni, E. Pellicer, J. Sort, S. E. Pratsinis *et al.*, "Shape-switching microrobots for medical applications the influence of shape in drug delivery and locomotion," *ACS applied materials & interfaces*, vol. 7, no. 12, pp. 6803–6811, 2015.
- [41] A. Lendlein and S. Kelch, "Shape-memory polymers," *Angewandte Chemie International Edition*, vol. 41, no. 12, pp. 2034–2057, 2002.
- [42] H. Jiang, S. Kelch, and A. Lendlein, "Polymers move in response to light," *Advanced Materials*, vol. 18, no. 11, pp. 1471–1475, 2006.
- [43] J. M. McCracken, B. R. Donovan, and T. White, "Materials as machines," *Advanced Materials*, p. 1906564, 2020.
- [44] E. Hornbogen, "Comparison of shape memory metals and polymers," *Advanced engineering materials*, vol. 8, no. 1-2, pp. 101–106, 2006.
- [45] K. Takashima, J. Rossiter, and T. Mukai, "Mckibben artificial muscle using shape-memory polymer," *Sensors and Actuators A: Physical*, vol. 164, p. 116, 2010.
- [46] F. Connolly, P. Polygerinos, C. J. Walsh, and K. Bertoldi, "Mechanical programming of soft actuators by varying fiber angle," *Soft Robotics*, vol. 2, p. 26, 2015.
- [47] S. A. Morin, S. W. Kwok, J. Lessing, J. Ting, R. F. Shepherd, A. A. Stokes, and G. M. Whitesides, "Elastomeric tiles for the fabrication of inflatable structures," *Advanced Functional Materials*, vol. 24, p. 5541, 2014.
- [48] P. Polygerinos, N. Correll, S. A. Morin, B. Mosadegh, C. D. Onal, K. Petersen, M. Cianchetti, M. T. Tolley, and R. F. Shepherd, "Soft robotics: Review of fluid-driven intrinsically soft devices; manufacturing, sensing, control, and applications in human-robot interaction," *Advanced Engineering Materials*, vol. 19, p. 1700016, 2017.
- [49] K. C. Galloway, K. P. Becker, B. Phillips, J. Kirby, S. Licht, D. Tchernov, R. J. Wood, and D. F. Gruber, "Soft robotic grippers for biological sampling on deep reefs," *Soft Robotics*, vol. 3, p. 23, 2016.
- [50] R. L. Truby, M. Wehner, A. K. Grosskopf, D. M. Vogt, S. G. M. Uzel, R. J. Wood, and J. A. Lewis, "Soft somatosensitive actuators via embedded 3d printing," *Advanced Materials*, vol. 30, p. 1706383, 2018.

-
- [51] "A glove powered by soft robotics to interact with virtual reality environments." [Online]. Available: http://jacobsschool.ucsd.edu/news/news_releases/release.sfe?id=2225
- [52] "Human dexterity, anywhere in the world." [Online]. Available: <https://haptx.com/robotics/>
- [53] I. Choi, N. Corson, L. Peiros, E. W. Hawkes, S. Keller, and S. Follmer, "A soft, controllable, high force density linear brake utilizing layer jamming," *IEEE Robotics and Automation Letters*, vol. 3, no. 1, pp. 450–457, 2017.
- [54] S. V. Krichel, O. Sawodny, and A. Hildebrandt, "Tracking control of a pneumatic muscle actuator using one servovalve," in *Proceedings of the 2010 American Control Conference*. IEEE, 2010, pp. 4385–4390.
- [55] B. Wang, A. McDaid, M. Biglari-Abhari, T. Giffney, and K. Aw, "A bimorph pneumatic bending actuator by control of fiber braiding angle," *Sensors and Actuators A: Physical*, vol. 257, pp. 173–184, 2017.
- [56] A. Miriyev, K. Stack, and H. Lipson, "Soft material for soft actuators," *Nature communications*, vol. 8, no. 1, pp. 1–8, 2017.
- [57] R. Pelrine, R. Kornbluh, Q. B. Pei, and J. Joseph, "High-speed electrically actuated elastomers with strain greater than 100%," *Science*, vol. 287, pp. 836–839, 2000.
- [58] G. Y. Gu, J. Zhu, L. M. Zhu, and X. Y. Zhu, "A survey on dielectric elastomer actuators for soft robots," *Bioinspiration & Biomimetics*, vol. 12, 2017.
- [59] X. Ji, X. Liu, V. Cacucciolo, M. Imboden, Y. Civet, A. Haitami, S. Cantin, Y. Perriard, and H. Shea, "An autonomous untethered fast soft robotic insect driven by low-voltage dielectric elastomer actuators," *Science Robotics*, vol. 4, p. eaaz6451, 2019.
- [60] M. Duduta, E. Hajiesmaili, H. Zhao, R. J. Wood, and D. R. Clarke, "Realizing the potential of dielectric elastomer artificial muscles," *Proceedings of the National Academy of Sciences*, vol. 116, p. 2476, 2019.
- [61] S. Hau, G. Rizzello, and S. Seelecke, "A novel dielectric elastomer membrane actuator concept for high force applications," *Extreme Mechanics Letters*, vol. 23, p. 24, 2018.
- [62] G. Kovacs, L. Düring, S. Michel, and G. Terrasi, "Stacked dielectric elastomer actuator for tensile force transmission," *Sensors and Actuators A: Physical*, vol. 155, p. 2009, 2009.
- [63] T. Lu, J. Huang, C. Jordi, G. Kovacs, R. Huang, D. R. Clarke, and Z. Suo, "Dielectric elastomer actuators under equal-biaxial forces, uniaxial forces, and uniaxial constraint of stiff fibers," *Soft Matter*, vol. 8, no. 22, pp. 6167–6173, 2012.
- [64] L. Hines, K. Petersen, G. Z. Lum, and M. Sitti, "Soft actuators for small-scale robotics," *Advanced Materials*, vol. 29, p. 1603483, 2017.

Bibliography

- [65] E. Diller, J. Zhuang, G. Z. Lum, M. R. Edwards, and M. Sitti, "Continuously distributed magnetization profile for millimeter-scale elastomeric undulatory swimming," *Applied Physics Letters*, vol. 104, p. 174101, 2014.
- [66] A. Beyzavi and N. Nguyen, "Programmable two-dimensional actuation of ferrofluid droplet using planar microcoils," *Journal of Micromechanics and Microengineering*, vol. 20, p. 015018, 2010.
- [67] S. W. Jin, J. Park, S. Y. Hong, H. Park, Y. R. Jeong, J. Park, S. S. Lee, , and J. S. Ha, "Stretchable loudspeaker using liquid metal microchannel," *Scientific Reports*, vol. 5, 2015.
- [68] T. N. Do, H. Phan, T. Nguyen, and Y. Visell, "Miniature soft electromagnetic actuators for robotic applications," *Advanced Functional Materials*, vol. 28, p. 1800244, 2018.
- [69] C. Liu, H. Qin, and P. T. Mather, "Review of progress in shape-memory polymers," *Journal of Materials Chemistry*, vol. 17, p. 1543, 2007.
- [70] C. Liu, S. B. Chun, P. T. Mather, L. Zheng, E. H. Haley, and E. B. Coughlin, "Chemically crosslinked polycyclooctene. synthesis, characterization, and shape memory behavior," *Macromolecules*, vol. 35, p. 9868, 2002.
- [71] W. M. Huang, Z. Ding, C. C. Wang, J. Wei, Y. Zhao, and H. Purnawali, "Shape memory materials," *Materials Today*, vol. 13, p. 54, 2010.
- [72] D. Ratna and J. Karger-Kocsis, "Recent advances in shape memory polymers and composites: a review," *Journal of Materials Science*, vol. 43, no. 1, pp. 254–269, 2008.
- [73] M. Behl, M. Y. Razzaq, and A. Lendlein, "Multifunctional shape-memory polymers," *Advanced Materials*, vol. 22, p. 3388, 2010.
- [74] T. Chen, O. R. Bilal, K. Shea, and C. Daraio, "Harnessing bistability for directional propulsion of soft, untethered robots," *Proceedings of the National Academy of Sciences*, vol. 115, p. 5698, Chen2018.
- [75] Q. Ge, A. H. Sakhaei, H. Lee, C. K. Dunn, N. X. Fang, and M. L. Dunn, "Multimaterial 4d printing with tailorable shape memory polymers," *Scientific Reports*, vol. 6, 2016.
- [76] A. Lendlein and O. E. C. Gould, "Reprogrammable recovery and actuation behaviour of shape-memory polymers," *Nature Reviews Materials*, vol. 4, p. 116, 2019.
- [77] M. Behl, K. Kratz, J. Zotzmann, U. Nöchel, and A. Lendlein, "Reversible bidirectional shape-memory polymers," *Advanced Materials*, vol. 25, p. 4466, 2013.
- [78] H. Zhao, A. M. Hussain, M. Duduta, D. M. Vogt, R. J. Wood, and D. R. Clarke, "Compact dielectric elastomer linear actuators," *Advanced Functional Materials*, vol. 28, no. 42, p. 1804328, 2018.

-
- [79] P. Brochu and Q. Pei, "Dielectric elastomers for actuators and artificial muscles," in *Electroactivity in Polymeric Materials*. Springer, 2012, pp. 1–56.
- [80] Y. Chen, H. Zhao, J. Mao, P. Chirarattananon, E. F. Helbling, N.-s. P. Hyun, D. R. Clarke, and R. J. Wood, "Controlled flight of a microrobot powered by soft artificial muscles," *Nature*, vol. 575, no. 7782, pp. 324–329, 2019.
- [81] F. Carpi, C. Salaris, and D. De Rossi, "Folded dielectric elastomer actuators," *Smart Materials and Structures*, vol. 16, no. 2, p. S300, 2007.
- [82] M. Duduta, E. Hajiesmaili, H. Zhao, R. J. Wood, and D. R. Clarke, "Realizing the potential of dielectric elastomer artificial muscles," *Proceedings of the National Academy of Sciences*, vol. 116, no. 7, pp. 2476–2481, 2019.
- [83] W. Liang, H. Liu, K. Wang, Z. Qian, L. Ren, and L. Ren, "Comparative study of robotic artificial actuators and biological muscle," *Advances in Mechanical Engineering*, vol. 12, no. 6, p. 1687814020933409, 2020.
- [84] M. Shahinpoor and K. J. Kim, "Ionic polymer–metal composites: Iv. industrial and medical applications," *Smart materials and structures*, vol. 14, no. 1, p. 197, 2004.
- [85] C. Huang, Q. Zhang, and A. Jáklí, "Nematic anisotropic liquid-crystal gels—self-assembled nanocomposites with high electromechanical response," *Advanced Functional Materials*, vol. 13, no. 7, pp. 525–529, 2003.
- [86] V. Srivastava, S. A. Chester, and L. Anand, "Thermally actuated shape-memory polymers: Experiments, theory, and numerical simulations," *Journal of the Mechanics and Physics of Solids*, vol. 58, no. 8, pp. 1100–1124, 2010.
- [87] K. Wang, Y.-G. Jia, and X. Zhu, "Two-way reversible shape memory polymers made of cross-linked cocrystallizable random copolymers with tunable actuation temperatures," *Macromolecules*, vol. 50, no. 21, pp. 8570–8579, 2017.
- [88] T. Mitsumata, Y. Horikoshi, and K. Negami, "High-power actuators made of two-phase magnetic gels," *Japanese Journal of Applied Physics*, vol. 47, no. 9R, p. 7257, 2008.
- [89] Y. Kim, H. Yuk, R. Zhao, S. A. Chester, and X. Zhao, "Printing ferromagnetic domains for untethered fast-transforming soft materials," *Nature*, vol. 558, no. 7709, pp. 274–279, 2018.
- [90] S. Miyashita, E. Diller, and M. Sitti, "Two-dimensional magnetic micro-module reconfigurations based on inter-modular interactions," *The International Journal of Robotics Research*, vol. 32, no. 5, pp. 591–613, 2013.
- [91] T. Guin, M. J. Settle, B. A. Kowalski, A. D. Augustine, R. V. Beblo, G. W. Reich, and T. J. White, "Layered liquid crystal elastomer actuators," *Nature communications*, vol. 9, no. 1, pp. 1–7, 2018.

Bibliography

- [92] B. Mosadegh, P. Polygerinos, C. Keplinger, S. Wennstedt, R. F. Shepherd, U. Gupta, J. Shim, K. Bertoldi, C. J. Walsh, and G. M. Whitesides, "Pneumatic networks for soft robotics that actuate rapidly," *Advanced functional materials*, vol. 24, no. 15, pp. 2163–2170, 2014.
- [93] S. M. Mirvakili and I. W. Hunter, "Artificial muscles: Mechanisms, applications, and challenges," *Advanced Materials*, vol. 30, no. 6, p. 1704407, 2018.
- [94] M. Ma, L. Guo, D. G. Anderson, and R. Langer, "Bio-inspired polymer composite actuator and generator driven by water gradients," *Science*, vol. 339, no. 6116, pp. 186–189, 2013.
- [95] X. Niu, X. Yang, P. Brochu, H. Stoyanov, S. Yun, Z. Yu, and Q. Pei, "Bistable large-strain actuation of interpenetrating polymer networks," *Advanced Materials*, vol. 24, p. 6513, 2012.
- [96] D. McCoul, S. Rosset, N. Besse, and H. Shea, "Multifunctional shape memory electrodes for dielectric elastomer actuators enabling high holding force and low-voltage multisegment addressing," *Smart Materials and Structures*, vol. 26, p. 025015, 2017.
- [97] A. Khaldi, J. A. Elliott, and S. K. Smoukov, "Electro-mechanical actuator with muscle memory," *J. Mater. Chem. C*, vol. 2, p. 9318, 2014.
- [98] Y. Qiu, Z. Lu, and Q. Pei, "Refreshable tactile display based on a bistable electroactive polymer and a stretchable serpentine joule heating electrode," *ACS Applied Materials and Interfaces*, vol. 10, p. 24807, 2018.
- [99] N. Besse, S. Rosset, J. J. Zarate, and H. Shea, "Flexible active skin. large reconfigurable arrays of individually addressed shape memory polymer actuators," *Advanced Materials Technologies*, vol. 2, p. 1700102, 2017.
- [100] X. Niu, P. Brochu, H. Stoyanov, S. R. Yun, and Q. Pei, "Bistable electroactive polymer for refreshable braille display with improved actuation stability," *Electroactive Polymer Actuators and Devices (EAPAD)*, 2012.
- [101] J. Peirs, D. Reynaerts, and H. Van Brussel, "Scale effects and thermal considerations for micro-actuators," in *Proceedings. 1998 IEEE International Conference on Robotics and Automation (Cat. No. 98CH36146)*, vol. 2. IEEE, 1998, pp. 1516–1521.
- [102] B. Aksoy, N. Besse, R. J. Boom, B.-J. Hoogenberg, M. Blom, and H. Shea, "Latchable microfluidic valve arrays based on shape memory polymer actuators," *Lab on a Chip*, vol. 19, no. 4, pp. 608–617, 2019.
- [103] N. Besse, B. Aksoy, and H. Shea, "Large arrays of microfabricated shape memory polymer actuators for haptics and microfluidics," in *ACTUATOR 2018; 16th International Conference on New Actuators*. VDE, 2018, pp. 1–4.
- [104] N. Besse, R. Boom, B. Hoogenberg, B. Aksoy, M. Bloom, and H. Shea, "Array of independent microfluidic valves driven by shape memory polymer actuators using a single

- pneumatic supply,” in *Miniaturized Systems for Chemistry and Life Sciences (MicroTAS)*, October 2017, pp. 651–652.
- [105] W. H. Grover, R. H. Ivester, E. C. Jensen, and R. A. Mathies, “Development and multiplexed control of latching pneumatic valves using microfluidic logical structures,” *Lab on a Chip*, vol. 6, no. 5, pp. 623–631, 2006.
 - [106] K. Eyer, P. Kuhn, C. Hanke, and P. S. Dittrich, “A microchamber array for single cell isolation and analysis of intracellular biomolecules,” *Lab on a Chip*, vol. 12, no. 4, pp. 765–772, 2012.
 - [107] E. C. Jensen, A. M. Stockton, T. N. Chiesl, J. Kim, A. Bera, and R. A. Mathies, “Digitally programmable microfluidic automaton for multiscale combinatorial mixing and sample processing,” *Lab on a Chip*, vol. 13, no. 2, pp. 288–296, 2013.
 - [108] S. J. Maerkl and S. R. Quake, “Experimental determination of the evolvability of a transcription factor,” *Proceedings of the National Academy of Sciences*, vol. 106, no. 44, pp. 18 650–18 655, 2009.
 - [109] D. Mark, S. Haeberle, G. Roth, F. Von Stetten, and R. Zengerle, “Microfluidic lab-on-a-chip platforms: requirements, characteristics and applications,” in *Microfluidics based microsystems*. Springer, 2010, pp. 305–376.
 - [110] D. W. Lee and Y.-H. Cho, “High-radix microfluidic multiplexer with pressure valves of different thresholds,” *Lab on a Chip*, vol. 9, no. 12, pp. 1681–1686, 2009.
 - [111] A. Richter, D. Kuckling, S. Howitz, T. Gehring, and K.-F. Arndt, “Electronically controllable microvalves based on smart hydrogels: magnitudes and potential applications,” *Journal of microelectromechanical systems*, vol. 12, no. 5, pp. 748–753, 2003.
 - [112] H. Takehara, C. Jiang, K. Uto, M. Ebara, T. Aoyagi, and T. Ichiki, “Novel microfluidic valve technology based on shape memory effect of poly (ϵ -caprolactone),” *Applied Physics Express*, vol. 6, no. 3, p. 037201, 2013.
 - [113] B. Yang and Q. Lin, “A latchable phase-change microvalve with integrated heaters,” *Journal of microelectromechanical systems*, vol. 18, no. 4, pp. 860–867, 2009.
 - [114] C. de Saint-Aubin, S. Rosset, S. Schlatter, and H. Shea, “High-cycle electromechanical aging of dielectric elastomer actuators with carbon-based electrodes,” *Smart Materials and Structures*, vol. 27, no. 7, p. 074002, 2018.
 - [115] H. J. Kim, D. Huh, G. Hamilton, and D. E. Ingber, “Human gut-on-a-chip inhabited by microbial flora that experiences intestinal peristalsis-like motions and flow,” *Lab on a Chip*, vol. 12, no. 12, pp. 2165–2174, 2012.
 - [116] Y. Reissis, E. García-Gareta, M. Korda, G. W. Blunn, and J. Hua, “The effect of temperature on the viability of human mesenchymal stem cells,” *Stem cell research & therapy*, vol. 4, no. 6, p. 139, 2013.

Bibliography

- [117] M. A. Unger, H.-P. Chou, T. Thorsen, A. Scherer, and S. R. Quake, "Monolithic microfabricated valves and pumps by multilayer soft lithography," *Science*, vol. 288, no. 5463, pp. 113–116, 2000.
- [118] H. Lai and A. Folch, "Design and dynamic characterization of "single-stroke" peristaltic pdms micropumps," *Lab on a Chip*, vol. 11, no. 2, pp. 336–342, 2011.
- [119] H. Chuang, A. Amin, S. Wereley, M. Thottethodi, T. VijayKumar, and S. Jacobson, "Polydimethylsiloxane (pdms) peristaltic pump characterization for programmable lab-on-a-chip applications," in *Proceedings of the 12th international conference on miniaturized systems for chemistry and life sciences*, vol. 12, 2008.
- [120] S. N. Bhatia and D. E. Ingber, "Microfluidic organs-on-chips," *Nature biotechnology*, vol. 32, no. 8, pp. 760–772, 2014.
- [121] E. K. Sackmann, A. L. Fulton, and D. J. Beebe, "The present and future role of microfluidics in biomedical research," *Nature*, vol. 507, no. 7491, pp. 181–189, 2014.
- [122] B. Aksoy and H. Shea, "Reconfigurable and latchable shape-morphing dielectric elastomers based on local stiffness modulation," *Advanced Functional Materials*, p. 2001597, 2020.
- [123] B. Aksoy and S. Herbert, "Dynamically reconfigurable DEAs incorporating shape memory polymer fibers," in *Electroactive Polymer Actuators and Devices (EAPAD) XXI*, Y. Bar-Cohen, Ed., vol. 10966, International Society for Optics and Photonics. SPIE, 2019, pp. 270 – 282.
- [124] B. Aksoy and H. R. Shea, "An analytical model and its validation for the design of multi-stable dielectric elastomer actuators with high-blocking forces (conference presentation)," in *Electroactive Polymer Actuators and Devices (EAPAD) XXII*, vol. 11375. International Society for Optics and Photonics, 2020, p. 113751N.
- [125] E. Hajiesmaili and D. R. Clarke, "Reconfigurable shape-morphing dielectric elastomers using spatially varying electric fields," *Nature communications*, vol. 10, no. 1, pp. 1–7, 2019.
- [126] J. A. Faber, A. F. Arrieta, and A. R. Studart, "Bioinspired spring origami," *Science*, vol. 359, no. 6382, pp. 1386–1391, 2018.
- [127] A. A. Stanley and A. M. Okamura, "Controllable surface haptics via particle jamming and pneumatics," *IEEE transactions on haptics*, vol. 8, no. 1, pp. 20–30, 2015.
- [128] R. Fernandes and D. H. Gracias, "Self-folding polymeric containers for encapsulation and delivery of drugs," *Advanced drug delivery reviews*, vol. 64, no. 14, pp. 1579–1589, 2012.
- [129] J. Blaber, B. Adair, and A. Antoniou, "Ncorr: open-source 2d digital image correlation matlab software," *Experimental Mechanics*, vol. 55, no. 6, pp. 1105–1122, 2015.

-
- [130] J. Sheng, H. Chen, J. Qiang, B. Li, and Y. Wang, "Thermal, mechanical, and dielectric properties of a dielectric elastomer for actuator applications," *Journal of Macromolecular Science, Part B*, vol. 51, no. 10, pp. 2093–2104, 2012.
- [131] G. Kofod, "The static actuation of dielectric elastomer actuators: how does pre-stretch improve actuation?" *Journal of Physics D: Applied Physics*, vol. 41, no. 21, p. 215405, 2008.
- [132] R. Huang and Z. Suo, "Electromechanical phase transition in dielectric elastomers," *Proceedings of the Royal Society A: Mathematical, Physical and Engineering Sciences*, vol. 468, no. 2140, pp. 1014–1040, 2012.
- [133] A. N. Gent, "A new constitutive relation for rubber," *Rubber chemistry and technology*, vol. 69, no. 1, pp. 59–61, 1996.
- [134] G. Holzapfel, "Nonlinear solid mechanics: A continuum approach for engineering."
- [135] X. Zhao and Z. Suo, "Method to analyze electromechanical stability of dielectric elastomers," *Applied Physics Letters*, vol. 91, no. 6, p. 061921, 2007.
- [136] G. G. Stoney, "The tension of metallic films deposited by electrolysis," *Proceedings of the Royal Society of London. Series A, Containing Papers of a Mathematical and Physical Character*, vol. 82, no. 553, pp. 172–175, 1909.
- [137] E. J. Hearn, *Mechanics of Materials 2: The mechanics of elastic and plastic deformation of solids and structural materials*. Elsevier, 1997.
- [138] G. Mao, M. Drack, M. Karami-Mosammam, D. Wirthl, T. Stockinger, R. Schwödiauer, and M. Kaltenbrunner, "Soft electromagnetic actuators," *Science advances*, vol. 6, no. 26, p. eabc0251, 2020.
- [139] M. J. Ford, D. K. Patel, C. Pan, S. Bergbreiter, and C. Majidi, "Controlled assembly of liquid metal inclusions as a general approach for multifunctional composites," *Advanced Materials*, vol. 32, no. 46, p. 2002929, 2020.
- [140] J. J. Zárate, G. Tosolini, S. Petroni, M. De Vittorio, and H. Shea, "Optimization of the force and power consumption of a microfabricated magnetic actuator," *Sensors and Actuators A: Physical*, vol. 234, pp. 57–64, 2015.

Nomenclature

CB/PDMS	Carbon-black loaded PDMS
DEA	Dielectric elastomer actuator
DIC	Digital Image Correlation
DMF	Dimethylformamide
DMSO	Dimethyl sulfoxide
DoF	Degress of freedom
E	Electric field
EGaIn	Eutectic Gallium Indium
EMSA	Electromagnetic soft actuator
ϵ	Permittivity
ϵ_f	Final strain after shape fixation
ϵ_m	Applied mechanical strain
ϵ_p	Permanent strain after shape recovery
ϵ_{xx}	Longitudinal component of strain
ϵ_{xy}	Shear component of strain
ϵ_{yy}	Lateral component of strain
FEM	Finite element modeling
IEAP	Ionic electroactive polymer
λ	Stretch ratio
LCE	Liquid crystal elastomer
LMC	Liquid metal coils
mLSI	Microfluidic large scale integration
n	Director field
NC	Normally closed
NO	Normally open

Nomenclature

ν	Poisson's ratio
PCB	Printed circuit board
PET	Polyethylene terephthalate
PMMA	Poly(methyl methacrylate)
PS	Polystyrene
PSA	Pneumatic soft actuator
r	neutral axis
R_f	Strain fixity rate
ρ	radius of curvature
R_r	Strain recovery rate
SEBS	Styrene-Ethylene-Butylene-Styrene
SEMA	Soft electromagnetic actuator
σ	Stress
SMP	Shape memory polymers
T_g	Glass transition temperature
T_m	Melting temperature
VCC	Voltage common collector
$W_{stretch}$	Helmholtz free energy
Y	Young's modulus
Y'	Storage modulus
Y''	Loss modulus

List of publications

Journal articles

- **B. Aksoy** and H. Shea, "Reconfigurable and latchable shape-morphing dielectric elastomers based on local stiffness modulation," *Advanced Functional Materials*, p. 2001597, 2020.
- **B. Aksoy**, N. Besse, R. J. Boom, B.-J. Hoogenberg, M. Blom, and H. Shea, "Latchable microfluidic valve arrays based on shape memory polymer actuators," *Lab on a Chip*, vol. 19, no. 4, pp. 608–617, 2019.

Conference proceedings and oral presentations

- **B. Aksoy** and H. Shea, "Modeling Shape-Programmable and Reconfigurable Dielectric Elastomer Actuator Sheets", 2020 MRS Spring and Fall Meeting.
- **B. Aksoy** and H. Shea, "An analytical model and its validation for the design of multi-stable dielectric elastomer actuators with high-blocking forces" in *Electroactive Polymer Actuators and Devices (EAPAD) XXII*, vol. 11375. International Society for Optics and Photonics, 2020, p. 113751N.
- **B. Aksoy** and H. Shea, "Dynamically reconfigurable DEAs incorporating shape memory polymer fibers," in *Electroactive Polymer Actuators and Devices (EAPAD) XXI*, vol. 10966. International Society for Optics and Photonics, 2019, p. 109661Y.
- N. Besse, **B. Aksoy**, and H. Shea, "Large arrays of microfabricated shape memory polymer actuators for haptics and microfluidics," in *ACTUATOR 2018; 16th International Conference on New Actuators*, VDE, 2018, pp. 1–4.
- N. Besse, R. J. Boom, B. J. Hoogenberg, **B. Aksoy**, M. Bloom, and H. Shea, "Array of independent microfluidic valves driven by shape memory polymer actuators using a single pneumatic supply," in *Miniaturized Systems for Chemistry and Life Sciences (Micro-TAS)*, October 2017, pp. 651–652.

Bekir Aksoy

Rue de la Dime 41, CH-2000 Neuchatel-Switzerland

+41 76 530 7252

bekir.aksoy@epfl.ch

Education

2017 – present	PhD in Microelectronics and Microsystems <i>Ecole Polytechnique Federale de Lausanne, Switzerland</i>
2014 – 2017	M.Sc. in Mechanical Engineering <i>Koc University, Turkey</i>
2014 – 2014	Exchange program <i>University of Pittsburgh, USA</i>
2008 – 2014	B.S. in Mechanical Engineering Double major in Electrical and Electronics Engineering <i>Koc University, Turkey</i>

Selected publications & Patent applications ([link to full list](#))

B. Aksoy and H. Shea, "Reconfigurable and latchable shape-morphing dielectric elastomers based on local stiffness modulation", *Adv. Funct. Mater.*, (2020).

B. Aksoy, and N. Besse, et al., "Latchable microfluidic valve arrays based on shape memory polymer actuators", *Lab Chip*, (2019).

S. Dogru, **B. Aksoy**, H. Bayraktar, and B.E. Alaca, "Poisson's ratio of PDMS thin films", *Polym. Test.*, (2018).

B. Aksoy, A. Rehman, H. Bayraktar, and B.E. Alaca, "High-resolution spatiotemporal strain mapping reveals non-uniform deformation in micropatterned elastomers", *J. Micromech. Microeng.*, (2017).

O. Aydin and **B. Aksoy** et. al, "Time-resolved local strain tracking microscopy for cell mechanics", *Rev. Sci. Instrum.*, (2016).

O. Onal, B. Gumus, **B. Aksoy**, G. Gerstein, B.E. Alaca, H.J. Maier, and D. Canadinc, "Micro-Scale Cyclic Bending Response of NiTi Shape Memory Alloy", *Mater. Trans.*, (2016).

B.E. Alaca, Y. Leblebici, I. Yorulmaz, Y. Kilinc, **B. Aksoy**, "Nanomechanical resonator array and production method thereof", US Patent: 9,413,333.

Selected conference presentations

B. Aksoy and H. Shea, "Modeling Shape-programmable and Reconfigurable Dielectric Elas-

Curriculum Vitae

tomers Actuator Sheets", MRS Spring/Fall Meeting, November 2020.

B. Aksoy and H. Shea, "An analytical model and its validation for the design of multistable dielectric elastomer actuators with high blocking forces", SPIE XXII, online conference presentation, April 2020.

B. Aksoy and H. Shea, "Dynamically reconfigurable DEAs incorporating shape memory polymer fibers", SPIE XXI, Denver, March 2019.

N.Besse, **B. Aksoy**, and H. Shea, "Large Arrays of Microfabricated Shape Memory Polymer Actuators for Haptics and Microfluidics", Actuators, Bremen, June 2018.

Technical skills

Simulation & CAD	Comsol, Siemens NX, Solidworks.
Programming	Matlab, LabVIEW, Python.
Design & word	Inkscape, Illustrator, Photoshop, MS Office, LaTeX.
Polymer processing	Soft lithography, pad-printing, FDM 3D printing, spin coating.
MEMS fabrication	Photolithography, etching, sputtering.
Characterization	Mechanical testing, DMA, fluorescence microscope, SEM.
Macro-machining	CNC machining, milling, laser cutting.

Teaching assistant

Fall	2019	Mechanism Design -BSc course at EPFL.
Spring	2019	Robotics Practicals -MSc course at EPFL.
Spring	2018	Statics and Dynamics -BSc course at EPFL.
Fall	2017	Product Design and System Engineering -MSc course at EPFL.
Spring	2017	Statics and Dynamics -BSc course at EPFL.
Fall	2016	Machine Design -BSc course at Koc University.
Spring	2016	Engineering Materials -BSc course at Koc University.
Fall	2015	Machine Design -BSc course at Koc University. Mechanical Engineering Lab -BSc course at Koc University.
Spring	2015	Engineering Materials -BSc course at Koc University.
Fall	2014	Programming with Java -BSc course at Koc University.

Internships

Summer 2013	TOFAS Automotive Company. Bursa, Turkey
Summer 2012	Silverline Appliances. Amasya, Turkey

Scholarships & Awards

2016 – 2017	Koc University Graduate Scholarship <i>full MSc scholarship</i>
2014 – 2016	Tubitak Graduate Scholarship - <i>from the Scientific and Technological Research Council of Turkey.</i>
2009 – 2014	5 times Vehbi Koc Honor Award - <i>given to students with SPA higher than 3.50.</i>
2008 – 2014	Koc University undergraduate full-scholarship - <i>for high ranking in the national university entrance exam.</i>

Soft skills

Language	Kurdish (native), Turkish (bilingual), English (fluent)
Interests	Toastmasters, Charcoal drawing, Football & cycling.